# Oxide-Ion Conductors for Energy Applications: Structure and Properties

## MATTHEW SIMON CHAMBERS

# Oxide-Ion Conductors for Energy Applications: Structure and Properties

Matthew Simon Chambers

Durham University

Diamond Light Source Ltd

A thesis submitted in partial fulfilment of the requirements for the degree of Doctor of Philosophy.

Supervisors: Prof. Ivana Radosavljevic Evans, Prof. John S. O. Evans, Dr Phil A. Chater

Department of Chemistry

Durham University

2019

# Abstract

***Oxide-Ion Conductors for Energy Applications: Structure and Properties***

PhD Thesis                      Matthew S. Chambers                      2019

This thesis describes experiments aimed at understanding the average and local structure of a range of different oxide-ion conductors, with the aim of applying this insight to designing better materials.

The main experimental technique used was neutron total scattering, and **Chapter 1** reviews the previous literature concerning the application of this technique to oxide-ion conductors.

**Chapter 2** describes the synthetic and characterisation techniques employed to investigate the materials in this study.

**Chapter 3** discusses the attempted synthesis of $Ge_{5-x}Al_x(PO_4)_6O_{1-x/2}$ ($x$ = 0, 0.1, 0.2, 0.3, 0.5, 1, 2) materials, which we hoped would be new examples of mixed-coordination-number oxide-ion conductors. Powder X-ray diffraction and elemental analysis suggested that $Al^{3+}$ was successfully doped into the parent. The electrical properties of $x$ = 0, 0.2, 0.5 and 1 samples were measured for the first time, and showed an increase in conductivity with increasing $x$. However, solid-state nuclear magnetic resonance spectroscopy experiments showed that $Al^{3+}$ was not incorporated in the main phase, but instead formed a likely amorphous aluminium-phosphate phase. These materials have therefore not been pursued further.

**Chapter 4** discusses investigations into the long range and local structures of $La_8R_2(GeO_4)_6O_{3-y}$ (R = Sr, La, Bi; $y$ = 0, 1) apatite-type oxide-ion conductors using high-resolution powder synchrotron diffraction, high-resolution powder neutron diffraction and neutron total scattering. $La_8Sr_2(GeO_4)_6O_2$ was found to adopt $P6_3/m$ symmetry at all temperatures, whilst $La_8R_2(GeO_4)_6O_3$ (R = La, Bi) adopt $P$-1 symmetry at room temperature and $P6_3/m$ at 780–800 °C. The excess interstitial oxygen in $La_8R_2(GeO_4)_6O_3$ (R = La, Bi) was found to be distributed over three similar sites at room temperature. Local structural studies gave the first detailed picture of the local coordination geometry of the interstitial oxygen atoms, which are important for ionic conductivity. Whilst a range of Ge coordination numbers are present, the dominant feature is the formation of $GeO_5$ units. These are predominantly square pyramidal at room temperature, but become more like trigonal bipyramids at high temperature. This shows that the local structure appears to increase in symmetry as the long-range structure increases in symmetry.

**Chapter 5** reports the synthesis of nominal $La_8R_2(SiO_4)_6O_3$ (R = La, Bi) apatite-type oxide-ion conductors, the electrical properties and the composition limits. These are commonly referred to as A-10, O-27 compositions in the literature due to their formula of $A_{10}Si_6O_{27}$. The results from

Rietveld refinement, energy-dispersive X-ray spectroscopy and solid state nuclear magnetic resonance spectroscopy call into question the existence of "oxygen-excess" or O-27 lanthanum silicate apatites.

**Chapter 6** investigates the long-range and local structure of the perovskite-derivative, $Ba_3NbMoO_{8.5}$, which has been shown to have high oxide-ion conductivity. High resolution powder synchrotron diffraction revealed for the first time that there is a low-temperature phase and a high-temperature phase and that the sample shows structural hysteresis. Total scattering analysis indicates that the most common coordination number for $Nb^{5+}/Mo^{6+}$ is CN = 5 at both room temperature and 600 °C. The local structure of the O2/O3 sublattice is also highly disordered, forming hexagonal sheets of atomic density even at room temperature. The O2 and O3 sites are more localised at room temperature, but spread across the hexagonal sheets at 600 °C. The results give good insight into the potential conduction pathways in the material.

**Chapter 7** reports work done on rhombohedral $Bi_{0.775}Ln_{0.225}O_{1.5}$ (Ln = La, Dy) phases. High-resolution powder synchrotron diffraction and powder neutron diffraction show that the (0 0 *l*) reflections are poorly fitted. An investigation into stacking faults was made, but none of the models produced a good fit to the data. Small box PDF analysis shows that the average crystallographic structure is insufficient to describe the local structure. The structural complexities of the system are yet to be fully understood.

# Oxide-Ion Conductors for Energy Applications: Structure and Properties

Matthew Simon Chambers

Durham University

Diamond Light Source Ltd

A thesis submitted in partial fulfilment of the requirements for the degree of Doctor of Philosophy.

Supervisors: Prof. Ivana Radosavljevic Evans, Prof. John S. O. Evans, Dr Phil A. Chater

Department of Chemistry

Durham University

2019

# Contents

# Acknowledgements

## Declaration

The work presented in this thesis is entirely the work of the author, except where help is acknowledged from a named person, or a reference provided to a published source.

The research presented within was performed in the Department of Chemistry, Durham University, and Diamond Light Source Ltd, between October 2015 and April 2019. The results of this research have not been submitted for a degree in this or any other university. This thesis conforms to the word limit detailed in the Degree Regulation of the university.

The copyright of this thesis rests solely with the author. No quotation from it should be published without the consent of the author. Information derived from this thesis should be acknowledged in the form of a reference.

## List of Abbreviations

| | |
|---|---|
| ADP | Atomic Displacement Parameter |
| EDX | Energy-Dispersive X-ray Spectroscopy |
| FWHM | Full Width at Half Maximum |
| ICP-MS | Inductively Coupled Plasma Mass Spectrometry |
| MAS | Magic Angle Spinning |
| PDF | Pair Distribution Function |
| RMC | Reverse Monte Carlo |
| SEM | Scanning Electron Microscopy |
| SOFC | Solid Oxide Fuel Cell |
| SSNMR | Solid State Nuclear Magnetic Resonance |
| STEM | Scanning Transmission Electron Microscopy |
| TEC | Thermal Expansion Coefficient |
| TGA | Thermogravimetic Analysis |
| TOF | Time of Flight |
| YSZ | Yttria-Stabilised Zirconia |

# 1. Literature Review

## 1.1 Introduction

Ionic conductivity is a form of electrical conductivity, where current flows through the movement of ions. It occurs in molten salts, where the ions are highly mobile, but it can also occur in solids by the diffusion of ions through the crystal.[1] Ionic conductors have lower conductivities than metallic conductors, with typical values being $10^{-3} - 10^0$ S cm$^{-1}$ for good solid electrolytes at their operating temperatures and $10^1 - 10^5$ S cm$^{-1}$ for metals.[1-2] Ionic conductors are needed in devices for energy conversion and storage such as fuel cells and batteries.[3]

One important class of ionic conductors is the oxide-ion conductors, where $O^{2-}$ anions are the charge carriers. Oxide-ion conductors are used as electrolyte materials in solid oxide fuel cells (SOFCs).[4-6] Unlike heat engines, SOFCs are not limited by the Carnot cycle and can achieve efficiencies of 85%.[7] Furthermore, SOFCs allow a transition from fossil fuels to synthetic hydrocarbons, to hydrogen and then a fully renewable source.

Both the long-range and local structure of oxide-ion conductors are crucial to their conduction properties. Long-range structure has been studied with crystallography for decades. Whilst techniques such as extended X-ray absorption fine structure spectroscopy (EXAFS)[8] and solid-state nuclear magnetic resonance (SSNMR)[9] can be used to study the local structure of solid materials, total scattering has more recently been employed in order to study disordered crystalline materials, such as oxide-ion conductors.[10] Total scattering utilises both the Bragg and diffuse scattering in order to study both the long range and local structure simultaneously, providing information across a range of length scales. The fundamentals of this technique are discussed in more detail in Chapter 2. This literature review shall discuss oxide-ion conductors and focus on examples of total scattering improving our understanding of their structure and therefore conduction mechanisms. It will also briefly describe ionic conduction and SOFCs.

## 1.2 Ionic Conduction

In a crystal with $N$ equivalent, partially occupied sites per unit volume, the concentration of the occupied fraction be defined as $c$ and therefore the concentration of unoccupied sites is $(1 - c)$. Ionic mobility, $\mu$, can be related to the diffusion coefficient, $D$, using the Einstein relationship:[4]

$$\mu = \frac{qD}{kT} \qquad (1.1)$$

Where $q$ = charge of the particle, $k$ = Boltzmann constant and $T$ = temperature. The self-diffusion coefficient, $D$, can be related to the free energy of ion migration, $\Delta G_m$, by using random-walk theory in a 3D lattice:

$$D = \frac{z}{6}f(1-c)a_0^2 v_0 \exp\left(-\frac{\Delta G_m}{kT}\right) \qquad (1.2)$$

Where $z$ is the number of equivalent near neighbour sites, $a_0$ is the distance between equivalent sites, $v_0$ is the jump attempt frequency[5] and $f$ is the correlation factor, which represents the deviation from randomness of the walk, (~0.65[4] in a cubic lattice).[4] As $\Delta G_m = \Delta H_m - T\Delta S_m$, we can introduce the term $\gamma$, which is defined as:

$$\gamma = \frac{z}{6}f\exp\left(\frac{\Delta S_m}{k}\right) \qquad (1.3)$$

We can then substitute equations 1.3 and 1.2 into equation 1.1 to express mobility as:

$$\mu = \frac{q}{kT}\gamma(1-c)a_0^2 v_0 \exp\left(-\frac{\Delta H_m}{kT}\right) \qquad (1.4)$$

The equation to describe ionic conductivity is similar to electronic conductivity:

$$\sigma = nq\mu \qquad (1.5)$$

Where $n$ is the number of charge carriers. As the number of charge carriers will be the product of $N$ and $c$, by substituting equation 1.4 into equation 1.5, equation 1.6 can be obtained:

$$\sigma = N\frac{q^2}{kT}\gamma c(1-c)a_0^2 v_0 \exp\left(-\frac{\Delta H_m}{kT}\right) \qquad (1.6)$$

The factor $(1-c)$ can be expressed as $[V_O^{\cdot\cdot}]_s$, which is the Kröger-Vink notation for the concentration of oxygen vacancies.[4] The general Kröger-Vink notation can be written as $M_A^C$. In this notation, M is the species which replaces a previous species, $A$. $C$ is the overall charge that results from this substitution, where +1 is represented by $\cdot$ (middle dot). Thus $V_O^{\cdot\cdot}$ represents a vacancy on an oxygen site with a +2 charge. Substituting $(1-c)$ with the Kröger-Vink notation in equation 1.6, the ionic conductivity of a vacancy-driven oxide-ion conductor is given by:

$$\sigma = N\frac{q^2}{kT}\gamma[V_O^{\cdot\cdot}]_s(1-[V_O^{\cdot\cdot}]_s)a_0^2 v_0 \exp\left(-\frac{\Delta H_m}{kT}\right) \qquad (1.7)$$

The empirical, lattice (bulk) conductivity can be compared to equation 1.8:

$$\sigma = \frac{\sigma_0}{T}\exp\left(-\frac{E_a}{kT}\right) \qquad (1.8)$$

Where $\sigma_0$ is the preexponential factor and $E_a$ is the activation energy for oxide-ion conduction. We see from equation 1.7 that high conductivity will be favoured in materials with high concentrations of vacancies and low $\Delta H_m$.

## 1.3 Solid Oxide Fuel Cells

SOFCs consist of layers of a porous cathode, a dense electrolyte and a porous anode. The geometry of the SOFC can be tubular or planar.[5] The schematic of a planar SOFC is shown in

Figure 1.1. The electrodes are connected to an external circuit. Gas chambers feed oxygen/air to the cathode and fuel, such as $H_2$ or CO, to the anode. There is also a chamber to expel the products. The difference in oxygen chemical potential across the device creates an electromotive force across the electrolyte, from which power is generated when the electrodes are attached to an external circuit.
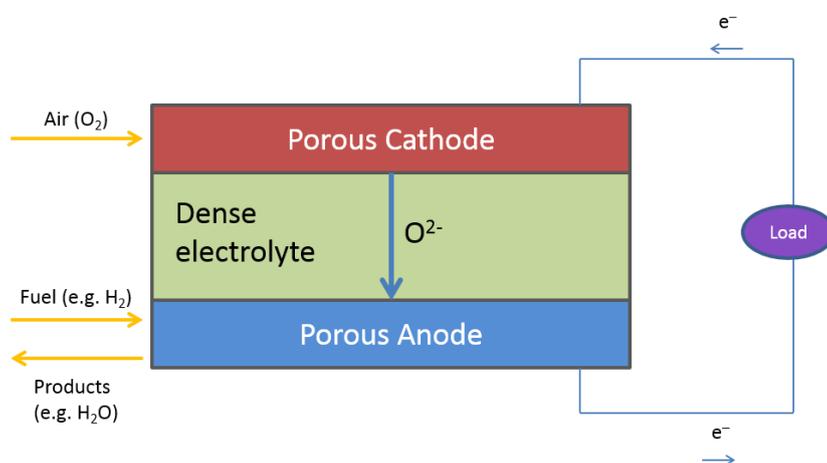


**Figure 1.1 –** Schematic of a planar SOFC.

The primary purpose of the cathode is to reduce $O_2$ gas into $O^{2-}$ anions and then incorporate them into the electrolyte. Cathode materials need to have good electronic conductivity, as they need to transport electrons from the external circuit to the surface of the cathode. The magnitude of electronic conductivity needed is approximately 100 S cm$^{-1}$ at operating temperatures (800 – 1000 C°).[5-6] The best current cathode material is $La_{1-x}Sr_xMnO_{3-\delta}$ (LSM).[5] Another required property in a cathode material is a high electrocatalytic activity with respect to the oxygen reduction reaction (ORR). The cathodic polarisation resistance is particularly high at lower temperatures due to the high $E_a$ of the ORR. Good ionic conductivity is also required in the cathode, so that the ORR does not need to occur at the point where the electrolyte, cathode and gas ($O_2$) meet, known as the triple-phase-boundary zone.[5] Additionally, the materials must be stable under oxidising conditions at the fabrication and operational temperatures, as well as have a similar thermal expansion coefficient (TEC) to the electrolyte and current collector.

 The oxidation of the fuel takes place at the anode. The desired properties in an anode material are catalytic activity for fuel oxidation, good electronic conductivity and compatibility with the electrolyte.[5-6] In that regard, Ni metal has been used as an anode material because of its high catalytic activity towards oxidation of fuels. It has a tendency, however, to sinter at operating temperatures and can form agglomerates, which decreases the area of triple-phase boundaries. Its TEC is quite different from regular electrolyte materials. To circumvent these problems, Ni is often mixed with the electrolyte material, such as yttria-stabilized zirconia (YSZ), to form a

cermet. The redox reactions that take place at the cathode (equation 1.9) and anode (equation 1.10) are:

$$\frac{1}{2}O_2(g) + 2e^-(\text{cathode}) \rightarrow O^{2-}(\text{electrolyte}) \qquad (1.9)$$

$$H_2(g) + O^{2-} \rightarrow H_2O(g) + 2e^- \qquad (1.10)$$
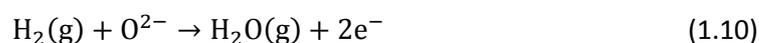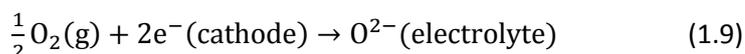
Where $H_2$ is assumed to be the fuel. This leads to an overall equation of:

$$\frac{1}{2}O_2(g) + H_2(g) \rightarrow H_2O(g) \qquad (1.11)$$

The third component of SOFCs is the electrolyte. The purpose of the electrolyte in SOFCs is to transport $O^{2-}$ ions from the cathode to the anode in order to oxidise the fuel. Electrolytes need to be good oxide ionic conductors but simultaneously be electronic insulators, as the purpose of the electrolyte is to allow the oxide anions to migrate from the cathode to the anode. The electrolyte must therefore have high ionic transport numbers in a variety of partial oxygen pressures. The ionic transport number is the fraction of the total electrical current that is carried by a particular ionic species, where $t_O = 1$ means that all of the electrical current is carried by the oxide ions. Additionally, the electrolyte must be easily made into thin layers and remain chemically stable at the SOFC operating temperatures.[4-6] The rest of this review focuses on the local structure studies that have been performed on potential electrolyte materials for SOFCs.

## 1.4 Total Scattering Studies of Oxide-Ion Conductors

### 1.4.1 Fluorite-type oxide-ion conductors

The fluorite oxide-ion conductors are amongst the most commonly used and studied electrolyte materials for SOFCs.[5-6, 11-14] The ideal fluorite $MO_2$ structure, named for $CaF_2$, consists of a cubic close packed array of $M^{4+}$ cations with all of the tetrahedral holes filled by anions, resulting in stoichiometry of $MO_2$ for oxides. It adopts *Fm*-3*m* symmetry. The structure is given in Figure 1.2. The $M^{4+}$ are in an eight-fold cubic coordination environment whilst the $O^{2-}$ adopt a tetrahedral coordination geometry.
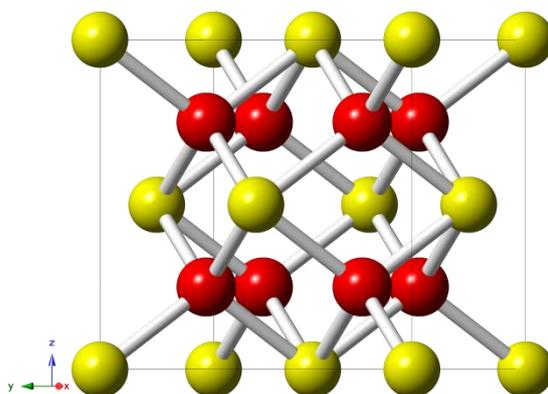
**Figure 1.2 –** The fluorite structure of $MO_2$. Yellow spheres = $M^{4+}$ cations; red spheres = $O^{2-}$ anions.

YSZ has been the electrolyte material of choice in SOFCs for decades.[5, 11, 13-16] Undoped $ZrO_2$ adopts a monoclinic ($P2_1/c$) structure at room temperature and tetragonal ($P4_2/nmc$) and cubic (fluorite) structures at higher temperatures.[17] The fluorite phase forms at 2300 °C.[14] Doping the trivalent $Y^{3+}$ on $Zr^{4+}$ sites not only stabilises the cubic structure at lower temperatures, but also introduces oxygen vacancies, forming $Zr_{1-x}Y_xO_{2-x/2}$. The oxide ions are able to hop *via* the vacancies, allowing oxide-ion conduction to occur. At 1000 °C, $Zr_{0.84}Y_{0.16}O_{1.92}$, the optimum composition for electrolytes, has a conductivity of approximately[13] 0.1 S cm$^{-1}$. The cubic sublattice can be stabilised with other aliovalent dopants, such as $Ca^{2+}$, forming calcia-stabilised zirconia (CSZ).[17] However, the different cations appear to not affect the oxide-ion migration: in both YSZ and CSZ, the oxide ions migrate between vacant sites by moving along the ⟨111⟩ direction through a non-direct path.[17]

CSZ was one of the first oxide-ion conductors to have its local structure studied using the reverse Monte Carlo (RMC) method.[18] This single crystal neutron RMC study showed that the vacancies tended to order along the ⟨111⟩ direction. In addition, it showed that when a cation site is occupied by a $Ca^{2+}$ cation, both the nearest and next nearest cation neighbours were slightly more likely to be $Zr^{4+}$ cations than from a random cation distribution. It also showed that M–O–M (M = Zr, Ca) distances tended to be shorter than average, whilst M–□–M (□ = O vacancy) distances were longer than average. However, the data were dominated by the effects of the long range structure, so the magnitudes of the displacements and correlations were small. The ordering was calculated to be caused by a balance of electro-static and elastic interactions.[19] A later PDF study[20] agreed that the vacancies order in the ⟨111⟩ direction in $Zr_{0.8}Sc_{0.2-x}Y_xO_{1.9}$ ($x$ = 0, 0.04, 0.08, 0.16, 0.2) materials. In all compositions, the partial radial distributions $g_{OO}(r)$ were similar, where the first peak was at $r \approx 2.58$ Å. The O⋯O distances in the Rietveld refinements were in the range of 2.55 – 2.57 Å, showing that the local ionic structure of all compositions is similar to the long-range average structure. However, Y–O distances are noticeably different (2.330 Å) than the Zr–O (~2.2 Å) and Sc–O (2.209 Å). In addition, it was found that there was no preference for vacancies to

order around $Zr^{4+}$ and $Sc^{3+}$ in $Zr_{0.8}Sc_{0.2}O_{1.9}$, but in $Zr_{0.8}Y_{0.2}O_{1.9}$, there is a preference for the vacancies to order around $Zr^{4+}$ compared to $Y^{3+}$, as $Zr^{4+}$ can preferentially adopt seven-fold coordination. The authors relate this increased vacancy clustering to the decrease in conductivity with increasing $Y^{3+}$ content. A follow up study[21] examined the importance of vacancy–vacancy interactions and found that the ordering did not differ when the identity of the dopant cation was changed. The vacancies distort the structure, which results in ordering to minimise these effects. The authors suggest that this is an intrinsic property of the fluorite structure, as the same distortion occurs with different cation dopants. They therefore suggest that scandia-doped zirconias represent the best possible conductors for stabilised zirconias, as the similar size of $Zr^{4+}$ and $Sc^{3+}$ leads to little preference for cation–vacancy interactions and the $Sc^{3+}$–vacancy interaction is particularly weak.

Another oxide-ion conductor that adopts the fluorite structure is $CeO_2$. $CeO_2$ adopts the cubic fluorite structure at room temperature, and can be doped with other rare earths such as $Gd_2O_3$, $Sm_2O_3$, $Pr_2O_3$, $Tb_2O_3$ and $Y_2O_3$ in order to create vacancies.[7, 22-27] $CeO_2$ has been found through Rietveld refinement and PDF analysis to have intrinsic interstitial oxide defects, though these defects became less populous when the sample was annealed at 800 °C for 4 h.[28] A more recent RMC/EXAFS combined analysis showed that Ce and O atoms are moved off their crystallographic sites due to thermal motions, and there is more disorder in samples with smaller particle sizes.[29] However, $Ce^{4+}$ can be reduced to $Ce^{3+}$, resulting in $CeO_{2-\delta}$,[28] which can cause some electronic conductivity.

A further investigation[30] into the local geometry in $CeO_2$ revealed the Ce–O–Ce bond angles follow a narrow Gaussian distribution close to the ideal tetrahedral angle of 109.5°, with mean = 109.14° and a full width at half maximum (FWHM) of ~6°, whilst the O–Ce–O bond distributions show the expected cubic geometry, with peaks at 70.35, 109.34 and 175.8°. A comparison of the O–Ce–O bond angle distribution obtained from the refined configuration and that of an ideal cubic coordination geometry is presented in Figure 1.3.
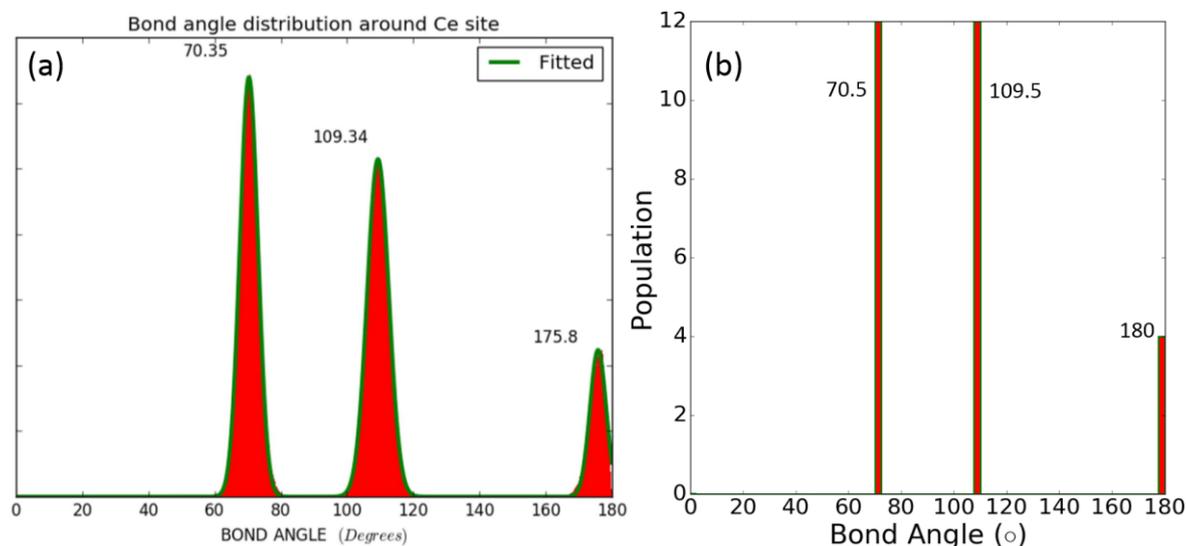
**Figure 1.3 –** The bond angle distributions of (a) O–Ce–O obtained by Clark *et al.*[30] in CeO$_2$ from RMC modelling and (b) in an ideal cubic coordination geometry.

This shows that there is very little deviation in the local structure of CeO$_2$ from the average structure. A RMC and MD analysis[7] of Ce$_{1-x}$Y$_x$O$_{2-x/2}$ ($x$ = 0.12, 0.26, 0.30, 0.36) showed that, contrary to YSZ, the vacancies do not preferentially cluster around Ce$^{4+}$ or Y$^{3+}$ at 800 °C, despite the weak preference at room temperature for vacancies to cluster around Y$^{3+}$. It is suggested that the increased disorder is the reason for the increase in conductivity compared to YSZ ($\sigma \approx 4.0 \times 10^{-2}$ S cm$^{-1}$ at 800 °C for Ce$_{0.88}$Y$_{0.12}$O$_{1.94}$, whilst $\sigma \approx 1.0 \times 10^{-2}$ S cm$^{-1}$ at 1000 °C for YSZ). The vacancy–vacancy pairs along the $\langle 111 \rangle$ direction increase with increasing $x$ values, adding further evidence that this vacancy ordering is intrinsic to the fluorite structure. Additionally, some ordering of vacancies along $\langle 210 \rangle$ and $\langle 211 \rangle$ directions was found in all compositions, indicating that this ordering independent of dopant concentration. RMC analysis of the co-doped (Ce$_{1-x}$Nb$_x$)$_{1-y}$Na$_y$O$_{2-\delta}$ ($x$ = 0, 0.10, 0.20, 0.30)[31] managed to reveal the local coordination of the Nb$^{5+}$ ions, whereas Rietveld analysis was still ambiguous. It showed that whilst Ce$^{4+}$ and Na$^+$ were only displaced by 0.10–0.14 Å from the ideal fluorite site, the Nb$^{5+}$ were uniaxially displaced 0.34 Å in order to achieve the ideal Nb–O bond lengths found in Nb$_2$O$_5$.

Another important fluorite-type oxide-ion conductor is Bi$_2$O$_3$. The fluorite-type $\delta$–Bi$_2$O$_3$ has one of the highest conductivities known for oxide-ion conductors, with $\sigma \approx 1$ S cm$^{-1}$ at 750 – 760 °C.[32] The large ionic conductivity is attributed to the polarisable Bi$^{3+}$ cation and the high concentration of oxide ion vacancies, where 25% of potential oxide sites are vacant.[32-33] In this structure, some of the O$^{2-}$ are displaced off the 8$c$ sites (see Figure 1.2) onto 32$f$ sites. The crystallographic details are given in Table 1.1.

**Table 1.1 – Crystallographic parameters of $\delta$-Bi$_2$O$_3$ at 1033 K.[34] Space group = *Fm*-3*m*; *a* = 5.6607(7) Å.**

| Label | Wyckoff site | *x* | *y* | *z* | Occupancy |
|-------|-------------|------|------|------|-----------|
| Bi1 | 4*a* | 0 | 0 | 0 | 1.0 |
| O1 | 8*c* | ¼ | ¼ | ¼ | 0.24 |
| O2 | 32*f* | 0.3344 | 0.3344 | 0.3344 | 0.13 |

Unfortunately, $\delta$-Bi$_2$O$_3$ is only stable in the temperature range of 730 – 825 °C,[35] above which it melts. At room temperature, it adopts the monoclinic $\alpha$-Bi$_2$O$_3$ phase with space group *P*2$_1$/*c*, though it can also form the tetragonal (*P*-42$_1$*c*) $\beta$-Bi$_2$O$_3$ phase or the body-centred cubic (*I*23) $\gamma$-phase upon cooling.[34] All phases except the $\delta$-phase are poor ionic conductors. There have been attempts to stabilise the $\delta$ phase through doping with the rare-earth sesquioxides and Y$_2$O$_3$,[32, 36-39] transition metals[33, 36, 40-47] such as W$^{6+}$, Nb$^{5+}$, Ta$^{5+}$, Re$^{7+}$, Mo$^{6+}$, Zr$^{4+}$ and V$^{5+}$, alkaline earths[32, 48] and even group 15 elements.[49-50] Discussion of each of the long-range, average structures of these phases is beyond the scope of this review, which will instead focus on total scattering studies performed on Bi$_2$O$_3$ phases. A total scattering study gave insights into the structure of $\beta$-Bi$_2$O$_3$ and $\delta$-Bi$_2$O$_3$.[34] The average structure of $\delta$-Bi$_2$O$_3$ models Bi$^{3+}$ cations in the centre of a cube with ¾ of the vertices occupied by O$^{2-}$, which are either randomly vacant, or form vacancy pairs along the $\langle 100 \rangle$, $\langle 110 \rangle$ or $\langle 111 \rangle$ directions. This model would result in O–Bi–O angle distributions that are found when Bi$^{3+}$ is in a cubic geometry, where the vacancy-ordered distributions only differ slightly from the completely random distribution. However, RMC analysis showed that there was a broad, pronounced peak at 70–80°, resembling the bond angle distribution in the room temperature $\alpha$ phase. Furthermore, the $g_{BiO}(r)$ partial radial distributions showed a peak at ~2.16 Å, much shorter than the average Bi–O bond distances in $\delta$-Bi$_2$O$_3$ of 2.45 Å and 2.33 Å. This shorter distance not only shows that the local structure in $\delta$-Bi$_2$O$_3$ resembles that of $\alpha$-Bi$_2$O$_3$, but it also shows that the Bi$^{3+}$ are also significantly displaced from their average positions. This was attributed to the presence of lone pair 6$s^2$ electrons, as this does not occur with spherical cations such as Zr$^{4+}$ and Y$^{3+}$. Furthermore, the study showed that the cation distributions in the $\delta$ and $\beta$ phases are similar, but the anion sublattice is much more disordered in the $\delta$ phase. The coordination environment of the Bi$^{3+}$ is similar in both phases.

Whilst doping with Yb$^{3+}$ generally leads to the formation of a rhombohedral phase at room temperature,[51] it has also led to the formation of $\delta$-Bi$_4$YbO$_{7.5}$.[52] In this structure there is a local clustering of YbO$_6$ octahedra, but not on the long-range scale, allowing the disordered cubic structure to be maintained at room temperature. Despite the fact that the overall oxygen content

per formula unit ($Bi_{1.6}Yb_{0.4}O_3$) is the same as $\delta$-$Bi_2O_3$, there are additional interstitial O3 atoms on 48$i$ sites, which are associated with $Yb^{3+}$, creating more vacancies on the O2 (see Table 1.1) sites. This results in a total tetrahedral vacancy content per unit cell > 2. The result is that there cannot be exclusive ⟨100⟩ or ⟨111⟩ vacancy pairs. Despite this, the ⟨100⟩ were found to be more favourable than ⟨111⟩, though ⟨110⟩ vacancy pairs were the most common ordering. This increase in tetrahedral vacancies was also found in the similar phase $Bi_3YbO_6$.[53]

The co-doped $Bi_{2.5+x}Pb_{0.5}YO_{5.75+3x/2}$ ($x$ = 0, 1, 2) phases adopt the $\delta$ structure at room temperature and have high oxide-ion conductivities, where the $x$ = 1 sample has a conductivity of $\sigma$ = 0.4 S cm$^{-1}$ at 800 °C.[54] RMC analysis performed on $\delta$-$Bi_5PbY_2O_{11.5}$ ($x$ = 0), which has a higher concentration of vacancies than the parent $\delta$-$Bi_2O_3$ phase ($^3/_8$ vacancies compared to ¼), gave further insights into the structure of this phase. The local environment of $Pb^{2+}$ was observed to deviate from those of $Bi^{3+}$ and $Y^{3+}$. The average coordination number for $Pb^{2+}$ (~3.5) was found to be lower than that of $Bi^{3+}$ (~5.0) and $Y^{3+}$ (~5.5) at 20 °C, 500 °C and 700 °C. As a result, there is a strong preferential association for the tetrahedral vacancies with the $Pb^{2+}$ ions. The O–Pb–O bond angle distribution also differs from the O–Bi/Y–O bond angle distributions. The first peak in the O–Pb–O distribution is at ~70°, whilst the first peaks O–Bi/Y–O distributions are at ~76°. However, the other two peaks in the O–Pb–O distribution are in similar positions to the peaks in the O–Bi/Y–O distributions, which are a result of a distorted cubic geometry. This difference is attributed by the authors[55] to the extent of the stereochemical activity of the $Pb^{2+}$ $6s^2$ lone pair. They also found that there is a larger next-nearest neighbour ordering of $Pb^{2+}$–$Pb^{2+}$, whilst for the other two cations the next-nearest neighbours are random. Finally, the authors[55] state that there is a clear preference for ordering in the ⟨100⟩ direction, considering that with >2 vacancies per unit cell, there must always be a ⟨110⟩ vacancy ordering. Their molecular dynamics results suggested that oxide-ion conduction happens along the ⟨100⟩ direction.

### 1.4.1.1 Fluorite-related oxide-ion conductors

Pyrochlores are materials with the formula $A_2B_2O_7$. The pyrochlore structure is similar to the fluorite structure ($M_2M_2O_8$), but there is an ordering of the A and B cations and of the $O^{2-}$ and vacancies, resulting in a doubling of the unit cell with space group $Fd$-$3m$.[56] The structure is shown in Figure 1.4. In the average structure, the larger A cations adopt an eight-fold scalenohedral/distorted cubic coordination geometry and the smaller B cations adopt a distorted octahedral geometry.
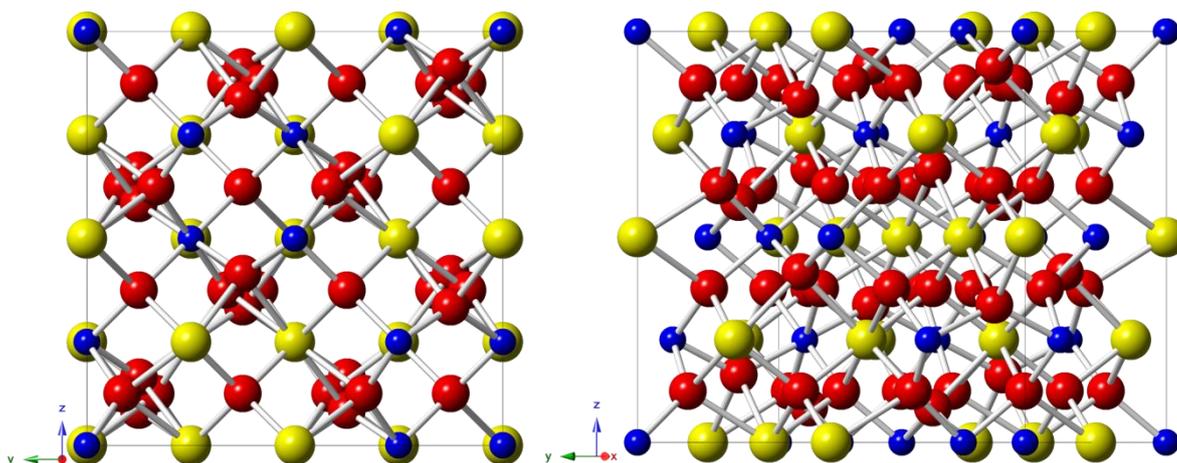
**Figure 1.4** – The pyrochlore structure viewed along (a) the $x$ axis and (b) slightly tilted. Yellow spheres = A cations; blue = B cations; red = $O^{2-}$.

The series of $Y_2(Ti_{1-x}Zr_x)_2O_7$ phases undergo a transition from pyrochlore when $x = 0$ to fluorite when $x = 1$, which is accompanied by an increase in the conductivity by an order of magnitude at 1000 °C from $\sigma \approx 1.0 \times 10^{-4}$ S cm$^{-1}$ to $1.0 \times 10^{-3}$ S cm$^{-1}$.[57] The neutron powder diffraction patterns of $Y_2(Ti_{1-x}Zr_x)_2O_7$ ($x$ = 0, 0.15, 0.30, 0.5, 0.65, 0.8, 1) showed considerable diffuse scattering and Rietveld refinements were unable to determine the distribution of the three cation species. On the other hand, total scattering analysis was able to determine the cation ordering, revealing that at low values of $x$, the $Y^{3+}$ are exclusively on the A site and the $Ti^{4+}$ (and $Zr^{4+}$) are exclusively on the B site. As $x$ increased, the $Zr^{4+}$ and $Ti^{4+}$ ions begin to populate the A site as well, and by $x$ = 0.8, the cations are completely disordered. Whilst the coordination number of the $Ti^{4+}$ increased at a very slow rate as $x$ increased, the coordination number of $Zr^{4+}$ increased to ~7.0 as the coordination number of $Y^{3+}$ decreased to ~7.25. The slightly larger coordination number of the $Y^{3+}$ reflects the preference for vacancies to order around $Zr^{4+}$ seen in the fluorites.[20] The O–M–O (M = Y, Ti, Zr) bond angle distributions also showed that whilst $Y^{3+}$ and $Ti^{4+}$ maintain their distorted cubic and distorted octahedral geometries respectively, the $Zr^{4+}$ adopted an angle distribution similar to a distorted cubic geometry, despite primarily occupying the B site at low values of $x$ in $Y_2(Ti_{1-x}Zr_x)_2O_7$,[57] revealing that this increase in disorder is what leads to the formation of the fluorite phase.

$Nd_2Zr_2O_7$ is a pyrochlore that can also be synthesised with the fluorite structure depending on synthesis conditions.[56] Rietveld analysis of $Nd_2Zr_2O_7$ prepared by heating an amorphous precursor suggested that the fluorite structure was adopted, but due to the broad peaks caused by the small (~10 nm) particle size, the results were inconclusive. RMC analysis[56] allowed the local structure to be probed and revealed that the fluorite structure was adopted, as the Nd–O–Nd and Zr–O–Zr bond angle distributions obtained from the refined models were centred around the ideal fluorite bond angle of ~109.5°, regardless of whether the starting model was a pyrochlore or fluorite

structure. The O–Zr–O bond angle distributions also followed those expected from a fluorite. Annealing the fluorite-type $Nd_2Zr_2O_7$ resulted in a pyrochlore structure, which could be determined from Rietveld analysis. This study showed that the fluorite and pyrochlore structures are better described as a continuum of an evolving structure type, rather than two distinct structures. In addition, it has been shown that the local structure of the pyrochlore $Ho_2Zr_2O_7$ can be modelled better with an orthorhombic (*Ccmm*) weberite-type structure in the short-range regime,[58] where at longer ranges it is described by the pyrochlore structure and at Rietveld ranges as the fluorite structure.

There are several other fluorite-related structures that have been studied with total scattering. $Nd_5Mo_3O_{16+\delta}$ adopts a cubic $2a_f \times 2a_f \times 2a_f$ ($a_f$ = fluorite $a$ cell) fluorite supercell with space group *Pn*-3*n* and has an ionic conductivity of $\sigma \approx 4.9 \times 10^{-3}$ S cm$^{-1}$ at 800 °C.[59-60] The total scattering study of anion-deficient $Nd_5Mo_3O_{15.63(4)}$ showed that the cations are arranged in a face-centred cubic lattice, whilst the cation-anion $g_{MO}(r)$ partials showed that it is arranged in a primitive cubic lattice as the Rietveld analysis shows.[61] One of the oxide ions (O2) is displaced from its ideal position by ~0.7 Å, which the authors propose[61] shows that the conduction mechanism can take place through the movement of these oxide ions. There is a vacancy–vacancy ordering along the ⟨100⟩ direction, contrary to the ordering found in YSZ and ScSZ,[21] which suggests that structures, which depart more from fluorite do not necessarily have vacancy ordering along the ⟨111⟩ direction.

$Bi_7WO_{13.5}$ adopts the tetragonal ($I4_1$) type Ib fluorite-type structure and has a conductivity of $\sigma = 3.01(7) \times 10^{-4}$ S cm$^{-1}$ at 300 °C and 0.11(2) S cm$^{-1}$ at 800 °C.[42] It undergoes a phase transition to the $\delta$ phase above 850 °C. The authors[42] of the study were unable to measure its conductivity in the cubic fluorite phase. RMC analysis showed that the average coordination of W at room temperature is lower than expected from the average structure (3.6 *vs*. 4.8). Vacancies were preferentially found to be in the coordination environment of the $W^{6+}$ ions. The W–O distances are shorter than the Bi–O distances. The room temperature local structure showed a preference for $W^{6+}$ nearest neighbours to be $Bi^{3+}$. The vacancy pairs are aligned in the ⟨100⟩ direction, which again suggests that the vacancy ordering along the ⟨111⟩ direction found in YSZ and ScSZ[21] may be a quality of zirconia-based fluorites rather than the fluorite structure itself. At 900 °C, when $Bi_7WO_{13.5}$ exists as the *Fm*-3*m* phase, the preference for specific cationic nearest neighbours is no longer present, and there is an even more marked preference for the vacancy pairs to be aligned in the ⟨100⟩ direction. An intriguing aspect of this structure is that there are two peaks in the $g_{BiO}(r)$ partial, suggesting that the $Bi^{3+}$ ions have moved off-centre from their ideal site. The O–Bi–O angle distribution does not change much between the room temperature and 900 °C structures, but the mean of the peak in the O–W–O bond angle distribution moves from 105° (close to the

ideal tetrahedral angle) at room temperature to ~95°. Interestingly, the authors suggest that there are isolated WO$_4$ tetrahedra at 900 °C based on the W : O2 (on the 48$i$ position) ratio, yet the bond angles show that this geometry must be significantly distorted.

The C-type cubic ($Ia$-3) rare earth oxide structure adopted by Y$_2$O$_3$ is also related to fluorite and pyrochlore structures.[62] La$_2$Ce$_2$O$_7$ has an oxygen-deficient fluorite structure, whilst the structure for Nd$_2$Ce$_2$O$_7$ best fit neutron diffraction data when two phases consisting of the fluorite and C-type structure were used with equal weighting. RMC analysis of La$_{2-x}$Nd$_x$Ce$_2$O$_7$ ($x$ = 0, 0.5, 1, 1.5, 2) showed vacancy-vacancy ordering along the ⟨100⟩ and ⟨110⟩, as opposed to the ⟨111⟩ direction normally found in oxygen-deficient CeO$_{2-\delta}$ phases. When combined with Rietveld analysis and molecular dynamics, it was determined that the increased vacancy–vacancy ordering in Nd$_2$Ce$_2$O$_7$ is the reason for the lower conductivity compared to La$_2$Ce$_2$O$_7$.

### 1.4.2 Cubic perovskite-type and related structure type oxide-ion conductors

Perovskites are a group of materials that exhibit multiple desirable properties, one of which is oxide-ion conductivity.[5-6] The perovskite structure consists of layers of AO$_3$ stacked in a cubic manner with all of the octahedral holes filled with B cations, resulting in a stoichiometry of ABO$_3$. The ideal perovskite adopts $Pm$-3$m$ symmetry. It can also be described in terms of corner-shared BO$_6$ octahedra surrounding the 12 coordinate A site as emphasised in Figure 1.5a. The AO$_3$ layers may also stack in a hexagonal manner and with various A : B ratios, producing a wide range of derivative structures.[63-64]
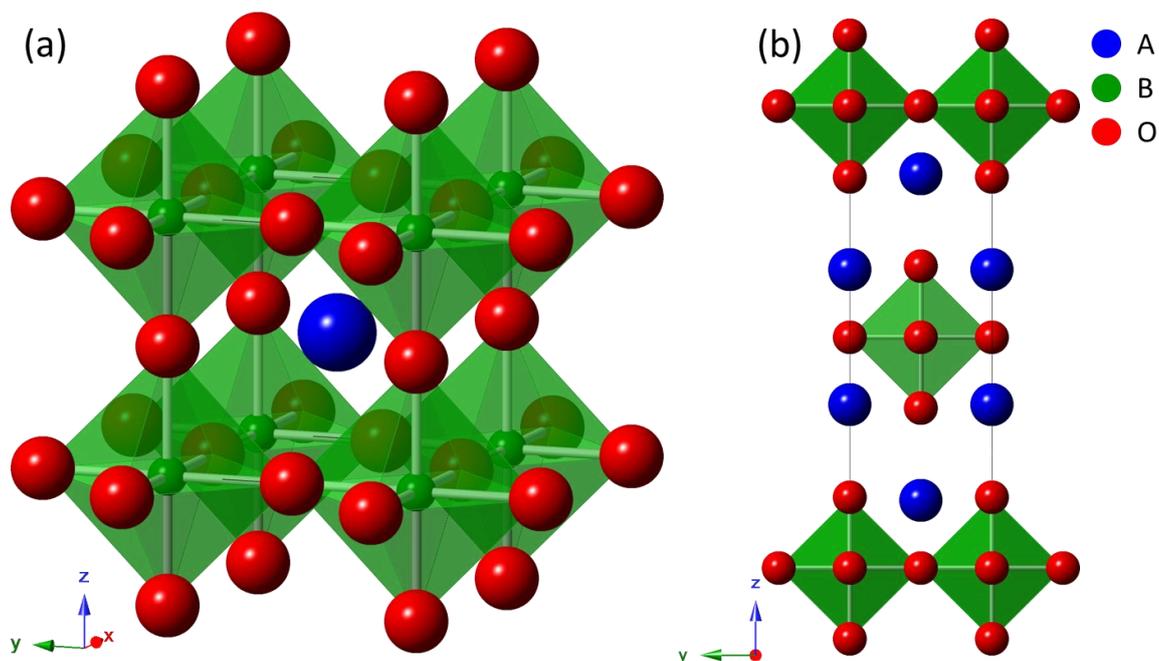


**Figure 1.5** – Structures of (a) ABO$_3$ cubic perovskite; (b) A$_2$BO$_4$ layered perovskite.

One of the earliest discovered perovskite solid electrolytes was $La_{1-x}Sr_xGa_{1-y}Mg_yO_{3-0.5(x+y)}$ (LSGM).[65] The phase $La_{0.8}Sr_{0.2}Ga_{0.83}Mg_{0.17}O_{2.815}$ has an ionic conductivity of 0.166 S cm$^{-1}$ at 800 °C and is an almost pure ionic conductor.[66] LSGM electrolytes have a better compatibility with lanthanum-transition metal oxide electrodes than YSZ.[13] The analogous $La_{0.95}Ba_{0.05}Ga_{0.8}Mg_{0.2}O_{2.732}$ (LBGM) was studied with a combination of PDF and density functional theory (DFT).[67] It was found that LGBM, which adopts an orthorhombic structure at room temperature rather the $Pm$-$3m$ symmetry, likely has a lower conductivity as vacancies tend to associate with the $Ba^{2+}$ ions, resulting in defect clustering.

### 1.4.2.1 Perovskite derivative oxide-ion conductors

As mentioned previously, there are a wide range of derivative perovskite structures. Whilst LSGM adopts the cubic perovskite structure, by varying the stoichiometry to $LaSrGaO_4$, the $K_2NiF_4$-type layered perovskite structure (Figure 1.5b) is adopted (space group = $I4/mmm$), an example of which is the series of $LaSrGa_{1-x}Mg_xO_{4-\delta}$ ($x$ = 0, 0.03, 0.05, 0.1) phases.[68] Rietveld refinement only showed that the two oxygen sites had anisotropic displacements at room temperature, so an analysis using DFT and PDF was performed. This revealed that the oxygen vacancies were more likely to be present in the perovskite layer, which suggested that the oxide-ion conductivity is two dimensional, explaining why the conductivity of these phases is lower than the cubic $LaGaO_3$-based materials.

Another important class of perovskite-derivatives is the brownmillerites. Brownmillerites are vacancy-ordered perovskite derivatives with the general formula of $A_2B_2O_5$.[14] $Ba_2In_2O_5$ is one of the brownmillerite oxide-ion conductors. $Ba_2In_2O_5$ adopts orthorhombic $Icmm$ symmetry at room temperature and undergoes a phase transition to the perovskite structure ($Pm$-$3m$) at 900 °C. X-ray small box PDF refinements were performed by Mancini $et$ $al.$[69] on $Ba_2In_2O_5$, $Ba_2In_{1.7}S_{0.3}O_{5.45}$ and $Ba_2In_{1.7}P_{0.3}O_{5.3}$. Whilst $Ba_2In_2O_5$ adopts $Icmm$ symmetry at room temperature, $Ba_2In_{1.7}S_{0.3}O_{5.45}$ and $Ba_2In_{1.7}P_{0.3}O_{5.3}$ both adopt $Pm$-$3m$ symmetry at room temperature on the long range scale. The local structure of $Ba_2In_2O_5$ is described well by its long range structure. On the other hand, the space group $Pm$-$3m$ did not describe the local structure for $Ba_2In_{1.7}S_{0.3}O_{5.45}$ and $Ba_2In_{1.7}P_{0.3}O_{5.3}$ at $r$ < 10 Å, though it did provide a satisfactory fit at $r \geq 10$ Å. Instead, the $Icmm$ space group was found to describe the structure at $r$ < 10 Å, indicating that the phase transition in $Ba_2In_2O_5$ most likely arises from static oxygen defects becoming dynamic.

### 1.4.3 Lanthanum molybdate

$La_2Mo_2O_9$ was found to have a high oxide-ion conductivity in its high temperature cubic ($P2_13$) $\beta$-phase, with a conductivity of $6 \times 10^{-2}$ S cm$^{-1}$ at 800 °C.[70] It undergoes a phase transition from its low temperature $\alpha$ form to the cubic phase at 580 °C, where there is an increase in conductivity. A single crystal X-ray diffraction study[71] revealed that the room temperature $\alpha$-phase adopts a

complex monoclinic ($P2_1$) structure with 312 crystallographically unique sites. The structures are presented in Figure 1.6. The average structure of $\beta$-La$_2$Mo$_2$O$_9$ is a time-averaged form of $\alpha$-La$_2$Mo$_2$O$_9$. The Mo$^{6+}$ cations are in fourfold, fivefold and six-fold coordination environments. The variable coordination number of the Mo$^{6+}$ cation is related to the large oxide-ion mobility.

The nature of the phase transition was explored through the use of small-box neutron PDF analysis.[72] It was found that despite the long-range structures differing, the local structure of $\beta$-La$_2$Mo$_2$O$_9$ at 600 °C was extremely similar to $\alpha$-La$_2$Mo$_2$O$_9$ at 500 °C. Better fits were obtained to the high temperature local structure using the monoclinic structure than the cubic structure. Furthermore, the cubic phase poorly described the oxygen ion coordination. The results confirmed that the $\alpha \rightarrow \beta$ transition is that from a static oxygen lattice to a dynamic one (as previously suggested by Evans *et al.*[71]) and showed that the apparently disordered oxygen distribution was in fact locally well-defined.
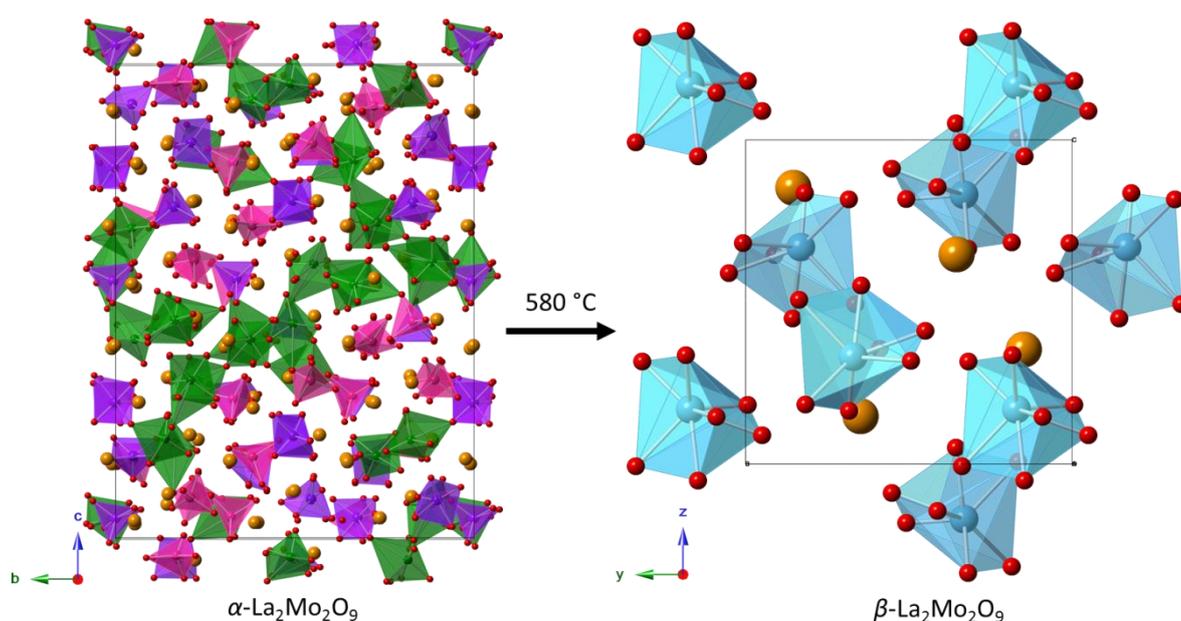


**Figure 1.6 –** The structures of $\alpha$-La$_2$Mo$_2$O$_9$ and $\beta$-La$_2$Mo$_2$O$_9$. Orange spheres = La; red spheres = O; pink = MoO$_4$; purple; green = MoO$_6$; light blue = disordered MoO$x$ polyhedra. The oxygen sites in the $\beta$-phase are all partially occupied.

### 1.4.4 Melilite-type oxide-ion conductors

Melilite-type oxides with stoichiometry (A,B)$_2$C$_3$O$_7$ are layered structures (space group = $P42_1m$), where the (A,B) cations sit in pentagonal channels formed by two different types of CO$_4$ tetrahedra: C1O$_4$ tetrahedra, that are corner-connected at all vertices to C2O$_4$ tetrahedra; C2O$_4$ corner connect at only three vertices to C1O$_4$ tetrahedra. The structure is shown in Figure 1.7. LaSrGa$_3$O$_7$-derived melilites have shown particular promise, where La$_{1.54}$Sr$_{0.46}$Ga$_3$O$_{7.27}$ was found

to have a conductivity of $0.02 - 0.1$ S cm$^{-1}$ in the temperature range of $600 - 900$ °C.[73] In this series of phases, increasing the La$^{3+}$ content at the expense of Sr$^{2+}$ content adds excess interstitial oxide ions, which are believed to be the mobile species.
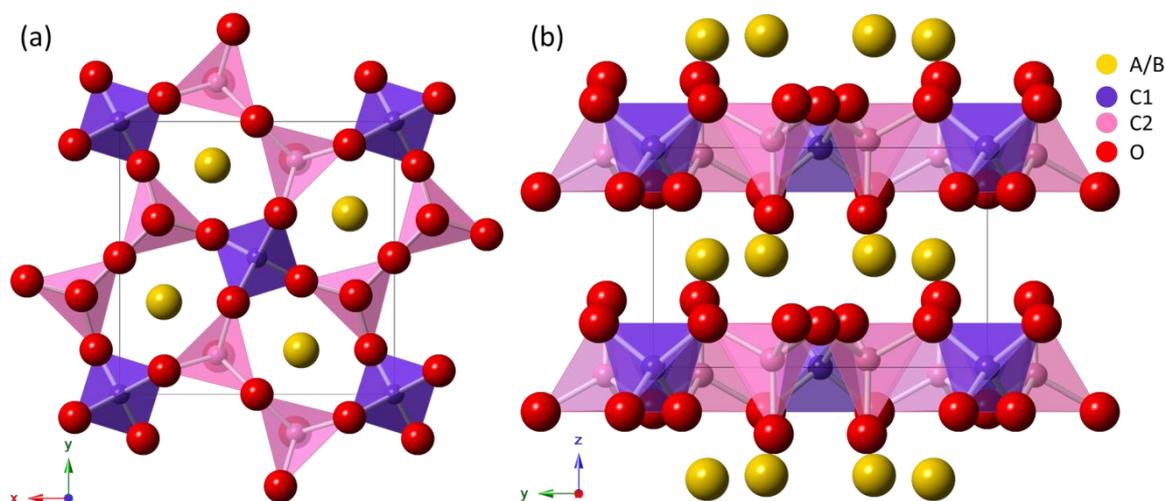


**Figure 1.7 –** The melilite structure viewed down (a) (001) projection and (b) (100) projection.

The average structural model for La$_{1.54}$Sr$_{0.46}$Ga$_3$O$_{7.27}$ proposed by Kuang *et al.*[73] placed the interstitial oxide in the centre of the pentagonal ring, forming GaO$_5$ distorted trigonal bipyramids, but a PDF analysis at 15 K by Mancini *et al.*[74] of La$_{1.5}$Sr$_{0.5}$Ga$_3$O$_{7.25}$ indicated that it shifts from the centre, reducing the Ga–O$_{int}$ distance from 3.0 Å to 2.5 Å. There was also a small peak present in the PDF of La$_{1.5}$Sr$_{0.5}$Ga$_3$O$_{7.25}$ that is not present in LaSrGa$_3$O$_7$, possibly originating from Ga–O pairs. We will probe similar features in the Chapter 4 study of the lanthanum germanate apatite oxide-ion conductors.

## 1.5 Conclusions and Outlook

In this chapter, total scattering studies have been reviewed, showing how they can be used in order to study the local structure of oxide-ion conductors in various family types, including:

1.  Fluorites and the related pyrochlores;
2.  Perovskites, related K$_2$NiF$_4$ phases and brownmillerites;
3.  Lanthanum molybdate (La$_2$Mo$_2$O$_9$);
4.  Melilite-type oxide-ion conductors.

These studies have shown that analysis of the local structure of oxide-ion conductors gives key insights into their structure and conduction mechanisms that cannot be obtained from long-range, Rietveld analysis alone. With this in mind, the following investigations were undertaken on a range of other oxide-ion conductors and are presented in the following chapters below. An overview of the relevant literature for each material family is given in individual chapters.

- Chapter 3 is an investigation into the oxide-ion conductivity properties $Ge_{5-x}Al_x(PO_4)_6O_{1-x/2}$. Whilst the structure of $Ge_5(PO_4)_6O$ is already known,[75] it has never been investigated as a potential oxide-ion conductor, nor has there been an attempt to dope $Al^{3+}$ into the structure. The hope was that the variable coordination geometry exhibited by Ge could lead to variable-coordination-derived conductivity found in apatites, LAMOX and other molybdates.

- Chapter 4 is a combined Rietveld and total scattering study on $La_8R_2(GeO_4)_6O_{3-y}$ (R = Sr, La, Bi) apatite-type oxide-ion conductors. Apatite-type lanthanum germanates are known oxide-ion conductors, believed to conduct through migration of an interstitial oxide ion.[6] A total scattering study has previously been performed on the apatite-type $La_{9.33}(SiO_4)_6O_2$,[76] but not on the oxygen-excess lanthanum germanate apatites. The implications of the excess interstitial oxide ions on the structure of the material cannot be fully realised through the average structure alone.

- Chapter 5 describes a study on related apatite $La_8R_2(SiO_4)_6O_3$ (R = La, Bi) oxide-ion conductors through Rietveld analysis, impedance spectroscopy, SEM-EDX and SSNMR. Despite extensive prior studies on these materials, there is a question whether the $La_{10}(SiO_4)_6O_3$ phase really exists and previous literature on $La_8Bi_2(SiO_4)_6O_3$ is inconclusive.[77] The focus of the study is on whether these phases exist and to measure their oxide-ion conductivity properties.

- Chapter 6 discusses average and local structural analysis of $Ba_3NbMoO_{8.5}$. This phase was recently discovered to be a good oxide-ion conductor,[78] but its average structure consists of several disordered sites, which means it cannot be understood by the long range structure alone. This chapter presents big box total scattering analysis, which fully describes the local structure and gives further insights into the conduction mechanism.

- Chapter 7 investigates the long-range structure of the rhombohedral $Bi_{0.775}Ln_{0.225}O_{1.5}$ (Ln = La, Dy) phases and investigates their local structure using small box PDF analysis. These phases adopt layered structures,[51] with oxide ions potentially residing in "interslab" spaces.[79] There are questions concerning the existence of these interslab oxide ions, as well as on any long-range effects such as stacking faults. The work performed revealed that these systems are complex and a full understanding of their properties was not possible within the time frame of this project.

## 1.6 References

1.      Smart, L. E.; Moore, E. A., *Solid State Chemistry: an Introduction*. CRC press: London, 2012.
2.      Bruce, P. G., *Solid State Electrochemistry*. Cambridge University Press: Cambridge, 1997; Vol. 5.
3.      Islam, M. S.; Driscoll, D. J.; Fisher, C. A.; Slater, P. R., Atomic-scale investigation of defects, dopants, and lithium transport in the LiFePO₄ olivine-type battery material. *Chemistry of Materials* **2005,** *17* (20), 5085-5092.
4.      Kilner, J. A., Fast oxygen transport in acceptor doped oxides. *Solid State Ionics* **2000,** *129*, 13-26.

5.      Kilner, J. A.; Burriel, M., Materials for Intermediate-Temperature Solid-Oxide Fuel Cells. *Annual Review of Materials Research* **2014,** *44*, 365-393.

6.      Orera, A.; Slater, P. R., New Chemical Systems for Solid Oxide Fuel Cells. *Chemistry of Materials* **2009,** *22* (3), 675-690.

7.      Burbano, M.; Norberg, S. T.; Hull, S.; Eriksson, S. G.; Marrocchelli, D.; Madden, P. A.; Watson, G. W., Oxygen Vacancy Ordering and the Conductivity Maximum in $Y_2O_3$-Doped $CeO_2$. *Chemistry of Materials* **2012,** *24* (1), 222-229.

8.      Newville, M., Fundamentals of XAFS. *Reviews in Mineralogy and Geochemistry* **2014,** *78* (1), 33-74.

9.      Apperley, D. C.; Harris, R. K.; Hodgkinson, P., *Solid-state NMR: Basic principles and practice*. Momentum Press: New York, 2012.

10.     Tucker, M. G.; Dove, M. T.; Keen, D. A., Application of the reverse Monte Carlo method to crystalline materials. *Journal of Applied Crystallography* **2001,** *34* (5), 630-638.

11.     Goodenough, J. B., Oxide-ion electrolytes. *Annual Review of Materials Research* **2003,** *33* (1), 91-128.

12.     Skinner, S. J.; Kilner, J. A., Oxygen ion conductors. *Materials Today* **2003,** *6* (3), 30-37.

13.     Jacobson, A. J., Materials for solid oxide fuel cells. *Chemistry of Materials* **2009,** *22* (3), 660-674.

14.     Malavasi, L.; Fisher, C. A.; Islam, M. S., Oxide-ion and proton conducting electrolyte materials for clean energy applications: structural and mechanistic features. *Chemical Society Reviews* **2010,** *39* (11), 4370-4387.

15.     Grosso, R. L.; Reis, S. L.; Muccillo, E. N. S., Improved ionic conductivity of zirconia-scandia with niobia addition. *Ceramics International* **2017,** *43* (14), 10934-10938.

16.     Asadikiya, M.; Zhong, Y., Oxygen ion mobility and conductivity prediction in cubic yttria-stabilized zirconia single crystals. *Journal of Materials Science* **2018,** *53* (3), 1699-1709.

17.     Kahlert, H.; Frey, F.; Boysen, H.; Proffen, T.; Mason, S.; Weppner, W., Structural Investigations of the Ionic Conductivity in Zirconia Crystals by Neutron Diffraction at High Temperatures and Simultaneously Applied Electric Field. *Ionics* **1996,** *2* (2), 88-96.

18.     Proffen, T.; Welberry, T. R., Analysis of diffuse scattering from single crystals via the reverse Monte Carlo technique. II. The defect structure of calcium-stabilized zirconia. *Journal of Applied Crystallography* **1998,** *31*, 318-326.

19.     Bogicevic, A.; Wolverton, C., Nature and strength of defect interactions in cubic stabilized zirconia. *Physical Review B* **2003,** *67* (2), 024106.

20.     Norberg, S. T.; Hull, S.; Ahmed, I.; Eriksson, S. G.; Marrocchelli, D.; Madden, P. A.; Li, P.; Irvine, J. T. S., Structural Disorder in Doped Zirconias, Part I: The $Zr_{0.8}Sc_{0.2-x}Y_xO_{1.9}$ ($0.0 \leq x \leq 0.2$) System. *Chemistry of Materials* **2011,** *23* (6), 1356-1364.

21.     Marrocchelli, D.; Madden, P. A.; Norberg, S. T.; Hull, S., Structural Disorder in Doped Zirconias, Part II: Vacancy Ordering Effects and the Conductivity Maximum. *Chemistry of Materials* **2011,** *23* (6), 1365-1373.

22.     Bhabu, K. A.; Theerthagiri, J.; Madhavan, J.; Balu, T.; Muralidharan, G.; Rajasekaran, T. R., Cubic fluorite phase of samarium doped cerium oxide $(CeO_2)_{0.96}Sm_{0.04}$ for solid oxide fuel cell electrolyte. *Journal of Materials Science – Materials in Electronics* **2016,** *27* (2), 1566-1573.

23.     D'Angelo, A. M.; Webster, N. A. S.; Chaffee, A. L., Vacancy Generation and Oxygen Uptake in Cu-Doped Pr-$CeO_2$ Materials using Neutron and in Situ X-ray Diffraction. *Inorganic Chemistry* **2016**.

24.     Rainwater, B. H.; Velisavljevic, N.; Park, C.; Sun, H. B.; Waller, G. H.; Tsoi, G. M.; Vohra, Y. K.; Liu, M. L., High pressure structural study of samarium doped $CeO_2$ oxygen vacancy conductor - Insight into the dopant concentration relationship to the strain effect in thin film ionic conductors. *Solid State Ionics* **2016,** *292*, 59-65.

25.     Van Laethem, D.; Deconinck, J.; Depla, D.; Hubin, A., Finite element modelling of the ionic conductivity of acceptor doped ceria. *Journal of the European Ceramic Society* **2016,** *36* (8), 1983-1994.

26.     Artini, C., Rare-Earth-Doped Ceria Systems and Their Performance as Solid Electrolytes: A Puzzling Tangle of Structural Issues at the Average and Local Scale. *Inorganic Chemistry* **2018,** *57* (21), 13047-13062.

27.     Zhang, L.; Meng, J.; Yao, F.; Zhang, W.; Liu, X.; Meng, J.; Zhang, H., Insight into the Mechanism of the Ionic Conductivity for Ln-Doped Ceria (Ln = La, Pr, Nd, Pm, Sm, Gd, Tb, Dy, Ho, Er, and Tm) through First-Principles Calculation. *Inorganic Chemistry* **2018,** *57* (20), 12690-12696.

28.     Mamontov, E.; Egami, T., Structural defects in a nano-scale powder of $CeO_2$ studied by pulsed neutron diffraction. *Journal of Physics and Chemistry of Solids* **2000,** *61* (8), 1345-1356.

29.     Marchbank, H. R.; Clark, A. H.; Hyde, T. I.; Playford, H. Y.; Tucker, M. G.; Thompsett, D.; Fisher, J. M.; Chapman, K. W.; Beyer, K. A.; Monte, M.; Longo, A.; Sankar, G., Structure of Nano-sized $CeO_2$ Materials: Combined Scattering and Spectroscopic Investigations. *ChemPhysChem* **2016,** *17* (21), 3494-3503.

30.     Adam, H. C.; Huw, R. M.; Timothy, I. H.; Helen, Y. P.; Matthew, G. T.; Gopinathan, S., Reverse Monte Carlo studies of $CeO_2$ using neutron and synchrotron radiation techniques. *Physica Scripta* **2017,** *92* (3), 034002.

31.     Hiley, C. I.; Playford, H. Y.; Fisher, J. M.; Felix, N. C.; Thompsett, D.; Kashtiban, R. J.; Walton, R. I., Pair Distribution Function Analysis of Structural Disorder by $Nb^{5+}$ Inclusion in Ceria: Evidence for Enhanced Oxygen Storage Capacity from Under-Coordinated Oxide. *Journal of the American Chemical Society* **2018,** *140* (5), 1588-1591.

32.     Takahashi, T.; Iwahara, H.; Nagai, Y., High oxide ion conduction in sintered $Bi_2O_3$ containing SrO, CaO or $La_2O_3$. *Journal of Applied Electrochemistry* **1972,** *2* (2), 97-104.

33.     Kuang, X.; Payne, J. L.; Johnson, M. R.; Evans, I. R., Remarkably High Oxide Ion Conductivity at Low Temperature in an Ordered Fluorite-Type Superstructure. *Angewandte Chemie International Edition* **2012,** *51* (3), 690-694.

34.     Hull, S.; Norberg, S. T.; Tucker, M. G.; Eriksson, S. G.; Mohn, C. E.; Stølen, S., Neutron total scattering study of the δ and β phases of $Bi_2O_3$. *Dalton Transactions* **2009,** (40), 8737-8745.

35. Watanabe, A.; Kikuchi, T., Cubic-hexagonal transformation of yttria-stabilized δ-bismuth sesquioxide, $Bi_{2-2x}Y_{2x}O_3$ ($x = 0.215 - 0.235$). *Solid State Ionics* **1986,** *21* (4), 287-291.

36. Orlova, E. I.; Kharitonova, E. P.; Gorshkov, N. V.; Goffman, V. G.; Voronkova, V. I., Phase formation and electrical properties of $Bi_2O_3$-based compounds in the $Bi_2O_3$–$La_2O_3$–$MoO_3$ system. *Solid State Ionics* **2017,** *302*, 158-164.

37. Shitara, K.; Moriasa, T.; Sumitani, A.; Seko, A.; Hayashi, H.; Koyama, Y.; Huang, R.; Han, D.; Moriwake, H.; Tanaka, I., First-Principles Selection of Solute Elements for Er-Stabilized $Bi_2O_3$ Oxide-Ion Conductor with Improved Long-Term Stability at Moderate Temperatures. *Chemistry of Materials* **2017,** *29* (8), 3763-3768.

38. Sanna, S.; Esposito, V.; Andreasen, J. W.; Hjelm, J.; Zhang, W.; Kasama, T.; Simonsen, S. B.; Christensen, M.; Linderoth, S.; Pryds, N., Enhancement of the chemical stability in confined $δ$-$Bi_2O_3$. *Nature Materials* **2015,** *14* (5), 500-504.

39. Takahashi, T.; Iwahara, H.; Arao, T., High oxide ion conduction in sintered oxides of the system $Bi_2O_3$-$Y_2O_3$. *Journal of Applied Electrochemistry* **1975,** *5* (3), 187-195.

40. Wind, J.; Auckett, J. E.; Withers, R. L.; Piltz, R. O.; Maljuk, A.; Ling, C. D., Type II $Bi_{1-x}W_xO_{1.5 + 1.5x}$: a (3+3)-dimensional commensurate modulation that stabilizes the fast-ion conducting delta phase of bismuth oxide. *Acta Crystallographica Section B: Structural Science Crystal Engineering and Materials* **2015,** *71* (6), 679-687.

41. Wind, J.; Kayser, P.; Zhang, Z.; Radosavljevic Evans, I.; Ling, C. D., Stability and range of the type II $Bi_{1-x}W_xO_{1.5+1.5x}$ solid solution. *Solid State Ionics* **2017,** *308* (Supplement C), 173-180.

42. Borowska-Centkowska, A.; Leszczynska, M.; Krok, F.; Malys, M.; Wrobel, W.; Hull, S.; Abrahams, I., Local structure and conductivity behaviour in $Bi_7WO_{13.5}$. *Journal of Materials Chemistry A* **2018,** *6* (13), 5407-5418.

43. Tate, M. L.; Hack, J.; Kuang, X.; McIntyre, G. J.; Withers, R. L.; Johnson, M. R.; Evans, I. R., $Bi_{1-x}NbxO_{1.5+x}$ ($x$=0.0625, 0.12) fast ion conductors: Structures, stability and oxide ion migration pathways. *Journal of Solid State Chemistry* **2015,** *225*, 383-390.

44. Gambino, M.; Giannici, F.; Longo, A.; Di Tommaso, S.; Labat, F.; Martorana, A., Dopant Clusterization and Oxygen Coordination in Ta-Doped Bismuth Oxide: A Structural and Computational Insight into the Mechanism of Anion Conduction. *Journal of Physical Chemistry C* **2015,** *119* (47), 26367-26373.

45. Firman, K.; Tan, K. B.; Khaw, C. C.; Zainal, Z.; Tan, Y. P.; Chen, S. K., Doping mechanisms and electrical properties of bismuth tantalate fluorites. *Journal of Materials Science* **2017,** *52* (17), 10106-10118.

46. Payne, J. L.; Farrell, J. D.; Linsell, A. M.; Johnson, M. R.; Evans, I. R., The mechanism of oxide ion conductivity in bismuth rhenium oxide, $Bi_{28}Re_2O_{49}$. *Solid State Ionics* **2013,** *244*, 35-39.

47. Pandey, J.; Shrivastava, V.; Nagarajan, R., Metastable $Bi_2Zr_2O_7$ with Pyrochlore-like Structure: Stabilization, Oxygen Ion Conductivity, and Catalytic Properties. *Inorganic Chemistry* **2018,** *57* (21), 13667-13678.

48. Mercurio, D.; Farissi, M. E.; Champarnaud-Mesjard, J. C.; Frit, B.; Conflant, P.; Roult, G.; Vogt, T., Etude structurale par diffraction X sur monocristal et diffraction neutronique sur poudre de l'oxyde mixte $Bi_{0.7}La_{0.3}O_{1.5}$. *Journal of Solid State Chemistry* **1989,** *80* (1), 133-143.

49. Darriet, J.; Launay, J. C.; Zúniga, F. J., Crystal structures of the ionic conductors $Bi_{46}M_8O_{89}$ (M=P, V) related to the fluorite-type structure. *Journal of Solid State Chemistry* **2005,** *178* (6), 1753-1764.

50. Mauvy, F.; Launay, J. C.; Darriet, J., Synthesis, crystal structures and ionic conductivities of $Bi_{14}P_4O_{31}$ and $Bi_{50}V_4O_{85}$. Two members of the series $Bi_{18-4m}M_{4m}O_{27+4m}$ (M=P, V) related to the fluorite-type structure. *Journal of Solid State Chemistry* **2005,** *178* (6), 2015-2023.

51. Drache, M.; Obbade, S.; Wignacourt, J. P.; Conflant, P., Structural and Conductivity Properties of $Bi_{0.775}Ln_{0.225}O_{1.5}$Oxide Conductors (Ln=La, Pr, Nd, Sm, Eu, Gd, Tb, Dy) with Rhombohedral Bi–Sr–O Type. *Journal of Solid State Chemistry* **1999,** *142* (2), 349-359.

52. Leszczynska, M.; Liu, X.; Wrobel, W.; Malys, M.; Krynski, M.; Norberg, S. T.; Hull, S.; Krok, F.; Abrahams, I., Thermal Variation of Structure and Electrical Conductivity in $Bi_4YbO_{7.5}$. *Chemistry of Materials* **2013,** *25* (3), 326-336.

53. Leszczynska, M.; Liu, X.; Wrobel, W.; Malys, M.; Norberg, S. T.; Hull, S.; Krok, F.; Abrahams, I., Total scattering analysis of cation coordination and vacancy pair distribution in Yb substituted $δ$-$Bi_2O_3$. *Journal of Physics: Condensed Matter* **2013,** *25* (45), 454207.

54. Borowska-Centkowska, A.; Liu, X.; Holdynski, M.; Malys, M.; Hull, S.; Krok, F.; Wrobel, W.; Abrahams, I., Conductivity in lead substituted bismuth yttrate fluorites. *Solid State Ionics* **2014,** *254*, 59-64.

55. Borowska-Centkowska, A.; Liu, X.; Krynski, M.; Leszczynska, M.; Wrobel, W.; Malys, M.; Hull, S.; Norberg, S. T.; Krok, F.; Abrahams, I., Defect structure in $δ$-$Bi_5PbY_2O_{11.5}$. *RSC Advances* **2019,** *9* (17), 9640-9653.

56. Payne, J. L.; Tucker, M. G.; Evans, I. R., From fluorite to pyrochlore: Characterisation of local and average structure of neodymium zirconate, $Nd_2Zr_2O_7$. *Journal of Solid State Chemistry* **2013,** *205*, 29-34.

57. Norberg, S. T.; Hull, S.; Eriksson, S. G.; Ahmed, I.; Kinyanjui, F.; Biendicho, J. J., Pyrochlore to Fluorite Transition: The $Y_2(Ti_{1-x}Zr_x)_2O_7$ ($0.0 ≤ x ≤ 1.0$) System. *Chemistry of Materials* **2012,** *24* (22), 4294-4300.

58. Shamblin, J.; Feygenson, M.; Neuefeind, J.; Tracy, C. L.; Zhang, F.; Finkeldei, S.; Bosbach, D.; Zhou, H.; Ewing, R. C.; Lang, M., Probing disorder in isometric pyrochlore and related complex oxides. *Nature Materials* **2016,** *15*, 507.

59. Voronkova, V. I.; Leonidov, I. A.; Kharitonova, E. P.; Belov, D. A.; Patrakeev, M. V.; Leonidova, O. N.; Kozhevnikov, V. L., Oxygen ion and electron conductivity in fluorite-like molybdates $Nd_5Mo_3O_{16}$ and $Pr_5Mo_3O_{16}$. *Journal of Alloys and Compounds* **2014,** *615*, 395-400.

60. Ishikawa, Y.; Danilkin, S. A.; Avdeev, M.; Voronkova, V. I.; Sakuma, T., Crystal structure of $R_{10}Mo_6O_{33}$ (R = Nd, Pr) from 3 K to 973 K by neutron powder diffraction. *Solid State Ionics* **2016,** *288*, 303-306.

61. Jacas Biendicho, J.; Playford, H. Y.; Rahman, S. M. H.; Norberg, S. T.; Eriksson, S. G.; Hull, S., The Fluorite-Like Phase $Nd_5Mo_3O_{16±δ}$ in the $MoO_3$–$Nd_2O_3$ System: Synthesis, Crystal Structure, and Conducting Properties. *Inorganic Chemistry* **2018,** *57* (12), 7025-7035.

62.     Kalland, L.-E.; Norberg, S. T.; Kyrklund, J.; Hull, S.; Eriksson, S. G.; Norby, T.; Mohn, C. E.; Knee, C. S., C-type related order in the defective fluorites $La_2Ce_2O_7$ and $Nd_2Ce_2O_7$ studied by neutron scattering and ab initio MD simulations. *Physical Chemistry Chemical Physics* **2016,** *18* (34), 24070-24080.

63.     Katz, L.; Ward, R., Structure Relations in Mixed Metal Oxides. *Inorganic Chemistry* **1964,** *3* (2), 205-211.

64.     García-González, E.; Parras, M.; González-Calbet, J. M., Electron Microscopy Study of a New Cation Deficient Perovskite-like Oxide: $Ba_3MoNbO_{8.5}$. *Chemistry of Materials* **1998,** *10* (6), 1576-1581.

65.     Skowron, A.; Huang, P.-n.; Petric, A., Structural Study of $La_{0.8}Sr_{0.2}Ga_{0.85}Mg_{0.15}O_{2.825}$. *Journal of Solid State Chemistry* **1999,** *143* (2), 202-209.

66.     Huang, K.; Tichy, R. S.; Goodenough, J. B., Superior Perovskite Oxide-Ion Conductor; Strontium-and Magnesium-Doped LaGaO3: I, Phase Relationships and Electrical Properties. *Journal of the American Ceramic Society* **1998,** *81* (10), 2565-2575.

67.     Kitamura, N.; Vogel, S. C.; Idemoto, Y., Local structure analysis on $(La,Ba)(Ga,Mg)O_{3-\delta}$ by the pair distribution function method using a neutron source and density functional theory calculations. *Solid State Communications* **2013,** *163*, 46-49.

68.     Kitamura, N.; Hamao, N.; Vogel, S. C.; Idemoto, Y., Oxide-Ion Conduction, Average and Local Structures of $LaSrGa_{1-x}Mg_xO_{4-\delta}$ with Layered Perovskite Structure. *Electrochemistry* **2013,** *81* (6), 448-453.

69.     Mancini, A.; Shin, J. F.; Orera, A.; Slater, P. R.; Tealdi, C.; Ren, Y.; Page, K. L.; Malavasi, L., Insight into the local structure of barium indate oxide-ion conductors: An X-ray total scattering study. *Dalton Transactions* **2012,** *41* (1), 50-53.

70.     Lacorre, P.; Goutenoire, F.; Bohnke, O.; Retoux, R.; Laligant, Y., Designing fast oxide-ion conductors based on $La_2Mo_2O_9$. *Nature* **2000,** *404* (6780), 856-858.

71.     Evans, I. R.; Howard, J. A. K.; Evans, J. S. O., The crystal structure of $\alpha$-$La_2Mo_2O_9$ and the structural origin of the oxide ion migration pathway. *Chemistry of Materials* **2005,** *17* (16), 4074-4077.

72.     Paul, T.; Tsur, Y., A protocol to detect the phase transition in $La_2Mo_2O_9$ oxide ion conductor. *Materials Letters* **2018,** *220*, 325-327.

73.     Kuang, X.; Green, M. A.; Niu, H.; Zajdel, P.; Dickinson, C.; Claridge, J. B.; Jantsky, L.; Rosseinsky, M. J., Interstitial oxide ion conductivity in the layered tetrahedral network melilite structure. *Nature Materials* **2008,** *7* (6), 498-504.

74.     Mancini, A.; Tealdi, C.; Malavasi, L., Interstitial oxygen in the Ga-based melilite ion conductor: A neutron total scattering study. *International Journal of Hydrogen Energy* **2012,** *37* (9), 8073-8080.

75.     Mayer, H.; Völlenke, H., Die Kristallstruktur von $Ge_5O[PO_4]_6$. *Monatshefte für Chemie* **1972,** *103*, 1560-1571.

76.     Masson, O.; Berghout, A.; Béchade, E.; Jouin, J.; Thomas, P.; Asaka, T.; Fukuda, K., Local structure and oxide-ion conduction mechanism in apatite-type lanthanum silicates. *Science and Technology of Advanced Materials* **2017,** *18* (1), 644-653.

77.     Kim, D.-Y.; Lee, S.-G., Fabrication and electrical properties of Si-based $La_{10-x}Bi_x(SiO_4)_6O_3$ apatite ionic conductor. *Materials Research Bulletin* **2012,** *47* (10), 2856-2858.

78.     Fop, S.; Skakle, J. M. S.; McLaughlin, A. C.; Connor, P. A.; Irvine, J. T. S.; Smith, R. I.; Wildman, E. J., Oxide Ion Conductivity in the Hexagonal Perovskite Derivative $Ba_3MoNbO_{8.5}$. *Journal of the American Chemical Society* **2016,** *138* (51), 16764-16769.

79.     Obbade, S.; Huve, M.; Suard, E.; Drache, M.; Conflant, P., Powder Neutron Diffraction and TEM Investigations of $Bi_{0.775}Ln_{0.225}O_{1.5}$ Oxide Conductors (Ln=La, Pr, Nd, Sm, Tb, Dy) with Rhombohedral Bi–Sr–O type: Structural Relationships with Monoclinic $\epsilon$-$Bi_{4.86}La_{1.14}O_9$ Form. *Journal of Solid State Chemistry* **2002,** *168* (1), 91-99.

# 2. Experimental Methods

## 2.1 Synthetic Techniques

### 2.1.1 Solid-state synthesis

There are many ways to prepare solids, depending on the form of the product desired, such as foams, ceramics, powders, fibres or single crystals.[1] The commonest and most straight-forward of these methods is the ceramic method.[2] The ceramic method involves the mixing of reactant materials in accurately weighed, stoichiometric quantities, followed by heating. In order to achieve a homogenous mixture, tools such as a mortar and pestle or a milling machine are employed. The first step in the reaction is the nucleation of the product phases. Product nuclei need to be tens of angstroms in size in order to be stable,[1] which requires a certain quantity of atoms of reactants to be arranged correctly. This process is assisted when there is a surface that the products can form on and if that substrate has a similar packing arrangement (*e.g.* close cubic packing or hexagonal cubic packing), allowing a coherent interface to form. This process, whilst simple to perform, has several flaws. In an idealised, perfect mixture of reactants, the product can form at the interface of the two different reactant particles. After this initial reaction, however, a layer of product begins to form, and the atoms from the reactants must diffuse through this layer in order for the reaction to proceed, illustrated in Figure 2.1.
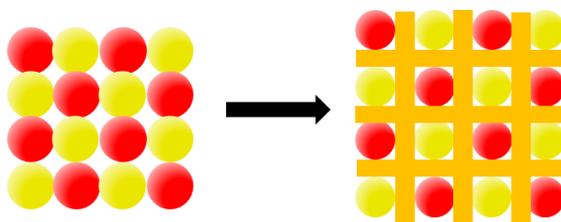


**Figure 2.1 –** The solid state reaction between perfectly mixed, 1:1 reactants. Red circles represent one reactant; yellow circles represent the other reactant; orange represents the product that forms at the interface of the two reactants.

The reaction requires high temperatures, typically from 500 °C up to 2000 °C,[2] as high levels of thermal energies are required in order for diffusion of the ions to take place. An additional problem is that as the reaction proceeds, the thickness of the layer of product increases, increasing the diffusion path length, creating a challenge to complete the reaction. This can be overcome by intermittent regrinding, which forms new interfaces.

### 2.1.2 Sol-gel method

Whilst solid state synthesis is highly versatile, the difficulty in diffusion can result in heterogeneous mixtures and high temperatures, consistent grinding and long synthesis times are required in order to synthesise a sample. One method that can be employed to overcome these

problems is the sol-gel method. The principle of the sol-gel method is to begin with a homogeneous solution that contains all the cations desired for the final product,[1] which is heated. This produces a viscous sol, which is a colloid containing solid particles of 1-100 nm suspended in a liquid.[2] These particles can be highly homogenous, allowing a faster reaction. Upon further treatment, the sol dries into a gel, a homogeneous, amorphous solid, which has the solvent suspended within the gel framework. The final step is to calcine the gel, removing any volatile solvents or chemically-bonded organic components.[1] The source of cations is usually an alkoxide.[3] Tetraethylorthosilicate (TEOS), $Si(OCH_2CH_3)$ for example, is used as a source of $SiO_2$. The alkoxides are hydrolysed by water, where ethanol is also employed to improve miscibility, and an acid or base is used to catalyse the reaction. The hydrolysis reaction, which involves two steps, is given in equations 2.1.1 and 2.1.2:

$$Si(OR)_4 + H_2O \rightarrow Si(OR)_3(OH) + ROH \qquad (2.1.1)$$

$$(RO)_3Si\!-\!OH + (RO)_3Si\!-\!OH \rightarrow (RO)_3Si\!-\!O\!-\!Si(OR)_3 \qquad (2.1.2)$$
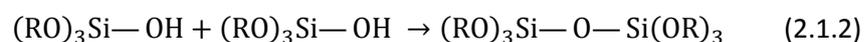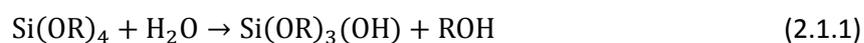
If different cationic species are required, then a cross-condensation may be required. Additional reagents may also be present by dissolving the oxides in an acid before adding to the alkoxide.[4]

## 2.2 X-ray and Neutron Bragg Diffraction

### 2.2.1 X-ray generation in laboratory diffractometers

X-rays are electromagnetic radiation with a wavelength of 0.1 to 100 Å, between UV and gamma rays in the electromagnetic spectrum. X-rays are produced when charged particles with high energies collide with matter, such as electrons accelerated by a potential difference of 30-40 keV. The collision of the electrons with matter results in a loss of energy, emitted as X-ray radiation with a distribution of wavelengths, or "white" X-rays.[5] Accelerated electrons can also ionise an element's 1s electrons, referred to as the core electrons or K shell. An electron from higher orbitals, such as 2p or 3p drops down to occupy the empty space, releasing energy during the transition. As the energies of orbitals in each element are quantised, monochromatic X-rays are emitted. The X-rays produced by the 2p → 1s transition are called Kα radiation and the X-rays produced by the 3p → 1s transition are called Kβ radiation. This process is outlined in Figure 2.2.
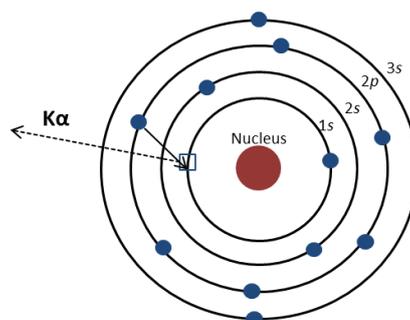
**Figure 2.2[5] –** Production of Kα X-rays in Cu showing an electron from the 2p orbital filling the empty 1s level accompanied by the release of X-ray radiation.

The energy levels of atoms are dependent on their atomic numbers, *Z*, such that a transition from a non-hydrogen element will emit a photon with energy, *E*, of:

$$E = hc(Z-1)^2 R \left( \frac{1}{n_1^2} - \frac{1}{n_2^2} \right)$$  (2.2)

where *h* is Planck's constant, $6.626 \times 10^{-34}$ J s, *c* is the speed of light in a vacuum, $2.998 \times 10^{10}$ cm s$^{-1}$, *R* is the Rydberg constant, $1.097 \times 10^5$ cm$^{-1}$ and $n_1$ and $n_2$ are principal quantum numbers, where $n_1 < n_2$. Many laboratory powder diffractometers use Cu as the target metal to generate X-rays, where Kα = 1.5418 Å and Kβ = 1.3922 Å, though the Kα line is actually a doublet due to the two possible spin states of the 2*p* electrons producing slightly different energies during the transition, $K\alpha_1$ = 1.54051 Å and $K\alpha_2$ = 1.54433 Å.[5] Another common target used in diffractometers is Mo, which gives shorter wavelengths of $K\alpha_1$ = 0.7093Å and $K\alpha_2$ = 0.7135 Å. In diffractometers, an evacuated chamber, known as the X-ray tube, contains the target metal, a tungsten filament and beryllium windows, as well as lead shielding. The tungsten filament is heated so that it emits electrons, which are accelerated to the target using a high potential difference (usually ≥ 30 kV), producing X-rays. Beryllium windows are used to aim the X-rays from the chamber due to its small absorption (Z = 4) of X-rays. As white X-rays and Kβ radiation are also produced, in Cu tubes, Ni foil is used, as it absorbs at 1.488 Å, between the Kα and Kβ lines of Cu,[5] removing the Kβ and white X-rays.

## 2.2.2 Diffraction and laboratory X-ray sources

Diffraction occurs when a wave interacts with an object or slit that is a similar size to the wavelength of the wave interacting with it bending it.[6] When there are multiple points in an object, such as diffraction grating, we imagine that light is radiated from these points in all directions, allowing interference to occur. Waves that are in phase with each other, *i.e.* with no difference in amplitude at the same point in time (illustrated by Figure 2.3a), will undergo constructive interference, whilst waves that are out of phase with each other will undergo destructive interference.
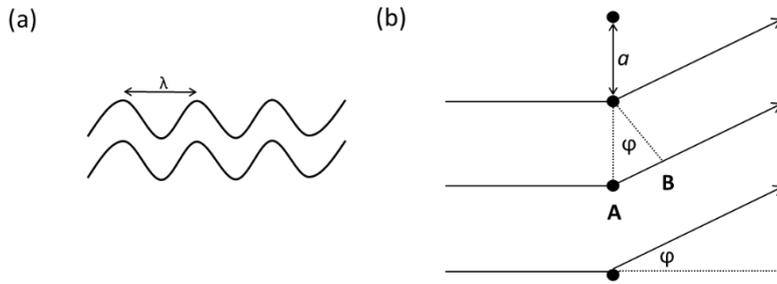
**Figure 2.3** – (a) Waves in phase and (b) constructive interference in diffraction grating, where the arrows represent the direction of waves in phase, $\varphi$ is the angle of diffraction of a wave and a is the slit size.

Constructive interference is governed by the wavelength, $\lambda$, and the slit length, $a$. In order for constructive interference to occur, the condition[5] $\mathbf{AB} = a\sin\varphi$ (shown in Figure 2.3b) must be an integer number of wavelengths. Therefore:

$$a\sin\varphi = n\lambda \qquad (2.3)$$

Crystals, which are periodic arrays of atoms, ions or molecules,[2] can be considered analogous to a diffraction grating, where the slit size is the distance between an atom, an ion or a molecule. Bragg's law is a simple model that can be used to help understand diffraction by crystal line solids. Considering crystals as planes of semi-transparent mirrors, described by their Miller indices $hkl$, separated by a distance $d_{hkl}$, some X-rays will be reflected from the first plane, A, at the angle of incidence, or Bragg angle $\theta$, but some will travel through the first plane and be reflected by the second plane, B. This is illustrated in Figure 2.4.
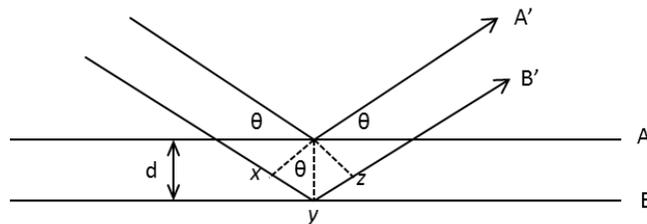


**Figure 2.4**[5] – Illustration of Bragg's law.

Beam B' must travel the distance $xyz$ further than beam A', and $xyz$ must be an integer number of the wavelengths in order for beam A' and beam B' to be in phase. As $xy = yz = d_{hkl}\sin\theta$, $xyz = 2d_{hkl}\sin\theta$, and as $xyz = n\lambda$ during constructive interference, it means that the condition below must be satisfied:

$$n\lambda = 2d_{hkl}\sin\theta \qquad (2.4)$$

The diffraction order, $n$ is an integer number. A diffraction order of $n = 1$ corresponds to the Bragg condition that must be satisfied between the first two planes. If the diffraction order is greater than 1, *e.g.* 2, this would correspond to the condition that must be satisfied if diffraction were to

occur between the first plane and a second plane with a separation $d/2$, which would therefore produce a $d_{hkl}$ of ½ that for $n$ = 1. Therefore, a diffraction order of $n$ = 1 is most often used for expressing the $hkl$ values of each corresponding Bragg peak. Using the value of $d_{hkl}$ obtained from this equation, the unit cell parameters $a$, $b$ and $c$ can be related to the indices $h$, $k$ and $l$, such as for an orthorhombic system using equation 2.5:

$$\frac{1}{d^2} = \frac{h^2}{a^2} + \frac{k^2}{b^2} + \frac{l^2}{c^2}$$
(2.5)

For crystals, interference is destructive in most directions, leading to scattered intensity being constrained to specific directions. This gives beams of diffracted intensity, which become spots on a detector or film surface.

X-rays are scattered by the electron cloud of an atom. As interference occurs between X-rays scattered from different parts of the electron cloud, such as the core or valence electrons, the atomic scattering factor, $f_n$, is reduced as the scattering angle $2\theta$ is increased.[7] At $\sin(\theta)/\lambda = 0$, $f_n$ is proportional to Z. The structure factor, which is the sum of the scattering from each atom in a unit cell at particular reflections, is defined by equation 2.6:[1, 8]

$$F_{hkl} = \sum_n f_n \cos 2\pi(hx_n + ky_n + lz_n) + i\sin 2\pi(hx_n + ky_n + lz_n)$$
(2.6)

where $x_n$, $y_n$ and $z_n$ are the fractional coordinates of the nth atom. The resulting intensity that is detected in diffraction, $I_{hkl}$, is directly proportional to $F_{hkl}^2$, meaning that reflections with high structure factors will result in high intensities and those where $F_{hkl}$ = 0 result in zero intensity.[8] Therefore, the intensities of a pattern allow the structure factor to be determined, which itself allows the atomic coordinates to be determined. Together with the peak positions, which reveal the unit cell parameters, crystal structures can be solved. Known crystalline phases can therefore also be identified. It can be difficult to detect atoms with small Z, *e.g.* H, when they are in the same crystal as atoms with a large Z. In addition, it is difficult to differentiate atoms that have a similar Z, such as Fe and Co.

### 2.2.3 Synchrotron radiation

Another way of producing X-ray radiation is through the use of synchrotrons. An electron gun produces electrons by heating a metal filament. The electrons are accelerated using linear accelerators (linacs) into a booster synchrotron ring, which accelerates the electrons to relativistic speeds, after which they are injected into an outer ring and are driven around this ring using magnets. As the electrons travel around the ring, following a curved path, they emit radiation. The relativistic speeds also distort the angular distribution of the emitted radiation, resulting in a very narrow cone parallel to the instantaneous velocity.[7] Additional insertion devices, known as 'wigglers' and undulators can be employed, which make the electrons wiggle along their path,

producing very high energy X-rays in a wide cone, or make the electrons undulate, producing very bright light in a narrow beam. The emitted radiation goes from the ring into a beamline where the sample and detectors are placed. A schematic of the Diamond Light Source (DLS) synchrotron is shown in Figure 2.5.
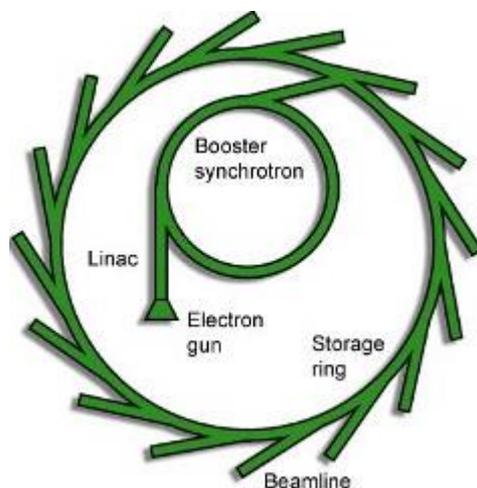


**Figure 2.5** – Schematic of Diamond Light Source (DLS) synchrotron.[9] Electrons are accelerated using the linac around the booster synchrotron until their velocities are close to the speed of light, at which point they are injected into the storage ring. The beamlines are placed so that they receive radiation emitted from the electrons as they bend around the ring**.**

Synchrotron radiation has several advantages over standard X-ray sources: it has a much higher intensity, the wavelength is tuneable, due to the insertion devices, and it can be made highly monochromatic. "White" X-rays from the ring are filtered by a monochromator, which is a crystal (usually Si) that is oriented such that only the radiation of the desired wavelength fulfils Bragg's law to be scatted in the direction of the sample. The high intensity means that beamlines can also be equipped with high-resolution detectors, such as the I11 beamline at DLS, which was used for high resolution and variable temperature (VT) powder diffraction in this report. The I11 beamline receives X-rays over an energy range of 5-25 keV ($\lambda$ = 0.4 – 2.1 Å) and utilises five multi-analysing crystal (MAC) devices as detectors.

### 2.2.4 Neutron generation

Although waves are commonly used to explain diffraction, subatomic particles such as electrons and neutrons can also be diffracted due to wave-particle duality, expressed by the de Broglie relationship:

$$\lambda = \frac{h}{mv} \qquad\qquad (2.7)$$

where $h$ = Planck's constant, $m$ = mass of the particle and $v$ is the velocity of the particle. Neutrons are scattered by the nucleus. The neutron scattering length, b, which is analogous to the X-ray scattering factor $f_n$, is defined as:[10]

$$b = b_c + \frac{2b_i}{\sqrt{I(I+1)}} s \cdot I \qquad (2.8)$$

where $b_c$ and $b_i$ are the bound coherent and incoherent scattering lengths, s is the spin of the neutron (= ½) and I is the spin of the nucleus. There is no smooth dependence on Z in neutron diffraction. This, in general, allows for light elements to be located with more precision amongst heavier elements and to be able to distinguish between neighbouring elements. Isotopes of elements also have different scattering powers. Furthermore, the scattering length does not decrease with increasing $\theta$, as the nucleus is so small that the neutrons do not scatter differently from different parts of the nucleus. As neutrons have a magnetic moment, they can also be used to study magnetic ordering in solids.[5]

Neutrons can be generated in a nuclear reactor, or through spallation. Spallation involves the acceleration of protons at high energies (800 MeV[8]) to a target metal, such as tungsten, ejecting neutrons from the target. The neutrons produced have a variety of different energies, which means that their wavelengths differ. At the UK's spallation source, the ISIS facility in the Rutherford Appleton Laboratory, time-of-flight (TOF) diffraction is used, where the time (TOF) taken for the neutrons to reach the detectors along a known distance is measured, allowing the velocity (and therefore $\lambda$ using equation 2.7) to be determined as $v = \frac{d}{TOF}$. The angle of the detectors to the sample is fixed and the wavelength of the diffracted radiation varies, so the Bragg condition is satisfied by the varying wavelength of the diffracted neutrons.

### 2.2.5 Analysis – Rietveld and Pawley refinements

Rietveld refinement is a method to fit a model to the experimental powder diffraction pattern, using the least squares method to minimise the difference between the calculated values and the observed values.[11] The starting structural model requires lattice parameters, atomic fractional coordinates, atomic occupancies, atomic displacement parameters and the space group. Additional parameters are also included, such as the sample height or zero offset, instrumental parameters and the background, which can be fitted using a Chebyshev polynomial. Additionally, the peak shape is included, often using a pseudo-Voigt function. These parameters are refined in order to minimise the difference between the observed powder pattern and the calculated powder pattern. The sum of the squared differences, S, is defined by equation 2.9:[12]

$$S = \sum_i w(y_{io} - y_{ic})^2 \qquad (2.9)$$

where $y_{io}$ is the observed intensity at $2\theta$ ($i$), $y_{ic}$ is the calculated intensity and $w$ is a weighting factor, $\frac{1}{\sigma^2}$, where $\sigma$ is the experimental uncertainty of $y_{io}$. A residual factor, $R_{wp}$, is used to assess the fit of the model to the data:

$$R_{wp} = \left[\frac{\sum_i w_i (y_{io} - y_{ic})^2}{\sum_i w_i (y_{io})^2}\right]^{\frac{1}{2}} = \left[\frac{S}{\sum_i w_i (y_{io})^2}\right]^{\frac{1}{2}} \qquad (2.10)$$

Additionally, the statistically expected fit, $R_{exp}$, allows an assessment of the fit based on the number of parameters used:

$$R_{exp} = \left[\frac{N-P}{\sum_{i=1}^{n} w_i (y_{io})^2}\right]^{\frac{1}{2}} \qquad (2.11)$$

where $N$ = number of data points and $P$ = the number of refined parameters. The goodness of fit, $\chi^2$, which is the square of the ratio between $R_{wp}$ and $R_{exp}$, is also used. $\chi^2$ is defined by equation 2.12:

$$\chi^2 = \left(\frac{R_{wp}}{R_{exp}}\right)^2 \qquad (2.12)$$

The Pawley refinement is another least squares minimisation method for fitting a model to a powder diffraction pattern. Unlike the Rietveld method, the Pawley refinement fits the observed data without taking into account the contents of the unit cell, *i.e.* the atomic sites.[13] Instead, the fit is defined only by the cell parameters, the space group symmetry, and background and peak intensities are refined in order to minimise the difference between the observed data and calculated pattern. It is useful for determining if the symmetry and unit cell parameters can fit the observed data, before any further structural parameters are applied.

## 2.3 Total Scattering

### 2.3.1 – Background theory

Bragg diffraction is a result of the periodicity within crystals. This analytical technique, however, only reveals the average structure of a material and says little about local distortions that may be present. In fact, perfect periodicity does not truly exist in crystals due to the quantum-mechanical motions that cause atoms to vibrate at any temperature, which in crystallography is accounted for by the Debye-Waller or "temperature" factor.[14] In a diffraction pattern of a perfect crystal with no motion or defects, only the Bragg peaks would be present, but in real patterns there is further elastic scattering present as a background underneath the Bragg peaks. This background is the diffuse scattering, which is caused by thermal motions of atoms and the defects present in real crystals, which deviate from the perfect periodicity.[15] By analysing the diffuse scattering, information about local structure can be obtained, for example revealing a local ordering which

cannot be distinguished from random local ordering using Bragg scattering alone.[16] This method is also used for studying the structure of amorphous materials, which have no long-range order but do contain short-range structure, such as glasses and liquids. Total scattering utilises both the Bragg diffraction and the diffuse scattering to simultaneously obtain information about both long-range ordering and short-range structure.[14-15, 17] In order to obtain high quality information from the diffuse scattering, the magnitude of the diffraction vector $\boldsymbol{Q}$, must be as large as possible, ideally in the range of[14, 17] $20 - 60$ Å$^{-1}$, where the diffuse scattering no longer overlaps with the Bragg scattering. In elastic scattering, this is defined as:

$$|\boldsymbol{Q}| = Q = \frac{4\pi \sin \theta}{\lambda} \tag{2.13}$$

where $\theta$ is the angle of incidence of the wave to be diffracted and $\lambda$ is its wavelength. The real-space resolution, $\Delta r$, is dominated by the maximum $Q$ collected according to:

$$\Delta r \approx \frac{2\pi}{Q_{max}} \tag{2.14}$$

where $Q_{max}$ is the maximum $Q$ value used in the scattering experiment. Using a Cu K$\alpha$ source of $\lambda \approx$ 1.54 Å, which is typically used in laboratory X-ray diffractometers, the $Q_{max}$ is only ~8.15 Å$^{-1}$. This range of $Q$ is dominated by Bragg scattering and therefore does not yield much information about the local structure. For this reason, total scattering is usually collected at dedicated neutron sources and at synchrotrons, which produce lower wavelength radiation, giving higher $Q$. From the total scattering, the atomic pair distribution function (PDF), which describes the probability of finding a pair of atoms at a given separation, can be derived.

### 2.3.2 – Definitions and formalisms

Within total scattering, there are different definitions used by different researches for the various functions. Here, the functions as defined by Keen[18] are used. The total scattering structure factor, *F(Q)*, is the experimentally measured quantity. It is the sum of the scattering from every pair of atoms *i* and *j*, $A_{ij}(Q)$, and is defined as:

$$F(Q) = \sum_{i,j=1}^{n} c_i c_j b_i b_j \left[ A_{ij}(Q) - 1 \right] \tag{2.15}$$

where $c_i$ and $c_j$ are the concentrations of atom *i* and *j* in atoms per formula unit, $b_i$ and $b_j$ are the coherent neutron scattering lengths and $A_{ij}(Q)$ are the Faber-Ziman partial structure factors; *i.e.* the scattering factors from individual pairs *i* and *j* . X-ray scattering, however, is dependent on $2\theta$ through the form factor. One can replace the coherent neutron scattering lengths with the $Q$ dependent X-ray scattering coefficients, $f_e(Q)$ to modify the following definitions for X-ray scattering. In addition to *F(Q)*, the total structure factor may also be expressed as *S(Q)*, which is defined as:

$$S(Q) = \frac{F(Q)}{\left(\sum_{i=1}^{n} c_i b_i\right)^2} + 1 \qquad (2.16)$$

A Fourier transform of the total scattering structure factor, $F(Q)$, can yield the total radial distribution function, $G(r)$, shown in equations 2.17 and 2.18, which provides a histogram of all atom pairs in real space:

$$F(Q) = \rho_0 \int_0^{\infty} 4\pi r^2 G(r) \frac{\sin Qr}{Qr} \, dr \qquad (2.17)$$

and:

$$G(r) = \frac{1}{(2\pi)^3 \rho_0} \int_0^{\infty} 4\pi Q^2 F(Q) \frac{\sin Qr}{Qr} \, dQ \qquad (2.18)$$

where $\rho_0$ is the number density, $\rho_0 = \frac{N}{V}$, where $N$ is the number of atoms per unit cell and $V$ is the unit cell volume. $G(r)$, can be related to the partial radial distribution, $g_{ij}(r)$, analogous to the relationship of $F(Q)$ and $A_{ij}(Q)$:

$$G(r) = \sum_{i,j=1}^{n} c_i c_j b_i b_j \left[ g_{ij}(r) - 1 \right] \qquad (2.19)$$

Here $g_{ij}(r)$ is defined as:

$$g_{ij}(r) = \frac{n_{ij}(r)}{4\pi r^2 \, dr \rho_j} \qquad (2.20)$$

where $n_{ij}(r)$ is the number of particles of type $j$ within distances $r$ and $r + dr$ from a particle of type $i$ and $\rho_j = c_j \rho_0$. $G(r)$ is used to define the PDF. Another way of defining the PDF is through the related function $D(r)$, which is used as it has a greater dependence on $r$, so values at high-$r$ are more pronounced when compared to the $G(r)$. It is defined as:

$$D(r) = 4\pi r \rho_0 G(r) \qquad (2.21)$$

It can also be defined in relation to its own partial function, $d_{ij}(r)$:

$$D(r) = \sum_{i,j=1}^{n} c_i b_i b_j \left[ d_{ij}(r) \right] \qquad (2.22)$$

The $d_{ij}(r)$ is defined as:

$$d_{ij}(r) = 4\pi r c_j \rho_0 \left[ g_{ij}(r) - 1 \right] \qquad (2.23)$$

The total scattering data experimentally recorded were processed using Gudrun v5.[19] This software performs multiple tasks necessary for total scattering data processing. In the first step, any detectors where the normalised ratio of counts in the time channel to counts in the corresponding spectrum is either too low or too high are removed and detectors that have too little or too much noise are also removed. Gudrun extracts data from each detector used,

including the raw neutron counts and the final differential scattering cross section, combines all of the detectors in groups of detectors and merges this all into one single data set. The software subtracts the scattering that arises from the empty instrument, the sample environment and the empty can. GudrunN also normalises the data to a V rod, as V has a smooth incoherent scattering function. This allows the TOF data from each detector to be evaluated on an absolute scale, accounting for the fact that each detector is actually at a slightly different $2\theta$ from the target. The packing factor is also accounted for. The packing factor of a sample is the ratio of the measured density of the sample inside the can/capillary, $\rho_m$, and the theoretical density, $\rho_t$, *i.e.* $PF = \frac{\rho_m}{\rho_t}$.

Furthermore, GudrunN also performs the Fourier transform, during which a cut-off point for the minimum *r* in the PDF data can be defined and a Soper-Lorch correction can be applied. This latter function that smoothly sets $F(Q) = 0$ as $Q \rightarrow Q_{max}$ and allows the width of the broadening of the PDF peaks from this function to be changed. The correction lessens the effect of false Fourier ripples in PDF data without having to lower the $Q_{max}$. Overall, GudrunN can produce $F(Q)$, $S(Q)$, $G(r)$ and $D(r)$ data.

 Additionally, the STOG utility was used to produce PDF data. STOG uses the merged differential scattering with a Top Hat and deconvoluting function applied in real space to produce $G(r)$, $F(Q)$ and $S(Q)$ data. STOG allows a scale factor and an offset to be applied to the PDF data, which may sometimes be necessary for samples with incorrect packing factors.

### 2.3.3 – Analysis: small box modelling and Reverse Monte Carlo

There are two main methods of analysis that can be performed with PDF data: small box modelling and large box methods. Small box modelling refers to modelling of the structure using a single unit cell or a few unit cells. In this report, TOPAS Academic v6[20-21] was used for small box PDF modelling. TOPAS v6 uses structural parameters from the average structure and, as with Rietveld refinement, minimises the difference between calculated pattern and the observed pattern using least squares refinement, equations 2.10, 2.11 and 2.12, but with $y_{io}$ and $y_{ic}$ as PDF data instead of Bragg diffraction data. The native function used in TOPAS v6 PDF refinement is the $D(r)$.

The Reverse Monte Carlo (RMC) method was originally developed for analysis of diffuse scattering data from liquids and amorphous materials.[22] The algorithm consists of a starting model where there are *N* atoms in a box with periodic boundary conditions. A random move is calculated for an atom, and if the move would cause the distance to a neighbouring atom to be less than a predefined minimum distance, the move is rejected. If a move is accepted, the new PDF of the configuration is calculated and then compared to the observed data. If the move improves the fit, it is accepted. If the move would worsen the fit, the probability that the move would be accepted

is related to how much the fit would worsen, based on thermodynamic statistical mechanics. Further developments were made for the RMC method so that it could be applied to crystalline materials. One implementation of these ideas is in the RMCProfile software suite.[23] In this package, the periodic boundary conditions are the dimensions of a supercell of the crystallographic unit cell, usually on the order of ~ [5 × 5 × 5], containing tens of thousands of atoms. The RMCProfile software suite can simultaneously fit PDF, total structure factor and Bragg data. The $F(Q)$ calculated pattern is obtained by a Fourier transform of the calculated $G(r)$, which is limited by the size of the box used in the modelling. The goodness of fit (gof) value for the calculated and observed data, $\chi_{RMC}^2$, is defined as follows:

$$\chi_{RMC}^2 = \Sigma_j \chi_j^2 \tag{2.24}$$

where $\chi_j^2$ is the fit for data type $j$. This includes the gof for the PDF, $\chi_{G(r)}^2$, structure function , $\chi_{F(Q)}^2$, and the Bragg data, $\chi_{Bragg}^2$. They are given the following definitions:

$$\chi_{G(r)}^2 = \Sigma_j \frac{[G_{calc}(r_j) - G_{obs}(r_j)]^2}{\sigma_{G(r)^2}(r_j)} \tag{2.25}$$

$$\chi_{F(Q)}^2 = \Sigma_j \frac{[F_{calc}(Q_j) - F_{box}(Q_j)]^2}{\sigma_{F(Q)^2}(Q_j)} \tag{2.26}$$

$$\chi_{Bragg}^2 = \Sigma_{hkl} \frac{\left||F_{calc}(hkl)|^2 - s|F_{obs}(hkl)|^2\right|^2}{\sigma_{hkl}^2} \tag{2.27}$$

where the σ parameters represent standard errors on individual data values. RMCProfile is also capable of fitting $G(r)$ and $F(Q)$ data as $D(r)$ and $S(Q)$ respectively, if so desired. The inclusion of Bragg data means that over the whole big box the long range average structure should still be preserved. The RMCProfile method is useful for crystalline materials where there is disorder, such as oxide-ion conductors, as a local structural model can be determined that is fully consistent with the long range, average structure from diffraction.

## 2.4 Impedance Spectroscopy

### 2.4.1 Theory

Impedance spectroscopy is a technique that is used in order to determine the conductivity of a material. The impedance of a material, Z, is defined in equation 2.28:[24]

$$Z = \frac{V_0}{I_0} \tag{2.28}$$

where $V_0$ and $I_0$ are the maximum amplitudes of voltage, $V$, and current, $I$. A single frequency alternating voltage, $V = V_0 \sin(\omega t)$, where $\omega$ is the angular frequency $2\pi f$ , is applied over a range of frequencies and the resulting alternating current, $I = I_0 \sin(\omega t + \phi)$ and phase shift,

$\phi$, are determined. Except for the case of a perfect resistor, there is always a phase difference between the applied voltage and resultant current. Impedance is therefore a complex number with the real component $Z'$ and imaginary $Z''$, representing the magnitude, or resistance, and the phase shift respectively.[25] The results are often plotted with $Z''$ on the $y$ axis and $Z'$ on the $x$ axis.

Sintered ceramics can be thought of as consisting of grains of the bulk sample, which are separated by a distance known as the grain boundary. This is known as the "brickwork model"[26] and is illustrated in Figure 2.6.
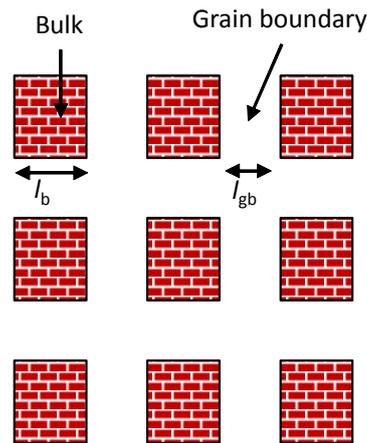


**Figure 2.6 –** The brickwork model of a sintered ceramic material showing the grains and grain boundaries, where $l_b$ is the length of a bulk crystallite and $l_{gb}$ is the length of the grain boundary.

The bulk, the grain boundary and the electrode/sample interface each contribute to their own resistance ($R$) and capacitance ($C$), as well as relaxation time, $\tau$, which is defined as:[26]

$$\tau = RC \tag{2.29}$$

The RC components are also related to the frequency shown in equation 2.30:

$$\omega_{\max}RC = 1 \tag{2.30}$$

where $\omega_{\max}$ is the frequency at the maximum of loss, which is $2\pi \times$ the frequency at the maximum of the semicircle. As the capacitance is related to the geometry of the system, the different length scales of the various regions allow them to be identified through the order of magnitude of the capacitance.[24] Figure 2.7 shows an idealised Nyquist plot, which is obtained from impedance measurements.
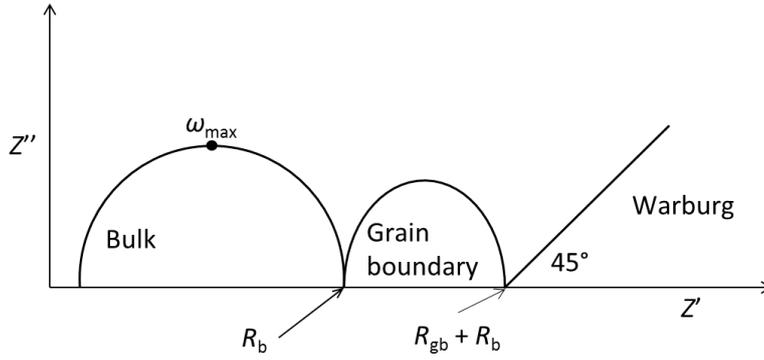
**Figure 2.7 –** Idealised Nyquist plot showing bulk, grain boundary and Warburg responses, where $R_b$ = bulk resistance and $R_{gb}$ = grain boundary resistance.

To determine which regions the responses correspond to, equation 2.30 can be used to calculate $C$, where the resistance, $Z'$, is obtained from the intercept shown in Figure 2.7 and $\omega_{max}$ is calculated from the frequency of the maximum of the semicircle. The order of magnitude of capacity for a bulk response[26] is $10^{-12}$ F, for a grain boundary it is $10^{-11} - 10^{-8}$ F and for the electrode/sample interface capacity is $10^{-7} - 10^{-5}$ F. There can also be a spiked incline of 45° at low frequencies due to infinite diffusion of the mobile species, referred to as a Warburg-type response,[24] which is indicative of ionic conduction. This occurs due to the charge transfer from the conducting species in the sample to the electrodes, which are metallic conductors. The conductivity can be determined using the equation:

$$\sigma = \frac{l}{RA} \tag{2.31}$$

where $l$ is the length of the sample and $A$ is the area. The activation energy of conduction, $E_a$, is determined by plotting the conductivity as a function of temperature. Thus, assuming Arrhenius behaviour, the activation energy can be determined from equation 2.32:

$$\ln(\sigma T) = \ln(\sigma_0) - \frac{E_a}{RT} \tag{2.32}$$

where $R$ = gas constant = 8.314 J K$^{-1}$ mol$^{-1}$ and $\sigma_0$ is the pre-exponential factor. The gradient of the straight line produced from this equation is $-E_a/R$, allowing $E_a$ to be determined.

## 2.5 Auxiliary Methods

### 2.5.1 – Solid-state nuclear magnetic resonance (SSNMR)

Solid state nuclear magnetic resonance (SSNMR) is a technique that can investigate local structure and dynamics. Nuclear spins interact with strong magnetic fields, inducing small perturbations in energy and causing transitions, which are then probed with radiofrequency radiation. These responses are recorded as the NMR spectra. There are further interactions that are all internal to

sample, giving chemical information: shielding, indirect spin coupling, dipolar spin coupling and quadrupolar spin coupling.[27] The shielding affects the chemical shift whilst the spin couplings induce splitting in the spectra. The internal interactions are all dependent on the orientation of the nuclei in the applied magnetic field ($B_0$) and are thus anisotropic. In solution, molecules rapidly change their position and orientation thereby producing an average spectrum over all possible orientations and removing the anisotropy and also negating the quadrupolar and dipolar interactions.

In contrast, solids are relatively static. This means that atomic sites that are in identical chemical positions will be in different orientations with respect to $B_0$, giving rise to different resonance frequencies and crystallographic splitting. In order to remove these effects, magic angle spinning NMR (MAS-NMR) can be employed. In MAS-NMR, the sample is spun rapidly about an angle of 54.73° (hence the name 'magic angle'), which averages the shielding from identical nuclei and eliminates crystallographic splitting. In addition, when a powder is used, the crystals have orientations that are randomly distributed, resulting in a spectrum with a summation of many sharp lines at different shifts. Solid state-NMR is a useful complementary technique to powder diffraction and total scattering, as it reveals additional information about the local environment. For example, in silicates a different chemical shift can occur due to lengthening or shortening of the $SiO_x$ polyhedral environment.[28-30] Furthermore, it can reveal the presence of an amorphous phase, which would be undetectable in powder diffraction and may have a similar PDF to the main phase.

### 2.5.2 – Thermogravimetric analysis

Thermogravimetric analysis (TGA) is a technique where a sample's weight is recorded as it is heated, in order to determine if there are changes during thermal evolution, caused by decomposition or the emission of volatile species that are incorporated in the crystal structure.

### 2.5.3 – Scanning electron microscopy – energy dispersive X-ray spectroscopy

Scanning electron microscopy – energy dispersive X-ray spectroscopy (SEM-EDX) is employed in order to determine atomic ratios of different compositions. SEM is used to examine different particles within the sample. EDX is then applied in each of the chosen particles. As each element has a unique emission profile, the ratio of elements can be determined from the relative intensities of each peak in the spectrum.

## 2.6 References

1. West, A. R., *Basic Solid State Chemistry*. 2nd ed. ed.; John Wiley & Sons: Chichester, 1999; p xv, 480 p. : ill ; 25cm.
2. Smart, L. E.; Moore, E. A., *Solid State Chemistry: an Introduction*. CRC press: London, 2012.
3. Danks, A. E.; Hall, S. R.; Schnepp, Z., The evolution of 'sol–gel' chemistry as a technique for materials synthesis. *Materials Horizons* **2016,** *3* (2), 91-112.

4.      Tao, S.; Irvine, J. T. S., Preparation and characterisation of apatite-type lanthanum silicates by a sol-gel process. *Materials Research Bulletin* **2001,** *36* (7), 1245-1258.

5.      West, A. R., *Solid State Chemistry and Its Applications*. John Wiley & Sons: Chichester, 1987.

6.      Atkins, P., *Physical Chemistry. 6th*. Oxford University Press: Oxford, 1998.

7.      Artioli, G.; Monaco, H. L.; Viterbo, D.; Ferraris, G.; Gilli, G.; Zanotti, G.; Catti, M., *Fundamentals of crystallography*. Oxford University Press: Oxford, 2002; Vol. 7.

8.      Cheetham, A. K.; Day, P., *Solid State Chemistry: Techniques*. Clarendon Press; Oxford University Press: Oxford, 1995.

9.      DLS http://www.diamond.ac.uk/Home/About/How-Diamond-Works.html (accessed February 2019).

10.     Sears, V. F., Neutron scattering lengths and cross sections. *Neutron news* **1992,** *3* (3), 26-37.

11.     Rietveld, H. M., A profile refinement method for nuclear and magnetic structures. *Journal of applied Crystallography* **1969,** *2* (2), 65-71.

12.     Young, R. A., *The Rietveld Method*. Oxford University Press: Oxford, 1995.

13.     Pawley, G. S., Unit-cell refinement from powder diffraction scans. *Journal of Applied Crystallography* **1981,** *14* (6), 357-361.

14.     Egami, T.; Billinge, S. J., *Underneath the Bragg peaks: structural analysis of complex materials*. 2nd ed.; Newnes: Oxford, 2012; Vol. 16.

15.     Proffen, T.; Page, K. L.; McLain, S. E.; Clausen, B.; Darling, T. W.; TenCate, J. A.; Lee, S.-Y.; Ustundag, E., Atomic pair distribution function analysis of materials containing crystalline and amorphous phases. *Zeitschrift für Kristallographie-Crystalline Materials* **2005,** *220* (12), 1002-1008.

16.     Blake, A. J.; Cole, J. M.; Evans, J. S.; Main, P.; Parsons, S.; Watkin, D. J., *Crystal structure analysis: principles and practice*. Oxford University Press: Oxford, 2009; Vol. 13.

17.     Dove, M. T.; Tucker, M. G.; Keen, D. A., Neutron total scattering method simultaneous determination of long-range and short-range order in disordered materials. *European Journal of Mineralogy* **2002,** *14* (2), 331-348.

18.     Keen, D., A comparison of various commonly used correlation functions for describing total scattering. *Journal of Applied Crystallography* **2001,** *34* (2), 172-177.

19.     Soper, A. K.; Barney, E. R., Extracting the pair distribution function from white-beam X-ray total scattering data. *Journal of Applied Crystallography* **2011,** *44* (4), 714-726.

20.     Coelho, A. A.; Chater, P. A.; Kern, A., Fast synthesis and refinement of the atomic pair distribution function. *Journal of Applied Crystallography* **2015,** *48* (3), 869-875.

21.     Coelho, A. *TOPAS Academic Version 6 Computer Software*, 6; Coelho Software: Brisbane, 2016.

22.     McGreevy, R. L., Reverse Monte Carlo modelling. *Journal of Physics: Condensed Matter* **2001,** *13* (46), R877.

23.     Tucker, M. G.; Keen, D. A.; Dove, M. T.; Goodwin, A. L.; Hui, Q., RMCProfile: reverse Monte Carlo for polycrystalline materials. *Journal of Physics: Condensed Matter* **2007,** *19* (33), 335218.

24.     Sinclair, D. C., Characterization of Electro-materials using ac Impedance Spectroscopy. *Boletín de la Sociedad Española de Cerámica y Vidrio* **1995,** *34* (2), 55-65.

25.     Barsoukov, E.; Macdonald, J. R., *Impedance spectroscopy: theory, experiment, and applications*. John Wiley & Sons: Hoboken, 2005.

26.     Irvine, J. T. S.; Sinclair, D. C.; West, A. R., Electroceramics: Characterization by Impedance Spectroscopy. *Adv. Mater.* **1990,** *2* (3), 132-138.

27.     Apperley, D. C.; Harris, R. K.; Hodgkinson, P., *Solid-state NMR: Basic principles and practice*. Momentum Press: New York, 2012.

28.     Magi, M.; Lippmaa, E.; Samoson, A.; Engelhardt, G.; Grimmer, A. R., Solid-state high-resolution silicon-29 chemical shifts in silicates. *The Journal of Physical Chemistry* **1984,** *88* (8), 1518-1522.

29.     Ashbrook, S. E.; Dawson, D. M., NMR spectroscopy of minerals and allied materials. *Nuclear Magnetic Resonance: Volume 45* **2016,** *45*, 1-52.

30.     Jähnigen, S.; Brendler, E.; Böhme, U.; Heide, G.; Kroke, E., Silicophosphates containing $SiO_6$ octahedra – anhydrous synthesis under ambient conditions. *New Journal of Chemistry* **2014,** *38*, 744-751.

# 3. Ge$_{5-x}$Al$_x$(PO$_4$)$_6$O$_{1-x/2}$: Structure and Properties

## 3.1 Introduction and Purpose of Study

Analysis of the ionic conductors La$_2$Mo$_2$O$_9$ by Evans *et al.*[1] and Bi$_{1-x}$V$_x$O$_{1.5+x}$ by Kuang *et al.*[2] revealed that the variable coordination of Mo$^{6+}$ and V$^{5+}$ is crucial to the oxide-ion conduction mechanism. Ge$^{4+}$ has a flexible coordination number ranging from four to six, including a coordination number of five[3-5]. Chapter 4 discusses how this enables high conductivity in lanthanum germanium apatites. This chapter focuses on germanium phosphate oxide, Ge$_5$(PO$_4$)$_6$O, which contains mixed Ge coordination, as a potential parent phase for promoting ionic conductivity.

Ge$_5$(PO$_4$)$_6$O was first identified by single-crystal X-ray diffraction studies.[6] The structure adopts *R*-3 symmetry and consists of GeO$_6$ octahedra that are corner-connected at all vertices with PO$_4$ tetrahedra, forming GeO$_6$–PO$_4$ helices along the *c* axis. The helical units are connected to each other through GeO$_4$ tetrahedra, which are corner-connected at three vertices with PO$_4$ tetrahedra and at the fourth with a GeO$_4$ tetrahedron. The GeO$_4$ tetrahedra are connected to each other with a Ge–O–Ge bond angle of 180°. The structure is shown in Figure 3.1 and the atomic coordinates are given in Table 3.1.

There has also been interest in GeO$_2$–P$_2$O$_5$ systems due to potential use in fibre optics, their thermal expansion properties[7] and potential use as Li$^+$ conductors in Li$_2$O–GeO$_2$–P$_2$O$_5$ systems, which have an ionic conductivity of 10$^{-4}$ S cm$^{-1}$ at room temperature.[8-10] In addition, the isostructural Si$_5$(PO$_4$)$_6$O[11] and the similar Ge$_3$Si$_2$(PO$_4$)$_6$O,[12] which adopts *P*-31*c* symmetry also exist. The ionic conductivity properties of Ge$_5$(PO$_4$)$_6$O, however, have not yet been investigated. Ge$_5$(PO$_4$)$_6$O contains GeO$_6$ octahedra and GeO$_4$ tetrahedra in a 3 : 2 ratio. By doping with an aliovalent cation with a charge < 4+ to replace Ge$^{4+}$, oxygen vacancies could be created. This could improve ionic conductivity by providing vacant O sites for O$^{2-}$ ions to hop into. The oxide-ion migration could be assisted by the variable coordination of the Ge$^{4+}$ cations. In this work, we attempted to synthesise Ge$_{5-x}$Al$_x$(PO$_4$)$_6$O$_{1-x/2}$ (*x* = 0, 0.1, 0.2, 0.5, 1, 2) samples and investigate their conductivity with impedance spectroscopy and their structures with powder X-ray diffraction and solid-state NMR (SSNMR).

**Table 3.1 – Crystallographic parameters of Ge$_5$(PO$_4$)$_6$O.[6] Space group = _R_-3.**

| Site label | Wyckoff site | $x$ | $y$ | $z$ | Site Occupancy | B(Å$^2$) |
|---|---|---|---|---|---|---|
| Ge1 | 3$a$ | 0 | 0 | 0 | 1 | 0.815(7) |
| Ge2 | 6$c$ | 0 | 0 | 0.1767(1) | 1 | 0.674(6) |
| Ge3 | 6$c$ | 0 | 0 | 0.4327(1) | 1 | 0.757(6) |
| P | 18$f$ | 0 | 0.2892(6) | 0.2668(6) | 1 | 0.738(8) |
| O1 | 3$b$ | 0 | 0 | $^1/_2$ | 1 | 0.417(4) |
| O2 | 18$f$ | 0.1347(17) | 0.2222(17) | 0.1334(5) | 1 | 1.459(2) |
| O3 | 18$f$ | 0.2185(17) | 0.1439(16) | 0.0412(5) | 1 | 1.224(19) |
| O4 | 18$f$ | 0.3616(17) | 0.4832(18) | 0.0738(5) | 1 | 1.459(19) |
| O5 | 18$fi$ | 0.4513(15) | 0.2462(15) | 0.1128(5) | 1 | 0.814(17) |
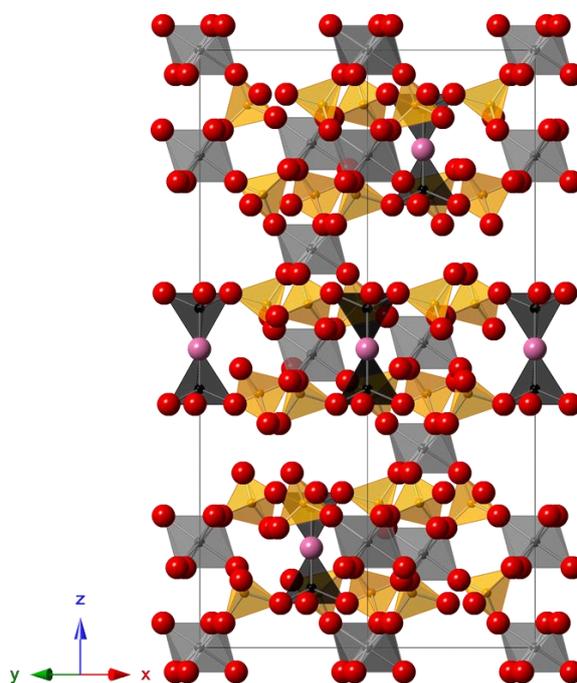


**Figure 3.1 –** Structure of Ge$_5$(PO$_4$)$_6$O. Grey octahedra represent GeO$_6$ units; orange tetrahedra = PO$_4$ units; black tetrahedra = GeO$_4$ units; pink spheres = O1; red spheres = other O.

# 3.2 Experimental Procedure

## 3.2.1 Synthesis

2 g of Ge$_{5-x}$Al$_x$(PO$_4$)$_6$O$_{1-x/2}$ ($x$ = 0, 0.1, 0.2, 0.3, 0.5, 1, 2) were prepared using stoichiometric quantities of GeO$_2$, H(NH$_4$)$_2$PO$_4$ and Al$_2$O$_3$. The heating times for each sample are summarised in Table 3.2.

**Table 3.2 – Synthesis times of $Ge_{5-x}Al_x(PO_4)_6O_{1-x/2}$ at temperatures of 1000 °C ($t_{1000}$), 1030 °C ($t_{1030}$) and $t_{1000}$ + $t_{1030}$ ($t_{tot}$).**

| Code | $x$ | $t_{1000}$ (h) | $t_{1030}$ (h) | $t_{tot}$ (h) |
|---|---|---|---|---|
| MSC006 | 0 | 72 | 108 | 180 |
| MSC011 | 0.1 | | 246 | 246 |
| MSC009 | 0.2 | 72 | 267 | 339 |
| MSC010 | 0.3 | | 294 | 294 |
| MSC005 | 0.5 | 72 | 168 | 240 |
| MSC008 | 1 | 72 | 219 | 291 |
| MSC031 | 2 | | 276 | 276 |

The reactants were ground together using a mortar and pestle and heated in an alumina crucible at 300 °C for 10 h in in air in order to decompose the $H(NH_4)_2PO_4$, after which the samples were reground. Samples MSC005, MSC006, MSC008 and MSC009 (see Table 3.2) were heated at 1000 °C in air for 72 h, but it was determined that this temperature was not high enough to remove triclinic $GeP_2O_7$ which appears as an intermediate product. Samples were therefore heated at 1030 °C with intermittent grinding for the times shown in Table 3.2 until they were deemed essentially pure. $T$ = 1030 °C was chosen because higher temperatures led to melting of the sample. All heating rates were 10 °C $min^{-1}$ and all cooling rates were set to 10 °C $min^{-1}$. All products were white in colour. Phase purity was determined using powder X-ray diffraction using a D8 Bruker Advance with a Cu target and Ni filter. The emitted wavelength is a mixture of Cu $K\alpha_1$ (1.54051 Å) and Cu $K\alpha_2$ (1.54433 Å). The range used was 5° ≤ $2\theta$ ≤ 60° with 0.02° steps with a scanning time 1 s $step^{-1}$. After samples were deemed essentially pure, a final powder pattern was obtained for each with 10° ≤ $2\theta$ ≤ 120° with the same steps and scanning time.

Rietveld refinements were performed against the powder X-ray diffraction data using the structure reported by Mayer & Völlenkle.[6] A single isotropic atomic displacement parameter (ADP) was used for all atoms. The $a$ and $c$ cell parameters were refined. The peak shapes were modelled using a Thompsons-Cox-Hastings instrumental peak shape and a size and strain dependent function for the sample.

### 3.2.2 Impedance spectroscopy

Impedance spectroscopy was performed using ~0.4 g pellets of samples of $Ge_{5-x}Al_x(PO_4)_6O_{1-x/2}$ ( $x$ = 0, 0.2, 0.5 and 1), sintered at 1030 °C, with pellet densities of 66 – 77% of the theoretical values. Table 3.3 presents the dimensions of each pellet used. Impedance spectra were collected using a Solartron 1260 Analyser with a Probostat cell.

**Table 3.3 – Dimensions of the pellets used in impedance spectroscopy.**

| Sample | $x$ | Mass (g) | Radius (cm) | Thickness (cm) | Area (cm$^2$) | % density |
|--------|-----|----------|-------------|----------------|---------------|-----------|
| MSC006a | 0 | 0.4301 | 0.494 | 0.229 | 0.767 | 71 |
| MSC009a | 0.2 | 0.4212 | 0.496 | 0.221 | 0.771 | 72 |
| MSC005a | 0.5 | 0.4496 | 0.490 | 0.225 | 0.753 | 77 |
| MSC008b | 1 | 0.4180 | 0.495 | 0.235 | 0.770 | 67 |

### 3.2.3 Solid-state NMR (SSNMR)

Direct excitation magic angle spinning SSNMR (MAS-SSNMR) was performed using 1 mg $Ge_{5-x}Al_x(PO_4)_6O_{1-x/2}$ ($x$ = 0, 0.1, 0.2, 0.3, 0.5, 1, 2) as well as with $Al_2O_3$. Data were collected at room temperature using a 400 MHz Varian VNMRS spectrometer using direct excitation. The two nuclei used were $^{31}P$ and $^{27}Al$, with the chemical shift references of 85% $H_3PO_4$ and 1M aq. $Al(NO_3)_3$ respectively. In addition, a $^{31}P$ rotational echo adiabatic passage double resonance (REAPDOR) experiment was performed on the $x$ = 2 and $x$ = 0.3 samples. A $^{31}P$ double-quantum single quantum correlation experiment with spc5 recoupling sequence was performed on the $x$ = 0.3 sample.

## 3.3 Results and Discussion

### 3.3.1 Rietveld refinements and phase purity

The final Rietveld refinements for each composition are shown in Figure 3.2. The lack of $Al_2O_3$ peaks in the data initially suggests that $Al^{3+}$ may be substituted into $Ge_5(PO_4)_6O$. However, as $Al_2O_3$ content increased, a peak at $2\theta \approx 21.8°$ increased in intensity (Figure 3.3). It is likely that this peak corresponds to an aluminium phosphate phase. There is the phase $AlPO_4$-11, which has a prominent peak at $2\theta \approx 22°$,[13] as well as prominent peaks in similar $2\theta$ values as $Ge_5(PO_4)_6O$. There is unexplained peak present at $2\theta \approx 35.8°$, which is only visible in $Ge_{5-x}Al_x(PO_4)_6O_{1-x/2}$ ($x$ = 1, 2).

In order to determine whether the alumina crucible was reacting with the sample, inductive coupled plasma mass spectrometry (ICP-MS) was performed on selected samples and results are given in Table 3.4. Sample compositions match those expected except for MSC005, where the experimental Al content is lower than expected. The reason for this is unknown (but later experiments showed this was not worth following up). These results show there is no interference from the crucible.

**Table 3.4 – Nominal and calculated $x$ values in $Ge_{5-x}Al_x(PO_4)_6O_{1-x/2}$ from ICP-MS results.**

| Sample code | Run ID | Nominal $x$ | Calculated $x$ | Calculated mean formula |
|---|---|---|---|---|
| MSC006 | E1 | 0 | 0.00462(9) | $Ge_{4.9971(2)}Al_{0.0029(2)}(PO_4)_6O_{0.9985(1)}$ |
| MSC006 | E2 | 0 | 0.0012(4) | |
| MSC011 | A1 | 0.1 | 0.0693(9) | $Ge_{4.9137(8)}Al_{0.0863(8)}(PO_4)_6O_{0.9568(4)}$ |
| MSC011 | A2 | 0.1 | 0.103(1) | |
| MSC009 | C1 | 0.2 | 0.216(2) | $Ge_{4.790(3)}Al_{0.210(3)}(PO_4)_6O_{0.895(2)}$ |
| MSC009 | C2 | 0.2 | 0.203(6) | |
| MSC010 | F1 | 0.3 | 0.28(1) | $Ge_{4.705(7)}Al_{0.295(7)}(PO_4)_6O_{0.853(3)}$ |
| MSC010 | F2 | 0.3 | 0.311(9) | |
| MSC005 | B1 | 0.5 | 0.432(4) | $Ge_{4.615(2)}Al_{0.385(2)}(PO_4)_6O_{0.807(1)}$ |
| MSC005 | B2 | 0.5 | 0.339(3) | |
| MSC008 | D1 | 1 | 1.00(1) | $Ge_{3.998(8)}Al_{1.002(8)}(PO_4)_6O_{0.499(4)}$ |
| MSC008 | D2 | 1 | 1.00(1) | |

Plots of the evolution of the cell parameters with increasing $Al^{3+}$ content are shown in Figure 3.4. There should be little change in the cell parameters as the $Al^{3+}$ content increases, as the ionic radii for $Ge^{4+}$ and $Al^{3+}$ are similar in all coordination environments.[14] Some change might be expected, however, as the oxygen vacancy content increases. The $a$ and $c$ cell parameters are similar throughout the entire series of $Ge_{5-x}Al_x(PO_4)_6O_{1-x/2}$ ($x$ = 0, 0.1, 0.2, 0.3, 0.5, 1, 2). The greatest difference in the $a$ cell is 0.0067(2) Å, the greatest difference in the $c$ cell is 0.0238(9) Å and the greatest difference in unit cell volumes is 0.9845(2) Å$^3$ between $x \approx 0.2$ and $x \approx 0.3$.
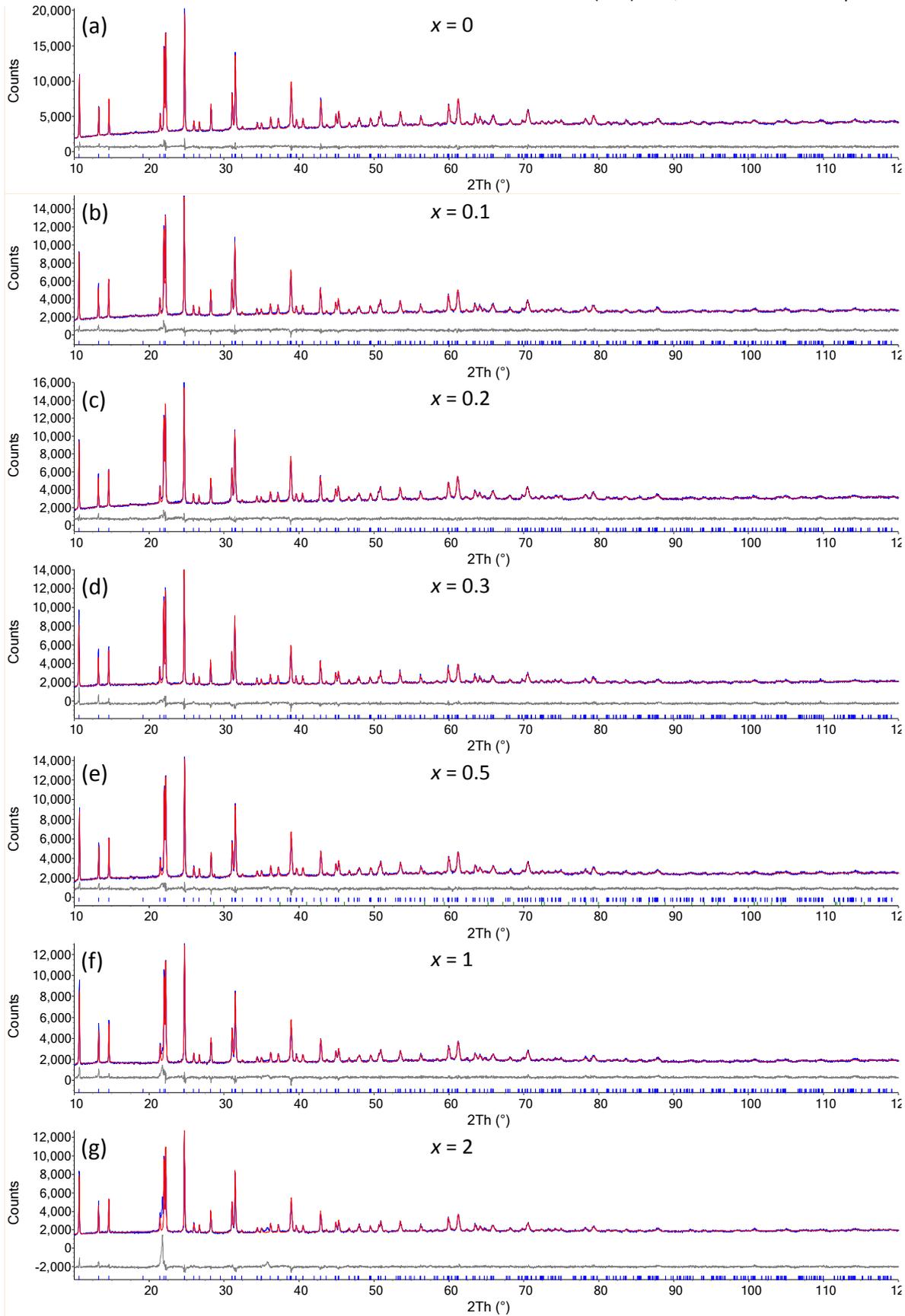
**Figure 3.2 –** Rietveld refinements of Ge$_{5-x}$Al$_x$(PO$_4$)$_6$O$_{1-x/2}$ from 10° ≤ 2$\theta$ ≤ 120°. The observed pattern is in blue whilst the calculated is in red. Blue tick marks correspond to reflections from of Ge$_{5-x}$Al$_x$(PO$_4$)$_6$O$_{1-x/2}$.
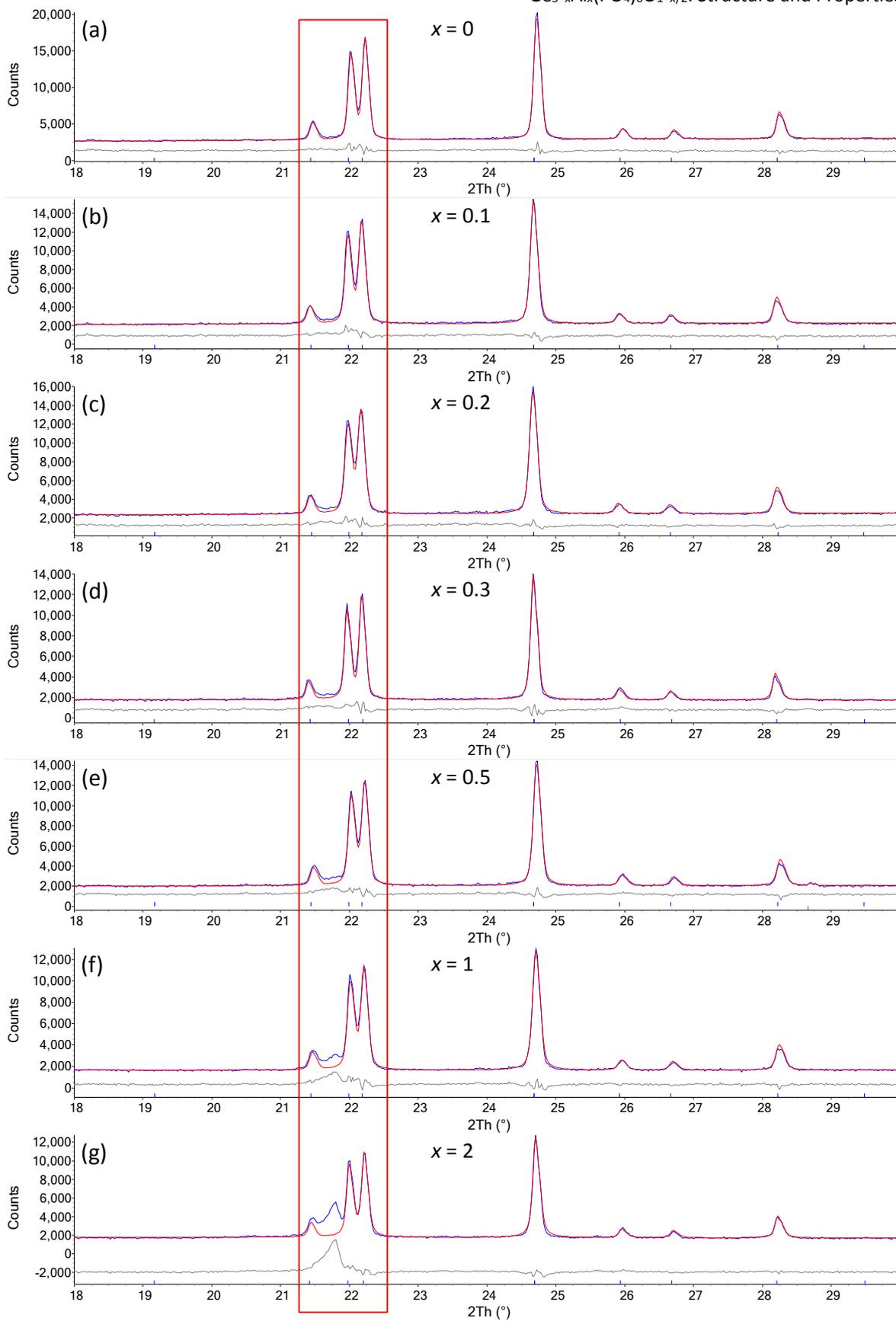
**Figure 3.3** – Rietveld refinements of Ge$_{5-x}$Al$_x$(PO$_4$)$_6$O$_{1-x/2}$ from 18° ≤ 2$\theta$ ≤ 30° to highlight the impurity peak at 2$\theta$ ≈ 21.8°.
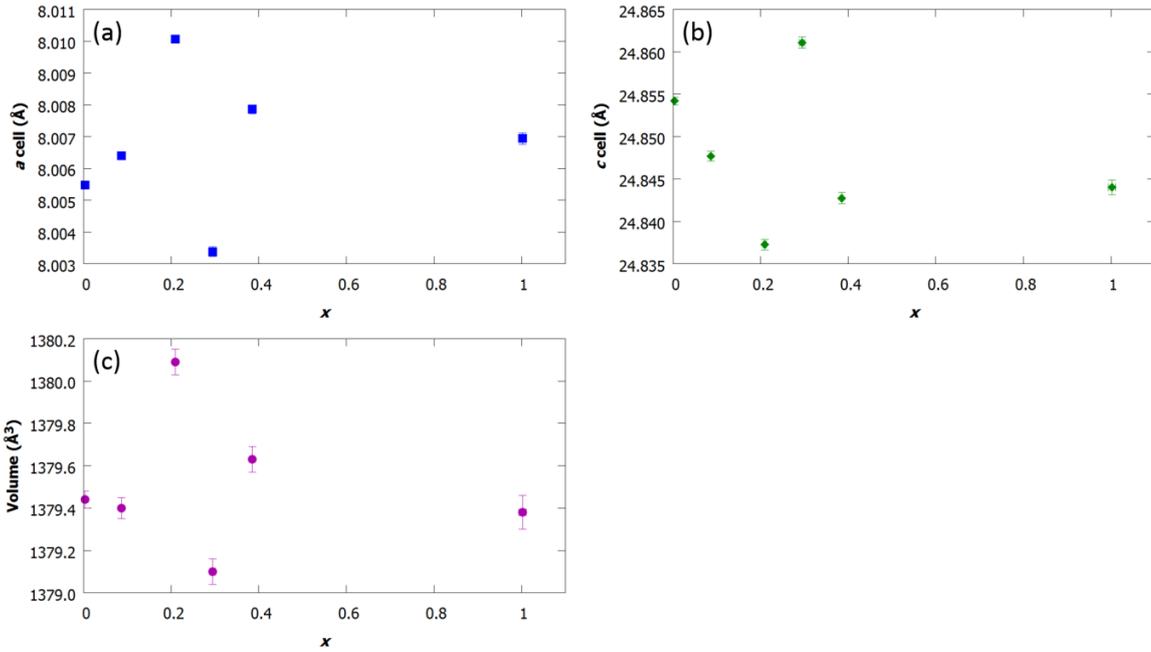
**Figure 3.4 –** Evolution of the cell parameters of Ge$_{5-x}$Al$_x$(PO$_4$)$_6$O$_{1-x/2}$ with $x$ as determined from ICP analysis: (a) $a$ cell; (b) $c$ cell; (c) cell volume.

## 3.3.2 Impedance spectroscopy

Impedance spectra were collected for Ge$_{5-x}$Al$_x$(PO$_4$)$_6$O$_{1-x/2}$ ($x$ = 0, 0.2 0.5 and 1) to probe the potential ionic conductivity. Figure 3.5 shows the Nyquist plot for $x$ = 0 at 802 °C and at 414 °C.
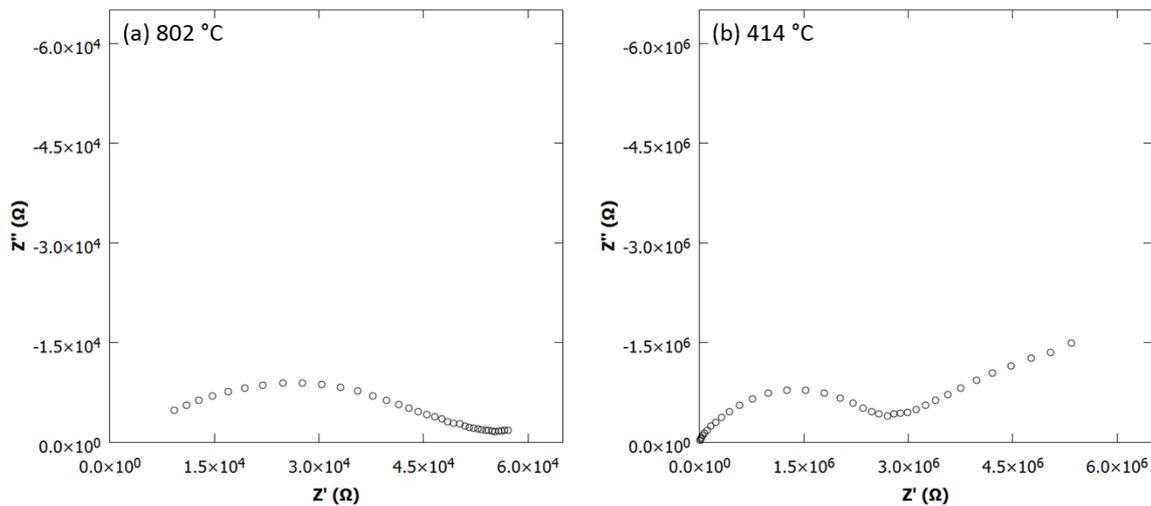


**Figure 3.5 –** Nyquist plots for Ge$_5$(PO$_4$)$_6$O at (a) 802 °C and (b) 414 °C, showing an overlapping of the bulk and grain boundaries in (a) and (b) and a Warburg-type response in (b).

The Nyquist plot at 802 °C shows a single semicircle, which consists of an overlapping of the bulk and grain boundary semicircles, which is indicative of ionic conductivity[15] followed by the beginning of a Warburg-type response. The capacitance of the first semicircle is 1.14 × 10$^{-10}$ F, which is a typical value for grain boundaries.[16] As the temperature decreased, the Warburg response appeared at higher frequencies until it was quite visible at 414 °C (Figure 3.5b). The bulk and grain boundary regions remained overlapped through all measurements, producing

54

asymmetric semicircles. The capacitance of the semicircle at 414 °C is $3.71 \times 10^{-11}$ F, which can again be assigned to a grain boundary response. Due to the overlap of the bulk and grain boundary responses, only the total conductivities can be extracted.
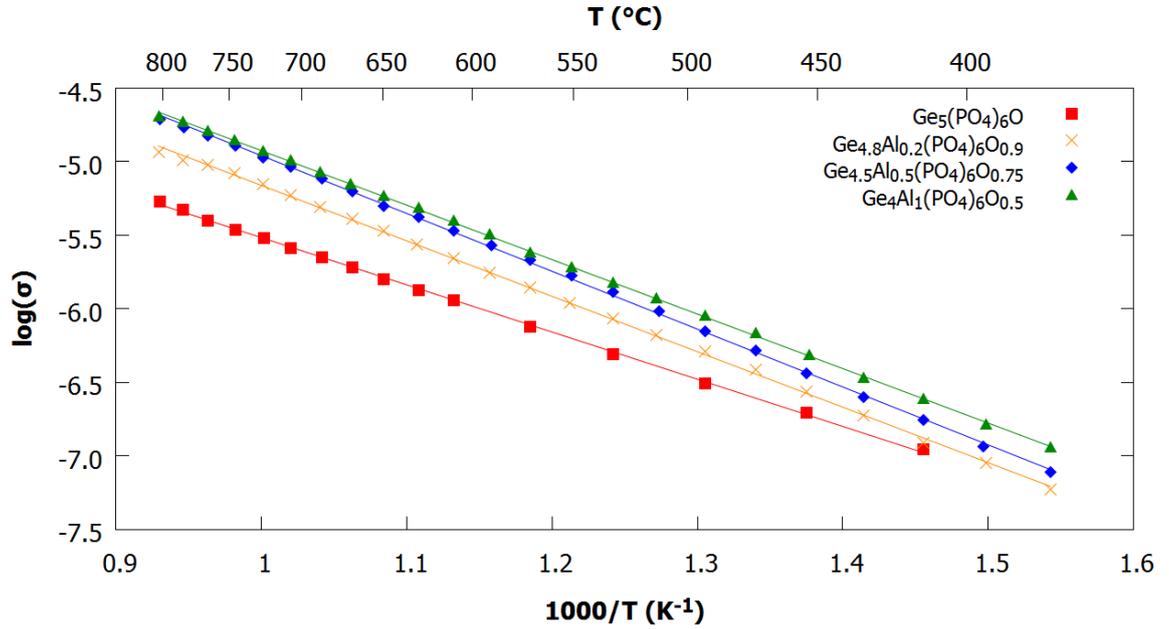


**Figure 3.6** – Total conductivities of Ge$_{5-x}$Al$_x$(PO$_4$)$_6$O$_{1-x/2}$ ($x$ = 0, 0.2, 0.5, 1).

**Table 3.5 – Activation energies, conductivities at 802 °C and relative densities of Ge$_{5-x}$Al$_x$(PO$_4$)$_6$O$_{1-x/2}$.**

| Sample code | $x$ | $E_a$ (eV) | $\sigma$ (S cm$^{-1}$) | Relative density (%) |
|---|---|---|---|---|
| MSC006 | 0 | 0.711(5) | $5.4 \times 10^{-6}$ | 71 |
| MSC009 | 0.2 | 0.820(3) | $1.2 \times 10^{-5}$ | 72 |
| MSC005 | 0.5 | 0.852(2) | $1.9 \times 10^{-5}$ | 77 |
| MSC008 | 1 | 0.806(2) | $2.0 \times 10^{-5}$ | 67 |

The total conductivity of each sample at different temperatures is shown in Figure 3.6 and the conductivities at 802 °C and activation energies ($E_a$) are given in Table 3.5. There is a trend in Ge$_{5-x}$Al$_x$(PO$_4$)$_6$O$_{1-x/2}$ ($x$ = 0, 0.2, 0.5, 1) for the conductivity to increase with $x$. The $x$ = 0.5 sample has a conductivity ($1.9 \times 10^{-5}$) approximately four times larger than that of $x$ = 0 ($5 \times 10^{-6}$ S cm$^{-1}$ at 802 °C). The conductivity of $x$ = 1 ($2.0 \times 10^{-5}$ S cm$^{-1}$ at 802 °C), is essentially the same as $x$ = 0.5, which could indicate that the maximum conductivity is produced around $x$ = 0.5 − 1. The conductivity of $x$ = 1 could also be affected by the quality of the pellet; for $x$ = 0.5, the pellet density was 77% compared to 67% for $x$ = 1. It could also be that the levels of impurity begin to interfere with the conductivity of the sample for $x$ > 0.5. The activation energy of the $x$ = 0 sample is 0.711(5) eV, whilst all of the doped samples have similar activation energies of $E_a \approx$ 0.83 eV. This could suggest that the conductive phase in the doped samples is not Ge$_{5-x}$(PO$_4$)O$_{1-x/2}$. The magnitude of conductivity of this series when compared to other oxide-ion conductors is poor: YSZ has a

conductivity of $1 \times 10^{-2}$ S cm$^{-1}$ at 700 °C[17] (500 times more conductive at a temperature 100 °C lower) and La$_2$Mo$_2$O$_9$ has an ionic conductivity of $6 \times 10^{-2}$ S cm$^{-1}$ at 800 °C[1] (3000 times more conductive). This suggests that the samples do not contain a significant number of (mobile) oxygen vacancies.

### 3.3.3 SSNMR

In order to determine possible doping sites, MAS-SSNMR was performed. Ge$_5$(PO$_4$)$_6$O and Al$_2$O$_3$ were used as reference materials, as they, contain exclusively P or Al. The $^{27}$Al MAS-NMR spectra, shown in Figure 3.7, all contained a small peak at $\delta = 12 - 13$ ppm; this peak is the only peak present in Al$_2$O$_3$ and corresponds to octahedral AlO$_6$. In the Ge$_{5-x}$Al$_x$(PO$_4$)$_6$O$_{1-x/2}$ ($x$ = 0.1, 0.2, 0.5, 1, 1.2) spectra, this peak could either correspond to AlO$_6$ within the Ge$_{5-x}$Al$_x$(PO$_4$)$_6$O$_{1-x/2}$ phase or to trace amounts of Al$_2$O$_3$. In all Ge$_{5-x}$Al$_x$(PO$_4$)$_6$O$_{1-x/2}$ ($x$ = 0.1, 0.2, 0.5, 1, 2) $^{27}$Al spectra, there is a peak at $\delta = 40$ ppm. A peak with similar chemical shift is seen in aluminium phosphate phases[18] and has been attributed to AlO$_4$ tetrahedra, with Al–O–P linkages. This could suggest that Al$^{3+}$ is doped onto $^{IV}$Ge$^{4+}$ sites. However, it is also possible that it corresponds to an aluminium phosphate second phase, which could be responsible for the peak at $2\theta \approx 21.8°$ seen in the X-ray powder diffraction patterns, or to an amorphous (X-ray invisible) aluminium phosphate phase. There is a third, very sharp peak in the NMR spectra at $\delta = -12$ ppm, which decreases in area with increasing $x$. It is unknown what this peak corresponds to. As it is sharp, it indicates a high symmetry site, though it is on top of a broader peak. It is slightly surprising that this peak is not present in the $x = 2$ spectrum, as the corresponding powder pattern has the largest impurity peak (Figure 3.3).
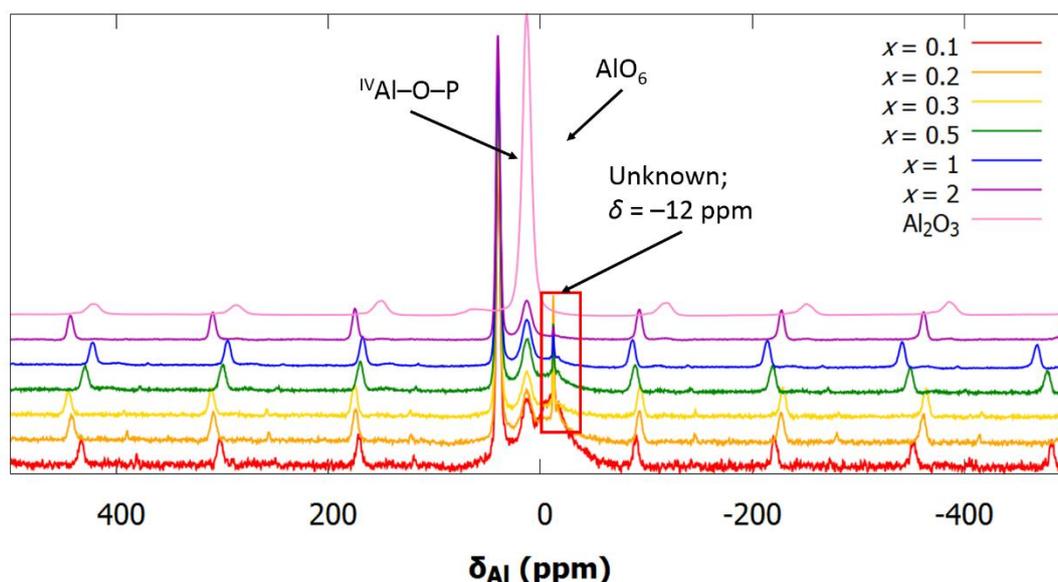


**Figure 3.7** – $^{27}$Al NMR spectra of Ge$_{5-x}$Al$_x$(PO$_4$)$_6$O$_{1-x/2}$ and Al$_2$O$_3$. The significant peaks have been labelled, with emphasis on the unknown peak at $\delta = -12$ ppm. The unlabelled peaks are from spinning sidebands.
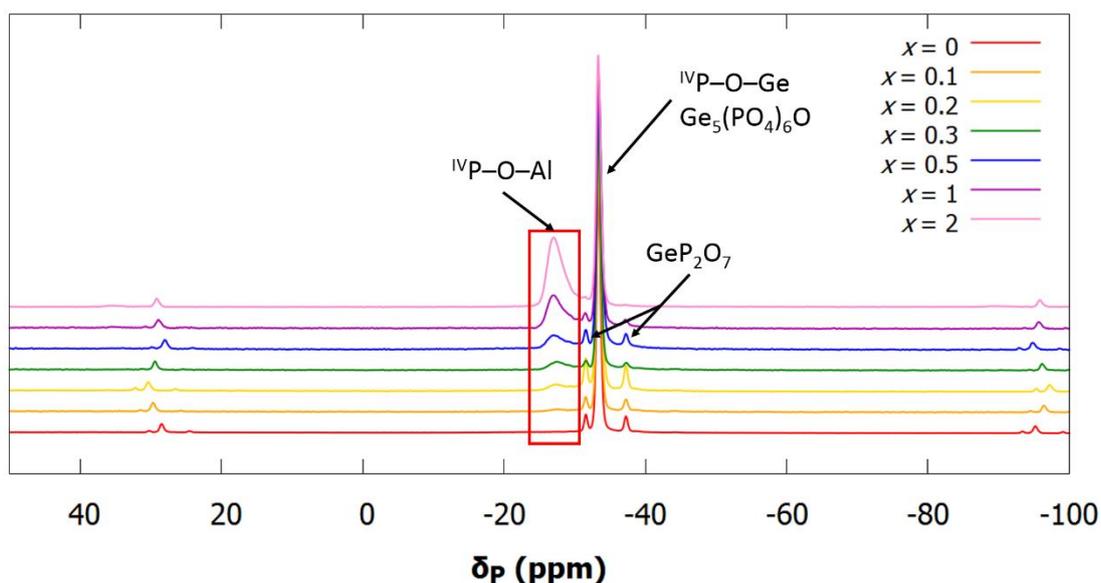
**Figure 3.8** – $^{31}$P NMR spectra of Ge$_{5-x}$Al$_x$(PO$_4$)$_6$O$_{1-x/2}$. The significant peaks have been labelled, with emphasis on the $^{IV}$P–O–Al peak at −27 ppm that increases with $x$. The unlabelled peaks are from spinning sidebands.

The $^{31}$P NMR spectra are shown in Figure 3.8. All $^{31}$P NMR spectra contain two weak peaks at $\delta$ = −32 and −37 ppm, except Ge$_3$Al$_2$(PO$_4$)$_6$ ($x$ = 2). These peaks were present in $^{31}$P NMR of $\beta$-GeP$_2$O$_7$,[7] which is the triclinic GeP$_2$O$_7$ phase that appears at lower temperatures during the synthesis. As the Rietveld refinements do not detect GeP$_2$O$_7$, there is presumably only a small amount of this compound present. The largest peak is at $\delta$ = −33 ppm and is present in all spectra. This peak was present in $^{31}$P NMR obtained by Losilla et al.,[7] indicating that it is a tetrahedral PO$_4$ that is part of a P–O–Ge linkage. There is an additional broad peak, which increases in area with increasing Al content, that is present in all Ge$_{5-x}$Al$_x$(PO$_4$)$_6$O$_{1-x/2}$ $^{31}$P NMR spectra with $x$ > 0 at $\delta$ = −27 ppm.
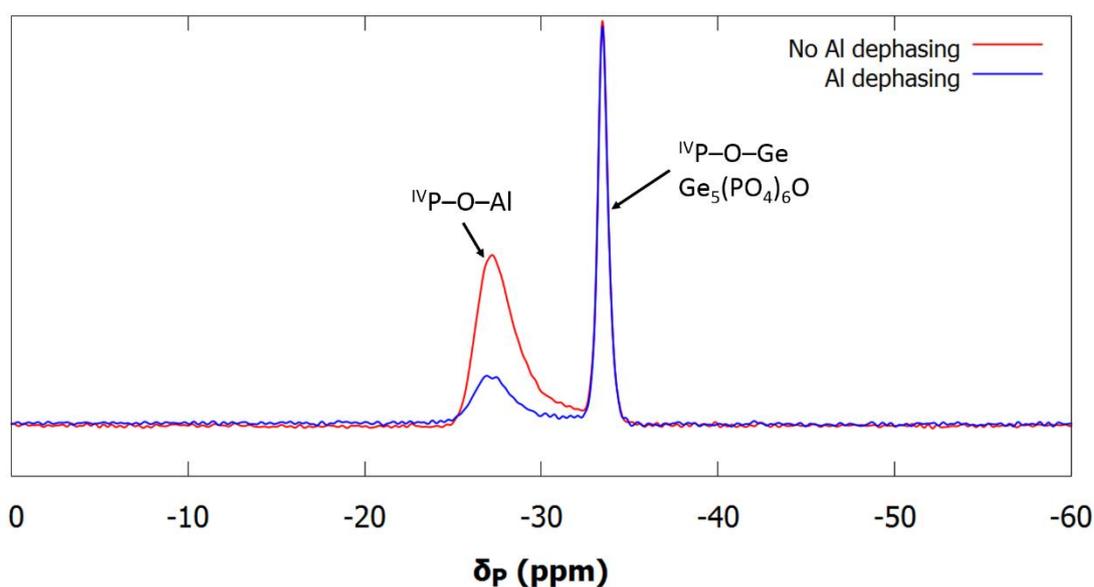


**Figure 3.9** – REAPDOR NMR spectra of Ge$_3$Al$_2$(PO$_4$)$_6$.

A REAPDOR analysis (Figure 3.9) was performed on the $x$ = 0.3 and 2 samples in order to determine if the peak at $\delta$ = −27 ppm arose from a P that is near an Al. If there is a difference between the $^{31}$P spectrum with and without dephasing, it indicates that there is Al–P coupling. There is in fact a difference between the two spectra at $\delta$ = −27 ppm, indicating that this peak does arise from $^{IV}$P–O–Al. No change is seen in the peak at $\delta$ = −33 ppm, suggesting that these $^{31}$P atoms are not close to Al. The REAPDOR experiments therefore strongly suggest that the Al is in a different phase to the Ge. In order to confirm this, a double quantum-single quantum correlation experiment was performed, which is shown in Figure 3.10. The only two peaks present in the spectrum are autocorrelation peaks. This shows that the two peaks arise from two separate phases, suggesting that in fact $Al^{3+}$ is not being doped onto $Ge^{4+}$, but instead forming a second phase. This phase is possibly amorphous, which is why it is not clearly visible in the X-ray powder patterns, or is the origin of the peak that is visible in the powder patterns of $x \geq 0.5$ at $2\theta \approx 21.8°$.
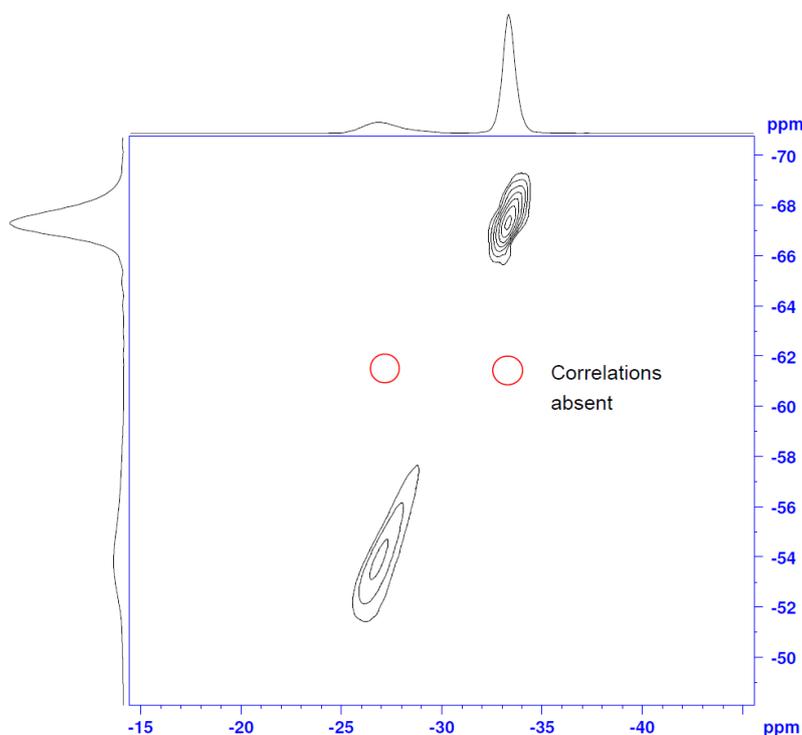


**Figure 3.10** – Double quantum-single quantum correlation $^{31}$P NMR experiment using $Ge_{4.7}Al_{0.3}(PO_4)_6O_{0.85}$. The horizontal axis is the single quantum axis and the vertical axis is the double quantum axis. The two peaks present are the separate species correlating with themselves.

## 3.4 Conclusions

The work undertaken in this chapter allows us to come to the following conclusions:

1. In the attempt to dope $Ge_{5-x}Al_x(PO_4)_6O_{1-x/2}$ with $Al^{3+}$, powder patterns seemingly show a single phase until $Al^{3+}$ is as high as $x$ = 0.5.

2. The conductivity appeared to improve in Ge$_{5-x}$Al$_x$(PO$_4$)$_6$O$_{1-x/2}$ pellets with increasing $x$ until $x$ = 0.5. However, the conductivity is still 2 – 3 orders of magnitude lower than the best oxide-ion conductors.[1, 17]

3. ^{27}Al and ^{31}P MAS-NMR revealed the presence of peaks with a similar chemical shift to that expected for [IV]P–O–Al and ^{31}P REAPDOR experiments confirmed their presence. This revealed that a phase containing Al and P was formed, but did not confirm whether this was a separate phase or due to Al$^{3+}$ doping onto a tetrahedral Ge$^{4+}$ site in Ge$_5$(PO$_4$)$_6$O.

4. Despite the increase in conductivity with increasing Al$^{3+}$ content and the lack of a clear secondary phase in powder X-ray diffraction, a double quantum-single quantum ^{31}P NMR experiment showed that peaks arising from the [IV]P–O–Al and [IV]P–O–Ge units were from two separate phases.

5. At low $x$, an amorphous (X-ray invisible) aluminium phosphate phase could be forming upon the introduction of Al$_2$O$_3$. This phase is likely the origin of the increase in conductivity, as the activation energies of the doped samples were all similar to each other (~0.83 eV) but different from the undoped Ge$_5$(PO$_4$)$_6$O sample ($E_a$ = 0.711(5) ev). At higher $x$, we see clear evidence for formation of a second poorly crystalline phase.

6. We conclude that Al$^{3+}$ cannot be doped onto Ge$_5$(PO$_4$)$_6$O through solid state synthesis.

## 3.5 References

1.　　　Evans, I. R.; Howard, J. A. K.; Evans, J. S. O., The crystal structure of $\alpha$-La$_2$Mo$_2$O$_9$ and the structural origin of the oxide ion migration pathway. *Chemistry of Materials* **2005,** *17* (16), 4074-4077.

2.　　　Kuang, X.; Payne, J. L.; Johnson, M. R.; Evans, I. R., Remarkably High Oxide Ion Conductivity at Low Temperature in an Ordered Fluorite-Type Superstructure. *Angewandte Chemie International Edition* **2012,** *51* (3), 690-694.

3.　　　Orera, A.; Slater, P. R., New Chemical Systems for Solid Oxide Fuel Cells. *Chemistry of Materials* **2009,** *22* (3), 675-690.

4.　　　Rada, S.; Chelcea, R.; Culea, E., The presence of fivefold germanium as a possible transitional phase in the iron–lead–germanate glass system. *Journal of Materials Science* **2010,** *45* (22), 6025-6029.

5.　　　Alderman, O. L. G.; Hannon, A. C.; Holland, D.; Umesaki, N., On the germanium–oxygen coordination number in lead germanate glasses. *Journal of Non-Crystalline Solids* **2014,** *386*, 56-60.

6.　　　Mayer, H.; Völlenke, H., Die Kristallstruktur von Ge$_5$O[PO$_4$]$_6$. *Monatshefte für Chemie* **1972,** *103*, 1560-1571.

7.　　　Losilla, E. R.; Cabeza, A.; Bruque, S.; Aranda, M. A. G.; Sanz, J.; Iglesias, J. E.; Alonso, J. A., Syntheses, structures, and thermal expansion of germanium pyrophosphates. *Journal of Solid State Chemistry* **2001,** *156* (1), 213-219.

8.　　　Fu, J., Fast Li$^+$ ion conducting glass-ceramics in the system Li$_2$O–Al$_2$O$_3$–GeO$_2$–P$_2$O$_5$. *Solid State Ionics* **1997,** *104* (3), 191-194.

9.　　　Zwanziger, J. W.; Shaw, J. L.; Werner-Zwanziger, U.; Aitken, B. G., A neutron scattering and nuclear magnetic resonance study of the structure of GeO$_2$–P$_2$O$_5$ glasses. *Journal of Physical Chemistry B* **2006,** *110* (41), 20123-20128.

10.　　　Hoppe, U.; Walter, G.; Brow, R. K.; Wyckoff, N. P., Structure of potassium germanophosphate glasses by X-ray and neutron diffraction: 2. Medium-range order. *Journal of Non-Crystalline Solids* **2008,** *354* (29), 3400-3407.

11.　　　Mayer, H., Die Kristallstruktur von Si$_5$O[PO$_4$]$_6$. *Monatshefte für Chemie* **1974,** *105*, 46-54.

12.　　　Leclaire, A.; Raveau, B., Ge$_3$P$_6$Si$_2$O$_{25}$ – A Cage Structure Closely Related to the Intersecting Tunnel Structure KMO$_3$P$_6$Si$_2$O$_{25}$. *Journal of Solid State Chemistry* **1988,** *75* (2), 397-402.

13.　　　Richardson, J. W., Jnr; Pluth, J. J.; Smith, J. V., Rietveld profile analysis of calcined AlPO$_4$-11 using pulsed neutron powder diffraction. *Acta Crystallographica Section B: Structural Crystallography and Crystal Chemistry* **1988,** *44* (4), 367-373.

14.　　　Shannon, R. D.; Prewitt, C. T., Effective Ionic Radii in Oxides and Fluorides. *Acta Crystallographica Section B: Structural Crystallography and Crystal Chemistry* **1969**, 925-946.

15.　　　Kuang, X.; Green, M. A.; Niu, H.; Zajdel, P.; Dickinson, C.; Claridge, J. B.; Jantsky, L.; Rosseinsky, M. J., Interstitial oxide ion conductivity in the layered tetrahedral network melilite structure. *Nature Materials* **2008,** *7* (6), 498-504.

16.      Sinclair, D. C., Characterization of Electro-materials using ac Impedance Spectroscopy. *Boletín de la Sociedad Española de Cerámica y Vidrio* **1995,** *34* (2), 55-65.

17.      Jacobson, A. J., Materials for solid oxide fuel cells. *Chemistry of Materials* **2009,** *22* (3), 660-674.

18.      Lookman, R.; Grobet, P.; Merckx, R.; Van Riemsdijk, W. H., NMR in Soil ScienceApplication of ^{31}P and ^{27}Al MAS NMR for phosphate speciation studies in soil and aluminium hydroxides: promises and constraints. *Geoderma* **1997,** *80* (3), 369-388.

# 4. Long Range and Local Structure of La$_8$R$_2$(GeO$_4$)$_6$O$_{3-y}$ (R = Sr, La, Bi; $y$ = 0, 1) Apatite-type Oxide-Ion Conductors

## 4.1 Introduction

### 4.1.1 Apatite-type oxide-ion conductors

#### 4.1.1.1 The apatite structure type

Apatites are materials with the general formula of A$_{10}$(MO$_4$)$_6$X$_{2\pm\delta}$, where A = alkaline or rare earth, M = Ge, Si or P and X = halides, O$^{2-}$ or [OH]$^-$. They usually adopt $P6_3/m$ symmetry, although they can adopt lower symmetry such as monoclinic $P2_1/m$ and triclinic $P$-1.[1-2] The prototypical apatite is fluoroapatite,[3] Ca$_{10}$(PO$_4$)$_6$F$_2$. This structure is adopted by La$_{9.33}$(SiO$_4$)$_6$O$_2$, which is shown in Figure 4.1, and the atomic coordinates and site occupancies are given in Table 4.1.[4]
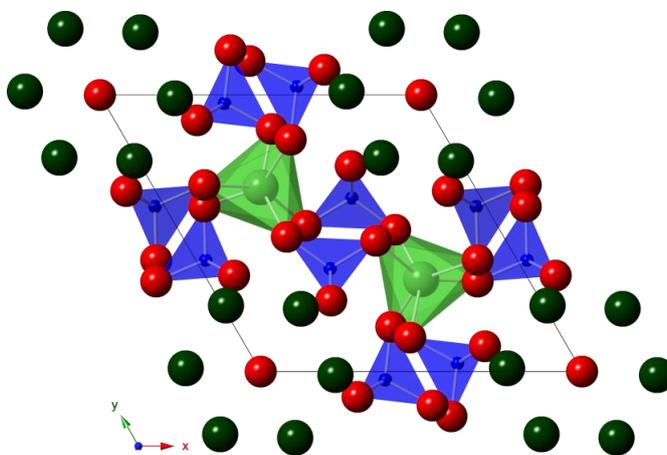


**Figure 4.1** – The crystal structure of La$_{9.33}$(SiO$_4$)$_6$O$_2$ viewed down the $c$ axis. Light green trigonal metaprism = La1O$_6$ units; dark green spheres = La2 atoms; blue tetrahedra = SiO$_4$ units; red spheres = O atoms.

**Table 4.1** – The crystallographic sites of La$_{9.33}$(SiO$_4$)$_6$O$_2$ with $P6_3/m$ symmetry.[4] The generic site name is included in parentheses.

| Site label | Wyckoff site | $x$ | $y$ | $z$ | Occupancy |
|---|---|---|---|---|---|
| La1 (A1) | 4$f$ | ⅔ | ⅓ | 0.00118(8) | 0.858(1) |
| La2 (A2) | 6$h$ | 0.01223(3) | 0.23921(3) | ¼ | 0.983 |
| Si1 (M) | 6$h$ | 0.4029(2) | 0.3728(2) | ¼ | 1.0 |
| O1 | 6$h$ | 0.3255(6) | 0.4873(6) | ¼ | 1.0 |
| O2 | 6$h$ | 0.5267(5) | 0.1232(5) | ¼ | 1.0 |
| O3 | 12$i$ | 0.3476(5) | 0.2564(3) | 0.0684(5) | 1.0 |
| O4 (X) | 2$a$ | 0 | 0 | ¼ | 1.0 |

Apatites can be described as an (A1)$_4$(MO$_4$)$_6$ framework consisting of A1O$_6$ trigonal metaprisms corner-connected to MO$_4$ tetrahedra, whose pores are filled with the remaining A2$_6$X$_2$ units. The A2 cations are arranged to form a hexagonal tunnel in which the X anions reside.[5-7] Additionally,

apatites with the formula of A$_{10}$(MO$_3$)$_6$O$_2$, such as Pb$_{10}$(AsO$_3$)$_6$Cl$_2$ and A$_{10}$(MO$_5$)$_6$O$_2$, such as Sr$_{10}$(ReO$_5$)Cl$_2$, are known.[2, 8] There are also "oxygen-excess" apatites, which adopt the general formula of A$_{9.33+x}$(MO$_4$)$_6$O$_{2+3x/2}$ such as La$_{9.33+x}$(MO$_4$)$_6$O$_{2+3x/2}$ (M = Si, Ge; $0 < x \leq 0.67$).[9-12] The existence of the oxygen-excess silicates is also questionable, as it has been found that Si$^{4+}$ can be present,[13] and work done in this thesis (see Chapter 5) also raises doubts about their existence. Symmetry lowering is a common property amongst apatites, as not all of the apatites adopt the parent $P6_3/m$ space group. Figure 4.2 shows the maximal non-isomorphic subgroups that can be derived from the parent $P6_3/m$ symmetry.
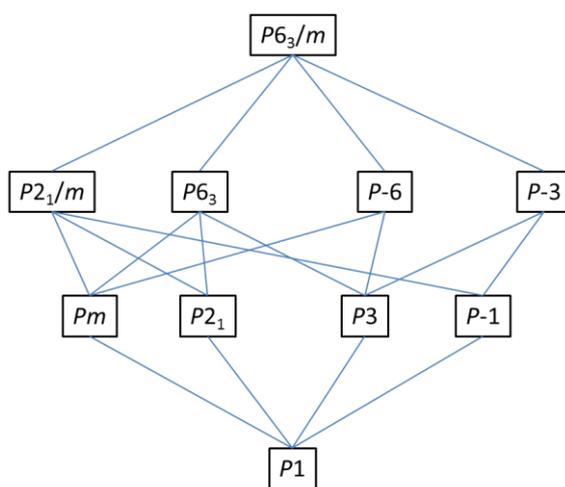


**Figure 4.2** – Symmetry tree showing the maximal non-isomorphic subgroups starting from $P6_3/m$.

Symmetry lowering in apatites has been attributed to a variety of factors. One parameter suggested to be highly correlated to the symmetry is the apatite twist angle, $\varphi$.[1] This is the O1–A1–O2 angle in the trigonal metaprisms when viewed along the (0 0 1) projection, shown in Figure 4.3.
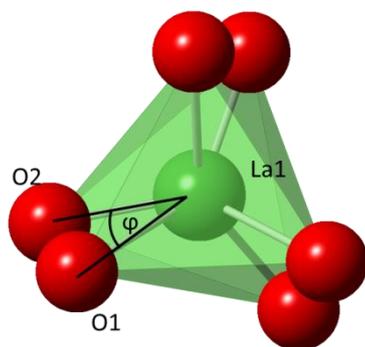


**Figure 4.3** – An individual A1O$_6$ metaprism from La$_{9.33}$(SiO$_4$)$_6$O$_2$ viewed down the (0 0 1) projection to illustrate the definition of a twist angle. The twist angle is the two-dimensional angle between the labelled atoms.

White *et al.*[1] also derived an equation (Equation 4.1) for determining the twist angle of a hexagonal apatite by using the fractional coordinates, so that the Cartesian coordinates and two-dimensional distances of O2–A1, A1–O1 and O2–O1 do not need to be determined.

$$\cos(\varphi) = \frac{(G_3-G_1)^2+(H_3-H_1)^2+(G_1-G_2)^2+(H_1-H_2)^2-(G_2-G_3)^2-(H_2-H_3)^2}{2\{[(G_3-G_1)^2+(H_3-H_1)^2]\times[(G_1-G_2)^2+(H_1-H_2)^2]\}^{1/2}} \qquad (4.1)$$

Where $G_1 = 0.866x_{A1}$, , $H_1 = y_{A1} - 0.5x_{A1}$  $G_2 = 0.866x_{O1}$, $H_1 = y_{O1} - 0.5x_{O1}$  $G_3 = 0.866x_{O2}$ and $H_3 = y_{O2} - 0.5x_{O2}$. A twist angle of $\varphi$ = 0° represents a perfect triangular or trigonal prism, a twist angle of $\varphi$ = 60° represents an octahedron, and a twist angle of $0 < \varphi < 60°$ is a trigonal metaprism. In apatites where there is only one type of A cation, a linear, inversely proportional relationship of $\varphi$ to the crystal radii is found, but with more than one type of A cation the relationship becomes more complex. Large twist angles of $\varphi$ > 25° have been proposed to result in symmetry lowering to the maximal non-isomorphic subgroups $P2_1/m$, $P2_1$, and $P$-1.[14] Examples of apatites with lower symmetry and high twist angles include Pb$_{10}$(PO$_4$)$_6$(OH)$_2$ ($\varphi$ = 26.7°) and Cd$_{10}$(PO$_4$)$_6$(OH)$_2$ ($\varphi$ = 25.8°).[1] It is thought that the strain caused by large A and M cations results in twisting of the A1O$_6$ and symmetry lowering.

Symmetry lowering may, however, occur due to reasons other than strain, revealed in a computational study by Balachandran *et al.*,[15] which investigated the link between apatite symmetry and the electronic configuration of the A atom. The study focussed on A$_{10}$(PO$_4$)F$_2$ (A = Ca, Sr, Pb, Cd and Hg) apatites. For A = Ca, Sr, Pb, $P6_3/m$ symmetry is adopted, whilst for A = Cd and Hg, triclinic $P$-1 symmetry is adopted. Cd and Hg contain fully occupied 4d and 5d orbitals respectively, whilst also containing empty 5s and 6s orbitals. The small energy difference between the fully occupied $(n-1)d^{10}$ orbitals and the empty $ns^0$ orbital allows mixing. This hybridisation of orbitals is enhanced by a cooperative atomic displacement of the PO$_4$ tetrahedra connected to the Hg1/Cd1O$_6$ metaprisms. This movement can be described by a displacement mode like the basis functions of an irreducible representation, $\Gamma^+_4\Gamma^+_6$. This results in a loss of the 6$_3$ screw axis due to the displacement of the O atoms connected to the PO$_4$ and Hg1/Cd1O$_6$ polyhedra. Furthermore, there is a reduction in the calculated band gap in the $P$-1 apatites. Whilst Cd$_{10}$(PO$_4$)$_6$F$_2$ has been synthesised, Hg$_{10}$(PO$_4$)$_6$F$_2$ is yet to be experimentally verified. A further factor that influences apatite symmetry is the presence of lone pairs. The apatite Bi$_4$Pb$_6$(GeO$_4$)$_6$ was found to be best described by the space group $P6_3$, where the Bi$^{3+}$ cations are displaced from the 2$b$ centre [(1/3, 2/3, $z$)], despite containing no channel anions.[16] This lower symmetry is attributed to the large volume of space occupied by the lone pairs on the Bi$^{3+}$ and Pb$^{2+}$ and that is necessary to minimise the lattice energy through compensation of the associated dipole moment.

### 4.1.1.2 Apatite-type oxide-ion conductors

Apatite-type lanthanide silicates, Ln$_{10}$(SiO$_4$)$_6$O$_3$ (Ln = La, Nd, Sm, Gd, Dy) with $P6_3/m$ symmetry were found to be good, purely oxide-ion conductors by Nakayama *et al.*,[9] with a conductivity of σ ≈ 1.4 × 10$^{-3}$ S cm$^{-1}$ at 700 °C for Ln = La. The authors also observed a relationship between the ionic radius of Ln and the conductivity, where La$_{10}$(SiO$_4$)$_6$O$_3$ possesses the largest conductivity. The lanthanum germanate analogue, La$_{10}$(GeO$_4$)$_6$O$_3$, was also reported to be a good oxide-ion conductor,[17] exceeding La$_{10}$(SiO$_4$)$_6$O$_3$ in conductivity at temperatures > 600 °C. A change in the activation energy for conductivity at $T$ ≈ 740 °C has been observed,[17] suggesting that La$_{10}$(GeO$_4$)$_6$O$_3$ undergoes a phase transition at this temperature. La$_{10}$(GeO$_4$)$_6$O$_3$ was later reported to adopt $P$-1 symmetry at room temperature and it also undergoes a phase transition in the range of 650 – 850 °C. Figure 4.4 shows the conductivity of a selection of apatites.
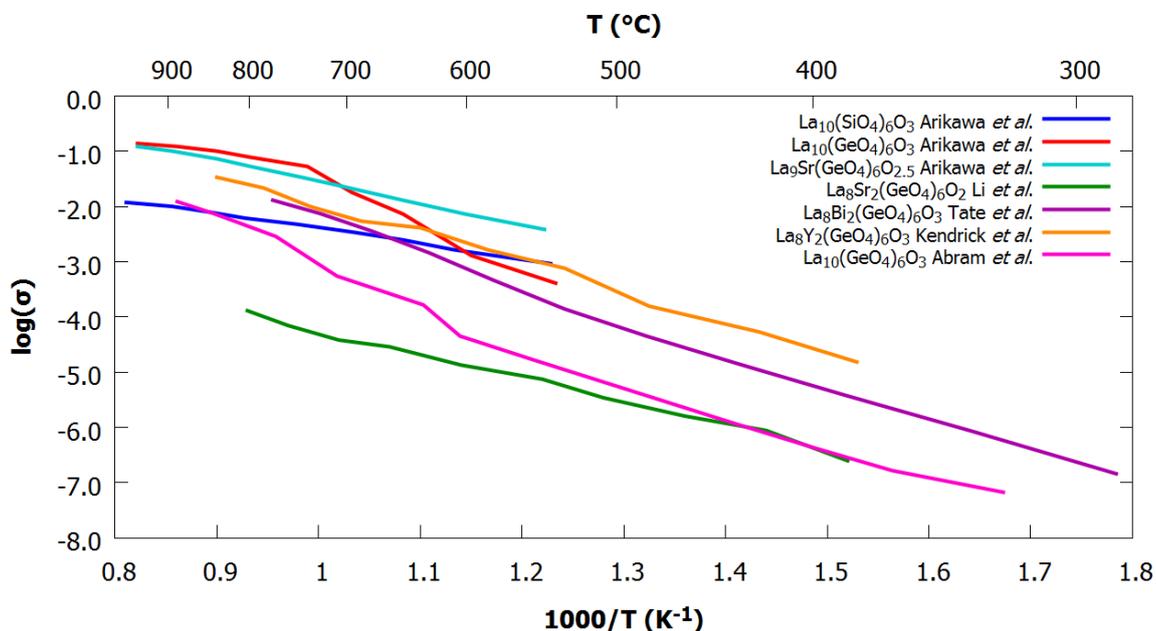


**Figure 4.4 –** Conductivity of a selection of apatite-type oxide-ion conductors:  blue = La$_{10}$(SiO$_4$)$_6$O$_3$, red = La$_{10}$(GeO$_4$)$_6$O$_3$ and cyan  = La$_9$Sr(GeO$_4$)$_6$O$_{2.5}$;[17] green =  La$_8$Sr$_2$(GeO$_4$)$_6$O$_2$;[18] purple =  La$_8$Bi$_2$(GeO$_4$)$_6$O$_3$;[19]  orange = La$_8$Y$_2$(GeO$_4$)$_6$O$_3$;[20] pink =  La$_{10}$(GeO$_4$)$_6$O$_3$.[21]

As mentioned above, the apatite structure is quite chemically flexible, and further studies compared the conductivity of La$_{9.33}$(SiO$_4$)$_6$O$_2$ with La$_{10}$(SiO$_4$)$_6$O$_3$[22] and La$_{10-x}$(GeO$_4$)$_6$O$_{3-3x/2}$.[10] In both cases, it was found that La$_{9.33}$(MO$_4$)$_6$O$_2$ (M = Si, Ge) has a lower conductivity than La$_{10}$(MO$_4$)$_6$O$_3$ or any example where the total oxygen content exceeds 26. On the other hand, La$_{9.33}$(GeO$_4$)$_6$O$_2$ has been reported to have a greater conductivity than La$_{10}$(GeO$_4$)$_6$O$_3$.[21] When the M site is substituted[23] with transition metals such as Fe$^{3+}$, Co$^{3+}$ and Mn$^{2+}$, the conductivity was greater when the total oxygen content > 26, though Co$^{3+}$ samples were found to have a significant electronic component. It is possible to dope the M site with a wide variety of lower oxidation

state dopants, such as $Mg^{2+}$, $Ga^{3+}$ and $Al^{3+}$,[24-28] where doping with $Al^{3+}$ was reported to improve the conductivity to values of 0.16 S cm$^{-1}$ at 800 °C.[24] Interestingly, both oxygen excess[27] (total O per formula unit > 26) and oxygen deficiency (total O per formula unit < 26) increase the conductivity relative to $La_{9.33}(SiO_4)_6O_2$. Doping onto the Si site with $In^{3+}$ has also been attempted, where the authors attribute an increase in conductivity due to formation of a single phase and the presence of O vacancies (in comparison to $La_{10}(SiO_4)_6O_3$).[29] They found the best conductor to be $La_{10}Si_{5.8}In_{0.2}O_{26.90}$, with $\sigma$ = 0.034 S cm$^{-1}$ at 800 °C.

There have also been attempts to dope the M site in the germanate analogues. Orera *et al.*[7] found that by doping $Ti^{4+}$ in $La_{10}Ge_{6-x}Ti_xO_{27}$, the symmetry increases from triclinic ($x$ < 1) to hexagonal ($x$ > 1), which resulted in higher conductivities compared to $x$ = 0 at low temperatures, but lower conductivities at higher temperatures. They also doped $Nb^{5+}$ and $W^{6+}$, achieving single phases with $La_{9.83}Ge_{5.5}Nb_{0.5}O_{27}$ and $La_{10}Ge_{5.5}W_{0.5}O_{27.5}$ respectively, which produced similar results: a stabilisation of the hexagonal $P6_3/m$ symmetry at room temperature, thereby increasing the conductivity at lower temperatures but decreasing it at higher temperatures. Doping with $Al^{3+}$, along with $La^{3+}$ vacancies, has yielded significant improvements in the ionic conductivity, giving a conductivity of 0.17 S cm$^{-1}$ for $La_{9.55}(Ge_{5.5}Al_{0.5}O_{24})O_2$ at 800 °C,[30] though $La_{9.8}Ge_{5.5}Al_{0.5}O_{26.45}$ was reported[31] to have a conductivity of 0.011 S cm$^{-1}$ at 700 °C, whilst $La_{10}Si_{5.5}Al_{0.5}O_{26.75}$ has a conductivity at the same temperature of 0.025 S cm$^{-1}$. The mixed $La_{9.33}Si_{6-x}Ge_xO_{26}$ ion conductor has also been investigated,[12] where an increase in $x$ also produced an increase in conductivity until a maximum at $x$ = 4, with 0.06 S cm$^{-1}$ at 800 °C; $x$ = 5, 6 produced single phases but were worse conductors at the same temperature.

The A site is also targeted for substitution. $La^{3+}$ has been substituted[8, 14, 17-18, 21] for $Sr^{2+}$, $Ca^{2+}$ and $Ba^{2+}$,[18, 32-34] producing $La_{10-x}A_x(GeO_4)_6O_{3-x/2}$ (A = Ca, Sr, Ba). For all examples of $x$ = 2, the conductivity is greatly reduced but those with $x$ = 1 have higher low-temperature conductivity and similar (though slightly lower) conductivities at high temperature (see Figure 4.3). All examples of $x$ = 2 in $La_{10-x}A_x(GeO_4)_6O_{3-x/2}$ (A = Ca, Sr, Ba) are reported as adopting $P6_3/m$ symmetry. However, A = Sr has also been reported as adopting $P2_1/m$ symmetry[14] and A = Ba has been also reported as adopting $P$-3 symmetry.[35] The same pattern was reported for the silicate analogues.[7] These claims are investigated in this chapter. Doping with the small cation $Y^{3+}$ has been reported to stabilise hexagonal symmetry at room temperature[20] and provided higher low-temperature conductivity but lower high temperature conductivities compared to the parent $La_{10}(GeO_4)_6O_3$. Doping $Bi^{3+}$ on the A cation site and $Ga^{3+}$ on the M cation site produced $La_8Bi_2Ge_5GaO_{26.5}$, with an ionic conductivity of 0.02 S cm$^{-1}$ at 800 °C showing a decrease the sintering temperatures required for making dense pellets.[35] More recently, investigations into $Bi^{3+}$ incorporation have

been carried out by Tate *et al.*,[19] where La$_8$Bi$_2$(GeO$_4$)$_6$O$_3$ was found to have a conductivity of 1.29 ×

10$^{-2}$ S cm$^{-1}$ at 775 °C. La$_{10}$(GeO$_4$)$_6$O$_3$ has been found to have a conductivity of 7.77 × 10$^{-3}$ S cm$^{-1}$ at

775 °C[36] and 2.85 × 10$^{-3}$ at 771 °C.[21] Like La$_{10}$(GeO$_4$)$_6$O$_3$, La$_8$Bi$_2$(GeO$_4$)$_6$O$_3$ adopts *P*-1 symmetry at

room temperature but undergoes a phase transition to *P*6$_3$/*m* at 680 – 750 °C.[19] There have been

reports of Bi co-doping with Ba, which decreased the ionic conductivity.[32] Co-doping on the A and

M site has also been performed in Bi$_2$Ca$_{8-2x}$La$_{2x}$[(VO$_4$)$_{6-2x}$(GeO$_4$)$_{2x}$]O$_2$ ($x$ = 1, 2, 3) and although a full

structural analysis has not been performed, they have been shown to adopt a hexagonal structure

with conductivities up to 1.1 × 10$^{-4}$ S cm$^{-1}$ at 775 °C.[36] Bi$_4$Ca$_2$La$_2$(GeO$_4$)$_6$O$_2$ and Bi$_4$Ca$_4$La$_2$[(VO-

$_4$)$_2$(GeO$_4$)$_4$]O$_2$ were also examined and showed an improvement in their conductivities compared

to the samples with less Bi$^{3+}$.

There are however, doubts whether La$_{10}$(SiO$_4$)$_6$O$_3$ actually exists. This is discussed in Chapter 5 of

this report. For the germanate analogue, La$_{10-x}$(GeO$_4$)$_6$O$_{3-3x/2}$ it has been suggested that the limit

for a pure phase is 9.52 ≤ 10–$x$ ≤ 9.75, as La$_2$GeO$_5$ or La$_2$Ge$_2$O$_7$ are formed due to germanium

volatilisation (synthesis temperatures often reach 1300 °C ).[10] However, there have been reports

of producing pure La$_{10}$(GeO$_4$)$_6$O$_3$ through the use of ball milling at room temperature and Pechini-

type sol-gel synthesis, which requires a maximum temperature of 800 °C.[32] Recent developments

in synthetic techniques also include the synthesis of La$_{9.33}$(GeO$_4$)$_6$O$_2$ using facile molten-salt

synthesis[37] and crystal growth of La$_{9.68}$(GeO$_4$)$_6$O$_{2.52}$ through reactive diffusion of La$_2$GeO$_5$

polycrystalline sample and GeO$_{(g)}$ + ½O$_{2(g)}$.[38] A co-precipitation method for the nominal

composition La$_{10}$(SiO$_4$)$_6$O$_3$ has also been developed,[39] but has not yet been applied to the

germanate analogue.

### 4.1.1.3 Structure-property relationships in lanthanum germanate apatite-type oxide-ion conductors

The lanthanum germanate apatites have been found to adopt a range of symmetries at room

temperature. Leon-Reina *et al.*[10] determined that for La$_{9.33+x}$(GeO$_4$)$_6$O$_{2+3x/2}$, the composition range

of 0 ≤ $x$ ≤ 0.27 adopts *P*6$_3$/*m* symmetry, whilst the composition range of 0.33 ≤ $x$ ≤ 0.67 adopts *P*-1

symmetry at room temperature. These findings were later reproduced by Abrams *et al.*[21] It was

initially thought that that the reason the germanate apatites adopt a triclinic structure is due to

the strain caused by the large Ge$^{4+}$ and La$^{3+}$ cations, as well as the flexibility of the GeO$_4$

tetrahedra.[10, 32] This has been further evidenced by substitution of Ge$^{4+}$ with smaller Al$^{3+}$, where

even the compositions of 10 − $x$ =9.80 in La$_{10-x}$□$_x$(Ge$_{5.5}$Al$_{0.5}$O$_4$)$_6$O$_{2.75-x}$ adopted *P*6$_3$/*m* symmetry.[30]

When the smaller Y$^{3+}$ ion is substituted onto the A site, La$_8$Y$_2$(GeO$_4$)$_6$O$_3$ is formed with *P*6$_3$/*m*

symmetry.[20] Substituting with Yb$^{3+}$ also resulted in a hexagonal material.[7] On the other hand,

when alkaline-earth elements with larger ionic radii[40] than La$^{3+}$ are substituted onto

La$_8$M$_2$(GeO$_4$)$_6$O$_2$ (M = Ca, Sr, Ba), the hexagonal *P*6$_3$/*m* symmetry is adopted,[8, 18, 32-34] though M = Sr

has also been reported as adopting monoclinic $P2_1/m$ symmetry[14] and M = Ba has been reported as adopting $P$-3 symmetry.[35] This would suggest that the excess oxygen is also an important factor in which symmetry is adopted by the lanthanum germanium apatites.

It is thought that the interstitial, "27$^{th}$" oxide ion is sandwiched between two $GeO_4$ tetrahedra, approximately at (½, 0, 0) in hexagonal apatites.[5, 8, 14, 19, 38, 41-42] In cells with $P6_3/m$ symmetry, there are six symmetrically equivalent sites corresponding to these coordinates. However, in cells with $P$-1 symmetry, these are six unique sites: (½, 0, 0), (½, 0, ½), (0, ½, ½), (0, ½, 0), (½, ½, ½) and (½, ½, 0). There are conflicting reports in regard to the specific location of the $O_{int}$ ion. It has also been reported to be in a similar location to that proposed in the silicate analogue. Leon-Reina et al.[11, 43] suggested it is at the periphery of the hexagonal channel in $La_{9.6}(GeO_4)_6O_{2.4}$ at [0.016(2), 0.228(2), 0.606(1)]. Pramana et al.[5] reported the location in $La_{10}(GeO_4)_6O_3$ at [0.028(4), 0.477(4), 0.511(5)], determined through high resolution powder neutron diffraction. They suggested that instead of the formula "$La_{10}(GeO_4)_6O_3$", "$La_{10}(GeO_4)_5(GeO_5)O_2$" should be used as it is a more accurate description of the structure. The same authors[8] found $La_9Sr(GeO_4)_6O_{2.5}$ to be isostructural with $La_{10}(GeO_4)_6O_3$, again with neutron diffraction, placing the $O_{int}$ ion in a similar position. Fukuda et al.[38] synthesised $La_{9.68}Ge_6O_{26.52}$ and studied it with single-crystal X-ray diffraction and not only reported it as adopting $P1$ symmetry (as opposed to $P$-1), but that the $O_{int}$ ion is located at [0.4718(16), 0.5694(16), 0.524(2)]. They determined this through residual electron density seen in the Fourier map near a Ge atom.

In $La_8Bi_2(GeO_4)_6O_3$, Tate et al.[19] found through neutron diffraction that the $O_{int}$ ion is present at ≈(0.475, 0.510, 0.024). The Fourier maps also showed that there was almost as much residual nuclear density at ~(½, 0, 0). In addition, they used scanning transmission electron microscopy (STEM) to directly image $La_8Bi_2(GeO_4)_6O_3$. As this technique produces an image that is a two dimensional projection of the unit cell, there are certain positions that cannot be resolved, where instead only columns of intensity can be inferred. It was found that the column at the centre of the cell had $O_{int}$ ions present and the column top and bottom of the unit cell was also populated with $O_{int}$ ions, but there was no evidence of $O_{int}$ ions at the "sides" of the unit cell [~(0 ½ 0) and ~(0 ½ ½)]. Although these reports disagree on the exact location, the majority maintain that the $O_{int}$ ion is between adjacent $GeO_4$ tetrahedra. The $O_{int}$ ion in hexagonal $La_8Y_2(GeO_4)_6O_3$ is also reported to be between $GeO_4$ tetrahedra at [0.070(2), 0.473(2), −0.043(3)],[41] producing $Ge_2O_9$ units. Further evidence that the $O_{int}$ is located between $GeO_4$ is found from spectroscopic studies. Pramana et al.[14] found bands in IR spectroscopy at 641 and 815 cm$^{-1}$ in $La_{10}(GeO_4)_6O_3$, which they attribute to $GeO_5$ units. Orera et al.[33] found a band in the Raman spectra of $La_{10-x}Ba_x(GeO_4)_6O_{3-x/2}$

at 645 cm$^{-1}$, which they attributed to stretching of Ge–O$_{int}$–Ge in Ge$_2$O$_9$ units. They also modelled the O$_{int}$ ion at (0.034, 0.49, –0.0281) in La$_9$Ba(GeO$_4$)$_6$O$_{2.5}$ with $P1$ symmetry.

Initially, it was postulated that La$_{9.33}$(GeO$_4$)$_6$O$_2$ has the same "S$_N$2-type" conduction mechanism as the silicate analogue.[32] A mechanistic study by Kendrick *et al.*[6] suggested that the primary conduction mechanism could be through the movement of O4 ions in the La2 hexagonal column into vacancies down the hexagonal channel, or through an interstitial mechanism. This interstitial mechanism involves a "fan-like" motion along the *c*-axis, moving between GeO$_4$ tetrahedra. This results in the formation of a Ge$_2$O$_9$ unit by connecting two GeO$_4$ tetrahedra to the interstitial oxide ion with Ge–O distances of 1.77 to 1.92 Å. The relaxed configuration when the O$_{int}$ ion is in this position is almost identical to the relaxed configuration when it is at the channel periphery. Neutron diffraction of La$_8$Y$_2$(GeO$_4$)$_6$O$_3$ added experimental evidence to the "fan-like" mechanism by revealing that the interstitial oxide ion is most likely between GeO$_4$ tetrahedra and forms Ge$_2$O$_9$ units.[41] However, this does not demonstrate that the "fan-like" mechanism is the mechanism of conduction.

An *ab initio* molecular dynamics (AIMD) study by Imaizumi *et al.*[44] provided further insights into the conduction mechanism. Using the $P6_3/m$ model for La$_{10}$(GeO$_4$)$_6$O$_3$ at 1000, 1500 and 2000 K, they found that the position (½, ½, 0) is the lowest energy site for the O$_{int}$ atom, resulting in Ge$_2$O$_9$ units with an equidistant Ge–O$_{int}$ distance of 2.09 Å between the two tetrahedra, but the position of the O$_{int}$ atoms can deviate by ~0.3 Å. Contrary to the findings by Kendrick *et al.*[6], Imaizumi *et al.*[44] found the most frequent (22 times in 90 ps at 2000 K) conduction mechanism to be an interstitialcy mechanism along *c*, where an O$_{int}$ atom moves onto an adjacent normal O site on the GeO$_4$ tetrahedra and a normal O atom moves into an adjacent, vacant O$_{int}$ site. The "fan-like" mechanism was found to occur only once in 90 ps at 2000 K and did not occur at all at 1000 and 1500 K. The second most frequent event was an interstitialcy mechanism where O4 channel oxide temporarily moves into regular site near a GeO$_4$ tetrahedron, displacing an O in the tetrahedron from a regular site into an interstitial site, forming a Ge$_2$O$_9$ unit. The O4 vacancy is then filled by a regular O atom that is part of an adjacent Ge$_2$O$_9$ unit, whilst the O$_{int}$ in that unit moves into a regular site. This event occurred 6 times at 2000 K and allows oxide-ion conduction to occur in any direction and occurred twice as often as the "S$_N$2-type" mechanism at the same temperature. The second most-frequent mechanism would explain why the oxide-ion conduction in a La$_{9.33}$(GeO$_4$)$_6$O$_2$ crystal was not as anisotropic as the silicate analogue.[45] With no excess oxides occupying the O$_{int}$ site, the conductivity would be dominated by this isotropic movement. A follow-up study[46] using the nudged elastic band (NEB) and kinetic Monte Carlo (KMC) methods confirmed these results, where the cooperative interstitialcy mechanism had the lowest

activation energy of 0.64 eV compared to 1.27 eV for the "fan-like" mechanism, though Kendrick *et al*.[6] calculated that mechanism to have an activation energy of 0.79 eV.

It was found that the previously studied mechanism where O4 atoms move into interstitial sites[44] has a potential barrier of 0.76 eV,[46] which again suggests there is less anisotropy than initially thought. The authors found that there were two key factors that determined the energy of the pathways: the Ge–O$_{int}$ distance and O–O repulsive interactions. Comparing the interstitial mechanism along *c* and *ab*, the Ge–O$_{int}$ distance begins at 2.06 Å and then goes down to 1.90 Å, and during the entire migration, a Ge–O$_{int}$ bond is maintained. In contrast, when travelling in the *ab* plane, there is a distance of 2.46 Å, resulting in a breaking of the Ge–O$_{int}$ bond. The same is true for the interstitialcy mechanisms, but this distance is longer, resulting in less repulsion and thus a lower potential energy barrier.

Apatites such as La$_8$Bi$_2$(GeO$_4$)$_6$O$_3$ contain a further complication to their conductivity and structure relationship due to the lone pairs on Bi$^{3+}$. Electron localisation function (ELF) calculations[47] have given further insight into the effect the lone pair has on the conductivity. It had initially been thought that lone pairs would reduce the conductivity as they would be oriented towards the hexagonal channel, thus impeding movement of oxide ions along it. However, these studies revealed that the presence of the anions actually repels the lone pairs. The lone pairs on Bi$^{3+}$ in La$_8$Bi$_2$(GeO$_4$)$_6$O$_3$ are consequently oriented 120° away from the channels. The lone pairs are still within the same *ab* plane as the cations. The increase in repulsion derives not just from the larger magnitude of charge of O$^{2-}$ versus Cl$^-$, but from the fact the O$^{2-}$ anions are in the same plane as the A2 cations. Since the Bi$^{3+}$ cations only occupying 1/3 of the A2 sites and because there are GeO$_4$ and GeO$_5$ on either side, the O$^{2-}$ anions remain in the same plane as Bi$^{3+}$ cations. The lone pairs are not oriented towards the hexagonal channel, but instead towards the GeO$_4$ and GeO$_5$ polyhedra, so the lone pairs would not interfere with oxide-ion conduction along the hexagonal channel. This explains why the conductivities of La$_6$Bi$_2$Ba$_2$(GeO$_4$)$_6$O$_2$ and La$_6$Bi$_2$Sr$_2$(GeO$_4$)$_6$O$_2$ can be higher than La$_8$Ba$_2$(GeO$_4$)$_6$O$_2$ and La$_8$Sr$_2$(GeO$_4$)$_6$O$_2$,[35, 47] as well as why there the can be an increase in conductivity for Bi$_4$Ca$_4$La$_2$[(VO$_4$)$_2$(GeO$_4$)$_4$]O$_2$ and Bi$_4$Ca$_2$La$_4$[(GeO$_4$)$_6$]O$_2$ compared to Bi$_2$Ca$_4$La$_4$[(VO$_4$)$_2$(GeO$_4$)$_4$]O$_2$ and Bi$_2$Ca$_2$La$_6$[(GeO$_4$)$_6$]O$_2$ respectively.[36]

A combined experimental and AIMD study elucidated the conduction mechanisms of La$_{10}$(GeO$_4$)$_6$O$_3$, La$_8$Bi$_2$(GeO$_4$)$_6$O$_3$ and La$_6$Bi$_4$(GeO$_4$)$_6$O$_3$.[48] The AIMD density of states (DOS), verified by the DOS measured by neutron scattering, indicated that there is long range diffusion in the materials. In addition to the three cooperative mechanism observed by Imaizumi *et al*.,[46] a fourth mechanism where oxides in the hexagonal column travel along the *c* axis was also observed.[48] The

maximum O$^{2-}$ displacements decreased with Bi$^{3+}$ content at 1500 K but increased at 1750 K and 2000 K over the course of the simulation. It is believed that the decrease at 1500 K is a result of steric hindrance by the Bi$^{3+}$ lone pair, which hinders the conduction mechanism along $c$. At the higher temperatures, the number of instances in the Bi$^{3+}$-containing samples increases compared to the pure lanthanum analogue, which is a result of the two mechanisms in the $ab$ plane becoming more dominant and suggests that an increase in Bi$^{3+}$ content makes conduction more isotropic, though most diffusion events still occur through movement $via$ the GeO$_4$ tetrahedra. This could be due to the change in geometry around Bi$^{3+}$ compared to La$^{3+}$ – there are shorter bonds around Bi$^{3+}$, resulting in a reduction in the distance between the O4 atoms and neighbouring GeO$_4$ tetrahedra. In addition, the Bi–O bonds are more polarisable than the La–O bonds, which enables greater oxide-ion conduction.

### 4.1.2 Purpose of study

From the results in previous studies, it is clear that the symmetry, structure and interstitial oxide ions are critical to the conductivity of the lanthanum germanate apatite-type oxide-ion conductors. The electronic configuration of the A site atoms may also affect the symmetry.[15] Although oxide-ion conduction is a long-range phenomenon, the nature of the local structure is crucial to the conduction mechanism. Therefore, an investigation into the long-range, average structure and the local structure has been carried out using powder synchrotron X-ray and neutron diffraction and neutron total scattering into three apatite-type oxide-ion conductors of formulae La$_8$R$_2$(GeO$_4$)$_6$O$_{3-y}$ (R = Sr, La, Bi). Table 4.2 summarises the room temperature symmetry, ionic radii for six-fold coordination and electronic configuration for each different R species.

**Table 4.2 – Reported symmetries of La$_8$R$_2$(GeO$_4$)$_6$O$_{3-y}$ (R = Sr, La, Bi) at room temperature (RT), the ionic radii for six-fold coordination and electronic configuration of R.**

|  | Sr$^{2+}$ | Bi$^{3+}$ | La$^{3+}$ |
|---|---|---|---|
| **RT symmetry** | $P2_1/m$;[14] $P6_3/m$[18] | $P$-1[19] | $P$-1[5] |
| **$^{VI}r$ (Å)[40]** | 1.18 | 1.03 | 1.032 |
| **Electronic configuration** | [Kr] | [Xe]$4f^{14}5d^{10}6s^2$ | [Xe] |

These three apatites were chosen for the following reasons: La$^{3+}$ and Bi$^{3+}$ have similar ionic radii, but Bi$^{3+}$ has a lone pair, which can reveal how important stress and electronic configuration are, as well as the local environments of La$^{3+}$ and Bi$^{3+}$ differing due to the lone pair.[1, 47-48] The 5$d^{10}$ and empty 6$s^0$ orbitals are also close in energy, which may result in additional symmetry lowering.[15] Sr$^{2+}$ also has a large ionic radius and a closed shell configuration like La$^{3+}$, but La$_8$Sr$_2$(GeO$_4$)O$_2$ has no excess oxygen. Studying these three apatites allows the importance of the presence of the O$_{int}$

ions and the ionic radii, as well as electronic configuration of the A atoms to be determined. In addition, the local geometry of the GeO$_x$ ($x$ = 4, 5) polyhedra should be different between La$_8$R$_2$(GeO$_4$)$_6$O$_3$ (R = La, Bi) and La$_8$Sr$_2$(GeO$_4$)$_6$O$_2$. The lone pairs of Bi$^{3+}$ could potentially affect this geometry. The long range, average structures were studied by using combined high-resolution neutron and synchrotron diffraction and Rietveld refinement, whilst the local structure was elucidated using neutron total scattering and reverse Monte Carlo (RMC) calculations after obtaining good average structure models.

## 4.2 Experimental Procedure

### 4.2.1 Synthesis

Two 5 g samples of La$_8$R$_2$(GeO$_4$)$_6$O$_3$ (R = Sr, La, Bi) were prepared by mixing stoichiometric amounts of La$_2$O$_3$ (Acros, 99.9%), SrCO$_3$ (Fisher, 99.9%), Bi$_2$O$_3$ (Fisher, 99.9%) and GeO$_2$ (Acros, 99.999%). La$_2$O$_3$ was calcined at 950 °C for 12 h prior to synthesis. After the samples were prepared, the two 5 g batches were mixed and then heated at 1300, 1200 and 1100 °C for R = Sr, La and Bi respectively in order to create 10 g batch of each sample with a similar thermal history. The samples were heated at 1100 °C for 16 − 36 h followed by a further heating at various temperatures with intermittent grinding until the reaction was deemed completed by powder X-ray diffraction. The maximum temperature ($T_{max}$) and total time heated at $T_{max}$ ($t_{tot}$) for each material are given in Table 4.3. All products were pale cream in colour. The samples were also heated at 1000 °C for 12 h prior to measurement on POLARIS, HRPD and I11 in order to dry the samples. A further 5 g sample of La$_8$Bi$_2$(GeO$_4$)$_6$O$_3$ was prepared (MSC046) at a later date for a second measurement on POLARIS; this sample was not heated at 1000 °C prior to the POLARIS measurement.

**Table 4.3 – Maximum heating temperature, $T_{max}$ and time heated at $T_{max}$, $t_{tot}$, in La$_8$R$_2$(GeO$_4$)$_6$O$_{3-y}$ (R = Sr, La, Bi).**

| Code | R | $T_{max}$ (°C) | $t_{tot}$ (h) |
|---|---|---|---|
| MSC015 | Sr | 1300 | 16 |
| MSC019 | Sr | 1300 | 16 |
| MSC022 (015 +019) | Sr | 1300 | 36 |
| MSC013 | La | 1300 | 16 |
| MSC014 | La | 1300 | 16 |
| MSC018 (013 + 014) | La | 1200 | 10 |
| MSC021 | Bi | 1100 | 36 |
| MSC024 | Bi | 1100 | 36 |
| MSC025 (021 + 024) | Bi | 1100 | 12 |
| MSC046* | Bi | 1100 | 54 |

*Synthesised at a later time, with no additional heating at 1000 °C prior to national facility collection

Additionally, three more samples of $La_8Sr_2(GeO_4)_6O_2$, derived from MSC022, were produced for synchrotron X-ray experiments: MSC040, MSC041 and MSC042. Table 4.4 outlines the additional processes. All heating rates were at 10 °C min$^{-1}$ and all cooling rates were set to 10 °C min$^{-1}$.

**Table 4.4 – Sample codes and additional processings of the three $La_8Sr_2(GeO_4)_6O_3$ materials derived from MSC022 (see Table 4.3).**

| Code | Process |
|---|---|
| MSC040 | Heated at 1100 °C for 168 h |
| MSC041 | Heated at 1300 °C for 168 h |
| MSC042 | Heated at 1350 °C for 16 h |

## 4.2.2 Powder diffraction: laboratory X-ray, synchrotron X-ray and neutron

Phase purity was determined using X-ray powder diffraction using a D8 Bruker Advance with a Cu target and Ni filter. The emitted wavelength is a mixture of Cu K$\alpha_1$ (1.54051 Å) and Cu K$\alpha_2$ (1.54433 Å). Data were collected using samples mounted on Si slides over a 10° ≤ 2$\theta$ ≤ 80° range, scanning in 0.02° steps for 1 second per step. For MSC046 (see Table 4.3), a powder pattern was obtained at 10° ≤ 2$\theta$ ≤ 100° in 0.02° steps with a scanning time of 6 seconds per step using a zero-background oriented Si slide. The Rietveld refinements carried out at this stage did not involve refinements of atomic coordinates, but just the cell parameters and an overall isotropic atomic displacement parameter (ADP) was also refined for all the atomic sites. The refinements were performed using models previously published: $La_{10}(GeO_4)_6O_3$ was from Pramana et al.,[5] $La_8Sr_2(GeO_4)_6O_2$ was from Pramana et al.[8] and $La_8Bi_2(GeO_4)_6O_3$ was obtained from Tate et al.[19]

High resolution neutron powder diffraction data were collected for $La_8R_2(GeO_4)_6O_{3-y}$ in vanadium cans with the sample heights and masses shown in Table 4.5 on the High Resolution Powder Diffraction (HRPD) instrument at ISIS Neutron and Muon Source. One 6 hour scan was collected at room temperature for all the samples, followed by 6 minute scans from 100 °C – 840 °C in 20°C increments, then six 1 hour scans at 850 °C. For $La_8Bi_2(GeO_4)_6O_3$, the 6 minute scans only went to 800 °C and the six 1 hour scans were also collected at 800 °C. For $La_8Sr_2(GeO_4)_6O_2$ (MSC022), the 6 minute scans were from 90 – 850 °C. The diameter of the cans used was 11 mm. Data collected from two banks were used: bank 1 (2$\theta$ = 168.567°) and bank 2 (2$\theta$ = 90.2481°). The starting models were the same starting models used in the laboratory X-ray powder diffraction.[5, 8, 19] The cell parameters, atomic positions, fractional occupancies of the O$_{int}$ sites and ADPs were refined. The background was fitted using a 12$^{th}$-order Chebyshev polynomial.

**Table 4.5 – Sample height and mass of La$_8$R$_2$(GeO$_4$)$_6$O$_{3-y}$ (R = Sr, La, Bi) used in high resolution neutron diffraction on the HRPD instrument at ISIS Neutron and Muon Source.**

| Sample code | R | Mass (g) | Height (cm) |
|---|---|---|---|
| MSC025 | Bi | 3.579 | 2.4 |
| MSC022 | Sr | 2.671 | 2.5 |
| MSC018 | La | 2.713 | 2.6 |

Synchrotron X-ray powder diffraction was collected using a wavelength of $\lambda$ = 0.8259211 Å, determined from a Si calibration, and the samples were loaded into 0.3 mm diameter fused quartz capillaries. A hot air blower was used to control the temperature for variable temperature data collection. Samples MSC040, MSC041 and MSC042 were used in a later experiment, where all three were scanned at room temperature for 30 minutes. The wavelength was $\lambda$ = 0.824681 Å. The temperatures and scan times for each sample are listed in Table 4.6.

**Table 4.6 – Data collection parameters used for La$_8$R$_2$(GeO$_4$)$_6$O$_{3-y}$ (R = Sr, La, Bi) samples on the I11 beamline at Diamond Light Source.**

| R | Nominal temperature range (°C) | Temperature steps (°C) | Scan time per temp step (min) |
|---|---|---|---|
| Sr | 30 | N/A | 60 |
| Sr | 30 – 930 | 25 | 5 |
| Sr | 950 | N/A | 60 |
| Bi | 25 | N/A | 2 × 60 |
| Bi | 30 – 790 | 20 | 5 |
| Bi | 800 – 920 | 20 | 5 |
| Bi | 950 | N/A | 2 × 60 |
| La | 30 | N/A | 2 × 60 |
| La | 30 – 930 | 25 | 5 |
| La | 950 | N/A | 2 × 60 |

The temperature of the hot air blower was calibrated using an Al$_2$O$_3$ standard. The cell parameters of the Al$_2$O$_3$ are measured over the nominal temperature range of 30 – 1000 °C. The cell parameters obtained from variable temperature Rietveld refinements are compared to literature values, giving calibration equations of:

$$\Delta T = 3.96617 \times 10^{-5}T^2 + 0.13374T - 7.59525 \qquad (4.2a)$$

$$T_{\text{corrected}} = T - \Delta T \qquad (4.2b)$$

Where $T$ is the nominal temperature and $\Delta T$ is the difference between the nominal temperature and the true temperature. Rietveld refinements were performed using the summed room temperature data refining the cell parameters and atomic coordinates, fractional occupancies of

the A sites for La$_8$R$_2$(GeO$_4$)$_6$O$_{3-y}$ (R = Sr, Bi), and peak shapes. The structural models obtained from the refinements from HRPD were used as a starting point. Additionally, the background was fitted using a 12$^{th}$-order Chebyshev polynomial. A peak to describe the scattering from the quartz capillary was inserted at 2$\theta$ = 11.52° and its position, width and intensity were allowed to refine. The absorption coefficient $\mu r$, was calculated based on a packing factor of 20% for samples and fixed at values from 0.95 − 1.3 for different compositions. The low packing factor was also observed when packing the samples for neutron diffraction and total scattering. The time of flight and 2$\theta$ ranges used in the final combined refinements are given in Table 4.7.

**Table 4.7 − Time of flight and 2θ ranges used in the final combined neutron and synchrotron Rietveld refinements of La$_8$R$_2$(GeO$_4$)$_6$O$_{3-y}$**

| R | HRPD bank 1 (µs) | HRPD bank 2 (µs) | I11 (°) |
|---|---|---|---|
| Sr | 32000 ≤ $t$ ≤ 125000 | 30000 ≤ $t$ ≤ 130000 | 5 ≤ 2$\theta$ ≤ 75 |
| La | 30000 ≤ $t$ ≤ 125000 | 29000 ≤ $t$ ≤ 132000 | 5 ≤ 2$\theta$ ≤ 65 |
| Bi | 34000 ≤ $t$ ≤ 125000 | 29000 ≤ $t$ ≤ 132000 | 5 ≤ 2$\theta$ ≤ 72 |

### 4.2.3 Neutron total scattering

Total scattering was performed on La$_8$R$_2$(GeO$_4$)$_6$O$_{3-y}$ in vanadium cans with a diameter of 8 mm with sample heights and masses shown in Table 4.8. For the MSCO046 sample of La$_8$Bi$_2$(GeO$_4$)$_6$O$_3$, data were collected in a vanadium can with a diameter of 6 mm at a later date.

**Table 4.8 − Sample height and mass of La$_8$R$_2$(GeO$_4$)$_6$O$_{3-y}$ (R = Sr, La, Bi) used in total scattering (POLARIS).**

| Sample code | R | Mass (g) | Height (cm) | Notes |
|---|---|---|---|---|
| MSC025 | Bi | 3.585 | 4.4 | |
| MSC022 | Sr | 2.660 | 4.6 | |
| MSC018 | La | 2.720 | 4.8 | |
| MSC046 | Bi | 2.46590 | 4.5 | Performed in a 6 mm V can at a later date to the other 3 samples |

PDF-quality data were collected for all samples at room temperature for a total of 6 × 1 h scans. Only room temperature data were collected for La$_8$Sr$_2$(GeO$_4$)$_6$O$_2$. For La$_8$Bi$_2$(GeO$_4$)$_6$O$_3$ (MSC025), 9 minute scans were collected at 70 − 280 °C in 30 °C increments, followed by 5 minute scans at 350 − 800 °C. PDF-quality data (6 × 1 h scans) were collected at 800 °C. For La$_{10}$(GeO$_4$)$_6$O$_3$, 5 minute scans were taken every 50 °C from 100 − 850 °C and PDF-quality data (6 × 1 h scans) were collected at 850 °C. For MSC046, 6 × 1 h scans were collected at room temperature and 800 °C. The data were processed for Rietveld refinement the data were processed using routines within Mantid software.[49]

The PDF-quality data were processed using GudrunN version 5[50] to produce $S(Q)$ data as defined in Chapter 2.3. The $S(Q)$ data produced by GudrunN were processed with the STOG software, creating $G(r)$ and $F(Q)$ files. The $G(r)$ data were produced using $Q_{max}$ = 35 Å$^{-1}$ and a Soper-Lorch correction was applied to remove Fourier ripples produced by using a Fourier transform to a limited $Q_{max}$. For La$_8$Sr$_2$(GeO$_4$)$_6$O$_2$, data for $r$ ≤ 1.6 Å were Fourier-filtered. For La$_{10}$(GeO$_4$)$_6$O$_3$, data for $r$ ≤ 1.52 Å and $r$ ≤ 1.55 Å for room temperature and 850 °C respectively were Fourier-filtered and for La$_8$Bi$_2$(GeO$_4$)$_6$O$_3$, the filter was applied for $r$ ≤ 1.55 Å and $r$ ≤ 1.57 Å at room temperature and 800 °C respectively. Total scattering analysis was performed using TOPAS v6[51] for small box analysis by converting the $G(r)$ data produced by STOG into $D(r)$ normalised to the sum of the scattering of all atomic pairs. RMCProfile[52] was used for big box analysis. The $G(r)$ and $F(Q)$ produced by STOG and the Bragg scattering data from bank 3 ($2\theta$ = 52.2461°) were used in the RMC refinement. The $G(r)$ data were fitted as $D(r)$.

### 4.2.4 SEM-EDX

SEM-EDX was performed on MSC018 and MSC025 [La$_8$R$_2$(GeO$_4$)$_6$O$_3$ (R = La, Bi); see Table 4.3] in order to confirm the composition of the main phase and the identity of any impurity phases. It was performed at the Research Complex at Harwell (RCaH) by James Gilchrist using a JEOL SEM 6610LV with an Oxford instruments EDS detector. The data were analysed using INCA software by Oxford Instruments. INCA reports weight percentage values calculated using a theoretical library of EDX spectra. The compositional data reported herein are values from INCA without any additional processing or calibration using standards; the accuracy of these compositions is therefore approximately to be ±10%. A small amount of both samples was attached to carbon paper and multiple scans were taken from different positions on different crystallites. Phase diagrams were created to determine the ratio of La : Ge and the ratio of La : Bi : Ge.

## 4.3 Results and Discussion

### 4.3.1 Long-range average structure

#### 4.3.1.1 La$_8$Sr$_2$(GeO$_4$)$_6$O$_2$

Analysis of the temperature-dependent behaviour of La$_8$Sr$_2$(GeO$_4$)$_6$O$_2$ (MSC022) was carried out using a combination of high resolution powder neutron diffraction from the HRPD instrument, at ISIS Neutron and Muon Source, and high resolution powder synchrotron diffraction from the I11 instrument at Diamond Light Source (DLS). An initial Rietveld refinement was performed using room temperature data and the $P6_3/m$ structure.[8] Figure 4.5 shows the thermal evolution of the cell parameters of this material.

The cell parameters follow a simple positive thermal expansion. The $a$ cell parameter shows essentially linear expansion, with a coefficient of $\alpha_a$ = 10.43(9) × 10$^{-6}$ K$^{-1}$ whilst the $c$ cell

parameter has $\alpha_c$ = 6.3(1) × 10$^{-6}$ K$^{-1}$, giving a volumetric thermal expansion coefficient of $\alpha_V$ = 27.4(3) × 10$^{-6}$ K$^{-1}$ over the temperature range of 303 – 1073 K (30 – 800 °C).
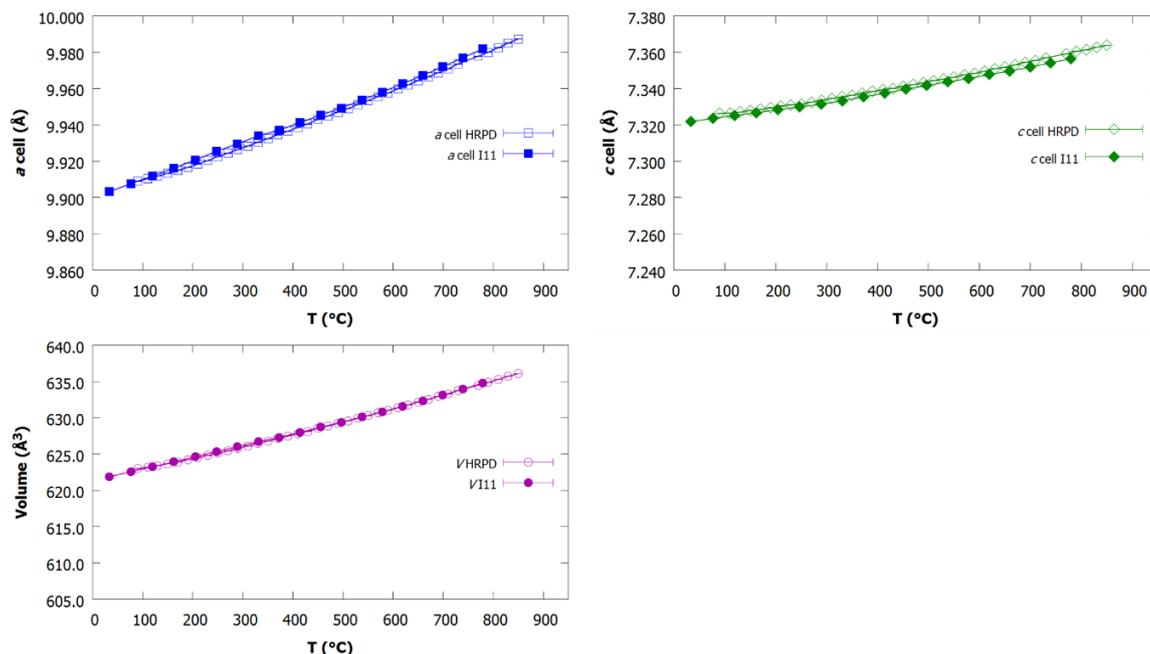


**Figure 4.5 –** The thermal evolution of the cell parameters of La$_8$Sr$_2$(GeO$_4$)$_6$O$_2$ obtained from a combination of high resolution powder neutron diffraction from HRPD and I11.

Combined neutron and synchrotron Rietveld refinements were performed using the long room temperature datasets. In the neutron datasets, vanadium was included as a phase in the refinement as some peaks arise due to the sample container. The data from HRPD included bank 1 and bank 2. The final refinement for each dataset is shown in Figure 4.6. A larger version of this figure is in Appendix A.

A strong asymmetry on the (0 0 $l$) peaks was noticeable in I11 data, but it is not visible in the lab X-ray data nor the HRPD data. An *hkl* dependent peak shape used to account for anisotropic strain[53] was included, but it did not fit the shoulders of these peaks. These broad shoulders were reported by Pramana *et al.*,[14] which led them to conclude that the actual symmetry is lowered to $P2_1/m$. A new approach was adopted in this work, where instead of a single apatite phase, a continuum of La$_{8+x}$Sr$_x$(GeO$_4$)$_6$O$_{2+x/2}$ ($x$ < 2) phases was introduced. The continuum was modelled by introducing six additional La$_{8+x}$Sr$_x$(GeO$_4$)$_6$O$_{2+x/2}$ ($x$ < 2) phases, whose cell parameters and La1/Sr1 and La2/Sr2 site occupancies were modelled with a simple linear equation following Vegard's law of $y$ = $mx + k$, where $y$ is the $a$ or $c$ cell parameter, $k$ was the $a$ or $c$ cell parameter of the main (La$_8$Sr$_2$(GeO$_4$)$_6$O$_2$) phase, $m$ is a refined gradient, which is positive for the $a$ cell and negative for the $c$ cell and $x$ is a fixed integer, such that for the main phase $x$ = 0 and the minor phases $x$ = 1 – 6.
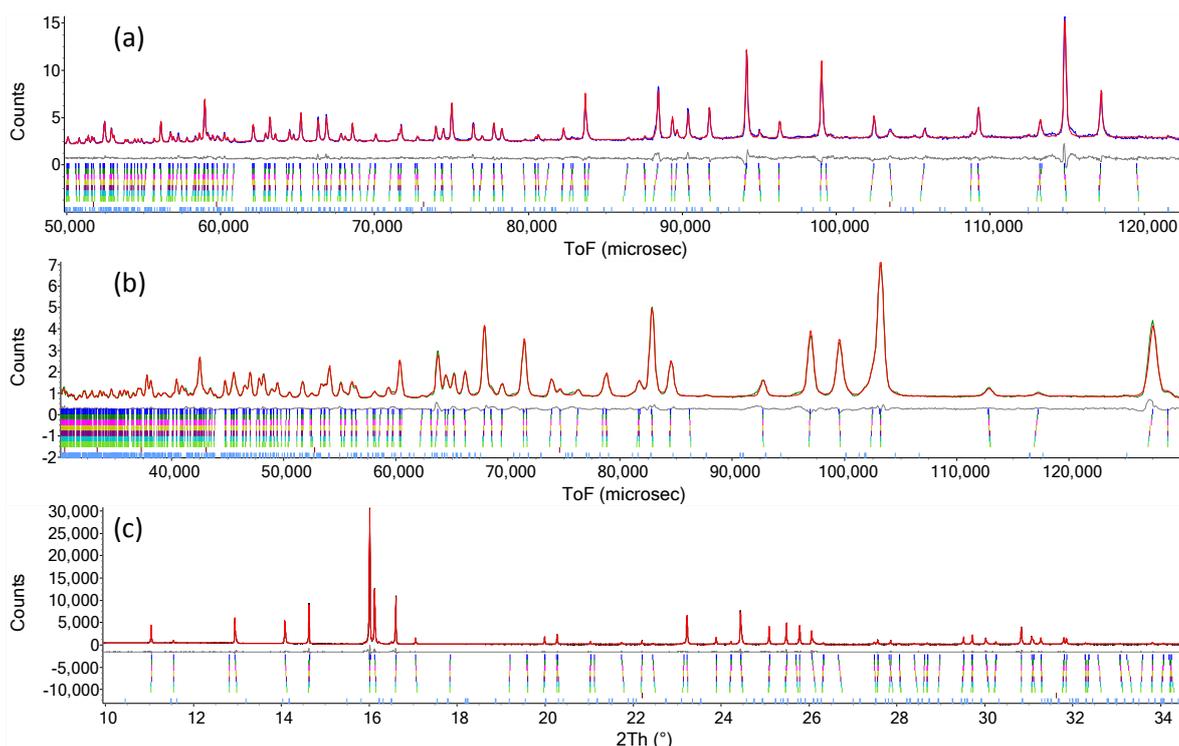
**Figure 4.6** – The combined Rietveld plots for La$_8$Sr$_2$(GeO$_4$)$_6$O$_2$ at room temperature; (a) HRPD bank 1, R$_{wp}$ = 2.567% and χ$^2$ = 1.960; (b) HRPD bank 2, R$_{wp}$ = 3.884% and χ$^2$ = 4.272; (c) I11, R$_{wp}$ = 8.394%; χ$^2$ = 1.888. The red curves represent the calculated patterns and the grey curves represent the difference between calculated and observed. Blue tick marks = reflections fit by La$_8$Sr$_2$(GeO$_4$)$_6$O$_2$; light blue tick marks = reflections fit by Sr$_2$(GeO$_4$); other tick marks = reflections fit by the continuum phases, La$_{8+x}$Sr$_{2-x}$(GeO$_4$)$_6$O$_{2+x/2}$.

In addition, the scale factors of the minor phases were also refined using a linear relationship, such that the higher the La content, the smaller the scale factor. The six-phase fit only adds ten parameters to the model. These phases have similar, but different cell parameters as the Sr content varies. All apatite phases, including the main phase, were fitted with a Stephens-type peak shape to describe anisotropic strain,[53] whilst the minor apatite phases were also fitted with a crystallite size and strain dependent peak shape. Figure 4.7 shows a close up of the I11 refinement, where the asymmetry of the peaks is more visible. A larger version of this figure is in Appendix A.
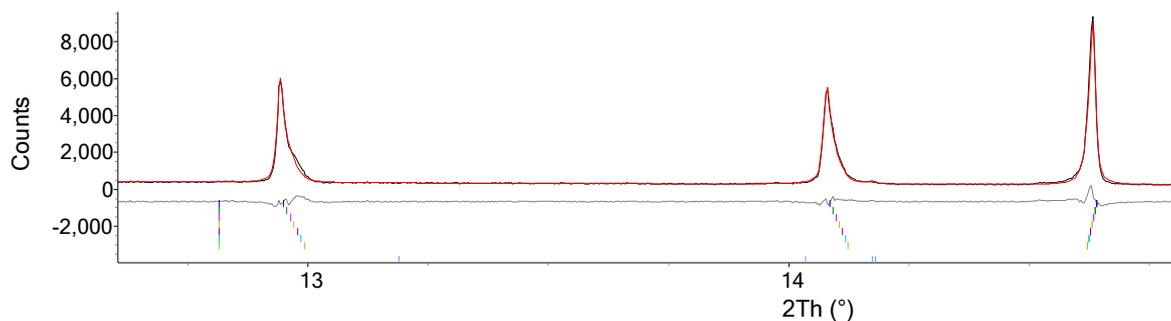
**Figure 4.7 –** Rietveld plot for La$_8$Sr$_2$(GeO$_4$)O$_2$ using I11 data, showing the asymmetry of the peaks. The left hand peak is the (002) reflection, where this is particularly noticeable.  Blue tick marks = reflections fit by La$_8$Sr$_2$(GeO$_4$)$_6$O$_2$; light blue tick marks = reflections fit by Sr$_2$(GeO$_4$); other tick marks = reflections fit by the continuum phases, La$_{8+x}$Sr$_{2-x}$(GeO$_4$)$_6$O$_{2+x/2}$.

 This approach resulted in a better fit of the shoulders and the final refinement indicated that the main phase was present with a weight percent of 85(1)%. The model is still approximate, however. Except for the La and Sr content, the structures of the continuum phases were the same as the main phase, which does not account for the fact that La$_{8+x}$Sr$_x$(GeO$_4$)$_6$O$_{2+x/2}$ ($x \geq 1$) phases have been reported to adopt $P$-1 symmetry at room temperature.[14] Furthermore, there is some Sr$_2$(GeO$_4$) present with a weight percentage of 1.32(7)%, which accounts for the lack of Sr in the apatite minor phases. Sr$_2$(GeO$_4$) was fitted with a Thompson-Cox-Hastings peak shape. The combined fit resulted in R$_{wp}$= 4.492% and $\chi^2$ = 2.119. The crystallographic parameters of the major apatite phase are given in Table 4.9 and the structure is shown in Figure 4.8.

**Table 4.9 – The crystallographic parameters of La$_8$Sr$_2$(GeO$_4$)$_6$O$_2$ at room temperature obtained from combined Rietveld refinement using I11 and HRPD data. Space group $P6_3/m$; cell parameters: $a$ = 9.90260(2) Å; $c$ = 7.32501(3) Å; $\alpha$ = 90°; $\gamma$ = 120°; $V$ = 622.067(3) Å$^3$.**

| Site label | Wyckoff site | $x$ | $y$ | $z$ | Occupancy | B (Å$^2$) |
|---|---|---|---|---|---|---|
| La1 | 4$f$ | $^1/_3$ | $^2/_3$ | 0.0011(2) | 0.576(5) | 0.58(1) |
| Sr1 | 4$f$ | $^1/_3$ | $^2/_3$ | 0.0011(2) | 0.424(5) | 0.58(1) |
| La2 | 6$h$ | 0.22991(6) | 0.98863(8) | $^1/_4$ | 0.949(3) | 0.175(8) |
| Sr2 | 6$h$ | 0.22991(6) | 0.98863(8) | $^1/_4$ | 0.051(3) | 0.175(8) |
| Ge1 | 6$h$ | 0.40012(8) | 0.37233(8) | $^1/_4$ | 1 | 0.00(1) |
| O1 | 6$h$ | 0.3132(2) | 0.4868(2) | $^1/_4$ | 1 | 0.52(3) |
| O2 | 6$h$ | 0.6043(2) | 0.4763(2) | $^1/_4$ | 1 | 0.50(3) |
| O3 | 12$i$ | 0.3390(1) | 0.2473(2) | 0.0630(1) | 1 | 1.12(2) |
| O4 | 2$a$ | 0 | 0 | $^1/_4$ | 1 | 1.35(6) |
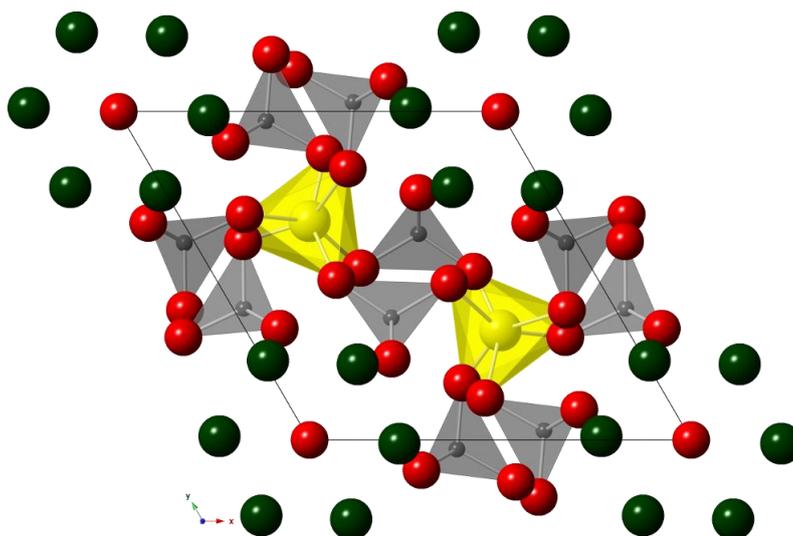
**Figure 4.8 –** The structure of $La_8Sr_2(GeO_4)_6O_2$ viewed down the $c$ axis. Yellow trigonal metaprisms = La1/Sr1O$_6$ units; grey tetrahedra = GeO$_4$; dark green spheres = La2/Sr2 atoms; red spheres = O atoms.

The twist angle was determined to be $\varphi$ = 23.086(4)°, which is smaller than that of fluoroapatite ($\varphi$ = 23.3)[1] and typical of $P6_3/m$ apatites. Whilst the shoulders on the (0 0 $l$) reflections were reported as being due to lower symmetry by Pramana *et al.*[14], Li *et al.*[18] have reported $La_8Sr_2(GeO_4)_6O_2$ as adopting $P6_3/m$ symmetry. There is a difference in the synthetic techniques employed between these two studies: Pramana *et al.*[14] heated at a maximum temperature of 1300 °C for 16 h, whilst Li *et al.*[18] heated at a maximum of 1350 °C for 16 h. In order to determine if additional heating would remove the minor apatite phases that were causing the shoulders on (0 0 $l$) reflections, a small amount of the same sample (MSC022) was further heated under three different conditions: 1100 °C for 168 h (MSC040); 1300 °C for 168 h (MSC041) and 1350 °C for 16 h. The samples were measured on I11 using the MAC detectors for 30 minutes at room temperature. The final Rietveld plots are shown in Figure 4.9.
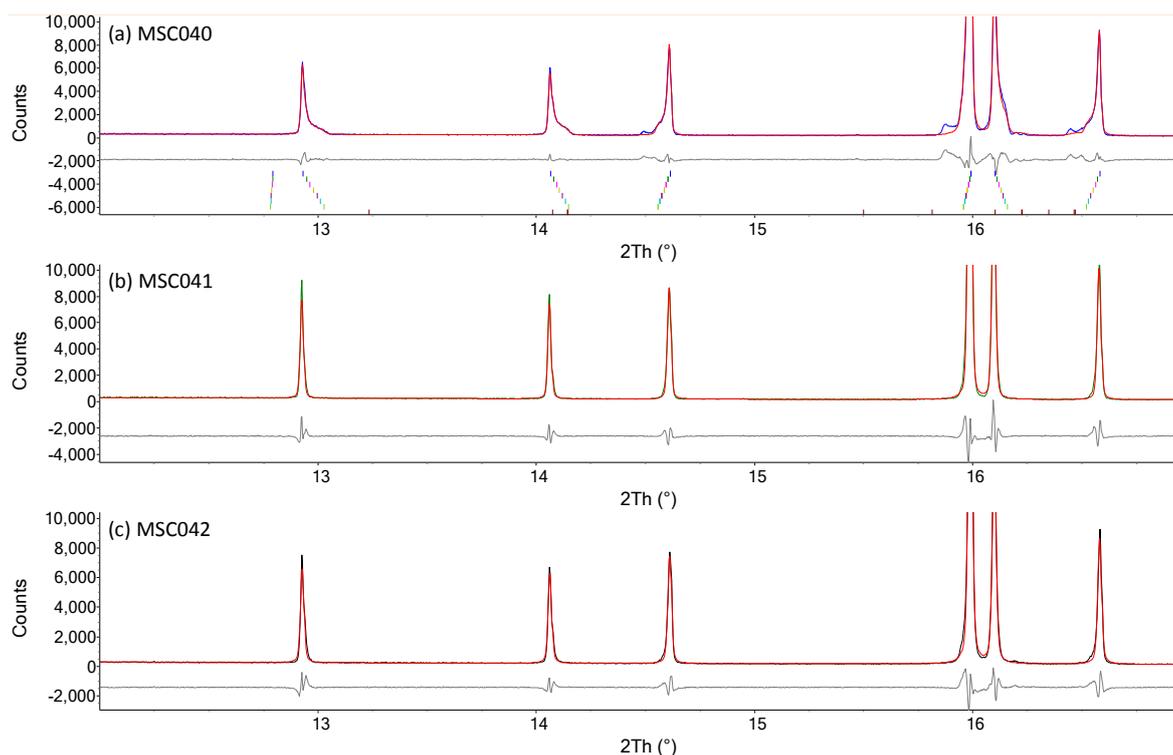
**Figure 4.9 –** The final Rietveld plots from La$_8$Sr$_2$(GeO$_4$)$_6$O$_2$ using I11 data after undergoing additional thermal treatment: (a) a further 1100 °C for 168 h (MSC040), R$_{wp}$ = 11.074%, $\chi^2$ = 2.412; (b) a further 1300 °C for 168 h (MSC041), R$_{wp}$ = 11.494%, $\chi^2$ = 2.603; (c) MSC022 + 1350 °C for 16 h, R$_{wp}$ = 11.547%, $\chi^2$ = 2.547. The tick marks represent the main phase and additional apatite phases and have been included in (a) to show the multi-phase refinement.

For MSC040, the same multi-phase model that was used for MSC022 was employed, with the main phase altered so that A1 occupancies are 50% La and 50% Sr and A2 occupancies are 100% La, which resulted in a much better fit. The Rietveld plot is shown in Figure 4.9a. There are some unaccounted for features at the shoulders of some peaks such as at $2\theta$ = 14.49°. For MSC041, the broad shoulders are no longer present and it was found a single phase of La$_8$Sr$_2$(GeO$_4$)$_6$O$_2$ was sufficient to fit the pattern, with no unaccounted for peaks. The starting model was that from Table 4.9. The same approach was applied to MSC042. The occupancies of the La2/Sr2 are 0.934(4)/0.066(4) for MSC041 and 0.941(4)/0.059(4) for MSC042; essentially the same as MSC022 (see Table 4.9). The atomic coordinates were all within 1 − 3σ of those from Table 4.9 in both MSC041 and MSC042. The results of these refinements confirm that the shoulders previously seen by Pramana *et al.*[14] correspond to a compositional range of La$_{8+x}$Sr$_x$(GeO$_4$)$_6$O$_{2+x/2}$ (0 < $x$ < 2) apatite phases caused by incomplete annealing, as opposed to La$_8$Sr$_2$(GeO$_4$)$_6$O$_2$ adopting $P2_1/m$ symmetry. They also show that these shoulders can be removed by heating at 1300 °C for a longer time period or at 1350 °C, so that a single phase of La$_8$Sr$_2$(GeO$_4$)$_6$O$_2$ is formed.

### *4.3.1.2 La$_{10}$(GeO$_4$)$_6$O$_3$*

Temperature-dependent behaviour of La$_{10}$(GeO$_4$)$_6$O$_3$ was investigated using both high resolution powder neutron diffraction and high resolution powder synchrotron diffraction. The starting model was based on the model for La$_8$Bi$_2$(GeO$_4$)$_6$O$_3$ as described by Tate *et al.*,[19] but with the A sites fully occupied by La. The cell parameters and isotropic ADPs for each atom type were refined and the *P*-1 space group was used. Figures 4.12a–e shows the thermal evolution of the cell parameters.

There is a clear convergence of the *a* and *b* cell parameters, $\alpha$, $\beta$ → 90° and γ → 120 at *T* ≈ 800 °C. This is similar to the observations of Abram *et al.*[21] and confirms that there is a phase transition to hexagonal symmetry.

The long-range, average structure was determined by using combined neutron and synchrotron Rietveld refinement. Initially, the interstitial oxide ion site was removed and the cell parameters, atomic coordinates and ADPs were determined. 8th-order spherical harmonic functions were used to model the *hkl*-dependent peak shape. After determining the average structure without excess oxygen, O$_{int}$ atoms were introduced near the six potential sites shown in Figure 4.11 with an occupancy of $^1/_{12}$ (Wyckoff sites = 2*i*). Table 4.10 gives the six sites and the corresponding labels used in this report, and Figure 4.11 illustrates the approximate positions in the apatite unit cell.
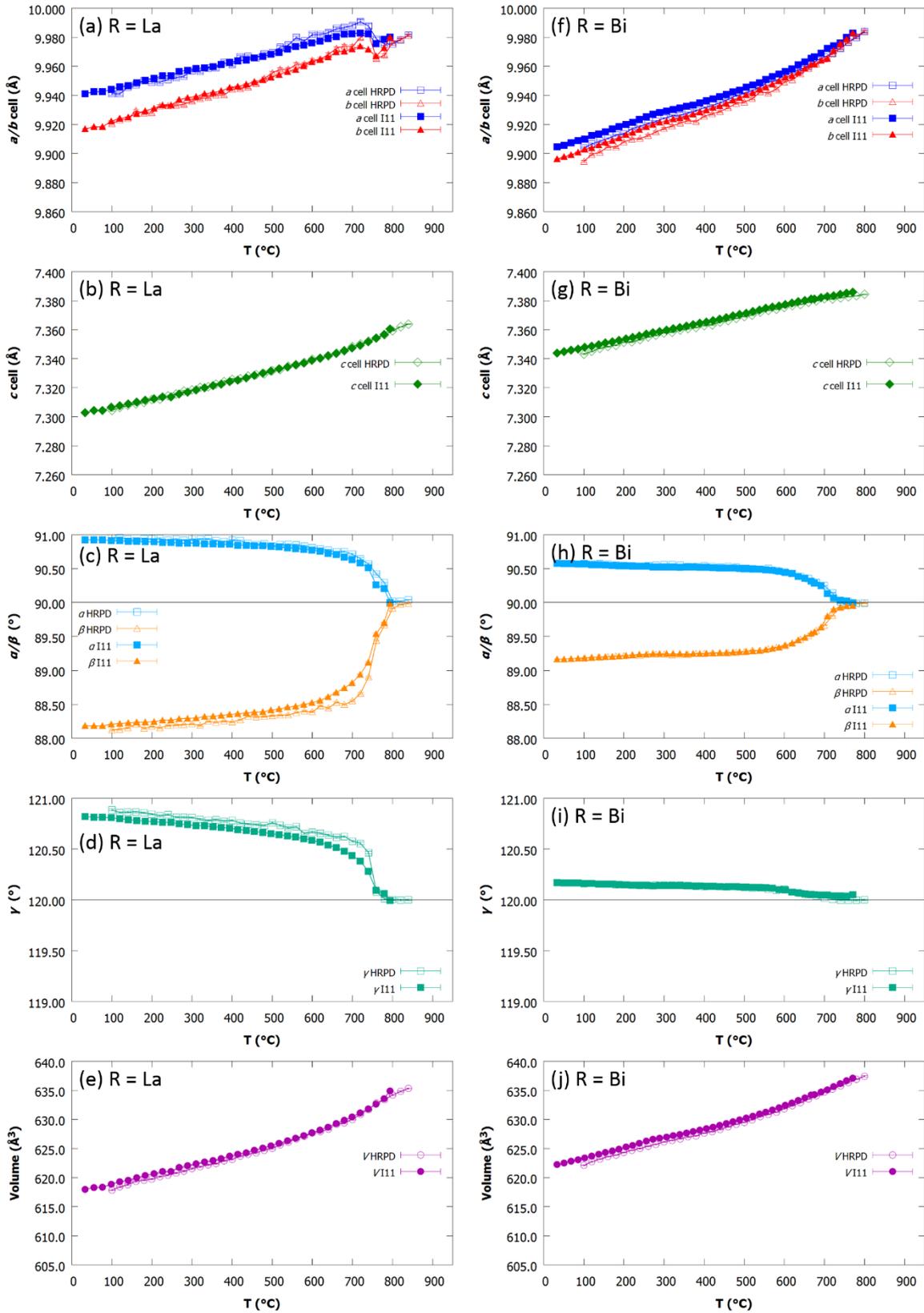
**Figure 4.10 –** The cell parameters and angles derived from variable temperature analysis of La$_8$R$_2$(GeO$_4$)$_6$O$_3$;

(a) – (e) R = La; (f) – (j) R = Bi.

**Table 4.10 – The approximate potential sites for the interstitial O in La$_8$Bi$_2$(GeO$_4$)$_6$O$_3$ and La$_{10}$(GeO$_4$)$_6$O$_3$ at room temperature.**

| Site label | Fractional coordinates | Wyckoff site |
|---|---|---|
| A | (½, 0, 0) | 1*d* |
| B | (0, ½, ½) | 1*g* |
| C | (½, 0, ½) | 1*f* |
| D | (0, ½, 0) | 1*c* |
| E | (½,½,½) | 1*h* |
| F | (½,½, 0) | 1*e* |
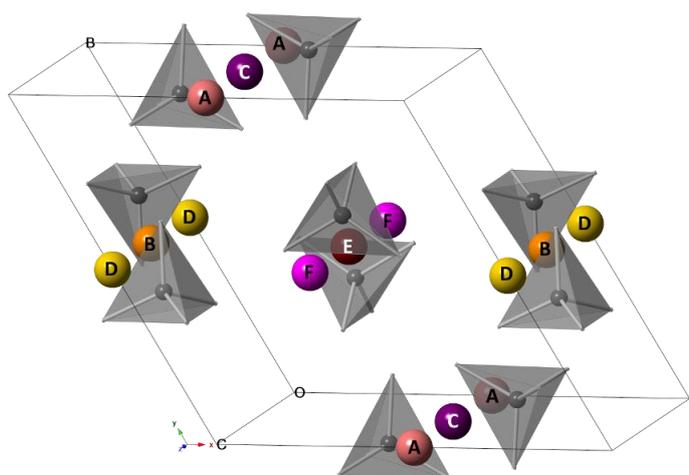


**Figure 4.11 –** The approximate location of the O$_{int}$ in the hexagonal lanthanum germanate apatite unit cell as found by high resolution powder neutron diffraction,[5, 8, 14, 19, 41] STEM,[19] single crystal X-ray diffraction,[38] and implied through IR spectroscopy[14] and Raman spectroscopy.[33, 38] The grey tetrahedra represent GeO$_4$ and are included to highlight their proximity to the O$_{int}$.

The O$_{int}$ occupancies and atomic coordinates were refined freely against neutron diffraction data. If the occupancies of an O$_{int}$ at a particular site reached 0, that site was removed from the refinement. La$_2$GeO$_5$ was also included as an impurity phase, corresponding to 0.81(1)% of the weight of the sample from the I11 refinement. The presence of La$_2$GeO$_5$ was also confirmed by SEM-EDX. This resulted in three sites being occupied with the following unconstrained occupancies: A = 0.12(1); B = 0.23(1) and D = 0.15(1), giving a total of 1.00(4) O$_{int}$ per unit cell. This matches the expected total oxygen content per unit cell (27 O per unit cell in total). The overall Rietveld plots are shown in Figure 4.13 and Appendix A. The combined fit gave values of R$_{wp}$ = 4.345%; $\chi^2$ = 2.860.

Previously, the B site has been reported as 100% occupied by Pramana *et al*.[5] The D site [(0, ½, 0)], which coordinates to the same GeO$_4$ tetrahedra as the B site [(0, ½, ½)], has also been modelled as being occupied in La$_9$Ba(GeO$_4$)$_6$O$_{2.5}$[33] with *P*1 symmetry, though their laboratory X-ray data suggested that the sample is hexagonal rather than triclinic. Furthermore, the F site [(½,½, 0)] has

been modelled as the only occupied site in $La_{9.68}Ge_6O_{26.52}$ with $P1$ symmetry.[38] The location of the $O_{int}$ ion found here is different from that reported for $La_{9.6}(GeO_4)_6O_{2.4}$ by Leon-Reina *et al.*,[11] where it was placed in the hexagonal channel periphery. Our results suggest that the position suggested by Leon-Reina *et al.* [11] is incorrect. The results are more in agreement with the structure proposed by Pramana *et al.*,[5] who also placed the $O_{int}$ position between two $GeO_4$ tetrahedra and at the B site, which was the most occupied site in this work. However, the analysis undertaken here is more robust, as the $O_{int}$ occupancies were refined at multiple sites, whilst Pramana *et al.*[5] constrained the $O_{int}$ occupancy to 0.5. Therefore, it is likely that the $O_{int}$ positions presented here are more accurate than the previous suggested model.[11] Table 4.11 gives the final crystallographic parameters from the room temperature combined refinement of $La_{10}(GeO_4)_6O_3$ and Figure 4.12 illustrates the average structure.
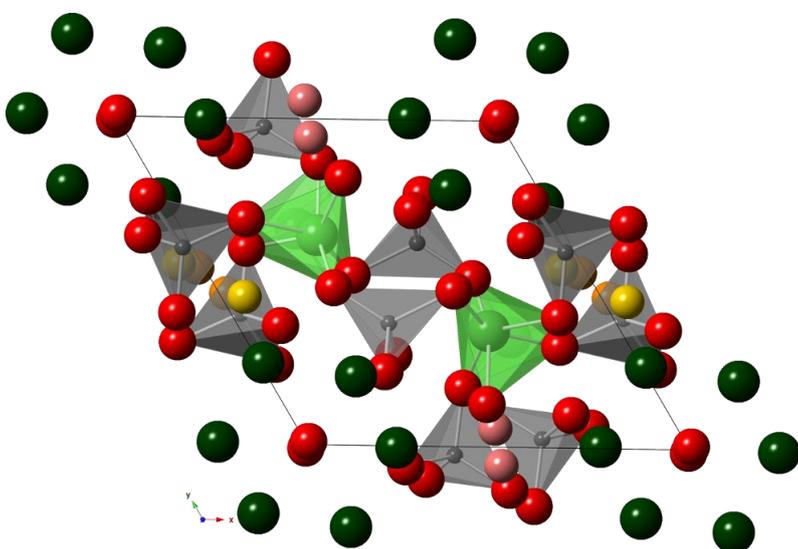


**Figure 4.12 –** The average structure of $La_{10}(GeO_4)_6O_3$ at room temperature viewed down the *c* axis. Light green trigonal metaprism = $La1O_6$; dark green spheres = La2; grey polyhedra = $GeO_4$; tetrahedra; red spheres = O1–O4; pink spheres = O5_A; orange spheres = O5_B; gold spheres = O5_D.

**Table 4.11 – Crystallographic parameters for La$_{10}$(GeO$_4$)$_6$O$_3$ at room temperature from combined Rietveld refinement using I11 and HRPD data. Space group $P$-1; cell parameters: $a$ = 9.9425(2) Å; $b$ = 9.9186(2) Å; $c$ = 7.30411(9) Å; $\alpha$ = 90.918(2)°; $\beta$ = 88.204(2)°; $\gamma$ = 120.82(1)°; $V$ = 618.28(2) Å$^3$.**

| Site label | Wyckoff site | $x$ | $y$ | $z$ | Occupancy | B (Å$^2$) |
|---|---|---|---|---|---|---|
| A1aLa | 2$i$ | 0.3016(7) | 0.6625(7) | 0.5015(8) | 1 | 0.7(1) |
| A1bLa | 2$i$ | 0.6526(7) | 0.3561(7) | 0.0022(9) | 1 | 0.7(1) |
| A2aLa | 2$i$ | 0.2309(7) | −0.0056(6) | 0.2487(8) | 1 | 0.4(1) |
| A2bLa | 2$i$ | 0.2336(9) | 0.2124(7) | 0.7714(8) | 1 | 0.4(1) |
| A2cLa | 2$i$ | 0.0104(7) | 0.2506(7) | 0.2597(9) | 1 | 0.4(1) |
| Ge1_1 | 2$i$ | 0.4008(7) | 0.3761(6) | 0.2756(9) | 1 | 0.9(1) |
| Ge1_2 | 2$i$ | 0.0255(7) | 0.3995(7) | 0.7599(8) | 1 | 0.9(1) |
| Ge1_3 | 2$i$ | 0.6275(7) | 0.0268(7) | 0.2451(8) | 1 | 0.9(1) |
| O1_1 | 2$i$ | 0.310(1) | 0.483(1) | 0.282(1) | 1 | 1.3(1) |
| O1_2 | 2$i$ | 0.816(1) | 0.3101(9) | 0.7930(1) | 1 | 1.3(1) |
| O1_3 | 2$i$ | 0.503(1) | 0.820(1) | 0.249(1) | 1 | 1.3(1) |
| O2_1 | 2$i$ | 0.622(1) | 0.478(1) | 0.297(1) | 1 | 1.3(1) |
| O2_2 | 2$i$ | 0.141(1) | 0.560(1) | 0.791(1) | 1 | 1.3(1) |
| O2_3 | 2$i$ | 0.536(1) | 0.131(1) | 0.236(1) | 1 | 1.3(1) |
| O3_1 | 2$i$ | 0.375(1) | 0.277(1) | 0.059(1) | 1 | 1.3(1) |
| O3_2 | 2$i$ | 0.039(1) | 0.245(1) | 0.603(1) | 1 | 1.3(1) |
| O3_3 | 2$i$ | 0.774(1) | 0.063(1) | 0.083(1) | 1 | 1.3(1) |
| O3_4 | 2$i$ | 0.684(1) | 0.773(1) | 0.551(1) | 1 | 1.3(1) |
| O3_5 | 2$i$ | 0.888(1) | 0.636(1) | 0.041(1) | 1 | 1.3(1) |
| O3_6 | 2$i$ | 0.260(1) | 0.899(1) | 0.556(1) | 1 | 1.3(1) |
| O4 | 2$i$ | 0.009(1) | 0.010(1) | 0.238(1) | 1 | 1.3(1) |
| O5_A | 2$i$ | 0.480(9) | −0.056(7) | 0.03(5) | 0.12(1) | 1.3(1) |
| O5_B | 2$i$ | 0.019(4) | 0.462(4) | 0.485(4) | 0.23(1) | 1.3(1) |
| O5_D | 2$i$ | 0.062(6) | 0.451(5) | 0.015(6) | 0.15(1) | 1.3(1) |

In triclinic apatites, there are two different metaprisms with three unique twist angles each, presented in Table 4.12. The twist angles for La$_{10}$(GeO$_4$)$_6$O$_3$ have values of  19.8 < $\varphi$ < 33.3°. The mean twist angle is $\varphi_{mean}$ = 24(5)°. This wide range of twist angles shows that La$_{10}$(GeO$_4$)$_6$O$_3$ is significantly distorted from the ideal apatite structure.
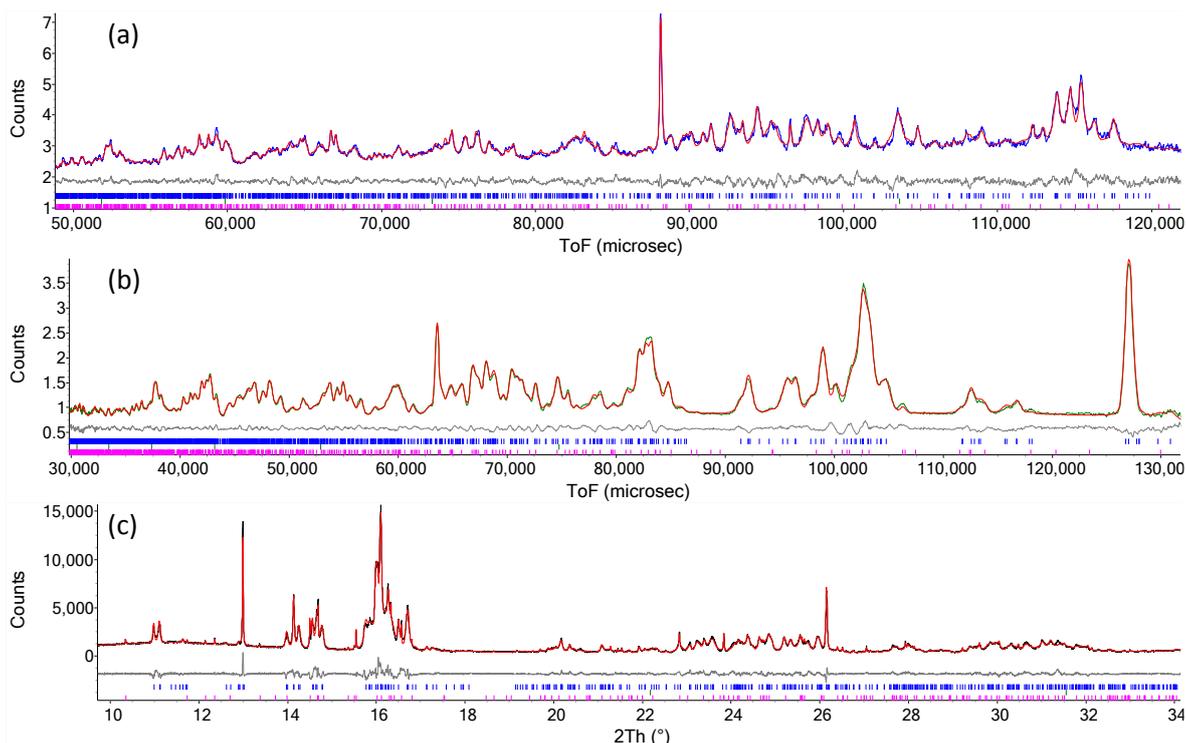
**Figure 4.13** – The combined Rietveld plots of La$_{10}$(GeO$_4$)$_6$O$_3$ from: (a) HRPD bank 1, R$_{wp}$ = 1.973%, χ$^2$ = 1.839; (b) HRPD bank 2, R$_{wp}$ = 2.273%, χ$^2$ = 3.509%; (c) I11 , R$_{wp}$ = 7.557%, χ$^2$ = 2.986. The blue tick marks represent reflections from La$_{10}$(GeO$_4$)$_6$O$_3$ and the pink represent the reflections from La$_2$GeO$_5$.

**Table 4.12** – The A1O$_6$ twist angles present in the *P*-1 La$_8$R$_2$(GeO$_4$)$_6$O$_3$ (R = La, Bi) apatites at room temperature.

| Sites | R = La $\varphi$ (°) | R = Bi $\varphi$ (°) |
|---|---|---|
| O1_1–A1a–O2_1 | 19.889(1) | 25.9054(7) |
| O1_2–A1a–O2_2 | 33.2653(5) | 21.022(8) |
| O1_3–A1a–O2_3 | 20.880(1) | 16.1479(6) |
| O1_1–A1b–O2_1 | 18.8459(9) | 27.4580(6) |
| O1_2–A1b–O2_2 | 23.4883(9) | 16.1585(9) |
| O1_3–A1b–O2_3 | 26.450(1) | 19.6621(6) |
| Mean | 24(5) | 21(4) |

Rietveld refinements were also performed using the high temperature data. As the highest temperature measured on I11 (800 °C) is different from that collected on HRPD and POLARIS (850 °C), I11 and HRPD data were not fitted simultaneously. Spherical harmonic functions were used to model the I11 peak shapes and La$_2$GeO$_5$ was included as a secondary phase, giving a fit with R$_{wp}$ = 14.443%, χ$^2$ = 3.986. This model was refined against HRPD data at 850 °C. The O$_{int}$ atom was introduced at the A site, as all six sites are equivalent in *P*6$_3$/*m* symmetry, with a fixed occupancy of $^1/_{12}$, but with coordinates refining freely. Distance restraints of 2.2 Å were applied to the O2/O3–O$_{int}$ (O$_{int}$ = O5; see Table 4.13) distances after initial refinements resulted in short O2/O3–

O$_{int}$ distances. Figure 4.14 shows the Rietveld plots for HRPD banks 1 and 2 and Table 4.13 gives
the crystallographic parameters produced by this fit. Appendix A shows an enlarged Rietveld plot.
The twist angle is $\varphi$ = 23.16(1)°, which is within the range of a hexagonal apatite defined by White
*et al.*[1]

**Table 4.13 – Crystallographic parameters for La$_{10}$ (GeO$_4$)$_6$O$_3$ at 850 °C from Rietveld refinement
using HRPD data. Space group $P6_3/m$; cell parameters: $a$ = 9.98442(7) Å; $c$ = 7.37265(8) Å; $\alpha$ =
90°; $\gamma$ = 120°; $V$ = 636.50(1) Å$^3$.**

| Site label | Wyckoff site | $x$ | $y$ | $z$ | Occupancy | B (Å$^2$) |
|---|---|---|---|---|---|---|
| La1 | 4$f$ | $^1/_3$ | $^2/_3$ | 0.0008(5) | 1 | 3.1(1) |
| La2 | 6$h$ | 0.2272(2) | 0.9869(3) | $^1/_4$ | 1 | 2.3(1) |
| Ge1 | 6$h$ | 0.4037(2) | 0.3755(2) | $^1/_4$ | 1 | 1.5(1) |
| O1 | 6$h$ | 0.3146(4) | 0.4863(4) | $^1/_4$ | 1 | 4.2(1) |
| O2 | 6$h$ | 0.6044(4) | 0.4727(4) | $^1/_4$ | 1 | 4.2(1) |
| O3 | 12$i$ | 0.3371(3) | 0.2483(3) | 0.0665(3) | 1 | 4.2(1) |
| O4 | 2$a$ | 0 | 0 | $^1/_4$ | 1 | 4.2(1) |
| O5 | 12$i$ | 0.441(3) | −0.039(3) | −0.037(4) | $^1/_{12}$ | 4.2(1) |
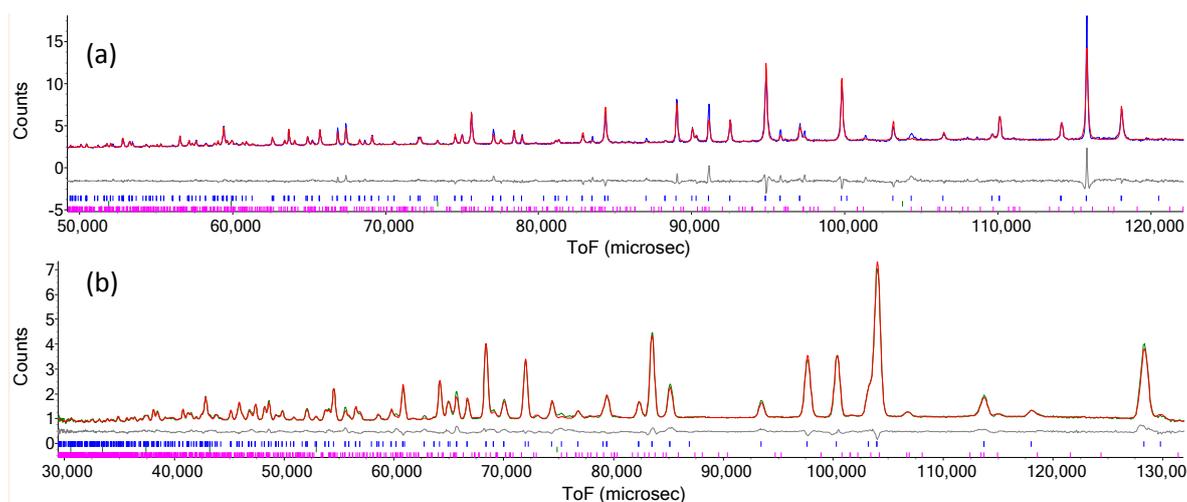


**Figure 4.14 –** The Rietveld plots of La$_{10}$(GeO$_4$)$_6$O$_3$ at 850 °C using HRPD data. (a) bank 1, R$_{wp}$ = 2.679%, $\chi^2$ =
2.417 ; (b) bank 2, R$_{wp}$ = 3.166%, $\chi^2$ = 4.879. The blue tick marks represent reflections arising from
La$_{10}$(GeO$_4$)$_6$O$_3$ and pink represent reflections arising from La$_2$GeO$_5$.

### 4.3.1.3 La$_8$Bi$_2$(GeO$_4$)$_6$O$_3$

Structural analysis of the temperature dependent behaviour of La$_8$Bi$_2$(GeO$_4$) using HRPD and I11
data was carried out. The model obtained by Tate *et al.*[19] was used as the starting point. The cell
parameters and ADPs were allowed to refine and $P$-1 symmetry was used throughout the
refinement. Figure 4.12a–e (shown earlier) shows the thermal evolution of the cell parameters. As
in La$_{10}$(GeO$_4$)$_6$O$_3$, the cell parameters converge to hexagonal cell metrics, which was also found by

Tate *et al.*[19] The transformation begins at $T \approx 700$ °C and is complete at $T \approx 780$ °C. It can be seen from Figure 4.12a–e that the cell parameters are closer to the hexagonal cell metrics prior to the phase transition than those of La$_{10}$(GeO$_4$)$_6$O$_3$. It is possible that this results in a lower phase transition temperature ($T \approx 780$ °C compared to 800 °C). This may also be induced by the additional disorder from the Bi$^{3+}$ that are present on the A sites.

SEM-EDX identified that there is La$_2$Ge$_2$O$_7$ present. It also suggested an additional phase with an approximate La : Ge ratio of 1 : 4 with very little Bi present. There are unaccounted for peaks that are visible in the I11 dataset, highlighted with black arrows in Figure 4.16, but there were not enough peaks to warrant indexing. There are no known phases with a La : Ge ratio of that magnitude; the highest ratio is 1 : 1 in the La$_2$Ge$_2$O$_7$ phase. Thus, the phase giving rise to the unaccounted for peaks has not been identified.

For the combined X-ray and neutron Rietveld refinement, a similar approach to that used for La$_{10}$(GeO$_4$)$_6$O$_3$ was employed. The refinement started with the model reported by Tate *et al.*,[19] but the O$_{int}$ atoms were removed at first. The I11 data was used to determine the cation distribution, with the occupancies restrained so that the total La and Bi content matched the expected stoichiometry and the overall A site occupancy constrained to 1.0. This resulted in a fractional occupancy of Bi on the A1a site of 0.13(2), which corresponds to 0.25(3) atoms per unit cell. A refinement was also performed against the I11 data where the A1a site was constrained to full La occupancy and A2 sites were constrained to 2/3 La and 1/3 Bi, which gave R$_{wp}$ = 8.372%, similar in magnitude to the R$_{wp}$ obtained when Bi was allowed on the A1a site (8.329%). It is seems likely that Bi is only present on the A2 sites, as it has been previously found to solely occupy that site both experimentally and with computational studies,[19, 47-48] as well as in the 800 °C structure in this work (discussed below). This model was therefore adopted.

After determining the average structure without the O$_{int}$ atoms, they were introduced near the six potential sites in Figure 4.11 and Table 4.10 with occupancies of $^1/_{12}$ and the same process as with La$_{10}$(GeO$_4$)$_6$O$_3$ was applied. This again resulted with O$_{int}$ only occupying the A, B and D sites, with occupancies of A = 0.16(2); B = 0.14(2); D = 0.09(2), adding up to a total of 0.78(5) O$_{int}$ per unit cell. A scale factor was applied so that O$_{int}$ = 1.0 per formula unit, resulting in A = 0.21(2); B = 0.18(2); D = 0.12(2). The introduction of this scale factor only altered the goodness of fit from $\chi^2$ = 3.224 to $\chi^2$ = 3.228, demonstrating that the quality of fit is not very sensitive to total O$_{int}$ occupancy. We use the fact that we obtained a "perfect" total oxygen content for La$_{10}$(GeO$_4$)$_6$O$_3$ as justification for this chemically sensible model. The final fit with neutron and synchrotron X-ray data gave R$_{wp}$ = 3.851% and $\chi^2$ = 2.288. The crystallographic parameters of this model are provided

in Table 4.14 and the average structure at room temperature is shown in Figure 4.15. The Rietveld plots are presented in Figure 4.16. The Rietveld plots are also presented in Appendix A.
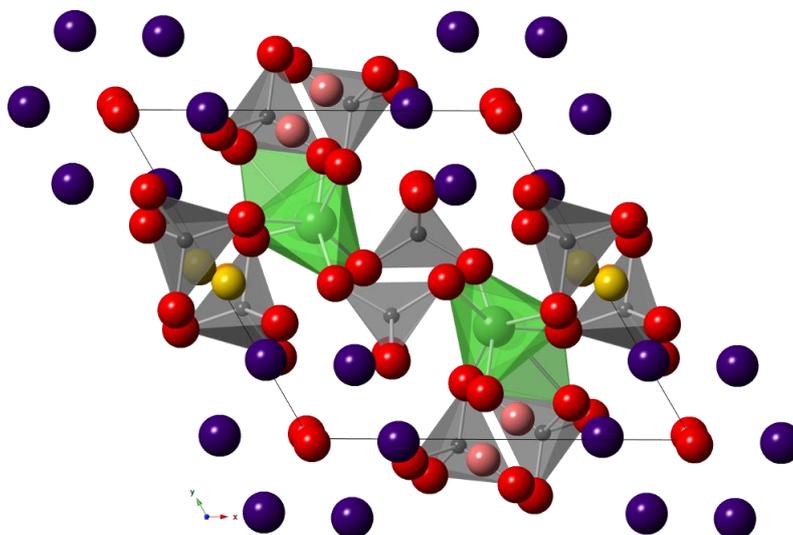


**Figure 4.15 –** The average room temperature structure of $La_8Bi_2(GeO_4)_6O_3$ viewed down the $c$ axis. Green metaprisms = La1/Bi1$O_6$; purple spheres = La2/Bi2; grey polyhedra = GeO$_4$ tetrahedra; red spheres = O1–O4; pink spheres = O5_A; orange spheres = O5_B; gold spheres = O5_D.

Although the same $O_{int}$ sites as found in $La_{10}(GeO_4)_6O_3$ are occupied, the values of the occupancies are different. The occupied $O_{int}$ sites are also different from those previously reported in the literature.[5, 8, 11, 19, 33] Tate *et al*.[19] reported that whilst the F site was the most occupied site, the A site was found to have the second highest nuclear density in a Fourier map from powder neutron diffraction and the STEM results agreed. In this work, the B and D sites were occupied and the A site was the most occupied, whilst the E and F sites were unoccupied. Whilst different sites are occupied, both models show that multiple sites are occupied simultaneously rather than only one out of the six potential $O_{int}$ sites (see Table 4.10).

The apatite twist angles are given in Table 4.12., which fall in the range of 16.0 < $\varphi$ < 27.5°. The mean is $\varphi$ = 21(4). It smaller than that obtained for $La_{10}(GeO_4)_6O_3$, $\varphi$ = 24(5). The smaller range of twist angles for $La_8Bi_2(GeO_4)_6O_3$ may indicate that it is less distorted from the ideal hexagonal apatite structure than $La_{10}(GeO_4)_6O_3$.
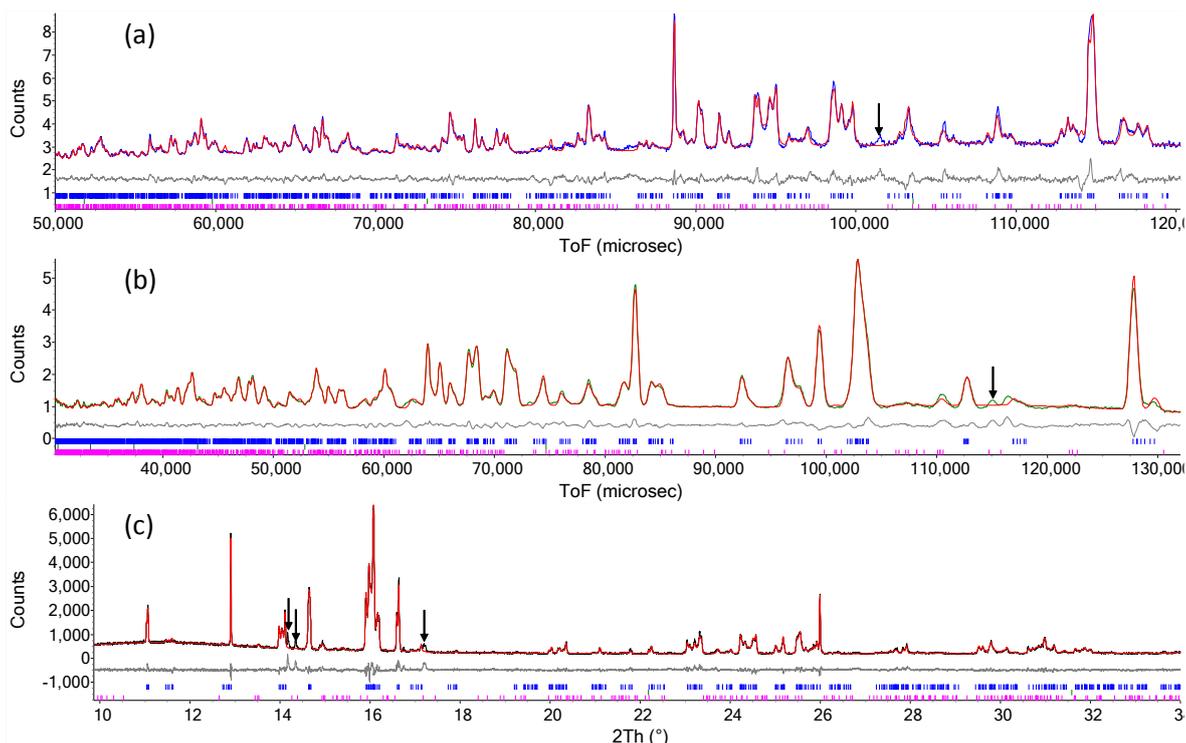
**Figure 4.16 –** The combined Rietveld plots of $La_8Bi_2(GeO_4)_6O_3$ from: (a) HRPD bank 1, $R_{wp}$ = 2.291%, $\chi^2$ = 2.233; (b) HRPD bank 2, $R_{wp}$ = 2.983%, $\chi^2$ = 4.808; (c) I11, $R_{wp}$ = 8.407%, $\chi^2$ = 1.955. The blue tick marks represent reflections from $La_8Bi_2(GeO_4)_6O_3$ and the pink represent the reflections from $La_2Ge_2O_7$. The black arrows highlight the unaccounted for peaks.

For the high-temperature hexagonal phase the same process used for $La_{10}(GeO_4)_6O_3$ was applied. When the La and Bi occupancies were freely refined, it resulted in a Bi1 occupancy of almost zero and a Bi2 occupancy of almost 1/3, so the Bi1 site was removed and the Bi2 occupancy fixed to $^1/_3$ and La2 at $^2/_3$. The $O_{int}$ position from $La_{10}(GeO_4)_6O_3$ with an occupancy of $^1/_{12}$ was added and its position was refined. The final refinement gave overall values of $R_{wp}$ = 3.352%, $\chi^2$ = 4.051. Table 4.15 gives the crystallographic parameters of this refinement and Figure 4.17 gives the Rietveld plots, which are also in Appendix A. The single twist angle obtained is $\varphi$ = 23.44(1)°. This is similar to the twist angle obtained for $La_{10}(GeO_4)_6O_3$ at 850 °C ($\varphi$ = 23.16(1)°) and the twist angle obtained for $La_8Sr_2(GeO_4)_6O_2$ at room temperature ($\varphi$ = 23.086(4)°), indicating that the high temperature structures are similar.

**Table 4.14 – Crystallographic parameters for La$_8$Bi$_2$(GeO$_4$)$_6$O$_3$ at room temperature from combined Rietveld refinement using I11 and HRPD data. Space group *P*-1; cell parameters: *a* = 9.9044(1) Å; *b* = 9.8965(1) Å; *c* = 7.344230(7) Å; *α* = 90.570(1)°; *β* = 89.1719(7)°; *γ* = 120.1707(6)°; *V* = 622.29(2) Å³.**

| Site label | Wyckoff site | *x* | *y* | *z* | Occupancy | B (Å²) |
|---|---|---|---|---|---|---|
| A1aLa | 2*i* | 0.3185(5) | 0.6648(6) | 0.4976(5) | 1 | 1.54(8) |
| A1bLa | 2*i* | 0.6541(5) | 0.3430(6) | 0.0012(4) | 1 | 1.54(8) |
| A2aLa | 2*i* | 0.2292(4) | −0.0087(4) | 0.2563(4) | $^2/_3$ | 1.99(7) |
| A2aBi | 2*i* | 0.2292(4) | −0.0087(4) | 0.2563(4) | $^1/_3$ | 1.99(7) |
| A2bLa | 2*i* | 0.2310(4) | 0.2251(4) | 0.7611(4) | $^2/_3$ | 1.99(7) |
| A2bBi | 2*i* | 0.2310(4) | 0.2251(4) | 0.7611(4) | $^1/_3$ | 1.99(7) |
| A2cLa | 2*i* | 0.0075(4) | 0.2403(4) | 0.2590(4) | $^2/_3$ | 1.99(7) |
| A2cBi | 2*i* | 0.0075(4) | 0.2403(4) | 0.2590(4) | $^1/_3$ | 1.99(7) |
| Ge1_1 | 2*i* | 0.4025(5) | 0.375(4) | 0.2544(6) | 1 | 0.81(7) |
| Ge1_2 | 2*i* | 0.0232(5) | 0.3965(5) | 0.7556(6) | 1 | 0.81(7) |
| Ge1_3 | 2*i* | 0.6197(4) | 0.0200(4) | 0.2515(5) | 1 | 0.81(7) |
| O1_1 | 2*i* | 0.3047(6) | 0.4736(6) | 0.2751(8) | 1 | 1.73(7) |
| O1_2 | 2*i* | 0.831(1) | 0.3321(9) | 0.791(1) | 1 | 1.73(7) |
| O1_3 | 2*i* | 0.5024(7) | 0.8288(6) | 0.2431(8) | 1 | 1.73(7) |
| O2_1 | 2*i* | 0.5977(8) | 0.4789(8) | 0.286(1) | 1 | 1.73(7) |
| O2_2 | 2*i* | 0.1528(7) | 0.6093(7) | 0.7671(8) | 1 | 1.73(7) |
| O2_3 | 2*i* | 0.5285(7) | 0.1386(6) | 0.2392(8) | 1 | 1.73(7) |
| O3_1 | 2*i* | 0.3401(9) | 0.2561(9) | 0.065(1) | 1 | 1.73(7) |
| O3_2 | 2*i* | 0.0435(9) | 0.2489(9) | 0.623(1) | 1 | 1.73(7) |
| O3_3 | 2*i* | 0.7702(8) | 0.0685(9) | 0.0827(9) | 1 | 1.73(7) |
| O3_4 | 2*i* | 0.6652(7) | 0.7629(7) | 0.5648(8) | 1 | 1.73(7) |
| O3_5 | 2*i* | 0.9017(8) | 0.6489(8) | 0.0514(9) | 1 | 1.73(7) |
| O3_6 | 2*i* | 0.259(1) | 0.889(1) | 0.561(1) | 1 | 1.73(7) |
| O4 | 2*i* | −0.0003(9) | −0.015(1) | 0.3134(6) | 1 | 1.73(7) |
| O5_A | 2*i* | 0.424(6) | −0.062(5) | 0.013(7) | 0.21(2) | 1.73(7) |
| O5_B | 2*i* | 0.029(7) | 0482(9) | 0.50(1) | 0.18(2) | 1.73(7) |
| O5_D | 2*i* | 0.03(1) | 0.47(1) | −0.01(1) | 0.12(2) | 1.73(7) |

**Table 4.15 – Crystallographic parameters for La$_8$Bi$_2$(GeO$_4$)$_6$O$_3$ at 800 °C from Rietveld refinement using HRPD data. Space group $P6_3/m$; cell parameters: $a$ = 9.99002(7) Å; $c$ = 7.38645(8) Å; $\alpha$ = 90°; $\gamma$ = 120°; $V$ = 638.41(1) Å$^3$.**

| Site label | Wyckoff site | $x$ | $y$ | $z$ | Occupancy | B (Å$^2$) |
|---|---|---|---|---|---|---|
| La1 | 4$f$ | $^1/_3$ | $^2/_3$ | 0.0021(5) | 1 | 2.6(2) |
| La2 | 6$h$ | 0.2266(3) | 0.9920(4) | $^1/_4$ | $^2/_3$ | 3.3(1) |
| Bi2 | 6$h$ | 0.2266(3) | 0.9920(4) | $^1/_4$ | $^1/_3$ | 3.3(1) |
| Ge1 | 6$h$ | 0.4019(3) | 0.3754(2) | $^1/_4$ | 1 | 1.7(1) |
| O1 | 6$h$ | 0.3184(5) | 0.4890(4) | $^1/_4$ | 1 | 4.4(1) |
| O2 | 6$h$ | 0.5990(4) | 0.4688(5) | $^1/_4$ | 1 | 4.4(1) |
| O3 | 12$i$ | 0.3389(3) | 0.2493(3) | 0.0706(3) | 1 | 4.4(1) |
| O4 | 2$a$ | 0 | 0 | $^1/_4$ | 1 | 4.4(1) |
| O5 | 12$i$ | 0.500(5) | −0.034(4) | 0.035(4) | $^1/_{12}$ | 4.4(1) |
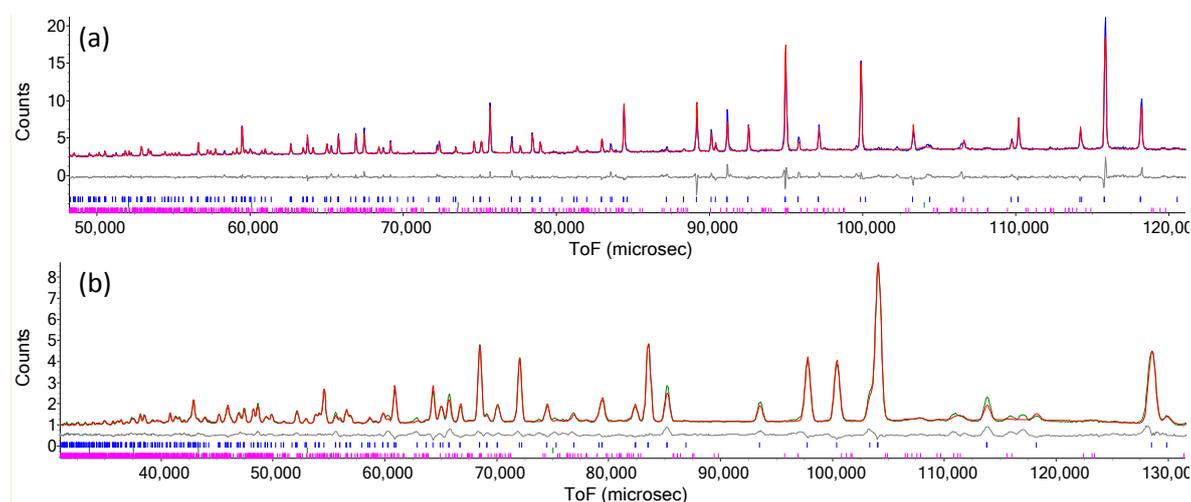


**Figure 4.17 –** The Rietveld plots of La$_8$Bi$_2$(GeO$_4$)$_6$O$_3$ at 850 °C using HRPD data. (a) Bank 1, R$_{wp}$ = 2.677%, $\chi^2$ = 2.639 ; (b) bank 2, R$_{wp}$ = 3.844%, $\chi^2$ = 6.231. The blue tick marks represent reflections arising from La$_8$Bi$_2$(GeO$_4$)$_6$O$_3$ and pink represent reflections arising from La$_2$Ge$_2$O$_7$.

## 4.3.2 Local structure of La$_8$R$_2$(GeO$_4$)$_6$O$_{3-y}$ (R = Sr, La, Bi)

### 4.3.2.1 Starting configurations

[5 5 4] supercells were produced for all materials using the data2config program. Where appropriate, RMCProfile was used to produce fully randomised configurations of A site cations and O$_{int}$ atoms by performing preliminary RMC runs without data and just atom site swapping. For La$_8$Sr$_2$(GeO$_4$)$_6$O$_2$, the La1 and Sr1 atoms were allowed to swap with each other but did not swap with La2 or Sr2 atoms. This starting configuration is referred to as La$_8$Sr$_2$(GeO$_4$)$_6$O$_2$ **SC1**. The supercell used has cell parameters $a$ = $b$ = 49.513 Å, $c$ = 29.300 Å, $\alpha$ = $\beta$ = 90° and $\gamma$ = 120°.

For La$_8$R$_2$(GeO$_4$)$_6$O$_3$ (R = La, Bi), the O$_{int}$ atoms are of particular interest. O$_{int}$ atoms were labelled as 'Te' for convenience, as the neutron scattering length of Te is essentially identical to O ($b_O$ = 5.803

fm; $b_{Te}$ = 5.80 fm). Dummy 'Va' atoms were also introduced on the same crystallographic sites as the $O_{int}$ atoms in order to model the vacant potential $O_{int}$ sites within RMCProfile. These atoms have no scattering, and are therefore not constrained by data, so they were not allowed to move. Due to the close proximity of the $O_{int}$ atoms to a crystallographic inversion centre, there exists the possibility of two $O_{int}$ atoms starting at unphysically small distances from each other. In order to prevent this in the starting configurations, a minimum distance constraint was applied to the 'Te'– 'Te' pairs of > 1.57 Å, which prevents two adjacent sites from being occupied simultaneously. 'Te' atoms were then swapped with the 'Va' atoms in order to model partially occupied crystallographic sites. There are 100 $O_{int}$ atoms in a [5 5 4] supercell and an additional 500 or 1100 dummy 'Va' atoms depending on whether the three $O_{int}$ sites found to be occupied by diffraction were included, or whether all six sites were permitted. This gives a total of 4800 or 5400 atoms per supercell, including the dummy 'Va' atoms.

For $La_{10}(GeO_4)_6O_3$, various $O_{int}$ starting configurations were produced to model room temperature and 850 °C data. These are summarised in Table 4.16. For the potential $O_{int}$ at sites C, E and F, the coordinates were chosen by selecting the last coordinates before they were removed from the Rietveld refinement. Starting configurations **SC1–SC4** all had cell parameters $a$ = 49.721733 Å; $b$ = 49.593200 Å; $c$ = 29.216440 Å; $\alpha$ = 90.01827°; $\beta$ = 88.204821°; $\gamma$ = 120.837054°. For **SC5**, a high temperature starting configuration, the 'Te' atoms were swapped with 'Va' atoms in order to obtain a truly random configuration as all sites (A – F) are symmetry equivalent in $P6_3/m$. **SC5–SC7** have cell parameters $a$ = $b$ = 49.922050 Å, $c$ = 29.490600 Å, $\alpha$ = $\beta$ = 90°, $\gamma$ = 120°.

**Table 4.16 – The number of different O$_{int}$ atoms on different sites within the multiple [5 5 4] supercell starting configurations (SC) and temperatures ($T$) used for total scattering analysis of La$_{10}$(GeO$_4$)$_6$O$_3$ (dummy 'Va' atoms are included in the total).**

| $T$ (°C) | Name | A | B | C | D | E | F | Total Atoms | Notes |
|---|---|---|---|---|---|---|---|---|---|
| 18 | SC1 | 24 | 45 | | 31 | | | 4800 | Only 3 O$_{int}$ sites available, occupancies based on the crystallographic occupancies. |
| 18 | SC2 | 33 | 33 | | 33 | | | 4800 | Only 3 O$_{int}$ sites that are occupied in the crystallographic model, all equally occupied. |
| 18 | SC3 | 24 | 45 | 0 | 31 | 0 | 0 | 5400 | All 6 O$_{int}$ sites available, occupancies based on the crystallographic occupancies. |
| 18 | SC4 | 17 | 17 | 17 | 17 | 16 | 16 | 5400 | All 6 O$_{int}$ sites equally occupied. |
| 850 | SC5 | 14 | 14 | 19 | 22 | 17 | 14 | 5400 | O$_{int}$ randomised with no discrimination between sites. |
| 850 | SC6 | 24 | 45 | 0 | 31 | 0 | 0 | 5400 | Uses atomic configuration of SC3 and cell parameters of SC5. |
| 850 | SC7 | 17 | 17 | 17 | 17 | 16 | 16 | 5400 | Uses atomic configuration of SC4 and cell parameters of SC5. |

For La$_8$Bi$_2$(GeO$_4$)$_6$O$_3$, a similar procedure was performed, creating analogous models (Table 4.17). Additionally, the Bi and La sites were randomised for room temperature analysis, where Bi2 swapped with La2; for the 800 °C analysis the random placement from data2config was deemed sufficient. The cell parameters for **SC1–SC4** are: $a$ = 49.524389 Å; $b$ = 49.482550 Å; $c$ = 29.377200 Å; $\alpha$ = 90.569480°; $\beta$ = 89.171919°; $\gamma$ = 120.175356°. The cell parameters for **SC5–SC7** are: $a$ = $b$ = 49.950100 Å; $c$ = 29.545800 Å; $\alpha$ = $\beta$ = 90°; $\gamma$ = 120°.

**Table 4.17 The number of different O$_{int}$ atoms on different sites within the multiple [5 5 4] supercell starting configurations used for total scattering analysis of La$_8$Bi$_2$(GeO$_4$)$_6$O$_3$.**

| $T$ (°C) | Name | A | B | C | D | E | F | Total Atoms | Notes |
|---|---|---|---|---|---|---|---|---|---|
| 18 | SC1 | 41 | 35 |  | 24 |  |  | 4800 | Only 3 O$_{int}$ sites available, occupancies based on the crystallographic occupancies. |
| 18 | SC2 | 33 | 33 |  | 33 |  |  | 4800 | Only 3 O$_{int}$ sites that are occupied in the crystallographic model, all equally occupied. |
| 18 | SC3 | 41 | 35 | 0 | 24 | 0 | 0 | 5400 | All 6 O$_{int}$ sites available, occupancies based on the crystallographic occupancies. |
| 18 | SC4 | 17 | 17 | 17 | 17 | 16 | 16 | 5400 | All 6 O$_{int}$ sites equally occupied. |
| 800 | SC5 | 15 | 17 | 20 | 17 | 18 | 13 | 5400 | O$_{int}$ randomised with no discrimination between sites. |
| 800 | SC6 | 41 | 35 | 0 | 24 | 0 | 0 | 5400 | Uses atomic configuration of SC3 and cell parameters of SC5. |
| 800 | SC7 | 17 | 17 | 17 | 17 | 16 | 16 | 5400 | Uses atomic configuration of SC4 and cell parameters of SC5. |

### *4.3.2.2 Refinement methodology*

The RMCProfile algorithm allows many refinement parameters to be tuned, including dataset weightings, distance constraints, atom swapping, maximum moves and bond valence sum (BVS) weightings. The appropriate weightings for each dataset were tested with La$_8$Sr$_2$(GeO$_4$)$_6$O$_2$ and it was determined that a weighting ratio for the PDF : $F$(Q) : Bragg of 0.01 : 0.02 : 0.02 was sensible. This means that the PDF data are weighted twice as heavily as the $F$(Q) and Bragg data. This resulted in the lowest $\chi^2_{dof}$ for the same refinement time. This weighting puts more of an emphasis on the local structure, which is the primary purpose of this investigation. The same weighting ratio was applied in all successive refinements for all three samples.

For La$_8$Sr$_2$(GeO$_4$)$_6$O$_2$, distance window constraints were applied to all refinements in order to maintain chemically sensible atom distances; these are given in Table 4.18. Two methodologies (procedures **P1** and **P2**) were explored with La/Sr site swapping either allowed or disallowed as discussed below. For La$_{10}$(GeO$_4$)$_6$O$_3$, multiple refinement procedures were explored at room temperature, which ultimately resulted in procedure **P1**. This consists of the minimum distances in Table 4.19, a refinement time of 15 h and allowed swapping between 'Va' atoms and 'Te' atoms with a probability of 20% of moves. BVS restraints were also applied, which are given in Table 4.20. The weightings applied to the BVS are very small and do not heavily influence the refinement. The weightings applied to each pair in the BVS restraints are given in Table 4.21. The 'Te' O$_{int}$ atoms were given the same constraints and BVS restraints as the O atoms.

**Table 4.18 – The distance window constraints applied in RMC refinements of La$_8$Sr$_2$(GeO$_4$)$_6$O$_2$.**

| La | Sr | Ge | O | |
|---|---|---|---|---|
| – | – | – | 2.15 – 2.90 Å | **La** |
| | – | – | 2.15 – 2.90 Å | **Sr** |
| | | – | 1.57 – 1.96 Å | **Ge** |
| | | | – | **O** |

**Table 4.19 – The minimum distance constraints applied in procedures** P1 **and** P2 **for La$_{10}$(GeO$_4$)$_6$O$_3$, where 'Te' means an O$_{int}$ atom and 'Va' vacancy.**

| La | Ge | O | 'Te' | 'Va' | |
|---|---|---|---|---|---|
| >1.55 Å | >1.55 Å | >2.1 Å | >2.1 Å | – | **La** |
| | >1.55 Å | >1.55 Å | >1.55 Å | – | **Ge** |
| | | >2.2 Å | >2.2 Å | – | **O** |
| | | | >2.2 Å | – | **'Te'** |
| | | | | – | **'Va'** |

**Table 4.20 – The R$_{ij}$ values applied for the BVS restraints in La$_{10}$(GeO$_4$)$_6$O$_3$ procedures** P1 **and** P2. **Values of '0' were applied to cation–cation and anion–anion BVS.**

| La | Ge | O | 'Te' | 'Va' | |
|---|---|---|---|---|---|
| – | – | 2.172 Å | 2.172 Å | – | **La** |
| | – | 1.748 Å | 1.748 Å | – | **Ge** |
| | | – | – | – | **O** |
| | | | – | – | **'Te'** |
| | | | | – | **'Va'** |

**Table 4.21 – The BVS restraint weightings for La$_{10}$(GeO$_4$)$_6$O$_3$ and La$_8$Bi$_2$(GeO$_4$)$_6$O$_3$. Lower numbers mean a higher weighing. The 'Va' are weighted so that they do not affect the refinement.**

| Procedure | La | Ge | O | Te | Va |
|---|---|---|---|---|---|
| P1 | 2 | 2 | 2 | 2 | 5000 |
| P2 | 4 | 4 | 4 | 4 | 8000 |

For the refinements using the data obtained at 850 °C, a similar procedure to **P1** was applied with the same distance constraints. The BVS restraint weightings were reduced; as the bond length should slightly increase at higher temperatures, but not by an amount that can be known *a priori*. Reduced BVS weightings to lower the impact of using room temperature R$_{ij}$ values.[54]

For La$_8$Bi$_2$(GeO$_4$)$_6$O$_3$, procedures that are similar to the ones used for La$_{10}$(GeO$_4$)$_6$O$_3$ were employed. Different minimum distance constraints and BVS restraints were used due to the

presence of Bi, where the Bi–O and Bi–'Te' pairs had a minimum distance constraint of >2.0 Å and a BVS R$_{ij}$ value of 2.094 Å. Procedure **P2** used a total refinement time of 30 h as opposed to 15 h.

When referring to the starting configuration and refinement procedure in the following sections, abbreviations will be used in square brackets. For example, for La$_8$Sr$_2$(GeO$_4$)$_6$O$_2$, **[SC1, P1]** refers to using starting configuration **SC1** and then the procedure **P1**.

After convergence of the RMC refinements for La$_8$R$_2$(GeO$_4$)$_6$O$_3$ (R = La, Bi) phases at room temperature and high temperature (850 °C for R = La; 800 °C for R = Bi) it became evident that the scaling of the $F(Q)$ data was not optimal; a final 10 min refinement was performed to fit the scale of the $F(Q)$ data which significantly improved the $\chi^2_{F(Q)}$ value and visual fit for the $F(Q)$ data, but will not have caused substantive changes to the atomistic models.

Python scripts were employed in the analysis of the local structure of La$_8$R$_2$(GeO$_4$)$_6$O$_3$. Full details of these scripts are in Appendix A. RMCProfile .dat control files are also included.

### 4.3.2.3 La$_8$Sr$_2$(GeO$_4$)$_6$O$_2$ – room temperature

The $D(r)$ data for hexagonal La$_8$Sr$_2$(GeO$_4$)$_6$O$_2$ were analysed with a small box refinement using TOPAS 6[51] and the model obtained from the average structure shown in Table 4.9. This was done as a "control test" on the simplest material. Figure 4.18 shows the resulting PDF fit. The small box fit, which used a fixed scale factor of 1.0, indicates that the scaling of the data from the processing is correct and that there is not too much deviation from the average structure on a local scale.
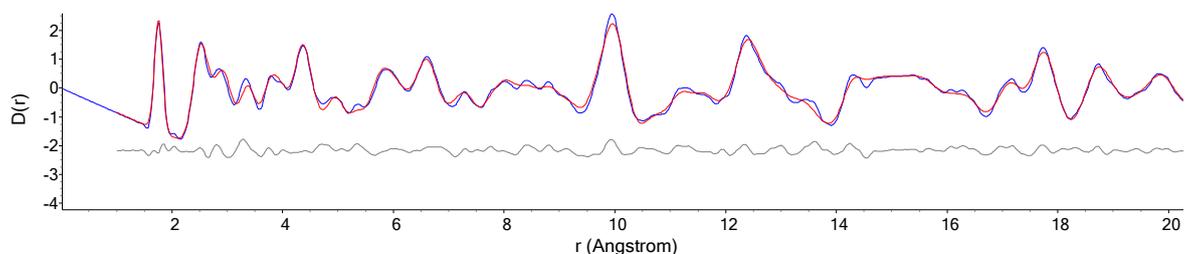


**Figure 4.18 –** The small box neutron PDF fit of La$_8$Sr$_2$(GeO$_4$)$_6$O$_2$ with range 0 < $r$ < 20 Å. R$_{wp}$ = 19.184%.

Big box modelling was performed using RMCProfile. Eight refinements were performed using **[SC1, P1]**, which resulted in an average occupancy of La1 = 0.666(7); La2 = 0.891(6); Sr1 = 0.334(7); Sr2 = 0.111(6), compared to the starting occupancies of **SC1**, which were La1 = 0.575; La2 = 0.950; Sr1 = 0.425; Sr2 = 0.050. The difference in site occupancies suggests a lack of sensitivity to the La/Sr occupation in the neutron RMC technique. The neutron scattering lengths for La and Sr are similar; $b_{La}$ = 8.24 fm and $b_{Sr}$ = 7.02 fm. There are also more La2 sites than La1 (600 : 400); when Sr atoms are allowed to swap with La atoms, they are more likely to swap with a La2 atom than La1 atom, which results in an apparent increase in the Sr2 occupancy when RMC refinement is used, which will always favour the more random atomic configurations. Therefore,

final refinements were performed with no swapping to maintain the crystallographic occupancies. Twelve refinements were performed using **[SC1, P2]**. Representative fits for the PDF and Bragg data are given in Figure 4.19. A representative fit for the $F(Q)$ data is given in Appendix A.
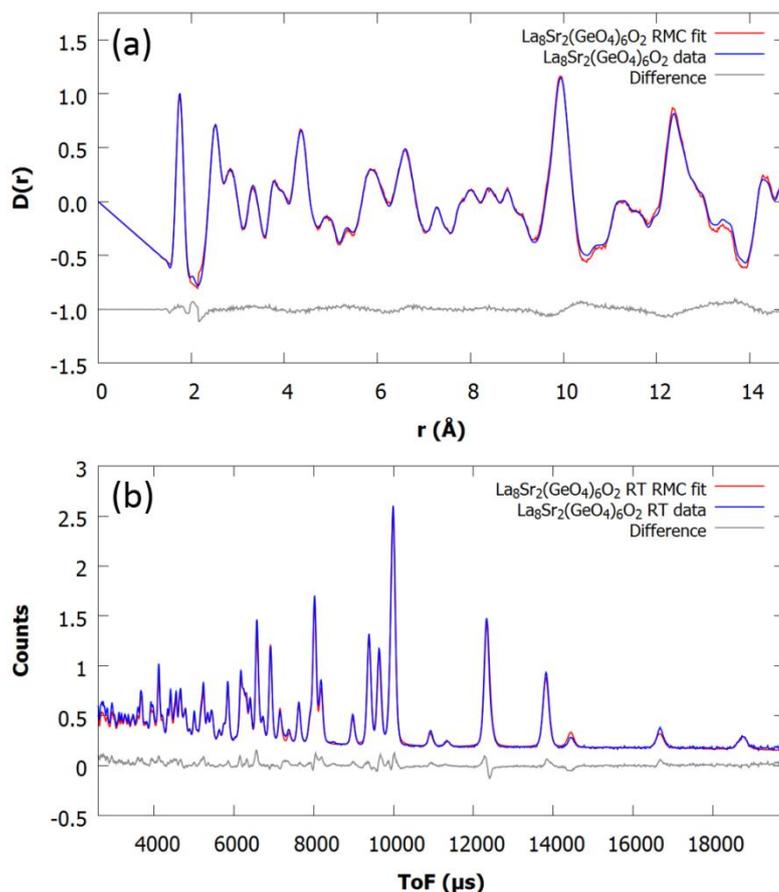


**Figure 4.19 –** Representative fits of La$_8$Sr$_2$(GeO$_4$)$_6$O$_2$ **[SC1, P2]** (a) PDF expressed as $D(r)$, $\chi^2_{pdf}$ = 8.722 and (b) Bragg, $\chi^2_{Bragg}$ = 4.593 calculated from a [5 5 4] supercell using RMCProfile.

These fits generate values of $\chi^2_{dof}$ = 3.7(2); $\chi^2_{pdf}$ = 8.8(1); $\chi^2_{Bragg}$ = 4.60(4); $\chi^2_{F(Q)}$ = 0.431(5), where the values in parentheses are the standard deviations of the $\chi^2$ values of the twelve individual fits. The unfitted peak at $r \approx 2.0$ Å is a "termination ripple", a result of the Fourier transform that generated the $G(r)$ data being performed over a limited $Q$ range. This was confirmed after inspection of the data after Fourier transform over different $Q$ ranges. Figure 4.20 shows the resulting atomic density map from the twelve refinements superimposed onto the average structure; although the atomic density remains close to the average positions, there is some elongation of the cloud along the cell diagonal.
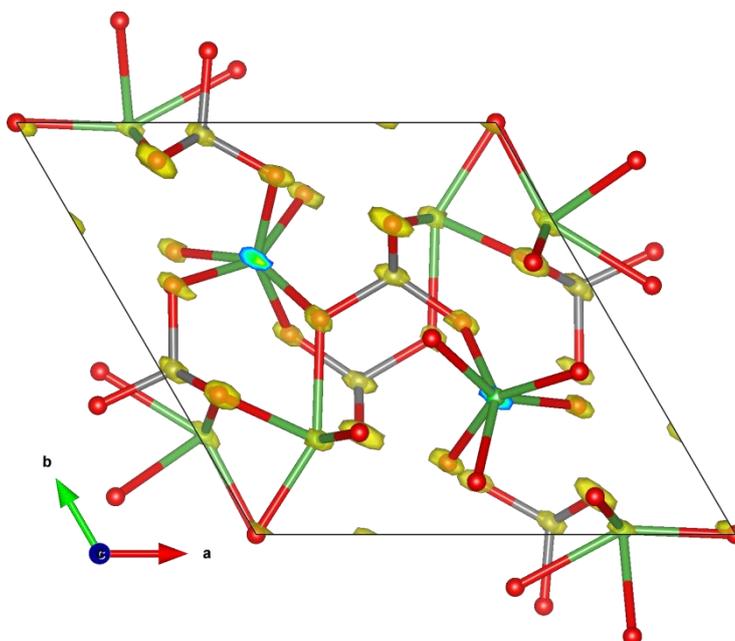
**Figure 4.20 –** The atomic density map from 12 collapsed $La_8Sr_2(GeO_4)_6O_2$ models **[SC1, P2]** superimposed on the average crystal structure. The yellow clouds represent a volume within which at least 16.4 atoms are present; the slice of the yellow cloud at ($^1/_3$, $^2/_3$, 0) and ($^2/_3$, $^1/_3$, 0) represents a varying density from 3 atoms (blue) to 331 (red), occurring at the boundary of the unit cell. Green spheres = La/Sr atoms; grey spheres = Ge atoms; red spheres = O atoms.

Geometric analysis was performed on the RMC configurations analysing the Ge–O bond distances and O–Ge–O internal bond angles. Figure 4.21 gives histograms of Ge–O bond distances and O–Ge–O bond angles from all twelve refinements. The histograms of bond lengths and angles were summed and then a Gaussian function was fitted to each. For the bonds, this produced a mean of $r$ = 1.7584(7) Å with a full width at half maximum (FWHM) of 0.176(1) Å with $R_{wp}$= 6.707%. The Gaussian fit to the bond angles resulted in a mean O–Ge–O bond angle = 108.91(3)°, FWHM = 20.33(7)°, with $R_{wp}$ = 3.166%. There is very little deviation from the average structure where the reported Ge–O bond length[54] is 1.747 Å. The slight reduction in bond length in the average structure presumably arises from the well-known effect of correlated local motions being poorly approximated with harmonic displacement parameters, leading to an overestimation of true bond lengths from Bragg analyses.[55]

$La_8Sr_2(GeO_4)_6O_2$ provides a benchmark for the local structure of an 'ideal' lanthanum germanate apatite structure, without an interstitial oxygen, as determined using RMCProfile. The refined local structure shows there is very little local distortion, despite the difference in ionic radii between $La^{3+}$ and $Sr^{2+}$.
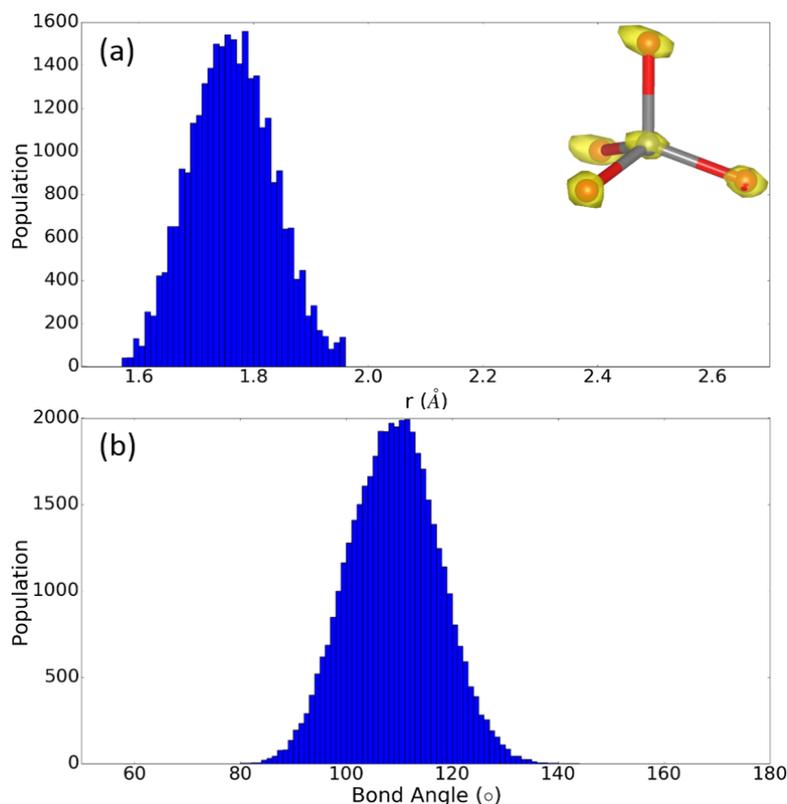
**Figure 4.21 –** The histograms of (a) Ge–O bond lengths and (b) GeO$_4$ internal angles present in 12 atomic room temperature La$_8$Sr$_2$(GeO$_4$)$_6$O$_2$ models **[SC1, P2]**. Bin size = (a) 0.01 Å and (b) 1°. The shape of an average GeO$_4$ with the atomic density from the 12 configurations has been included to illustrate the effect on the local environment.

### 4.3.2.4 La$_{10}$(GeO$_4$)$_6$O$_3$ – room temperature

Small box modelling was used initially to determine that the data were scaled correctly. RMC analysis was then performed using starting configurations **SC1–SC4** from Table 4.16 and procedure **P1**. There are four repeats in each of the models **[SC1–SC4, P1]**. Representative PDF fits for each of the four models and two representative Bragg fits from the two most important models are given in Figure 4.22. The average goodness of fit values for all of the fits are given in Table 4.22. Representative $F(Q)$ fits are in Appendix A.

**Table 4.22 – The goodness of fit values obtained in room temperature La$_{10}$(GeO$_4$)$_6$O$_3$ models [SC1–SC4, P1]. The $\chi^2_{F(Q)}$ reported were obtained from the final fits with the $F(Q)$ data rescaled.**

| Model | $\chi^2_{dof}$ | $\chi^2_{PDF}$ | $\chi^2_{Bragg}$ | $\chi^2_{F(Q)}$ |
|---|---|---|---|---|
| [SC1, P1] | 1.45(5) | 9.6(4) | 1.65(2) | 0.30(1) |
| [SC2, P1] | 1.47(7) | 9.8(7) | 1.64(4) | 0.31(1) |
| [SC3, P1] | 2.13(2) | 12.5(2) | 1.65(2) | 0.312(4) |
| [SC4, P1] | 2.09 | 12.4(5) | 1.68(2) | 0.303(6) |
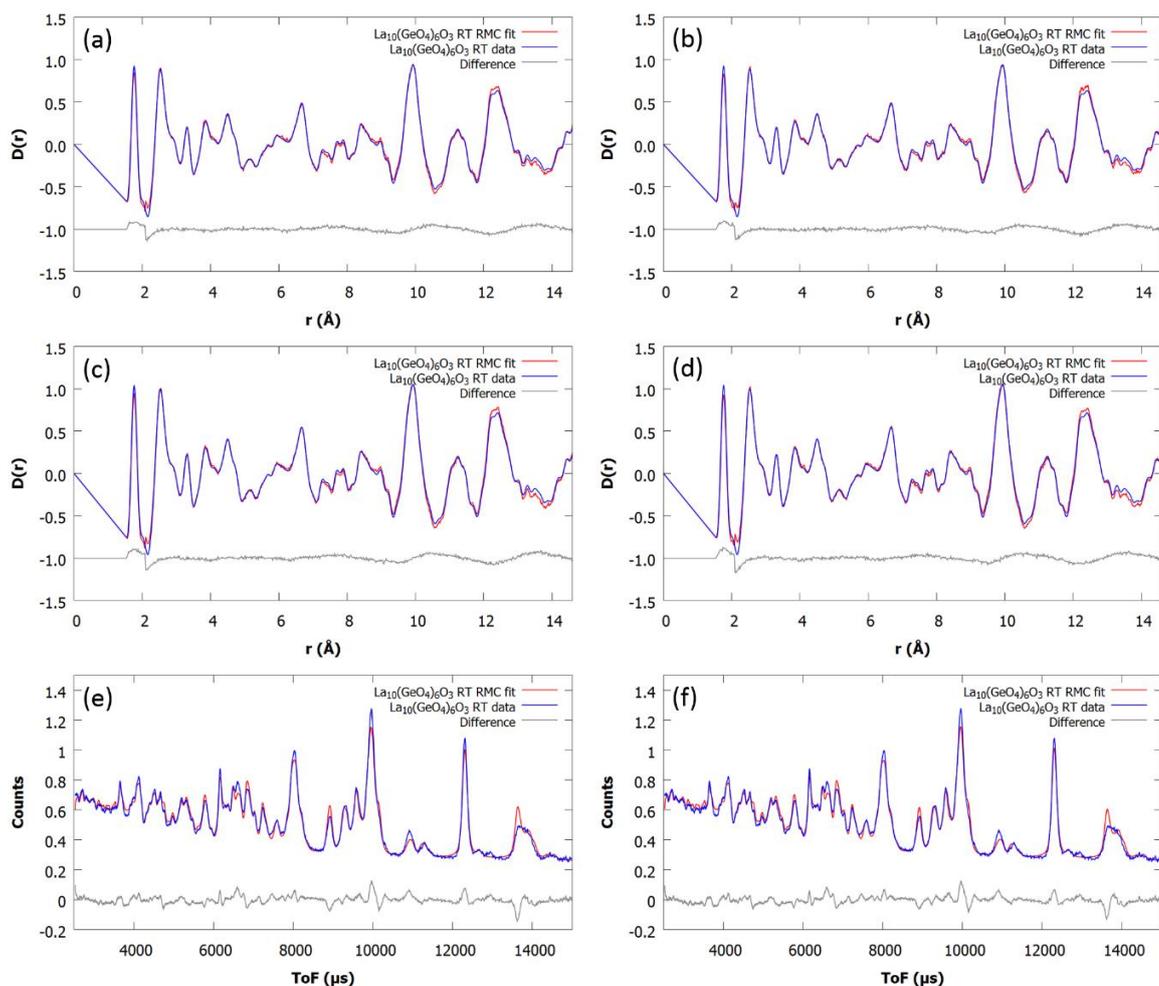
**Figure 4.22** – Representative PDFs expressed as $D(r)$ for La$_{10}$(GeO$_4$)$_6$O$_3$ at room temperature. (a) **[SC1, P1]**, $\chi_{PDF}^2$ = 9.119; (b) **[SC2, P1]**, $\chi_{PDF}^2$ = 9.017; (c) **[SC3, P1]**, $\chi_{PDF}^2$ = 12.69; (d) **[SC4, P1]**, $\chi_{PDF}^2$ = 12.01. Representative Bragg fits for (e) **[SC1, P1]**, $\chi^2_{Bragg}$ = 1.626 and (f) **[SC4, P1]**, $\chi^2_{Bragg}$ = 1.627.

The difference between the models tested lies in their starting configurations: there are only three O$_{int}$ sites available in **SC1** and **SC2** and all six sites are available in **SC3** and **SC4** (see Table 4.10 for the coordinates of these positions). The $\chi^2$ values for the Bragg fits obtained with the different models are all within one σ of each other, indicating that the average structure is fitted equally well from all starting configurations. In order to investigate the differences between these models, the number of O$_{int}$ atoms on each of the six crystallographic sites was counted after the refinements. Table 4.23 gives the number of O$_{int}$ atoms on each crystallographic site in models **[SC1–SC4, P1]**.

**Table 4.23 – The number of $O_{int}$ atoms on each position in room temperature $La_{10}(GeO_4)_6O_3$ models [SC1–SC4, P1]. For SC1 and SC2, the $O_{int}$ sites that were not permitted have been greyed out.**

|   | [SC1, P1] | [SC2, P1] | [SC3, P1] | [SC4, P1] |
|---|---|---|---|---|
| A | 20.5(9) | 21(2) | 20.8(8) | 13.8(8) |
| B | 76.8(8) | 76(2) | 75(2) | 66.0(7) |
| C | | | 0.5(5) | 16.5(5) |
| D | 2.8(4) | 1.8(8) | 4(2) | 0.5(8) |
| E | | | 0(0) | 0(0) |
| F | | | 0(0) | 3.3(4) |

The distribution of $O_{int}$ atoms is very similar in all of the models. In **[SC1–SC3, P1]**, there are very few $O_{int}$ atoms on the D site, approximately 20% on the A site and 75% on the B site.  All three of these models had starting configurations with no $O_{int}$ atoms on the C, E and F sites, but in **[SC3, P1]**, these sites were made available to be swapped onto whereas in models **[SC1–SC2, P1]**, they were not. **[SC4, P1]** is different, in that it started with all six $O_{int}$ sites equally occupied. Here the E site remains unpopulated, whilst the D and F sites have a low population after minimisation. The main difference in **[SC4, P1]** is that the C site remains populated after refinement, whereas it does not become populated in the other models.

The differences in the $O_{int}$ occupancies arise due to the methodology used in the RMC analysis. For example, when the C site starts unpopulated, the RMC algorithm does not swap $O_{int}$ atoms onto it due to local distance constraints. This is discussed further in the context of Figure 4.26 below. Instead, it fits the data by swapping the $O_{int}$ atoms onto other $O_{int}$ sites (A or B). When the C site is populated at the start of the refinement, the RMC algorithm displaces atoms in the local coordination sphere such that the site obeys the distance constraints that allow it to remain occupied. We therefore conclude that the precise $O_{int}$ distributions cannot be definitively obtained from this method. The analysis below shows, however, that each of the models **[SC1–SC4, P1]** give an equivalent picture of the local $O_{int}$ environment, so valuable information on the local $O_{int}$ environment can still be extracted.

The different models were compared by calculating the Ge–O bond distance and angle distributions from the refined configurations. The histograms of the bond distances and angles are shown in Figure 4.23. In these plots, Ge atoms near to an $O_{int}$ atom ($GeO_5$ – justified below) are separated from the $GeO_4$ units with no nearby $O_{int}$ atoms.
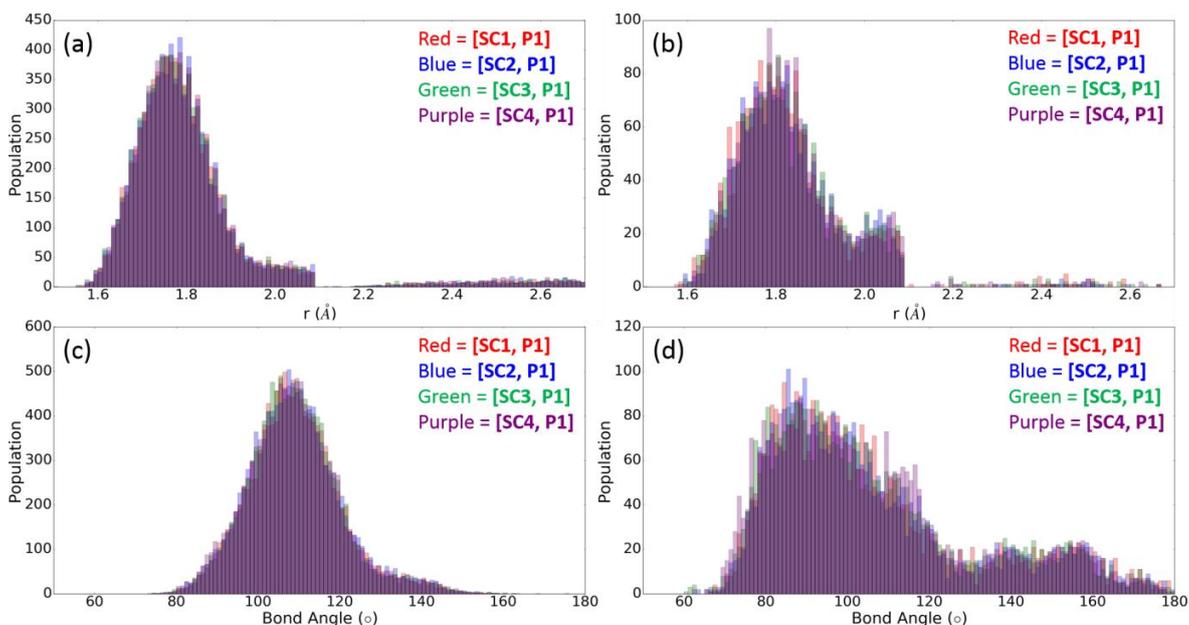
**Figure 4.23** – The histograms of La$_{10}$(GeO$_4$)$_6$O$_3$ at room temperature: (a) Ge–O bond distances in GeO$_4$; (b) Ge–O bond distances in GeO$_5$; (c) O–Ge–O bond angles in GeO$_4$; (d) O–Ge–O bond angles in GeO$_5$.

Figure 4.23 shows that the bond distance and angle distributions in the GeO$_4$ and GeO$_5$ polyhedra are similar across all models, irrespective of starting configuration. The bond distance distributions of the GeO$_4$ (Figure 4.23a) show a clear cut off point at *r* = 2.1 Å. This cut off occurs due to the distance between two GeO$_4$ tetrahedra. In addition, there are small populations at *r* > 2.3 Å. These distances are those to more remote O$_{int}$ atoms. In contrast, the bond distances in the GeO$_5$ polyhedra (Figure 4.23b) show a larger population at 1.9 ≤ *r* < 2.1 Å from the O$_{int}$ atoms, a clear cut-off at *r* = 2.1 Å and a much smaller relative population at *r* > 2.2 Å, which only corresponds to a few atoms. This demonstrates that a good way to define the coordination sphere of Ge atoms is *r* = 2.2 Å and that a good cut-off point to define the GeO$_5$ polyhedra is Ge–O$_{int}$ < 2.2 Å.

The bond angle distributions within the GeO$_4$ and GeO$_5$ units across the four models are again very similar. The mean O–Ge–O angles of the GeO$_4$ tetrahedra (Figure 4.23c) are close to the ideal tetrahedral bond angle of 109.5° in all four models, revealing that they have mostly maintained their tetrahedral geometry. However, there is a slight asymmetry in the distribution at 120–140°, which shows that there is a small amount of distortion in the GeO$_4$ tetrahedra. The mean and FWHM of the GeO$_4$ tetrahedral bond angle distributions are given in Table 4.24.

**Table 4.24 – The means and full-width at half maxima (FWHM) of the Gaussian fits from the bond angle histograms of GeO$_4$ tetrahedra obtained from room temperature RMC refinements of La$_{10}$(GeO$_4$)$_6$O$_3$.**

| Model | Mean (°) | FWHM (°) |
|---|---|---|
| [SC1, P1] | 107.75(9) | 23.2(2) |
| [SC2, P1] | 107.71(9) | 23.4(2) |
| [SC3, P1] | 107.88(9) | 22.7(2) |
| [SC4, P1] | 107.6(1) | 23.3(2) |

These configurations allow the local environment of the O$_{int}$ atoms to be probed based on the bond length distributions. There are two possible local coordination environments for O$_{int}$ atoms: GeO$_5$ which have been proposed in La$_{10}$(GeO$_4$)$_6$O$_3$ before[5] or Ge$_2$O$_9$ units, which have been suggested in hexagonal apatites.[20, 44] If the O$_{int}$ atoms were present in Ge$_2$O$_9$ units, the difference between the two Ge–O$_{int}$–Ge distances, ΔGe–O$_{int}$, would be 0 Å in an ideal unit. If the O$_{int}$ atoms were present in GeO$_5$ polyhedra (giving Ge---O$_{int}$–Ge or Ge–O$_{int}$---Ge), ΔGe–O$_{int}$ would be non-zero. Figure 4.24 shows the histogram of the ΔGe–O$_{int}$ distances found in all four of the models and an illustration of ΔGe–O$_{int}$ (Δ$r$).
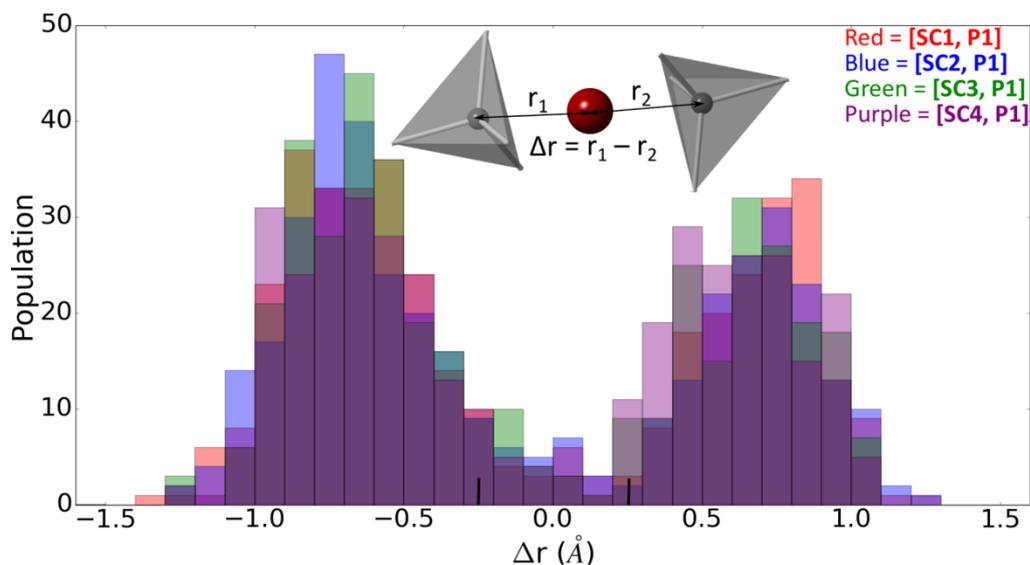


**Figure 4.24 –** Histograms of ΔGe–O$_{int}$ in room temperature La$_{10}$(GeO$_4$)$_6$O$_3$ models **[SC1–SC4, P1]** with an illustration of ΔGe–O$_{int}$ and the defined region of Ge$_2$O$_9$ units marked.

The fact that there are two clear distributions either side of 0 Å indicates that majority of the O$_{int}$ atoms are present in GeO$_5$ polyhedra. In order to quantify the (low) number of Ge$_2$O$_9$ units, a definition was adopted where the number of Ge$_2$O$_9$ units is the number of O$_{int}$ atoms that have ΔGe–O$_{int}$ distances that fall in the range of –0.25 ≤ ΔGe–O$_{int}$ ≤ 0.25 Å (the centre of Figure 4.24). Table 4.25 gives the number of Ge$_2$O$_9$ units defined in this way from all four of the room

temperature models. As there are 100 O$_{int}$ atoms in each model, these numbers will also correspond to the percentage of O$_{int}$ atoms in a Ge$_2$O$_9$ unit.

**Table 4.25 – The number of Ge$_2$O$_9$ units in room temperature La$_{10}$(GeO$_4$)$_6$O$_3$ models** [SC1–SC4, P1] **(four configurations per model) and the percentage of Ge atoms in a Ge$_2$O$_9$ compared to the total number of Ge (Ge$_{Tot}$ = 600).**

| Model | Number of Ge$_2$O$_9$ | Ge$_2$O$_9$/Ge$_{Tot}$ (%) |
|---|---|---|
| [SC1, P1] | 5(1) | 1.58(4) |
| [SC2, P1] | 7(1) | 2.33(5) |
| [SC3, P1] | 5(2) | 1.83(6) |
| [SC4, P1] | 5(2) | 1.83(6) |

The numbers of Ge$_2$O$_9$ units in all four models are all very similar, showing that there are similarities between the local structure models despite the difference in O$_{int}$ distributions. Furthermore, in all four models, < 10% of the total O$_{int}$ in the structure can be considered as belonging to Ge$_2$O$_9$ units.

In addition to Ge$_2$O$_9$ units and GeO$_5$ polyhedra, there could also be GeO$_6$ units present if two adjacent O$_{int}$ sites, such as A and C, are populated simultaneously. Table 4.26 gives the coordination numbers of GeO$_x$ ($x$ = 4, 5, 6). We conclude that there are essentially no GeO$_6$ present in all models. This is likely because of the low probability of nearby sites being occupied at the same time. As there are essentially no GeO$_6$ polyhedra and < 10% of the total O$_{int}$ are in Ge$_2$O$_9$ units, for the sake of simplicity Ge atoms that coordinate to the O$_{int}$ will be referred to as "GeO$_5$" polyhedra in the rest of this report.

**Table 4.26 – The average coordination numbers (CNs) of GeO$_x$ ($x$ = 4, 5, 6) where Ge–O$_{int}$ < 2.2 Å in room temperature La$_{10}$(GeO$_4$)$_6$O$_3$ models** [SC1–SC4, P1]**. The first number is the total number of Ge atoms with that coordination number and the second is the percentage that number represents out of the total Ge atoms.**

| | [SC1, P1] | [SC2, P1] | [SC3, P1] | [SC4, P1] |
|---|---|---|---|---|
| **CN = 4** | 8(2) / 9(3)% | 6(4) / 6(4)% | 7(1) / 8(1)% | 3(2) / 3(2)% |
| **CN = 5** | 87(3) / 91(5)% | 88(4) / 94(7)% | 88(3) / 92(5)% | 94(3) / 97(4)% |
| **CN = 6** | 0 (0) / 0(0)% | 0.3(4) / 0.3(5)% | 0.5(5) / 0.5(5)% | 0(0) / 0(0)% |
| **Average** | 4.91(3) | 4.94(4) | 4.93(2) | 4.97(2) |
| **Total** | 95(4) | 93(5) | 95(4) | 97(3) |

The bond angle distributions of the GeO$_5$ polyhedra (Figure 4.23d) show that the GeO$_5$ polyhedra have a markedly different coordination environment from the GeO$_4$ tetrahedra. They do not follow a single Gaussian distribution like the GeO$_4$ tetrahedra, but instead show a wide range of

bond angles. The distributions of GeO$_5$ bond angles are similar across all models. The GeO$_5$ polyhedra could exist as either trigonal bipyramids or square pyramids. The angles of a trigonal bipyramid are 90°, 120° and 180° in a ratio of 6 : 3 : 1, whilst the angles of a square pyramid are 90° and 180° in a ratio of 8 : 2. Additionally, the GeO$_5$ could exist in geometries that are intermediate between trigonal bipyramids and square pyramids. One way to quantify this geometry is using the $\tau$ value of Addison *et al.*,[56] which defines $\tau$ as:

$$\tau = \frac{\beta - \alpha}{60°} \qquad (4.3)$$

Where $\beta$ and $\alpha$ are the largest and second largest angles respectively. In a square pyramid, the two largest angles are 180° and in a trigonal bipyramid, the two largest angles are 180° and 120°. Therefore, $\tau$ has values from 0 for a square pyramid to 1 for a trigonal bipyramid. A histogram of $\tau$ values is shown in Figure 4.25.
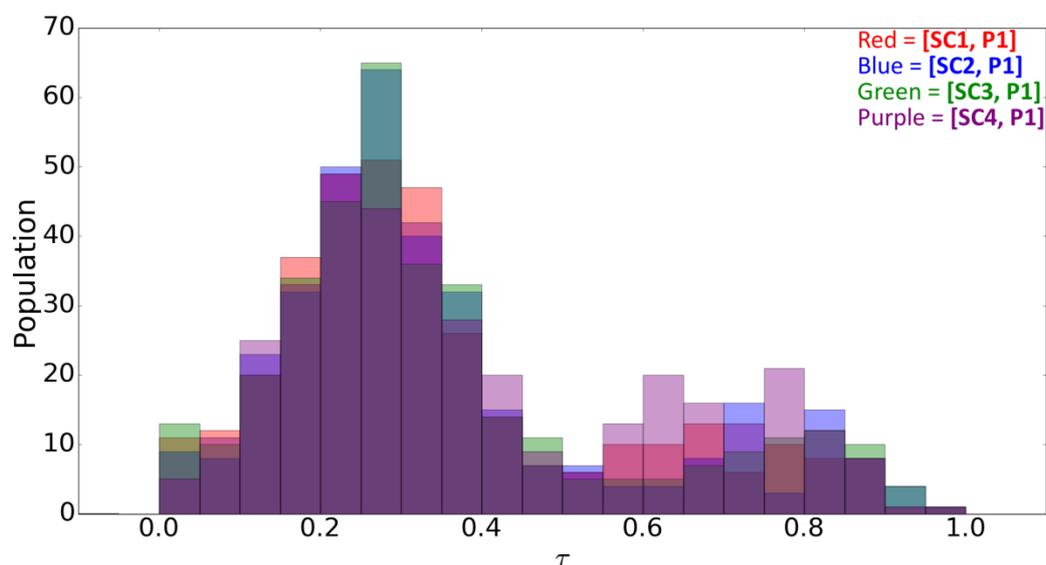


**Figure 4.25 –** The $\tau$ values obtained for GeO$_5$ units in La$_{10}$(GeO$_4$)$_6$O$_3$ for room temperature models **[SC1–SC4, P1]**. $\tau$ = 0 corresponds to a square pyramid and $\tau$ = 1 to a trigonal bipyramid.

Figure 4.25 shows that the majority of the GeO$_5$ polyhedra are more square pyramidal in their geometry than trigonal bipyramidal, revealing the large distortions of the originally tetrahedral environments that are induced by the presence of O$_{int}$ atoms. All four room temperature La$_{10}$(GeO$_4$)$_6$O$_3$ models contain GeO$_5$ with a more square pyramidal characteristic than trigonal bipyramidal.
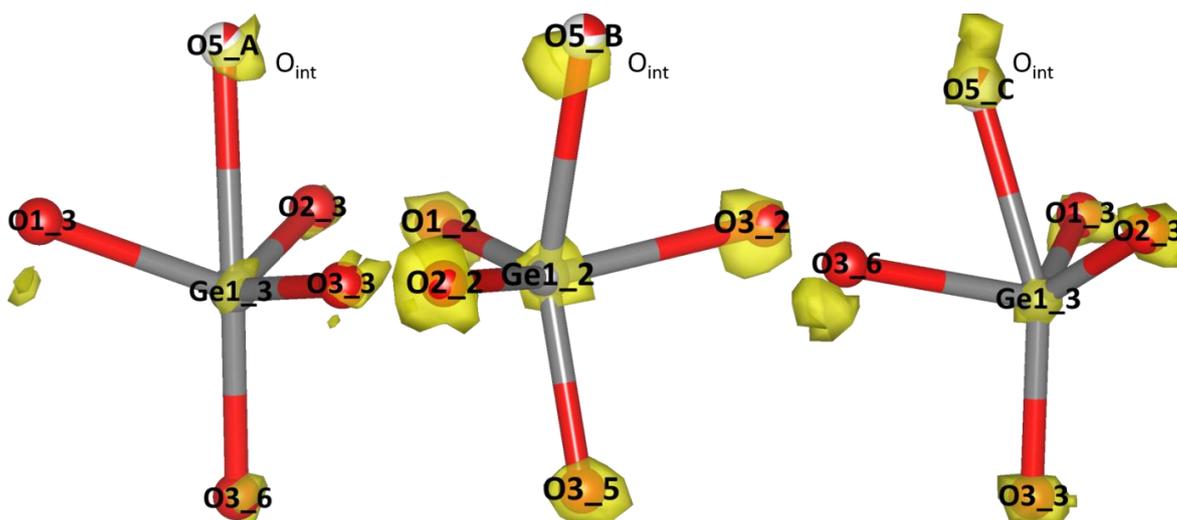
**Figure 4.26** – Atomic density maps from room temperature La$_{10}$(GeO$_4$)$_6$O$_3$ model **[SC4, P1]** around GeO$_5$ polyhedra superimposed on the average structure. O$_{int}$ atoms are labelled as O5 atoms in crystallographic models. Yellow clouds represent 0.2 × 0.2 × 0.2 Å$^3$ voxels where at least 1.2 atoms are present.

Atomic density maps around the GeO$_5$ polyhedra were created help visualise the local structure. These were calculated by collapsing the supercell back to a single cell and calculating the number of atoms in each voxel. Figure 4.26 shows atomic density maps around the three populated O$_{int}$ sites in model **[SC4, P1]**. The atomic density distributions are much more densely populated for the B site due to the increased number of O5_B atoms. It can be seen from the atomic density maps that all of the final O$_{int}$ local environments (yellow clouds) are similar, whereas in the average crystallographic structure, the A, B and C sites are different; the GeO$_5$ at the B site (Ge1_2O$_5$) are more distorted than the GeO$_5$ (Ge1_3O$_5$) at A and C in the average structure. Figure 4.26 also helps explain why different O$_{int}$ sites become populated with the occupancies shown in Table 4.23 for our different models **[SC1–SC4, P1]**. In order for O5_A atoms to be present (Figure 4.26 left), the O1_3 atoms need to move a significant distance from their average position due to the short distance of O5_A–O1_3 (= 2.15 Å). There is a similar situation with the O5_C atoms, where there is a short distance of O5_C–O3_6 (= 1.94 Å). In contrast, the O5_B atoms do not have any O5_B–O distances < 2.2 Å. This means that the average structure requires little distortion in order to accommodate O5_B atoms, and therefore occupation of this site is more likely to occur during RMC refinement. This is also seen from the data, where the average structure around the B site (Ge1_2O$_{4,5}$ polyhedra) is far more distorted than the average structure of the A and C (as well as the E and F) sites.
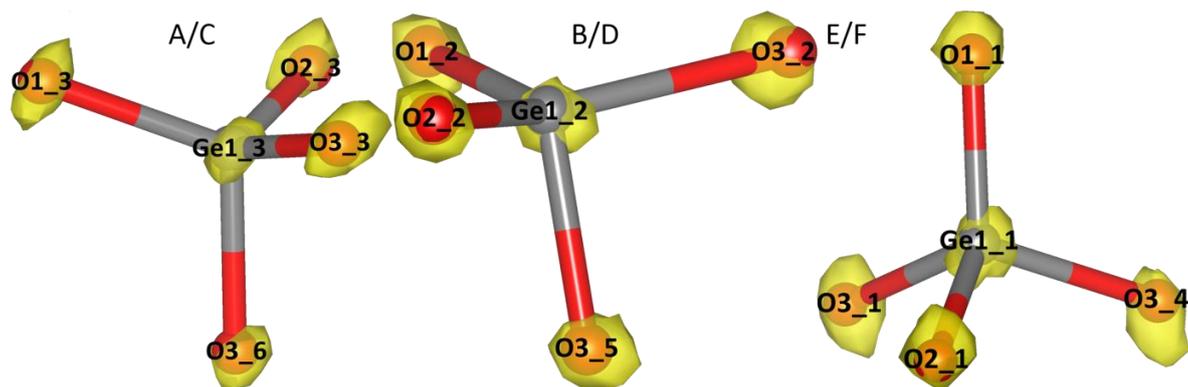
**Figure 4.27 –** The atomic density maps of three GeO$_4$ units near the A/C, B/D and E/F sites when no O$_{int}$ atom is present from room temperature La$_{10}$(GeO$_4$)$_6$O$_3$ model **[SC4, P1]**, superimposed onto the average structure. Yellow clouds represent 0.2 × 0.2 × 0.2 Å$^3$ voxels with at least 3.9 atoms in them.

The atomic density maps of the GeO$_4$ tetrahedra near the A/C, B/D and E/F sites when the O$_{int}$ sites remain unoccupied were also created and are illustrated in Figure 4.27. The E and F sites in model **[SC4, P1]** are almost entirely unpopulated (see Table 4.23). The average structure around those sites is very similar to a regular tetrahedron (see Figure 4.23a,c) and this is also reflected in the atomic density map (Figure 4.27 right). The coordination environment of the A and C sites (Figure 4.27, left) is also similar to a regular tetrahedron when there are no O$_{int}$ atoms present. However, the coordination environment around the B and D sites is different (Figure 4.27 centre). Despite the fact that the O3_2 atomic density has moved closer to the Ge1_2 site, when a GeO$_5$ polyhedron is present, the geometry of the adjacent GeO$_4$ tetrahedron is still distorted. This is shown by the fact that the atomic density maps have not moved much from the average position and are in a similar location as when an O5_B is present (see Figure 4.26, centre). The high number of B-site GeO$_5$ units also means that when adjacent GeO$_4$ tetrahedra are averaged, a significant proportion of them will be distorted by the neighbouring GeO$_5$ unit; this accounts for why the GeO$_4$ units near B/D sites appear to deviate further from the average position than units near less occupied A/C and E/F sites.

### 4.3.2.5 La$_{10}$(GeO$_4$)$_6$O$_3$ – high temperature

Similar procedures were performed with La$_{10}$(GeO$_4$)$_6$O$_3$ at 850 °C using the starting configurations in Table 4.16. We again found that the local structural features in each model were very similar, so we will only discuss model **[SC5, P2]**, which started from the 850 °C average structure. Figure 4.28 gives representative PDF and Bragg fits from **[SC5, P2]**. The representative fits for the $F(Q)$ data rare in Appendix A. The average values obtained from each fit in **[SC5, P2]** are: $\chi_{dof}^2$ = 2.37(4); $\chi_{PDF}^2$ = 13.2(3); $\chi_{Bragg}^2$ = 2.8(2). The value obtained after the $F(Q)$ data were scaled is $\chi_{F(Q)}^2$ = 0.316(5). The O$_{int}$ atoms are distributed equally over all six possible sites (Table 4.27), which is expected in a higher symmetry structure.
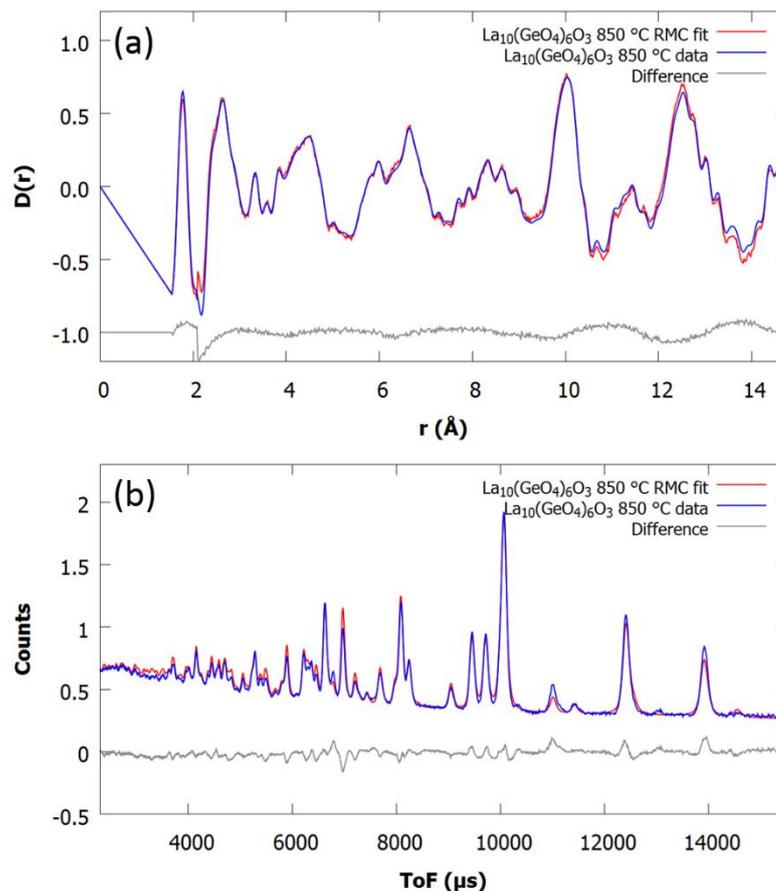
**Figure 4.28 –** Representative RMC fits room La$_{10}$(GeO$_4$)$_6$O$_3$ 850 °C from model **[SC5, P2]**. (a) PDF expressed as $D(r)$, $\chi_{PDF}^2$ = 13.51; (b) Bragg fit, $\chi^2_{Bragg}$ = 2.749.

**Table 4.27 – The number of O$_{int}$ atoms on each position in La$_{10}$(GeO$_4$)$_6$O$_3$  models** [SC5, P2]**.**

|   | O$_{int}$ atoms |
|---|---|
| **A** | 14(3) |
| **B** | 20(2) |
| **C** | 14(3) |
| **D** | 20(2) |
| **E** | 17(2) |
| **F** | 17(2) |

Geometric analyses of the Ge–O bond length and angle distributions were performed and are shown in Figure 4.29 alongside the equivalent distribution for the room temperature analysis. The Ge–O distances in the GeO$_4$ tetrahedra in the 850 °C model are similar to those at room temperature (Figure 4.29a), as are the bond distances for GeO$_5$ polyhedra (Figure 4.29b). The bond angle distribution of the GeO$_4$ tetrahedra (Figure 4.29c) has broadened from FWHM = 23.3(2)° at room temperature to FWHM = 28.24(2)°. Wider distributions of bond angles are expected at higher temperatures due to increased thermal motion.
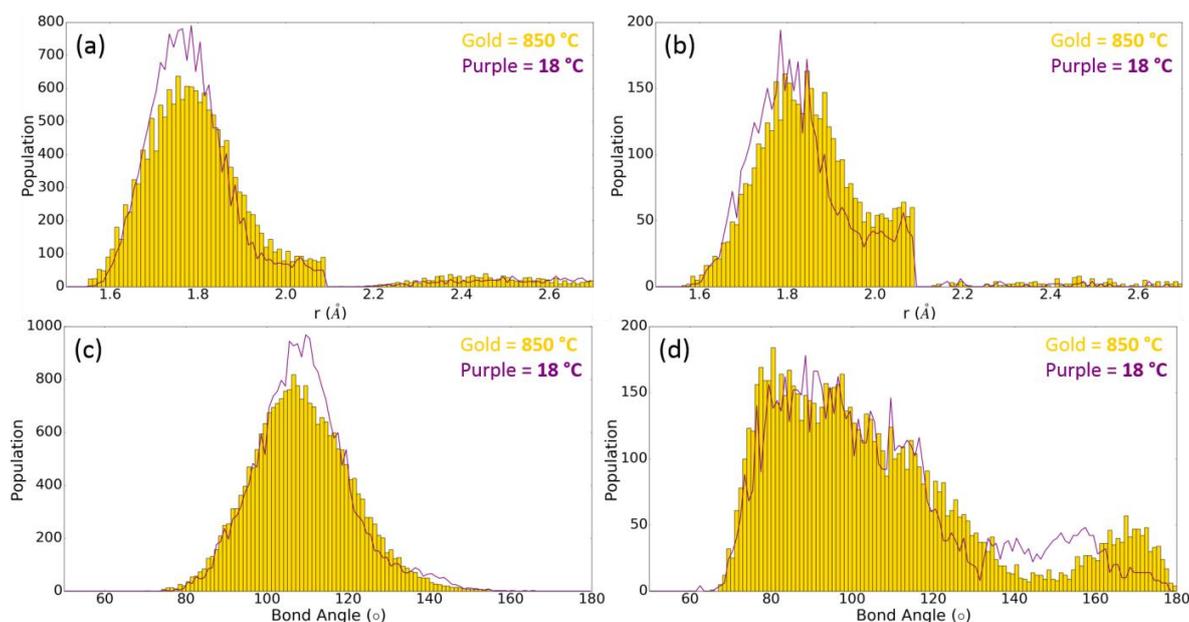
**Figure 4.29** – Histograms from $La_{10}(GeO_4)_6O_3$ at 850 °C **[SC5, P2]** (gold bars) with the equivalent room temperature histogram for **[SC4, P1]** (purple line) superimposed: (a) Ge–O bond distances in $GeO_4$; (b) Ge–O bond distances in $GeO_5$; (c) O–Ge–O bond angles in $GeO_4$; (d) O–Ge–O bond angles in $GeO_5$. The populations of **[SC4, P1]** in this and later figures have been doubled as half of the number of **[SC5, P2]** configurations were used.

**Table 4.28** – **The means and full-width at half maxima (FWHM) of the bond angle distributions of $La_8R_2(GeO_4)_6O_{3-y}$ (R = Sr, La, Bi) at room temperature and high temperature**

| Composition | $T$ (°C) | Model | Mean (°) | FWHM (°) |
|---|---|---|---|---|
| $La_8Sr_2(GeO_4)_6O_2$ | 18 | [SC1, P2] | 108.91(3) | 20.33(7) |
| $La_{10}(GeO_4)_6O_3$ | 18 | [SC4, P1] | 107.9(1) | 23.3(2) |
| $La_{10}(GeO_4)_6O_3$ | 850 | [SC5, P2] | 107.72(8) | 28.2(2) |
| $La_8Bi_2(GeO_4)_6O_3$ | 18 | [SC4, P1] | 108.0(2) | 30.2(3) |
| $La_8Bi_2(GeO_4)_6O_3$ | 800 | [SC5, P2] | 107.0(1) | 36.1(3) |

The local environment of the $O_{int}$ atoms was probed to determine whether they are present as $GeO_5$ polyhedra or $Ge_2O_9$ units using the same definitions as for the room temperature analysis. Figure 4.30 shows the histogram of $\Delta$Ge–$O_{int}$ distances obtained at 850 °C with room temperature values superimposed (**[SC5, P1]** and **[SC4, P1]**). We see two major differences compared to room temperature. Firstly, the population of $Ge_2O_9$ units has noticeably increased at 850 °C to 20(2), corresponding to 6.7(7)% of all Ge atoms, from 6(2) (1.83(6)% of Ge atoms). It also means that 20(2)% of $O_{int}$ atoms are in $Ge_2O_9$ units at 850 °C. This may be due to the increased disorder of the $O_{int}$ atoms; the interstitial site in between two GeO4 tetrahedra is likely to be an intermediary site during oxygen migration throughout the structure, so a higher occupation at temperatures where oxygen conductivity is significant may be expected. Computational studies found that the most

frequent conduction mechanism was an interstitialcy mechanism that involves an O$_{int}$ moving into a normal O site and a normal O site moving into a O$_{int}$ position.[44, 46, 48] Secondly, the distribution of ΔGe–O$_{int}$ distances is significantly narrowed at high temperature from |ΔGe–O$_{int}$| ≤ 1.4 Å at room temperature to |ΔGe–O$_{int}$| ≤ 1.1 Å. At higher temperatures, a wider distribution of bond lengths is expected, however this result indicates that the local structure also seems to have increased in symmetry. The coordination numbers (Table 4.29) show that at 850 °C, the majority of the O$_{int}$ atoms still coordinate with Ge atoms that adopt fivefold coordination. It also shows that GeO$_6$ polyhedra are essentially non-existent.

**Table 4.29 – The average coordination numbers (CNs) of GeO$_x$ ($x$ = 4, 5, 6) polyhedra with Ge–O$_{int}$ < 2.2 Å in La$_8$R$_2$(GeO$_4$)$_6$O$_3$ (R = La, Bi).**

|          | R = La [SC4, P1] (18 °C) | R = La [SC5, P2] (850 °C) | R = Bi [SC4, P1] (18 °C) | R = Bi [SC5, P2] (800 °C) |
|----------|--------------------------|----------------------------|--------------------------|----------------------------|
| **CN < 4**  | 0(0) / 0(0)%   | 0(0) / 0(0)%      | 0.8(8) / 0.7(8)%  | 6(2) / 6(2)%       |
| **CN = 4**  | 3(2) / 3(2)%   | 6(2) / 6(2)%      | 16(2) / 15(2)%    | 31(3) / 32(4)%     |
| **CN = 5**  | 94(3) / 97(4)% | 96(5) / 92(7)%    | 88(4) / 84(5)%    | 58(4) / 61(6)%     |
| **CN = 6**  | 0(0) / 0(0)%   | 2.0(9) / 1.9(8)%  | 0(0) / 0(0)%      | 0.8(4) / 0.8(5)%   |
| **Average** | 4.97(2)        | 4.96(3)           | 4.83(3)           | 4.56(5)            |
| **Total**   | 97(3)          | 104(6)            | 105(4)            | 96(6)              |
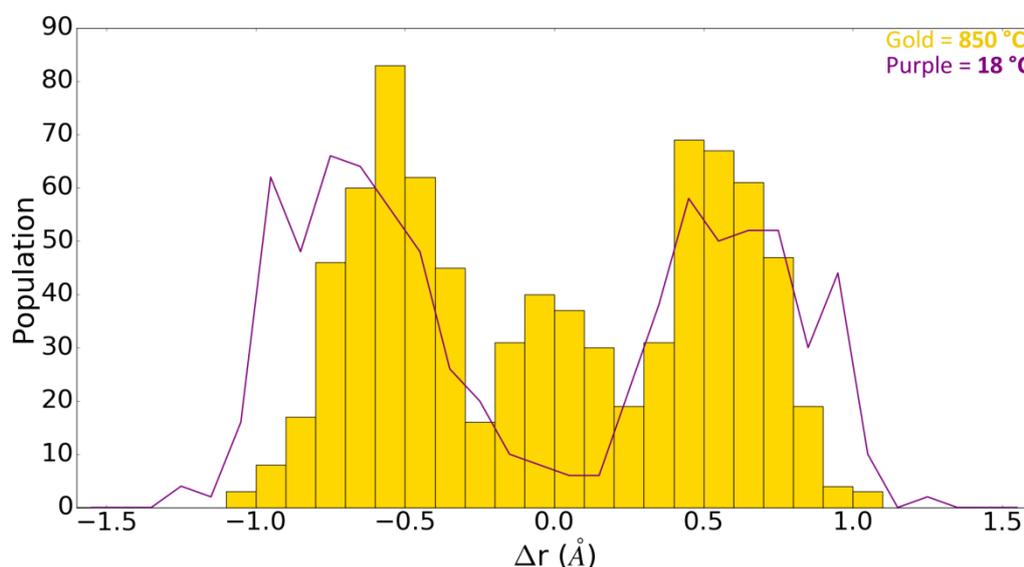


**Figure 4.30 –** The histogram of ΔGe–O$_{int}$ distances in 850 °C La$_{10}$(GeO$_4$)$_6$O$_3$ model **[SC5, P2]** with **[SC4, P1]** superimposed.

The GeO$_5$ bond angle distributions (Figure 4.29d) show a more marked change on heating. In particular, the number of bond angles at ~140° appears to decrease significantly. The change in the GeO$_5$ bond angle distributions can be further quantified by investigating the distribution of the τ values. Figure 4.31 shows the histograms of τ at 850°C with the room-temperature values

superimposed. It shows that the GeO$_5$ polyhedra have become more trigonal bipyramidal in character at 850 °C than at room temperature. This is shown by the GeO$_5$ bond angle distributions (Figure 4.29d), as well as by the increase in the number of Ge$_2$O$_9$ units.
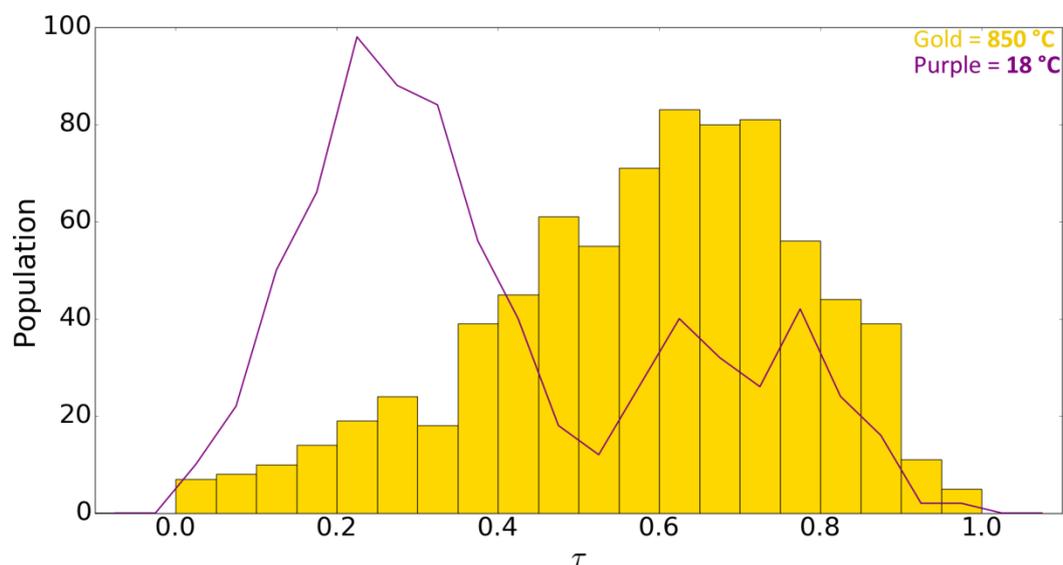


**Figure 4.31** – Histogram of $\tau$ values found in La$_{10}$(GeO$_4$)$_6$O$_3$ at 850 °C from model **[SC5, P2]** with the room temperature model **[SC4, P1]** superimposed.
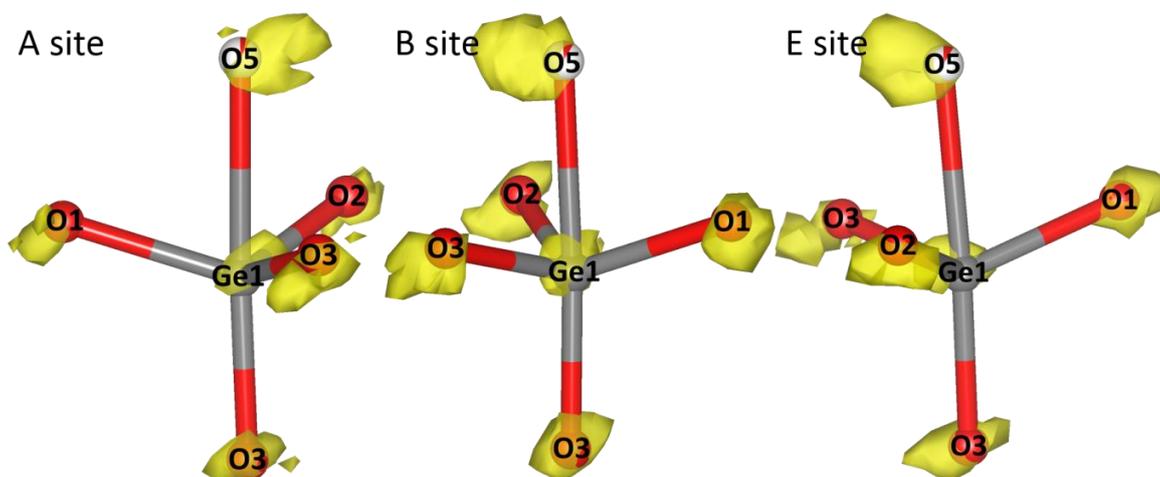


**Figure 4.32** – The average structure of La$_{10}$(GeO$_4$)$_6$O$_3$ at 850 °C with atomic density maps of GeO$_5$ around the (a) A site; (b) B site and (c) E site. Yellow clouds represent 0.2 × 0.2 × 0.2 Å$^3$ voxels where at least 1.2 atoms are present.

The atomic density maps of Ge atoms corresponding to the three symmetry unique sites in the *P*-1 structure are shown in Figure 4.32. The important observations shown by Figure 4.32 are that all sites are similar, but that the O5 density clouds are significantly larger than at room temperature (compare with Figure 4.26). This suggests significant disorder around the inversion centre and a rapid hopping of O$_{int}$ between adjacent tetrahedra. This is reflected in the $\tau$ histogram of Figure 4.31, which shows a significant shift to $\tau \approx 1$.
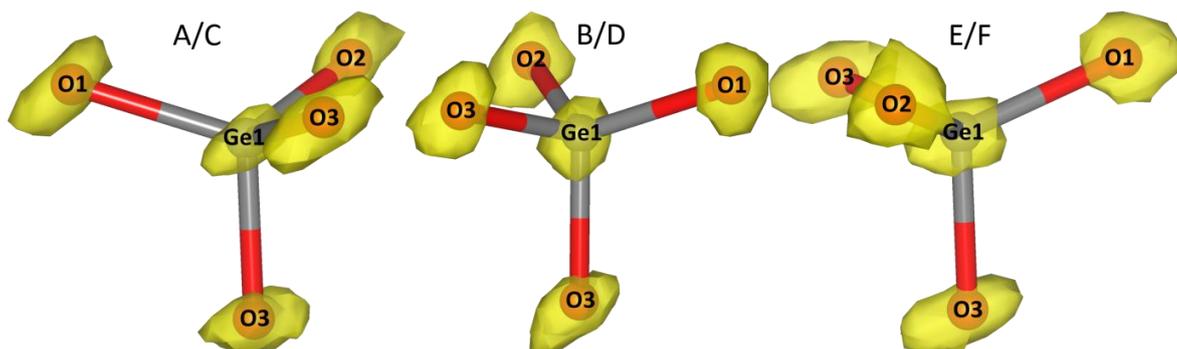
**Figure 4.33 –** The average structure of $GeO_4$ of $La_{10}(GeO_4)_6O_3$ at 850 °C from model **[SC5, P2]**. The yellow clouds represent a 0.2 × 0.2 × 0.2 Å$^3$ voxel with at least 3.9 atoms present.

Atomic density maps of the $O_{int}$-free $GeO_4$ tetrahedra (Figure 4.27) show no differences between the $GeO_4$ near the A, B and F sites at 850 °C – all appear tetrahedral. This is because the distortions caused by the high population of the B site are no longer present at high temperature as the $O_{int}$ are more evenly distributed across all six sites.

### 4.3.2.6 $La_8Bi_2(GeO_4)_6O_3$ – room temperature and high temperature

Total scattering analysis was performed on data collected on the impurity-free sample MSC046. Big box modelling was performed with four room temperature configurations and three 800 °C configurations (see Table 4.17) and the same analyses that were performed on $La_{10}(GeO_4)_6O_3$ were repeated. This report will only discuss the analyses of one room temperature model (**[SC4, P1]**) and one 800 °C model (**[SC5, P2]**), as similar fits and conclusions were obtained with the other models. Figure 4.34 gives representative PDF and Bragg fits from both of these models. The fits for the $F(Q)$ data obtained after the final refinement are given in Appendix A. Whilst some of the numerical $\chi^2$ values are high, this is caused by small experimental uncertainties in the data and the relative weightings applied. The visual fits are excellent (Table 4.30).
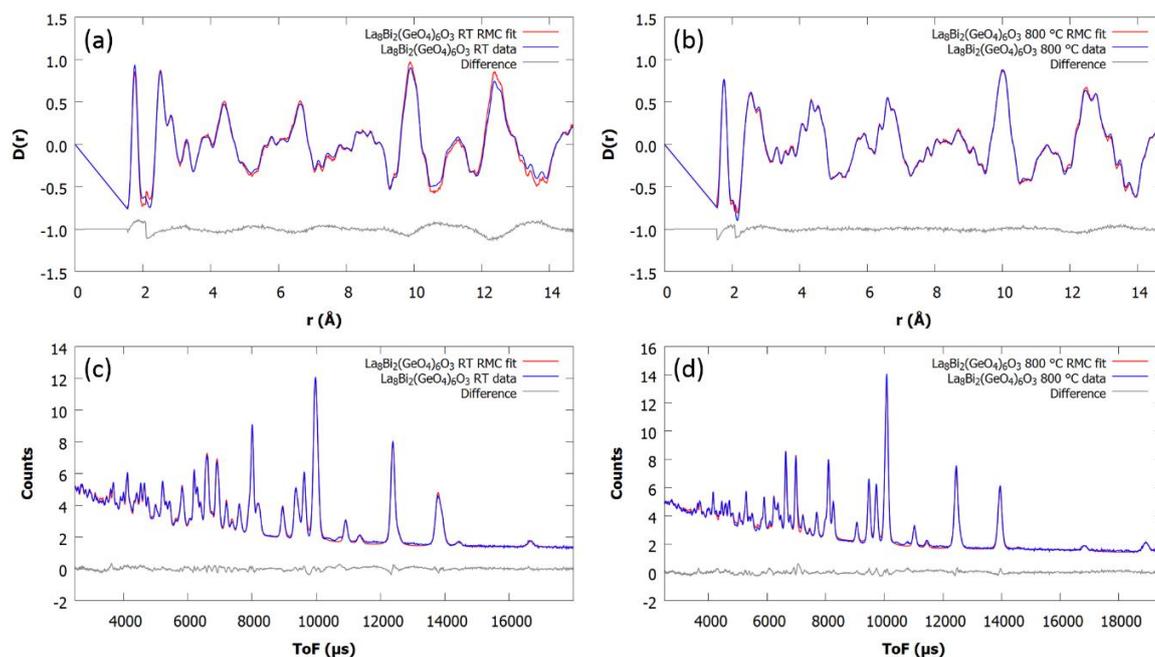
**Figure 4.34 –** Representative PDF fits expressed as $D(r)$ of $La_8Bi_2(GeO_4)_6O_3$ (a) room temperature model **[SC4, P1]**, $\chi_{PDF}^2$ = 18.73; (b) 800 °C model **[SC5, P2]**, $\chi_{PDF}^2$ = 4.385; and Bragg fits of (c) **[SC4, P1]**, $\chi^2_{Bragg}$ = 25.55; (d) **[SC5, P2]**, $\chi^2_{Bragg}$ = 28.70.

**Table 4.30 – The goodness of fit values obtained in $La_8Bi_2(GeO_4)_6O_3$ room temperature model** [SC4, P1] **and 800 °C model** [SC5, P2]**. The $\chi^2_{F(Q)}$ reported were obtained from the final fits with the $F(Q)$ data rescaled.**

| $T$ (°C) | Model | $\chi^2_{dof}$ | $\chi^2_{PDF}$ | $\chi^2_{Bragg}$ | $\chi^2_{F(Q)}$ |
|---|---|---|---|---|---|
| 18 | [SC4, P1] | 8.21(6) | 18.9(2) | 25.6(2) | 0.317(3) |
| 800 | [SC5, P2] | 7.99(5) | 4.8(1) | 30.5(2) | 0.256(6) |

The number of $O_{int}$ atoms on each of the crystallographic sites was counted in both models. The results are presented in Table 4.30. At room temperature, there is a clustering of $O_{int}$ atoms on the B site, whilst the next two most populated sites are the A site and F site. The A site was found to be the most populated site through crystallographic analysis. At high temperature, the $O_{int}$ atoms remain evenly distribution across all six sites. Geometric analyses of the bond distance and angle distributions were performed and are shown in Figure 4.34. The populations of **[SC4, P1]** have been doubled here and in later histograms as half of the number of configurations of **[SC5, P2]** were used.

**Table 4.30 – the number of O$_{int}$ on each position in room temperature La$_8$Bi$_2$(GeO$_4$)$_6$O$_3$  18 °C crystallographic (**SC1**),  room temperature model** [SC4, P1] **and 800 °C model** [SC5, P2]**.**

|   | SC1 (18 °C) | [SC4, P1] 18 °C | [SC5, P2] 800 °C |
|---|---|---|---|
| **A** | 41 | 25.8(8) | 12(2) |
| **B** | 35 | 42(1) | 19(3) |
| **C** | 0 | 7.3(4) | 16(3) |
| **D** | 24 | 5.3(4) | 19(2) |
| **E** | 0 | 3(1) | 19(3) |
| **F** | 0 | 17.3(4) | 17(2) |

The bond distances in the GeO$_4$ tetrahedra (Figure 4.34a) show a steep decrease in population at $r \geq 2.1$ Å as a result of the termination of the first coordination sphere of Ge–O bonds. The population slightly increases again at $r > 2.2$ Å in both room temperature and high temperature models. The observations are similar to those for La$_{10}$(GeO$_4$)$_6$O$_3$. The bond angles of the GeO$_4$ tetrahedra (Figure 4.34c) follow a single Gaussian distribution, although both distributions are broad (Table 4.28). At room temperature, the mean of the GeO$_4$ angles is 108.0(2)° with a FWHM of 30.2(3)°, which shows a large amount of disorder for a room temperature structure. This is possibly because of the wider distribution of O$_{int}$ atoms across the available sites in La$_8$Bi$_2$(GeO$_4$)$_6$O$_3$ than in La$_{10}$(GeO$_4$)$_6$O$_3$. Furthermore, the presence of Bi$^{3+}$ also increases disorder. At 800 °C, the distribution is even broader, with FWHM = 36.1(3)°. Both values are ~7° larger than for La$_{10}$(GeO$_4$)$_6$O$_3$.

The bond distance distribution in the GeO$_5$ polyhedra (Figure 4.34b) shows a larger relative population at $r > 2.2$ Å in the 800 °C model (**[SC5, P2]**). Coordination numbers were determined using the same cut-off distance of 2.2 Å as previously defined for La$_{10}$(GeO$_4$)$_6$O$_3$and are included in Table 4.29 (shown earlier).
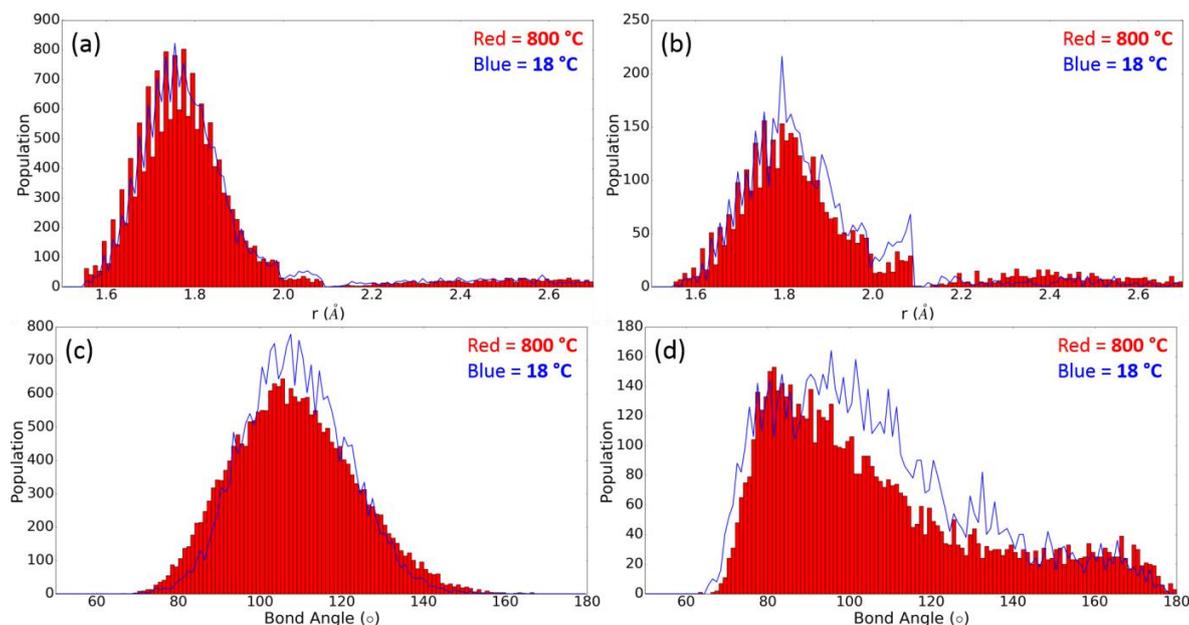
**Figure 4.34** – Histograms of La$_8$Bi$_2$(GeO$_4$)$_6$O$_3$ at 800 °C **[SC5, P2]** (red bars) with the room temperature model **[SC4, P1]** (blue line) superimposed: (a) Ge–O bond distances in GeO$_4$; (b) Ge–O bond distances in GeO$_5$; (c) O–Ge–O bond angles in GeO$_4$; (d) O–Ge–O bond distances in GeO$_5$.

The 800 °C model has a significant number of Ge atoms with nearby O$_{int}$ atoms that adopt a "fourfold" coordination by our definition of $r \leq 2.2$ Å (32(4)%), whilst 61(6)% of them adopt fivefold coordination. These atoms are expected to adopt only fivefold coordination as they are surrounded by four completely occupied O atoms and one O$_{int}$ atom. It can be seen by examining the bond distances of these "GeO$_5$" units (Figure 4.34b) that there is a small, but significant population at $r > 2.2$ Å in **[SC5, P2]**. This indicates that several of the O atoms have moved to a distance of $> 2.2$ Å from the Ge atoms, leading to a core GeO$_4$ unit which is only weakly coordinated to a fifth oxygen. This elongation does not occur in the room temperature model (**[SC4, P1]**).

An analysis of the local environment of the O$_{int}$ atoms through the $\Delta$Ge–O$_{int}$ distances, shown in Figure 4.35, reveals that the majority of the O$_{int}$ atoms are present in GeO$_5$ units at both room temperature (**[SC4, P1]**) and 800 °C (**[SC5, P2]**) than in Ge$_2$O$_9$ units which are present in only very small numbers. However, a larger proportion of the O$_{int}$ atoms are in Ge$_2$O$_9$ units, defined by $0 \leq \Delta$Ge–O$_{int} \leq 0.25$ Å. (12(4), 4.(1)% of all Ge atoms) at room temperature than at 800 °C [5(3), 2(1)%], where they are almost non-existent.
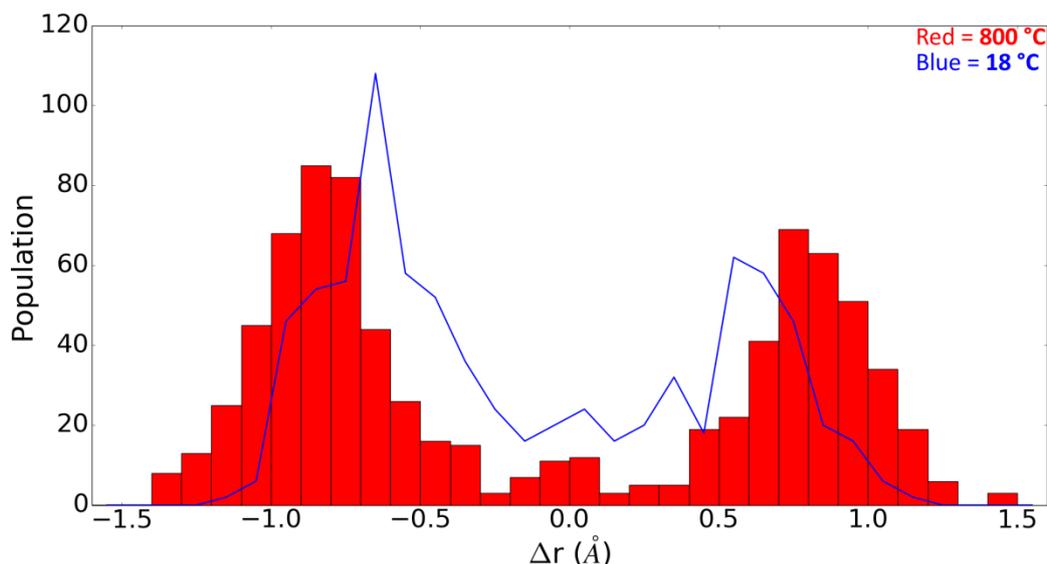
**Figure 4.35 -** The histogram of ΔGe–O$_{int}$ distances in 800 °C La$_8$Bi$_2$(GeO$_4$)$_6$O$_3$ model **[SC5, P2]** with **[SC4, P1]** superimposed.

The bond angle distributions of the GeO$_5$ polyhedra (Figure 4.34d) show a more noticeable change from room temperature to 800 °C compared to the GeO$_4$ bond angle distributions; the distribution has broadened and the proportion of the population at ~90° has increased. However, the bond angle distribution shows that despite the apparent increase in Ge atoms with a "fourfold" coordination in the 800 °C model, the geometry that they adopt is not tetrahedral. This is indicated by the fact that the largest peak is at ~90° and there is no additional maximum at ~109.5°. The geometries can be further described by comparing the $\tau$ values obtained in each model, which are shown in Figure 4.36.

At room temperature, the majority of the GeO$_5$ polyhedra have a coordination geometry more similar to that of a square pyramid as found in La$_{10}$(GeO$_4$)$_6$O$_3$. In contrast, at 800 °C, the GeO$_5$ adopt more of a geometry intermediate between square pyramids and trigonal bipyramids as the majority are in the range of $0.4 \leq \tau \leq 0.6$. It should be noted that the population histogram for the room temperature model is relatively larger, as not only do Ge$_2$O$_9$ units lead to an increased number of Ge atoms with nearby O$_{int}$, but Figure 4.36 excludes any polyhedron where CN ≠ 5. As previously discussed, the cut-off point of < 2.2 Å leads to a large number of apparently fourfold coordination Ge atoms. This means that only ~60 Ge atoms per configuration are included in Figure 4.36 for **[SC5, P2]** as opposed to the ~90 per configuration in **[SC4, P1]**. The definition of a coordinating O atom was extended to Ge–O < 2.3 Å and the analysis repeated, but this only changed the area of the distribution, and not its shape. The geometric analysis leads us to conclude that at high temperature the GeO5 environments are distorted arrangements,

intermediate between square pyramids and trigonal bipyramids with one elongated bond to oxygen.
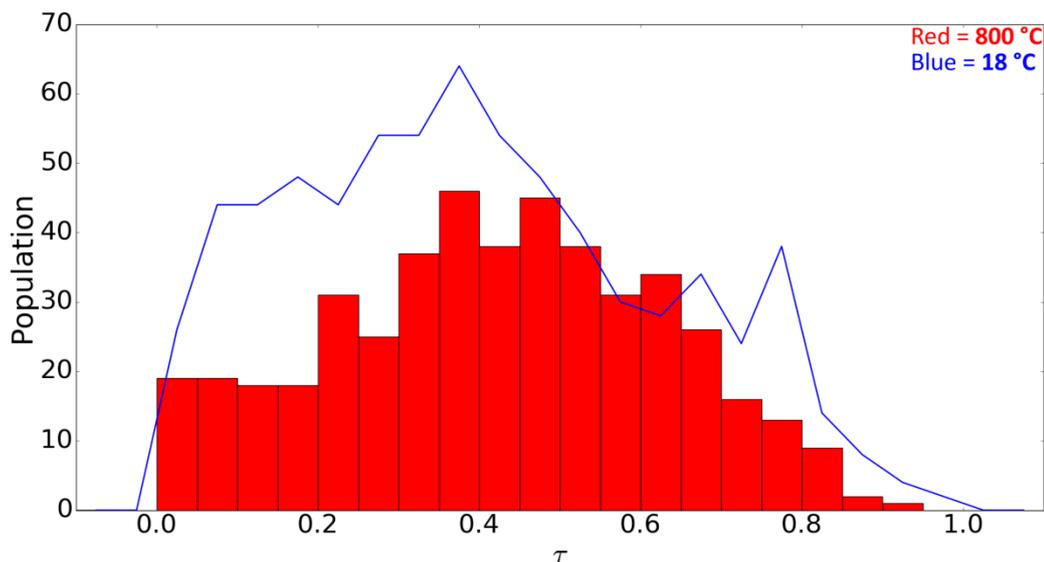


**Figure 4.36 –** Histogram of $\tau$ values found in $La_8(GeO_4)_6O_3$ at 800 °C from model **[SC5, P2]** with the room temperature model **[SC4, P1]** superimposed.

Figure 4.37 compares the atomic density maps of the $GeO_5$ polyhedra (*i.e.* Ge environments where Ge–$O_{int}$ < 2.2 Å) in room temperature and 800 °C $La_8Bi_2(GeO_4)_6O_3$. At room temperature, the regular site O atoms near the A site (Figure 4.37 top) move in order to accommodate the O5_A atoms, as was seen in $La_{10}(GeO_4)_6O_3$ (Figure 4.26a). The regular site O atoms at the B and the F sites do not need to move as much in order to accommodate the O5_B and O5_F atoms respectively. The O5_F atoms are likely responsible for the $Ge_2O_9$ units, as they are almost in the centre point between two $GeO_4$ tetrahedra. The atomic density maps of the 800 °C model (Figure 4.37 bottom row) are more diffuse, particularly around the $O_{int}$ sites. In contrast to $La_{10}(GeO_4)_6O_3$ (Figure 4.32), the $O_{int}$ atoms do not overlap across the inversion centre. The Ge–$O_{int}$ distances are 1.92 and 2.47 Å in the average structure of $La_8Bi_2(GeO_4)_6O_3$, whilst they are 2.08 and 2.29 Å in $La_{10}(GeO_4)_6O_3$. This results in the $O_{int}$ atoms becoming more localised on one $GeO_5$ polyhedron as opposed to forming $Ge_2O_9$ units. In order to determine if the starting model influenced the outcome, a further refinement was performed using a starting configuration where the $O_{int}$ was placed 0.01 Å away from the special position at (0.501, 0, 0) in the unit cell (**[SC8, P2]**), the results of which are shown in Figure A.11 (Appendix A).
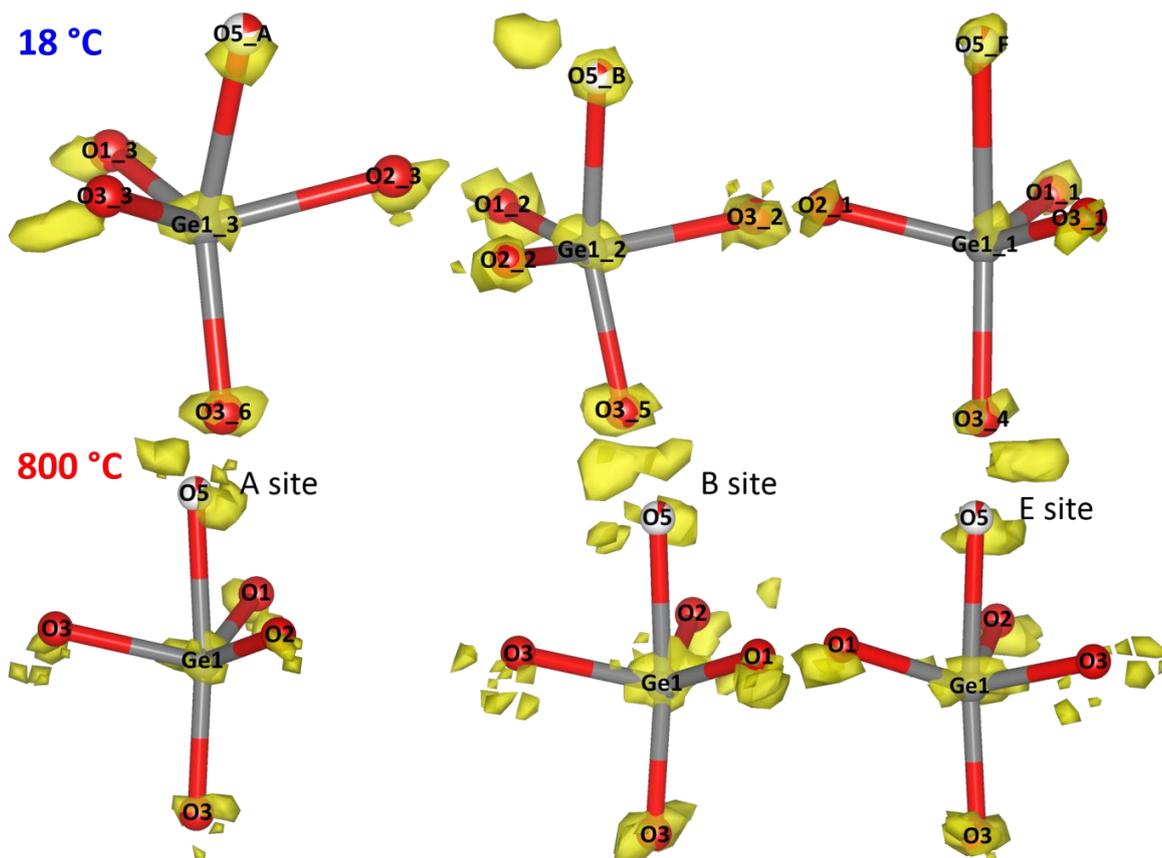
**Figure 4.37** – The average structure of La$_8$Bi$_2$(GeO$_4$)$_6$O$_3$ at room temperature **[SC4, P1]** (top row) and 800 °C **[SC5, P2]** (bottom row) with atomic density maps superimposed. Yellow clouds represent 0.2 × 0.2 × 0.2 Å$^3$ voxels where at least 1.2 atoms are present.

Atomic density maps of the GeO$_4$ tetrahedra are shown in Figure 4.38. The average structure of the GeO$_4$ tetrahedra at the A and B sites at room temperature is slightly distorted, which we attribute to the presence of O5_A and O5_B atoms on neighbouring Ge units. The atomic density maps of the GeO$_4$ tetrahedra represent a regular tetrahedron more than the average structure model but are still distorted. This is similar to what was seen in La$_{10}$(GeO$_4$)$_6$O$_3$ at room temperature (Figure 4.27), but as the O$_{int}$ atoms are more evenly distributed across the A and B sites, the total distortion of the A and B sites in La$_8$Bi$_2$(GeO$_4$)$_6$O$_3$ is less severe. The Ge1_1 site (Figure 4.38 top right), which is the adjacent Ge site to the E and F sites, show little distortion, despite the fact that there are 17 O5_F atoms. This is likely from a combination of the F atoms being low in population and the fact that they are positioned almost in the centre of two GeO$_4$ tetrahedra, so the impact on neighbouring GeO$_4$ units is minimised. In the python script employed to extract this atomic density shown in Figure 4.38, the atomic density from the Ge$_2$O$_9$ units is not included. At high temperature (Figure 4.38 bottom), the atomic density maps are very diffuse, revealing the large amount of disorder in La$_8$Bi$_2$(GeO$_4$)$_6$O$_3$, which is reflected in the very broad bond angle distribution (Figure 4.34c) of the GeO$_4$ tetrahedra.
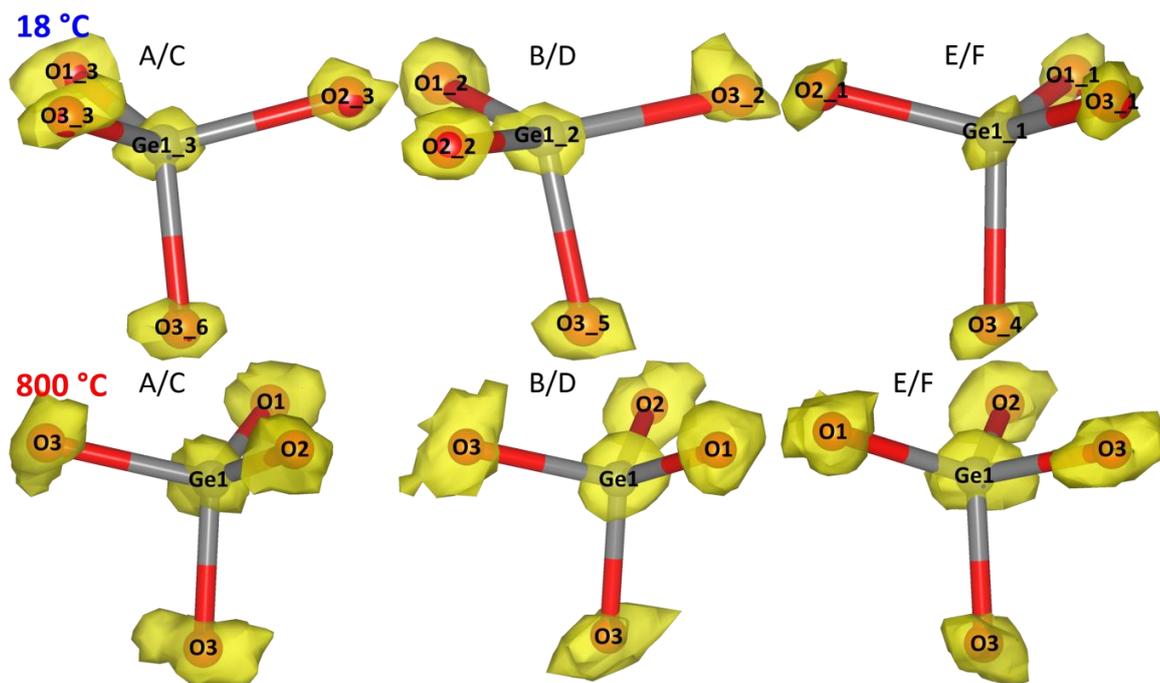
**Figure 4.38 –** The average structure of La$_8$Bi$_2$(GeO$_4$)$_6$O$_3$ at room temperature **[SC4, P1]** (top row) and 800 °C **[SC5, P2]** (bottom row) with the atomic density maps of the GeO$_4$ tetrahedra superimposed. The yellow clouds represent a 0.2 × 0.2 × 0.2 Å$^3$ voxel with at least 3.9 atoms present.

## 4.4 Conclusions

The work described in this chapter leads us to the following conclusions:

1. La$_8$Sr$_2$(GeO$_4$)$_6$O$_2$ adopts a simple $P6_3/m$ structure, rather than the $P2_1/m$ structure previously speculated,[14] but a range of La$_{8+x}$Sr$_{2-x}$(GeO$_4$)$_6$O$_{2+x/2}$ (0 ≤ $x$ ≤ 2) compositions forms when the synthesis time is not sufficient or a lower temperature is used.

2. La$_{10}$(GeO$_4$)$_6$O$_3$ and La$_8$Bi$_2$(GeO$_4$)$_6$O$_3$ both adopt $P$-1 symmetry at room temperature and $P6_3/m$ at high temperature, as previously reported.[5, 19, 21] La$_{10}$(GeO$_4$)$_6$O$_3$ shows more distortion at room temperature from a hexagonal metric than La$_8$Bi$_2$(GeO$_4$)$_6$O$_3$.

3. Rietveld refinement shows that the O$_{int}$ atoms lie between GeO$_4$ tetrahedra in La$_8$R$_2$(GeO$_4$)$_6$O$_3$ (R = La, Bi). Multiple sites are occupied simultaneously, but some sites are favoured at room temperature over others. The B site is favoured in La$_{10}$(GeO$_4$)$_6$O$_3$ and the A site is favoured in La$_8$Bi$_2$(GeO$_4$)$_6$O$_3$. The favouring of certain sites causes distortions, driving the phase transition to $P$-1. This result has revealed the cause of the phase transition.

4. High quality structural models are reported from combined X-ray and neutron Rietveld refinements.

5. Small box PDF analysis and RMCProfile analysis of La$_8$Sr$_2$(GeO$_4$)$_6$O$_2$ shows that the local structure does not deviate greatly from the average structure. This gives confidence in the RMC refinement methodology employed.

6. Local structure analysis has shown that the O$_{int}$ atoms are present in GeO$_5$ polyhedra in La$_8$R$_2$(GeO$_4$)$_6$O$_3$ (R = La, Bi) at room temperature, rather than Ge$_2$O$_9$ units. There are perhaps more Ge$_2$O$_9$ units in R = Bi. This conclusion is robust between different RMC models. At 850 °C, the number of units that could be classified as Ge$_2$O$_9$ increases in La$_{10}$(GeO$_4$)$_6$O$_3$ due to the increased motion of O$_{int}$ atoms and symmetry of the structure. The fact that there appear to be more Ge$_2$O$_9$ units in La$_{10}$(GeO$_4$)$_6$O$_3$ in the high-temperature, hexagonal structure than the low-temperature, triclinic structure possibly suggests that the number of Ge$_2$O$_9$ units is correlated with the symmetry. In this respect, La$_8$Bi$_2$(GeO$_4$)$_6$O$_3$ is more similar to the high-temperature structure of La$_{10}$(GeO$_4$)$_6$O$_3$ than the room-temperature structure. Therefore, the number of Ge$_2$O$_9$ units could be another parameter to suggest that La$_8$Bi$_2$(GeO$_4$)$_6$O$_3$ is more "hexagonal-like" at room temperature than La$_{10}$(GeO$_4$)$_6$O$_3$.

7. Analysis of the GeO$_5$ polyhedra shows a strong tendency towards square pyramidal geometry at room temperature. This breaks the threefold symmetry of the high-temperature structure and is a possible driving force for the low temperature *P*-1 symmetry.

8. There is good evidence that GeO$_4$ tetrahedra near to GeO$_5$ groups have local distortions in La$_{10}$(GeO$_4$)$_6$O$_3$.

9. At high temperature, the GeO$_5$ polyhedra in La$_{10}$(GeO$_4$)$_6$O$_3$ adopt a more trigonal bipyramid character. This is also a reflection of the increase in Ge$_2$O$_9$ units and a result of the higher average symmetry. Previous computation studies suggest that the most common conduction mechanism occurs through an interstitialcy mechanism that involves movement of O$^{2-}$ along the *c* axis between GeO$_4$ units *via* normal-site O$^{2-}$ and O$_{int}$.[44, 46, 48] These results suggest that the increased presence of trigonal bipyramids is linked with increased conductivity. A similar situation occurs in La$_8$Bi$_2$(GeO$_4$)$_6$O$_3$, although the increase in trigonal bipyramidal character is less dramatic.

10. The local structure of La$_8$Bi$_2$(GeO$_4$)$_6$O$_3$ at room temperature shows more disorder than La$_{10}$(GeO$_4$)$_6$O$_3$ as evidenced by the tetrahedral bond distance and angle distributions. This is linked with the smaller deviation from average hexagonal symmetry. There is also La$^{3+}$/Bi$^{3+}$ as well as O$_{int}$ disorder in La$_8$Bi$_2$(GeO$_4$)$_6$O$_3$, whilst in La$_{10}$(GeO$_4$)$_6$O$_3$ disorder only arises from the O$_{int}$ atoms.

11. The increased local disorder of O$_{int}$ at higher temperatures presumably enables hopping to neighbouring GeO$_5$ positions and is likely to be part of the migration mechanism. A significant increase in the diffusivity of the atomic density clouds is observed in both GeO$_4$ and GeO$_5$ from room temperature to high temperature to support this conclusion.

## 4.5 References

1. White, T. J.; Dong, Z., Structural derivation and crystal chemistry of apatites. *Acta Crystallographica Section B: Structural Science* **2003,** *59* (1), 1-16.
2. Baikie, T.; Ferraris, C.; Klooster, W. T.; Madhavi, S.; Pramana, S. S.; Pring, A.; Schmidt, G.; White, T. J., Crystal chemistry of mimetite, Pb$_{10}$(AsO$_4$)$_6$Cl$_{1.48}$O$_{0.26}$, and finnemanite, Pb$_{10}$(AsO$_3$)$_6$Cl$_2$. *Acta Crystallographica Section B: Structural Crystallography and Crystal Chemistry* **2008,** *64* (1), 34-41.
3. Sudarsanan, K.; Mackie, P. E.; Young, R. A., Comparison of synthetic and mineral fluorapatite, Ca$_5$(PO$_4$)$_3$F, in crystallographic detail. *Materials Research Bulletin* **1972,** *7* (11), 1331-1337.
4. Okudera, H.; Masubuchi, Y.; Kikkawa, S.; Yoshiasa, A., Structure of oxide ion-conducting lanthanum oxyapatite, La$_{9.33}$(SiO$_4$)$_6$O$_2$. *Solid State Ionics* **2005,** *176* (15), 1473-1478.
5. Pramana, S. S.; Klooster, W. T.; White, T., Framework 'interstitial' oxygen in La$_{10}$(GeO$_4$)$_5$(GeO$_5$)O$_2$ apatite electrolyte. *Acta Crystallographica Section B: Structural Crystallography and Crystal Chemistry* **2007,** *63* (4), 597-602.
6. Kendrick, E.; Islam, M. S.; Slater, P. R., Atomic-scale mechanistic features of oxide ion conduction in apatite-type germanates. *Chemical Communications* **2008,** (6), 715-717.
7. Orera, A.; Baikie, T.; Panchmatia, P.; White, T.; Hanna, J.; Smith, M. E.; Islam, M. S.; Kendrick, E.; Slater, P. R., Strategies for the Optimisation of the Oxide Ion Conductivities of Apatite-Type Germanates. *Fuel Cells* **2011,** *11* (1), 10-16.
8. Pramana, S. S.; Klooster, W. T.; White, T. J., A taxonomy of apatite frameworks for the crystal chemical design of fuel cell electrolytes. *Journal of Solid State Chemistry* **2008,** *181* (8), 1717-1722.
9. Nakayama, S.; Aono, H.; Sadaoka, Y., Ionic Conductivity of Ln$_{10}$(SiO$_4$)$_6$O$_3$ (Ln= La, Nd, Sm, Gd and Dy). *Chemistry Letters* **1995,** (6), 431-432.
10. León-Reina, L.; Martin-Sedeno, M.; Losilla, E.; Cabeza, A.; Martinez-Lara, M.; Bruque, S.; Marques, F.; Sheptyakov, D.; Aranda, M., Crystalchemistry and oxide ion conductivity in the lanthanum oxygermanate apatite series. *Chemistry of Materials* **2003,** *15* (10), 2099-2108.
11. León-Reina, L.; Losilla, E. R.; Martínez-Lara, M.; Bruque, S.; Aranda, M. A. G., Interstitial oxygen conduction in lanthanum oxy-apatite electrolytes. *Journal of Materials Chemistry* **2004,** *14* (7), 1142-1149.
12. Sansom, J. E. H.; Slater, P. R., Oxide ion conductivity in the mixed Si/Ge apatite-type phases La$_{9.33}$Si$_{6-x}$Ge$_x$O$_{26}$. *Solid State Ionics* **2004,** *167* (1), 23-27.
13. Fujii, K.; Yashima, M.; Hibino, K.; Shiraiwa, M.; Fukuda, K.; Nakayama, S.; Ishizawa, N.; Hanashima, T.; Ohhara, T., High oxide-ion conductivity in Si-deficient La$_{9.565}$(Si$_{5.826}$□$_{0.174}$)O$_{26}$ apatite without interstitial oxygens due to the overbonded channel oxygens. *Journal of Materials Chemistry A* **2018,** *6* (23), 10835-10846.
14. Pramana, S. S.; White, T.; Schreyer, M. K.; Ferraris, C.; Slater, P. R.; Orera, A.; Bastow, T.; Mangold, S.; Doyle, S.; Liu, T., Pseudomorphic 2$A$→ 2$M$→ 2$H$ phase transitions in lanthanum strontium germanate electrolyte apatites. *Dalton Transactions* **2009,** (39), 8280-8291.
15. Balachandran, P. V.; Rajan, K.; Rondinelli, J. M., Electronically driven structural transitions in A$_{10}$(PO$_4$)$_6$F$_2$ apatites (A = Ca, Sr, Pb, Cd and Hg). *Acta Crystallographica Section B: Structural Crystallography and Crystal Chemistry* **2014,** *70* (3), 612-615.
16. Otto, H. H., Crystal and domain structure of acentric Bi$_2$Pb$_3$(GeO$_4$)$_3$ apatite. *Crystal Research and Technology* **2015,** *50* (12), 922-928.
17. Arikawa, H.; Nishiguchi, H.; Ishihara, T.; Takita, Y., Oxide ion conductivity in Sr-doped La$_{10}$Ge$_6$O$_{27}$ apatite oxide. *Solid State Ionics* **2000,** *136*, 31-37.
18. Li, H.; Baikie, T.; Pramana, S. S.; Shin, J. F.; Slater, P. R.; Brink, F.; Hester, J.; Wallwork, K.; White, T. J., Synthesis and characterisation of vanadium doped alkaline earth lanthanum germanate oxyapatite electrolyte. *Journal of Materials Chemistry* **2012,** *22* (6), 2658-2669.
19. Tate, M. L.; Blom, D. A.; Avdeev, M.; Brand, H. E. A.; McIntyre, G. J.; Vogt, T.; Evans, I. R., New Apatite-Type Oxide Ion Conductor, Bi$_2$La$_8$[(GeO$_4$)$_6$]O$_3$: Structure, Properties, and Direct Imaging of Low-Level Interstitial Oxygen Atoms Using Aberration-Corrected Scanning Transmission Electron Microscopy. *Advanced Functional Materials* **2017,** *27* (8), 1605625.
20. Kendrick, E.; Slater, P. R., Synthesis of hexagonal lanthanum germanate apatites through site selective isovalent doping with yttrium. *Materials Research Bulletin* **2008,** *43* (8), 2509-2513.
21. Abram, E. J.; Kirk, C. A.; Sinclair, D. C.; West, A. R., Synthesis and characterisation of lanthanum germanate-based apatite phases. *Solid State Ionics* **2005,** *176* (23), 1941-1947.
22. Tao, S.; Irvine, J. T. S., Preparation and characterisation of apatite-type lanthanum silicates by a sol-gel process. *Materials Research Bulletin* **2001,** *36* (7), 1245-1258.

23.     McFarlane, J.; Barth, S.; Swaffer, M.; Sansom, J. E. H.; Slater, P. R., Synthesis and conductivities of the apatite-type systems, La$_{9.33+x}$Si$_{6-y}$M$_y$O$_{26+z}$ (M=Co, Fe, Mn) and La$_8$Mn$_2$Si$_6$O$_{26}$. *Ionics* **2002,** *8* (1), 149-154.

24.     Orera, A.; Slater, P. R., New Chemical Systems for Solid Oxide Fuel Cells. *Chemistry of Materials* **2009,** *22* (3), 675-690.

25.     Inoubli, A.; Kahlaoui, M.; Sobrados, I.; Chefi, S.; Madani, A.; Sanz, J.; Amara, A. B. H., Influence of anionic vacancies on the conductivity of La$_{9.33}$Si$_{6-x}$Al$_x$O$_{26-x/2}$ oxide conductors with an oxyapatite structure. *Journal of Power Sources* **2014,** *271*, 203-212.

26.     Yoshioka, H.; Mieda, H.; Funahashi, T.; Mineshige, A.; Yazawa, T.; Mori, R., Fabrication of apatite-type lanthanum silicate films and anode supported solid oxide fuel cells using nano-sized printable paste. *Journal of the European Ceramic Society* **2014,** *34* (2), 373-379.

27.     Marques, F. M. B.; Kharton, V. V.; Naumovich, E. N.; Shaula, A. L.; Kovalevsky, A. V.; Yaremchenko, A. A., Oxygen ion conductors for fuel cells and membranes: selected developments. *Solid State Ionics* **2006,** *177* (19), 1697-1703.

28.     Yin, G.-C.; Yin, H.; Zhong, L.-H.; Sun, M.-L.; Zhang, J.-K.; Xie, X.-J.; Cong, R.-D.; Wang, X.; Gao, W.; Cui, Q.-L., Crystal structure and ionic conductivity of Mg-doped apatite-type lanthanum silicates La$_{10}$Si$_{6-x}$Mg$_x$O$_{27-x}$ ( *x* = 0–0.4). *Chinese Physics B* **2014,** *23* (4), 048202.

29.     Xiang, J.; Liu, Z.-G.; Ouyang, J.-H.; Yan, F.-Y., Ionic conductivity of oxy-apatite La$_{10}$Si$_{6-x}$In$_x$O$_{27-\delta}$ solid electrolyte ceramics. *Journal of Power Sources* **2014,** *251*, 305-310.

30.     León-Reina, L.; Losilla, E. R.; Martínez-Lara, M.; Martín-Sedeño, M. C.; Bruque, S.; Núñez, P.; Sheptyakov, D. V.; Aranda, M. A. G., High Oxide Ion Conductivity in Al-Doped Germanium Oxyapatite. *Chemistry of Materials* **2005,** *17* (3), 596-600.

31.     Marrero-Lopez, D.; Diaz-Carrasco, P.; Pena-Martinez, J.; Ruiz-Morales, J. C.; Ramos-Barrado, J. R., Lanthanum Germanate-Based Apatites as Electrolyte for SOFCs. *Fuel Cells* **2011,** *11* (1), 65-74.

32.     Kendrick, E.; Islam, M. S.; Slater, P. R., Developing apatites for solid oxide fuel cells: insight into structural, transport and doping properties. *Journal of Materials Chemistry* **2007,** *17* (30), 3104-3111.

33.     Orera, A.; Sanjuan, M. L.; Kendrick, E.; Orera, V. M.; Slater, P. R., Raman spectroscopy studies of apatite-type germanate oxide ion conductors: correlation with interstitial oxide ion location and conduction. *Journal of Materials Chemistry* **2010,** *20* (11), 2170-2175.

34.     Orera, A.; Slater, P. R., Water incorporation studies in apatite-type rare earth silicates/germanates. *Solid State Ionics* **2010,** *181* (3–4), 110-114.

35.     Tolchard, J. R.; Sansom, J. E. H.; Slater, P. R.; Islam, M. S., Effect of Ba and Bi doping on the synthesis and sintering of Ge-based apatite phases. *Journal of Solid State Electrochemistry* **2004,** *8* (9), 668-673.

36.     Tate, M. L.; Fuller, C. A.; Avdeev, M.; Brand, H. E. A.; McIntyre, G. J.; Radosavljevic Evans, I., Synthesis and characterisation of new Bi(iii)-containing apatite-type oxide ion conductors: the influence of lone pairs. *Dalton Transactions* **2017,** *46* (37), 12494-12499.

37.     Yin, G.; Yin, H.; Sun, M.; Zhong, L.; Zhang, J.; Cong, R.; Gao, W.; Cui, Q., New approach to improve the conductivity of apatite-type lanthanum germanate La$_{9.33}$Ge$_6$O$_{26}$ as electrolyte for IT-SOFCs. *RSC Advances* **2014,** *4* (31), 15968-15974.

38.     Fukuda, K.; Asaka, T.; Hara, S.; Berghout, A.; Bechade, E.; Masson, O.; Jouin, J.; Thomas, P., Crystal Structure and Oxide-Ion Conductivity of Highly Grain-Aligned Polycrystalline Lanthanum Germanate Oxyapatite Grown by Reactive Diffusion between Solid La$_2$GeO$_5$ and Gases GeO +1/2O$_2$. *Crystal Growth & Design* **2015,** *15* (7), 3435-3441.

39.     Ma, Y.; Moliere, M.; Yu, Z.; Fenineche, N.; Elkedim, O., Novel chemical reaction co-precipitation method for the synthesis of apatite-type lanthanum silicate as an electrolyte in SOFC. *Journal of Alloys and Compounds* **2017,** *723*, 418-424.

40.     Shannon, R. D.; Prewitt, C. T., Effective Ionic Radii in Oxides and Fluorides. *Acta Crystallographica Section B: Structural Crystallography and Crystal Chemistry* **1969**, 925-946.

41.     Kendrick, E.; Orera, A.; Slater, P. R., Neutron diffraction structural study of the apatite-type oxide ion conductor, La$_8$Y$_2$Ge$_6$O$_{27}$: location of the interstitial oxide ion site. *Journal of Materials Chemistry* **2009,** *19* (42), 7955-7958.

42.     Matsunaga, K., Ionic conduction mechanisms of apatite-type lanthanum silicate and germanate from first principles. *Journal of the Ceramic Society of Japan* **2017,** *125* (9), 670-676.

43.     León-Reina, L.; Porras-Vázquez, J. M.; Losilla, E. R.; Aranda, M. A. G., Phase transition and mixed oxide-proton conductivity in germanium oxy-apatites. *Journal of Solid State Chemistry* **2007,** *180* (4), 1250-1258.

44.     Imaizumi, K.; Toyoura, K.; Nakamura, A.; Matsunaga, K., Stable sites and diffusion pathways of interstitial oxide ions in lanthanum germanate. *Solid State Ionics* **2014,** *262*, 512-516.

45.     Nakayama, S.; Sakamoto, M., Preparation of apatite-type La$_{9.33}$Ge$_6$O$_{26}$ single-crystal from sintered ceramics by a seeding method and its oxide ionic conduction. *Solid State Ionics* **2013,** *253*, 47-52.

46.     Imaizumi, K.; Toyoura, K.; Nakamura, A.; Matsunaga, K., Cooperative oxide-ion conduction in apatite-type lanthanum germanate – A first principles study. *Journal of the Ceramic Society of Japan* **2017,** *125* (3), 105-111.

47.     Peet, J. R.; Piovano, A.; Johnson, M. R.; Evans, I. R., Location and orientation of lone pairs in apatite-type materials: a computational study. *Dalton Transactions* **2017,** *46* (46), 15996-15999.

48.     Peet, J. R.; Chambers, M. S.; Piovano, A.; Johnson, M. R.; Evans, I. R., Dynamics in Bi(iii)-containing apatite-type oxide ion conductors: a combined computational and experimental study. *Journal of Materials Chemistry A* **2018,** *6* (12), 5129-5135.

49.     Project, M. https://www.mantidproject.org/Main_Page (accessed 11/04/2019).

50.     Soper, A. K. *GudrunN and GudrunX*, 5; 2012.

51.     Coelho, A. *TOPAS Academic Version 6 Computer Software*, 6; Coelho Software: Brisbane, 2016.

52.     Tucker, M. G.; Keen, D. A.; Dove, M. T.; Goodwin, A. L.; Hui, Q., RMCProfile: reverse Monte Carlo for polycrystalline materials. *Journal of Physics: Condensed Matter* **2007,** *19* (33), 335218.

53.     Stephens, P., Phenomenological model of anisotropic peak broadening in powder diffraction. *Journal of Applied Crystallography* **1999,** *32* (2), 281-289.

54.     Brown, I. D.; Altermatt, D., Bond-valence parameters obtained from a systematic analysis of the Inorganic Crystal Structure Database. *Acta Crystallographica Section B: Structural Crystallography and Crystal Chemistry* **1985,** *41* (4), 244-247.

55.     Busing, W. R.; Levy, H. A., The effect of thermal motion on the estimation of bond lengths from diffraction measurements. *Acta Crystallographica* **1964,** *17* (2), 142-146.

56.     Addison, A. W.; Rao, T. N.; Reedijk, J.; van Rijn, J.; Verschoor, G. C., Synthesis, structure, and spectroscopic properties of copper(II) compounds containing nitrogen–sulphur donor ligands; the crystal and molecular structure of aqua[1,7-bis(N-methylbenzimidazol-2'-yl)-2,6-dithiaheptane]copper(II) perchlorate. *Journal of the Chemical Society, Dalton Transactions* **1984,** (7), 1349-1356.

# 5. La$_8$R$_2$(SiO$_4$)$_6$O$_3$ (R = La, Bi) Apatites – Composition Limits and Electrical Properties

## 5.1 Introduction and Purpose of Study

As discussed in the previous chapter, whilst the germanate apatites have superior ionic conductivity at high temperatures, the silicate apatites are still of interest for potential applications in solid oxide fuel cell (SOFC) applications due to their reasonable conductivity at low temperatures, stability and cheaper material costs.[1-3]

The existence of the compound with formula "La$_{10}$(SiO$_4$)$_6$O$_3$" has been debated in the literature. There have been reports of La$_2$SiO$_5$ forming during attempts to synthesise La$_{10}$(SiO$_4$)$_6$O$_3$[4-5] and Leon-Reina *et al.*[6] suggest that the upper limit of La content is La$_{9.60}$(SiO$_4$)$_6$O$_{2.4}$. Furthermore, it has been suggested that "La$_{10}$(SiO$_4$)$_6$O$_3$" may not exist due to the small size of the unit cell, which would lead to a significant overbonding of the La/Si–O if interstitial oxides were introduced.[7] The impurity that often appears during synthesis, La$_2$SiO$_5$, has a higher La : Si ratio than the highest stoichiometry that has been apparently observed for the apatite silicates, "La$_{10}$(SiO$_4$)$_6$O$_3$". If "La$_{10}$(SiO$_4$)$_6$O$_3$" is in fact not stable, then there would be a greater La content in the La : Si ratio in the synthesis, which lends credibility to the hypothesis that La$_2$SiO$_5$ appears due to the solid solution limit of La$_{9.33+x}$(SiO$_4$)$_6$O$_{2+1.5x}$ (0 ≤ $x$ ≤ 0.67) being reached. On the other hand, when synthesising apatites with a lower La/Si ratio, La$_2$SiO$_5$ is less likely to form.  If a dopant intended to replace some La, such as an alkaline-earth M, were to fail to dope into the apatite structure, then this would lower the La : Si ratio and therefore give rise to the impurity La$_2$Si$_2$O$_7$. Figure 5.1 shows the SiO$_2$–La$_2$O$_3$ phase diagram with a range of possible lanthanum silicate stoichiometries.
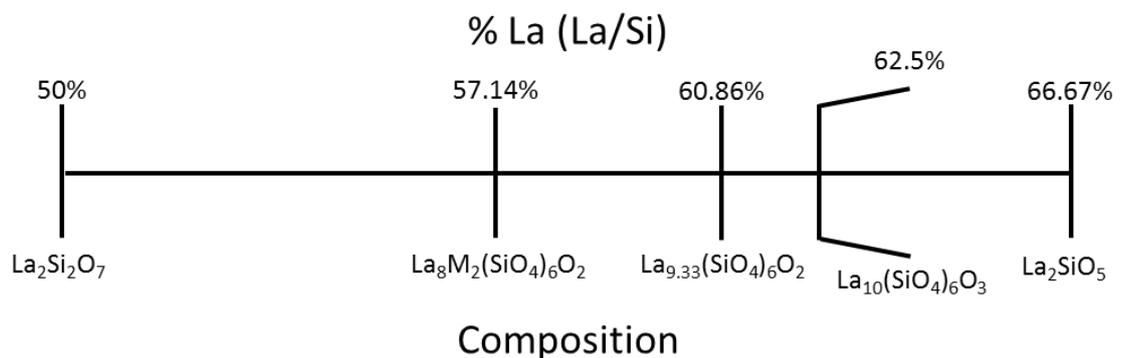


**Figure 5.1 –** SiO$_2$–La$_2$O$_3$ phase diagram plotted as a function of the %La content out of the La and Si content.

It was recently demonstrated[8] that Si-deficient apatites (*i.e.* total Si per formula unit < 6) also exist, *e.g.* La$_{9.565}$Si$_{5.826}$O$_{26}$. This apatite has a %La content of 62.1% when comparing the La : Si

cationic content, which is very similar to the %La content in La$_{10}$(SiO$_4$)$_6$O$_3$ (62.5%). This casts further doubt on the existence of oxygen-excess (*i.e.* total O per unit cell > 26) silicate apatites.

The cell parameters should change with the La content. Table 5.1 summarises the cell parameters reported for various nominal compositions and Figure 5.2 shows the unit-cell volume as a function of the nominal %La content per formula unit. The compositions shown in Figure 5.2 were determined through crystallographic refinements, rather chemical analysis.
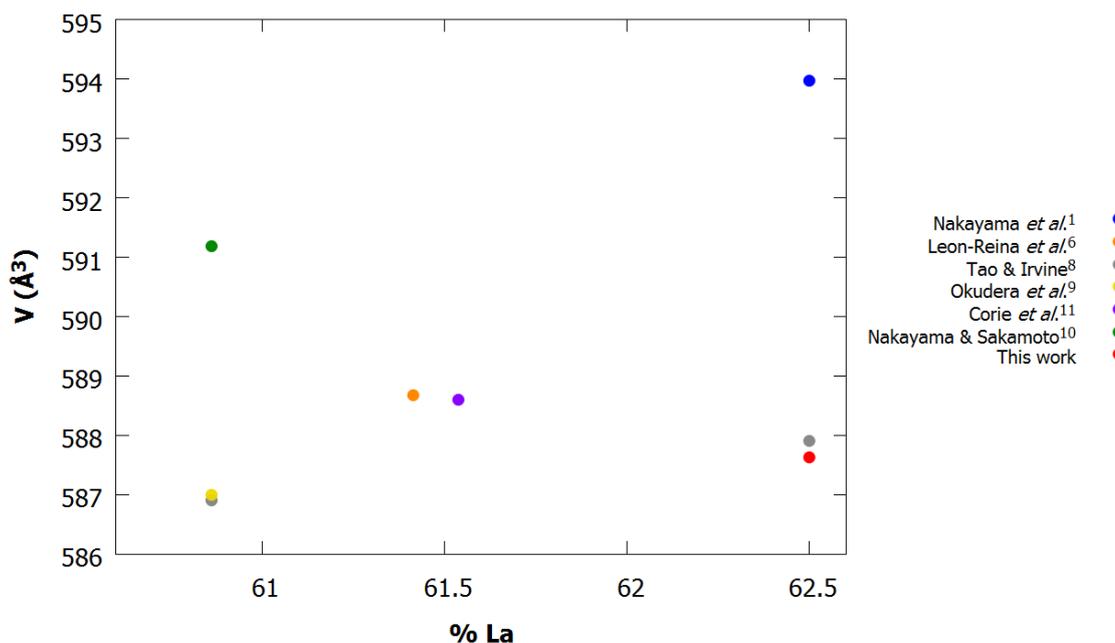


**Figure 5.2 –** The unit-cell volume at room temperature of La$_{9.33+x}$(SiO$_4$)$_6$O$_{2+1.5x}$ as reported by the various groups[1, 6, 9-12] that are included in Table 5.1 plotted as a function of the La content relative to the total cationic (La + Si) content.

It appears that there is very little correlation between the nominal La content and the unit-cell parameters, although two of the reported La$_{9.33}$(SiO$_4$)$_6$O$_2$ compositions do correspond to the smallest reported volume. The compositions with a total La of ≥ 9.55 have very similar volumes, which supports the maximum La content that Leon-Reina *et al.*[6] suggested. Nakayama *et al.*[1] have reported a particularly large unit-cell volume for the "La$_{10}$(SiO$_4$)$_6$O$_3$" composition and Nakayama and Sakamoto[11] also observed a large unit-cell volume for La$_{9.33}$(SiO$_4$)$_6$O$_2$. Furthermore, the unit-cell volume observed for "La$_{10}$(SiO$_4$)$_6$O$_3$" by Tao and Irvine[9] is lower than that reported for both La$_{9.6}$(SiO$_4$)$_6$O$_{2.4}$[12] and La$_{9.55}$(SiO$_4$)$_6$O$_{2.32}$.[6]

As discussed in detail in Chapter 4, the computational study by Peet *et al.*[13] indicated that in La$_8$Bi$_2$(GeO$_4$)$_6$O$_3$, the lone pairs of the Bi$^{3+}$ are directed towards the GeO$_4$/GeO$_5$ polyhedra in the framework. It was shown experimentally[14] that there is an increase in oxide-ion conductivity in La$_8$Bi$_2$(GeO$_4$)$_6$O$_3$ compared to La$_{10}$(GeO$_4$)$_6$O$_3$, and a complementary computational study[15]

suggested that conductivity is improved by increasing Bi$^{3+}$ content. The same trend has been observed in germanate apatites without the excess interstitial oxide.

It was discovered that La$_8$Ba$_2$(GeO$_4$)$_6$O$_2$ has a conductivity of 5.5 × 10$^{-5}$ S cm$^{-1}$ at 800 °C, whilst the conductivity of La$_6$Bi$_2$Ba$_2$(GeO$_4$)$_6$O$_2$ was found to be 0.001 S cm$^{-1}$ at the same temperature.[16] Furthermore, Tate *et al.*[14] observed that increasing the Bi$^{3+}$ content in apatites with compositions of Bi$_2$Ca$_{8-2x}$La$_{2x}$[(VO$_4$)$_{6-2x}$(GeO$_4$)$_{2x}$]O$_2$ and Bi$_4$Ca$_{6-2x}$La$_{2x}$[(VO$_4$)$_{6-2x}$(GeO$_4$)$_{2x}$]O$_2$ also improved the conductivity. This indicates that the effect that Bi$^{3+}$-doping has on the conduction mechanism is complex, as it has improved the conductivity of germanate apatites regardless of the presence of interstitial oxides. In the silicate apatites, the interstitial oxide ion (O$_{int}$) is believed to be in the hexagonal channel periphery.[7, 17-18] On the other hand, it is possible that Si-deficient apatites[8] form instead of oxygen-excess apatites as previously described. As a result of the excess O$_{int}$ being in a different location or not present at all, the conduction mechanism is thought to be different, where the hexagonal channel plays a much greater role than in the germanate analogues.[3, 19] This raises an interesting question about the effect that lone pair cation-doping may have on the conductivity. The potential presence of Si vacancies introduces another interesting question, as lone pairs in germanate apatites tended to be oriented towards the GeO$_4$/GeO$_5$ framework.[15]

Apatite-type materials with compositions La$_{10-x}$Bi$_x$(SiO$_4$)$_6$O$_3$ (x = 0.5, 1, 1.5, 2) have been previously investigated. Kim and Lee[20] reported that La$_8$Bi$_2$(SiO$_4$)$_6$O$_3$ possessed a conductivity of 2.4 × 10$^{-4}$ S cm$^{-1}$ at 700 °C with a pellet density of 98%. They comment that an increase in Bi content increases the conductivity, but no benchmark value for the conductivity of "La$_{10}$(SiO$_4$)$_6$O$_3$" was given. Furthermore, the conductivity for the x = 2 material is lower than that previously observed for "La$_{10}$(SiO$_4$)$_6$O$_3$" at the same temperature by a number of other workers:[1-2, 9] 3.43 × 10$^{-3}$ S cm$^{-1}$, 2.05 × 10$^{-3}$ S cm$^{-1}$ and 1.4 × 10$^{-3}$ S cm$^{-1}$. Table 5.2 summarises some of the conductivities reported for La$_8$R$_2$(SiO$_4$)$_6$O$_3$ (R = La, Bi) at 700 °C.

Additionally, the reasoning given by Kim and Lee[20] for the increase in conductivity in La$_{10-x}$Bi$_x$(SiO$_4$)$_6$O$_3$ (x = 0.5, 1, 1.5, 2) with increasing Bi content has little supporting evidence. They suggest that it is due to ionic radius of Bi$^{3+}$ being larger ($r_{Bi}$ = 1.20 Å) than the ionic radius of La$^{3+}$ (1.15 Å). These values for the ionic radii of La$^{3+}$ and Bi$^{3+}$ are not given for any coordination number in Shannon and Prewitt,[21] and Kim and Lee[20] do not provide a reference for the ionic radii that they quote. The relative density of their La$_8$Bi$_2$(SiO$_4$)$_6$O$_3$ sample was the highest at 98%. The exact values for the materials with compositions of La$_{10-x}$Bi$_x$(x = 0.5, 1, 1.5) are not given, but instead a range is given of 89 ≤ %$\rho$ < 98%. It is difficult to make a direct comparison because of this, but it is possible that the increase in conductivity is related to the increased pellet density rather than an intrinsic defect due to the increase in Bi content.

**Table 5.1 – The cell parameters reported for various nominal compositions of La$_{9.33+x}$(SiO$_4$)$_6$O$_{2+1.5x}$ at room temperature.**

| Nominal Composition | a (Å) | c (Å) | V (Å$^3$) | Unit cell determination method | Reference |
|---|---|---|---|---|---|
| La$_{10}$(SiO$_4$)$_6$O$_3$ | 9.76 | 7.20 | 593.97 | Laboratory powder X-ray diffraction | Nakayama et al.[1] |
| La$_{9.55}$(SiO$_4$)$_6$O$_{2.32}$ | 9.7257(1) | 7.1864(1) | 588.68(1) | Combined neutron and laboratory X-ray refinement | Leon–Reina et al.[6] |
| La$_{9.33}$(SiO$_4$)$_6$O$_2$ | 9.717(2) | 7.177(1) | 586.9(2) | Laboratory powder X-ray diffraction | Tao and Irvine[9] |
| La$_{10}$(SiO$_4$)$_6$O$_3$ | 9.722(1) | 7.182(1) | 587.9(1) | Laboratory powder X-ray diffraction | Tao and Irvine[9] |
| La$_{9.33}$(SiO$_4$)$_6$O$_2$ | 9.714(1) | 7.183(2) | 587.0(2) | Laboratory single crystal X-ray diffraction | Okudera et al.[10] |
| La$_{9.6}$(SiO$_4$)$_6$O$_{2.4}$ | 9.72441(4) | 7.18726(5) | 588.600(6) | Neutron powder diffraction | Corrie et al.[12] |
| La$_{9.33}$(SiO$_4$)$_6$O$_2$ | 9.7355(3) | 7.2023(2) | 591.18(3) | Laboratory single crystal X-ray diffraction | Nakayama and Sakamoto[11] |
| La$_{10}$(SiO$_4$)$_6$O$_3$ | 9.71797(3) | 7.18493(3) | 587.630(4) | Laboratory powder X-ray diffraction | This work |

**Table 5.2 – The conductivities and relative densities of the samples reported for La$_8$R$_2$(SiO$_4$)$_6$O$_3$ (R = La, Bi) at 700 °C.**

| Nominal Composition | σ (S cm$^{-1}$) | $E_a$ (eV) | Relative density (%) | Reference |
|---|---|---|---|---|
| La$_{10}$(SiO$_4$)$_6$O$_3$ | 1.4 × 10$^{-3}$ | 0.72 | Not reported | Nakayama et al.[1] |
| La$_{10}$(SiO$_4$)$_6$O$_3$ | 3.43 × 10$^{-3}$ | 0.62 | Not reported | Arikawa et al.[2] |
| La$_{10}$(SiO$_4$)$_6$O$_3$ | 2.05 × 10$^{-3}$ | 0.89 | 74 | Tao & Irvine[9] |
| La$_8$Bi$_2$(SiO$_4$)$_6$O$_3$ | 2.4 × 10$^{-4}$ | 0.72 | 98 | Kim & Lee[20] |

The reported properties of La$_8$Bi$_2$(SiO$_4$)$_6$O$_3$ are not well understood and this material warrants further investigation. Furthermore, the existence of an oxygen-excess silicate apatite is also in dispute. A compound with a nominal composition of La$_8$Bi$_2$(SiO$_4$)$_6$O$_3$ was therefore synthesised with the aim to measure the conductivity and examine its local structure *via* solid state NMR (SSNMR). As a benchmark, a nominal composition of La$_{10}$(SiO$_4$)$_6$O$_3$ was also synthesised and underwent the same analyses. Additionally, chemical analysis was performed using SEM-EDX.

## 5.2 Experimental Procedure

### 5.2.1 Synthesis

The following procedure was adapted from Tao & Irvine.[9] 2 g of "La$_{10}$(SiO$_4$)$_6$O$_3$" were prepared by dissolving stoichiometric amounts of La$_2$O$_3$ (Acros, 99.9%) in 20 mL of ~3.75 M HNO$_3$. The La$_2$O$_3$ had been calcined at 1000 °C for 12 h before use. Si(OC$_2$H$_5$)$_4$ (Sigma, 99.0%)  was mixed with 8 mL of 1:1 H$_2$O/C$_2$H$_5$OH and then glacial acetic acid (Fisher, 99%) was added drop-wise until a homogeneous solution formed.  The two solutions were mixed together and heated at 80 °C with stirring for 2 h until a gel formed. The gel was dried at 90 °C for 14 h, after which it was calcined for 7 h at 600 °C, ground with a mortar and pestle, and calcined at 800 °C for 6 h. The sample was heated at 1400 °C for a total of 120 h with intermittent grinding in order to minimise the amount of La$_2$SiO$_5$ impurity. This sample has a sample code of MSC047 (see Table 5.3) and a cream colour.

2 g of "La$_8$Bi$_2$(SiO$_4$)$_6$O$_3$" were prepared by mixing stoichiometric amounts of La$_2$O$_3$ (Acros, 99.9%) and Bi$_2$O$_3$ (Acros, 99.9%) with a mortar and pestle and dissolving them in 55 mL 2 M HNO$_3$ + 1 mL concentrated HNO$_3$ (Fisher). The La$_2$O$_3$ had been calcined at 1000 °C for 12 h before use. A solution containing stoichiometric amounts of Si(OC$_2$H$_5$)$_4$ (Sigma, 99.0%) and 20 mL of 1:1 H$_2$O/C$_2$H$_5$OH was prepared and glacial acetic acid (Fisher, 99%) was added drop-wise in order to produce a homogeneous  solution. The two solutions were mixed and heated at 80 °C with stirring for 6 h. The sample was dried at 90 °C for 12 h, calcined at 600 °C for 7 h, ground and calcined at 800 °C for 6 h. The sample was heated at 1100 °C for a total of 36 h with intermittent grinding. This sample has a sample code of MSC050 (see Table 5.3) and a cream colour. Some of the sample was heated at 1200 °C for 18 h, but this resulted in an impurity that could not be removed with further heating.

**Table 5.3 – Summary of the samples of La$_8$R$_2$(SiO$_4$)$_6$O$_3$ including formula, sample code, maximum synthesis temperature ($T_{max}$) and total synthesis time at $T_{max}$ ($t_{tot}$).**

| Sample code | Nominal formula | $T_{max}$ (°C) | $t_{tot}$ (h) |
|---|---|---|---|
| MSC047 | La$_{10}$(SiO$_4$)$_6$O$_3$ | 1400 | 120 |
| MSC050 | La$_8$Bi$_2$(SiO$_4$)$_6$O$_3$ | 1100 | 36 |

## 5.2.2 Powder X-ray diffraction

Powder X-ray diffraction patterns were obtained using a D8 Bruker Advance with a Cu target and Ni filter. The emitted wavelength is a mixture of Cu Kα$_1$ (1.54051 Å) and Cu Kα$_2$ (1.54433 Å). The patterns were initially collected using Si slides and a range of 10 ° ≤ 2$\theta$ ≤ 80° in 0.02° steps with a scan time per step of 1 s step$^{-1}$ in order to determine phase purity. Patterns were also collected using Si slides with a range of 10 ° ≤ 2$\theta$ ≤ 120° in 0.02° steps with a scan time per step of 6 s step$^{-1}$. The models were fitted using Rietveld refinement. The background of each sample was fitted using a Chebyshev polynomial function and the peak shapes were modelled using a Thompson-Hastings-Cox pseudo-Voigt function. The primary phases for both samples were fitted using La$_{9.33}$(SiO$_4$)$_6$O$_2$ as a starting model.[10] The site labels and atomic coordinates of the starting model are given in Table 5.4.

**Table 5.4 – The site labels, Wyckoff positions, coordinates and fractional occupancies in La$_{9.33}$(SiO$_4$)$_6$O$_2$ used as the starting model[10] for refinements. Space group = $P6_3/m$.**

| Site | Wyckoff site | $x$ | $y$ | $z$ | Occupancy |
|------|-------------|-----|-----|-----|-----------|
| La1 | 4$f$ | ⅔ | ⅓ | 0.0012 | 0.858 |
| La2 | 6$h$ | 0.01223 | 0.23921 | ¼ | 0.983 |
| Si1 | 6$h$ | 0.4029 | 0.3728 | ¼ | 1.0 |
| O1 | 6$h$ | 0.3255 | 0.4873 | ¼ | 1.0 |
| O2 | 6$h$ | 0.5267 | 0.1232 | ¼ | 1.0 |
| O3 | 12$i$ | 0.3476 | 0.2564 | 0.0684 | 1.0 |
| O4 | 2$a$ | 0 | 0 | ¼ | 1.0 |

To check phase purity, only the cell parameters and an overall atomic displacement parameter (ADP) were refined. In the final refinements using the higher quality scans, the fractional coordinates of all atoms and the La1/La2 occupancies were refined. For "La$_8$Bi$_2$(SiO$_4$)$_6$O$_3$", Bi$^{3+}$ was initially introduced onto the La2 site as Bi$^{3+}$ was found to occupy the A2 sites in La$_8$Bi$_2$(GeO$_4$)$_6$O$_3$.[22] Additionally, Bi$^{3+}$ was also introduced onto the La1 site and the La/Bi occupancies were refined. For both samples, the excess interstitial oxide was not introduced as the scattering from the O$^{2-}$ using X-rays would be too insignificant to detect. Therefore, both samples were modelled as "La$_8$R$_2$(SiO$_4$)$_6$O$_2$" (R = La, Bi).

## 5.2.3 Impedance spectroscopy

Impedance spectroscopy was performed using pellets with masses of ~0.46 g. The samples were pressed into $\varphi$ = 10 mm pellets and sintered at 1400 °C for 36 h and at 1100 °C for 18 h for "La$_{10}$(SiO$_4$)$_6$O$_3$" and "La$_8$Bi$_2$(SiO$_4$)$_6$O$_3$" respectively. Additionally, two samples of "La$_{10}$(SiO$_4$)$_6$O$_3$" that were synthesised by IRE group member Chloe Fuller (CAF012 and CAF015) were pressed into $\varphi$ = 10 mm pellets and sintered at 1400 °C for 36 h. CAF015 was mixed with ethanol when pressed. The % densities were estimated for all samples assuming that the nominal formulae were correct.

Impedance spectra were collected using a Solartron 1260 Analyser with a Probostat cell. Table 5.5 provides the final dimensions of each pellet.

**Table 5.5 – Summary of the sintering temperatures and times of each sample pellet used in impedance.**

| Sample code | Nominal formula | Mass (g) | Radius (cm) | Thickness (cm) | Area (cm$^2$) |
|---|---|---|---|---|---|
| MSC050 | La$_8$Bi$_2$(SiO$_4$)$_6$O$_3$ | 0.4611 | 0.494 | 0.141 | 0.765 |
| MSC047 | La$_{10}$(SiO$_4$)$_6$O$_3$ | 0.4594 | 0.499 | 0.159 | 0.782 |
| CAF012 | La$_{10}$(SiO$_4$)$_6$O$_3$ | 0.4574 | 0.494 | 0.172 | 0.765 |
| CAF015 | La$_{10}$(SiO$_4$)$_6$O$_3$ | 0.4398 | 0.497 | 0.168 | 0.774 |

The densities of the pellets calculated based on the refined formulae are given in Table 5.10.

### 5.2.4 Solid-state NMR (SSNMR)

Samples were submitted to the SSNMR service at Durham University Chemistry Department. $^{29}$Si magic angle spinning NMR (MAS-NMR) spectra were collected at room temperature using a 400 MHz Varian VNMRS spectrometer using tetramethylsilane (TMS) as the reference. Data were deconvoluted using a Gaussian peak shape, only varying the height and width between samples. In addition to the two samples described in Section 5.2.1, three other samples synthesised by Chloe Fuller were submitted in order to compare "La$_8$Bi$_2$(SiO$_4$)$_6$O$_3$" with "La$_{10}$(SiO$_4$)$_6$O$_3$" and La$_{9.33}$(SiO$_4$)$_6$O$_2$. Table 5.6 gives a summary of the different samples that underwent SSNMR analysis.

**Table 5.6 – Summary of the samples used for SSNMR and SEM-EDX.**

| Sample code | Nominal formula | Synthetic route |
|---|---|---|
| MSC050 | La$_8$Bi$_2$(SiO$_4$)$_6$O$_3$ | Sol-gel |
| MSC047 | La$_{10}$(SiO$_4$)$_6$O$_3$ | Sol-gel |
| CAF012 | La$_{10}$(SiO$_4$)$_6$O$_3$ | Sol-gel |
| CAF013 | La$_{9.33}$(SiO$_4$)$_6$O$_2$ | Solid state |
| CAF015 | La$_{10}$(SiO$_4$)$_6$O$_3$ | Solid state |

### 5.2.5 SEM-EDX

SEM-EDX data were obtained using a Hitachi SU-70 Field Emission Gun Scanning Electron Microscope (FEG SEM) by fellow IRE group member Melissa Rodriguez-Garcia. The samples were pressed into 8 mm diameter pellets and coated with 45-55 nm of carbon, depending of the charge build up experienced in each sample. The FEG SEM was optimised at an energy of 15 keV and calibrated with a cobalt chip. The same samples that were submitted to SSNMR were used for SEM-EDX (see Table 5.6)

The data were recorded with the software Aztec from Oxford Instruments plc. Each measurement had a process time of 4 s, acquisition time of 8 s, image resolution of 1024 × 724 pixels and a

dwell time of 9 μs and was collected in atomic %. The areas scanned for each spectrum have an approximate range of 80 – 1370 μm$^2$.

## 5.3 Results and Discussion

### 5.3.1 Phase purity and average structure

#### 5.3.1.1 Powder diffraction and Rietveld refinement

There was initial difficulty in obtaining a pure sample of "La$_{10}$(SiO$_4$)$_6$O$_3$" and 120 h of further heating at 1400 °C were required in order to obtain a 96.2(2)% pure sample. This is in contrast to the results reported by Tao and Irvine,[9] whose procedure was the basis for the synthesis employed here. They found that only 800 °C was required to make a pure phase and they only heated at 1400 °C to improve the crystallinity of the sample. The difference could be that they employed ball-milling, whilst that technique was not used here. On the other hand, ball-milling may have reduced the visible impact of the impurities in the powder diffraction, as the particle sizes are small, leading to broadening of the impurity peaks. As the existence of "La$_{10}$(SiO$_4$)$_6$O$_3$" is questioned, and that one of the reasons that its existence is doubted is due to the presence of La$_2$SiO$_5$, the site occupancies of La1 and La2 (see Table 5.4) were refined for the "La$_{10}$(SiO$_4$)$_6$O$_3$" sample (MSC047). Four approaches were employed to determine the La content. Firstly, the La site occupancies were fixed to those given in Table 5.4, which correspond to a total La content of 9.33. This resulted in a fit with $R_{wp}$ = 2.453%. Secondly, the La site occupancies were allowed to refine freely, resulting in a total La content of 9.24(5) and a fit with $R_{wp}$ = 2.450%. The third approach was to fix the occupancies of the La1 and La2 sites at 1, which resulted in a fit with $R_{wp}$ = 2.843%. Finally, the occupancies were freely refined again from fully occupied, which resulted in a total La content of 9.29(5) and a fit with $R_{wp}$ = 2.450%. These procedures are summarised in Table 5.7.

**Table 5.7 – Summary of the refinement procedures and results for determining the total La content in La$_{9.29(5)}$(SiO$_4$)$_6$O$_2$ (MSC047).**

| Refinement procedure | La1 occupancy | La2 occupancy | Total La | $R_{wp}$ (%) |
|---|---|---|---|---|
| Constrained occupancies, total La = 9.33 | 0.858 | 0.983 | 9.33 | 2.453 |
| Free refinement from total La = 9.33 | 0.855(5) | 0.969(7) | 9.24(5) | 2.450 |
| Constrained occupancies, total La = 10 | 1.0 | 1.0 | 10 | 2.843 |
| Free refinement from total La = 10 | 0.860(6) | 0.975(7) | 9.29(5) | 2.450 |

Table 5.7 shows that the $R_{wp}$ obtained for "La$_{10}$(SiO$_4$)$_6$O$_3$" is significantly higher than for the La-deficient models. Secondly, the total La content converged from two different starting points to essentially the same value. The composition La$_{9.29(5)}$(SiO$_4$)$_6$O$_2$ is 1σ from La$_{9.33}$(SiO$_4$)$_6$O$_2$, which suggests that the compound synthesised here most likely adopts that stoichiometry as opposed to

$La_{10}(SiO_4)_6O_3$. Furthermore, there is 3.8(2)% $La_2SiO_5$ present by mass, which, as previously discussed, could form when the solid solution limit of the apatite silicate phases has been reached. Therefore, the model with stoichiometry of $La_{9.29(5)}(SiO_4)_6O_2$ was adopted. The oxygen content was not refined, but the total La content is within 1σ of a charge-balanced material. The fit obtained for this refinement is shown in Figure 5.3 and given in Table 5.8. The resulting structural model has no short La–O bond distances and the shortest Si–O distance is 1.59(2) Å, which is close to the literature value of ~1.62 Å.[23]
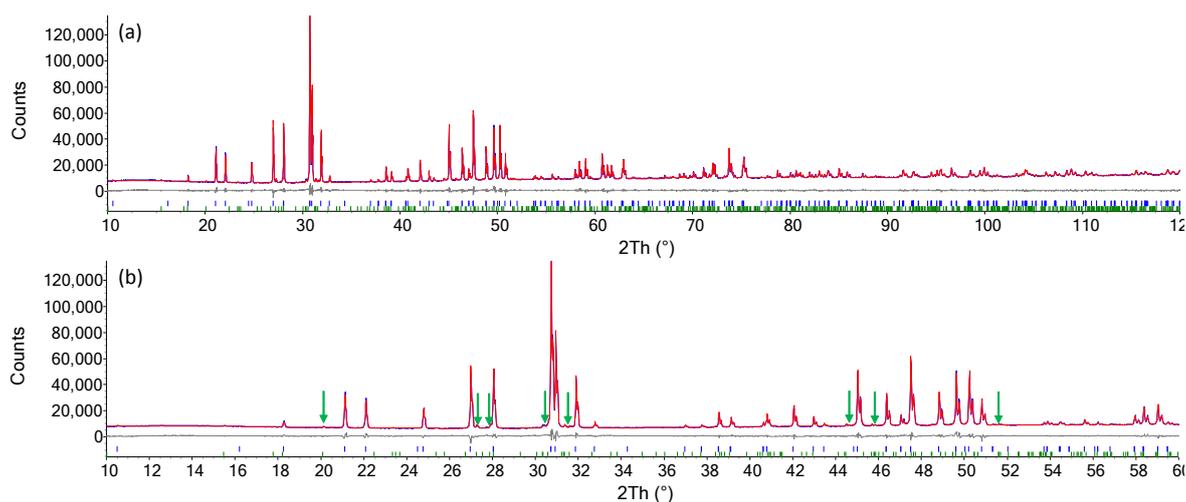


**Figure 5.3 –** The Rietveld plot of $La_{9.29(5)}(SiO_4)_6O_2$ (a) over the range of $10 \leq 2\theta \leq 120°$ and (b) $10 \leq 2\theta \leq 60°$; $R_{wp}$ = 2.450%. The green arrows highlight the most prominent peaks arising from $La_2SiO_5$.

**Table 5.8 – Crystallographic parameters from refinement of $La_{9.29(5)}(SiO_4)_6O_2$ with La occupancies refined freely. Space group = $P6_3/m$; $a$ = 9.71797(3) Å; $c$ = 7.18493(3) Å; α = 90°; γ = 120°; V = 587.630(4) Å³.**

| Site label | Wyckoff site | x | y | z | Occupancy | B (Å)² |
|---|---|---|---|---|---|---|
| La1 | 4f | ⅔ | ⅓ | 0.0025(4) | 0.860(6) | 1.20(3) |
| La2 | 6h | 0.0120(2) | 0.2406(1) | ¼ | 0.975(7) | 1.00(2) |
| Si1 | 6h | 0.4043(5) | 0.3734(5) | ¼ | 1 | 0.9(1) |
| O1 | 6h | 0.324(1) | 0.481(1) | ¼ | 1 | 2.1(2) |
| O2 | 6h | 0.529(1) | 0.123(1) | ¼ | 1 | 2.1(2) |
| O3 | 12i | 0.3435(7) | 0.2547(7) | 0.0709(7) | 1 | 2.1(2) |
| O4 | 2a | 0 | 0 | ¼ | 1 | 2.1(2) |

In the synthesis of "$La_8Bi_2(SiO_4)_6O_3$", the synthesis time and temperature were greatly reduced, only requiring 36 h at 1100 °C. Heating the sample at 1200 °C resulted in a significant proportion of $La_2Si_2O_7$, likely as a result of $Bi_2O_3$ volatilisation. The La : Si ratio of 8 : 6 is closer to that of $La_2Si_2O_7$ (1 : 1) than to $La_2SiO_5$ (2 : 1), shown in Figure 5.1. This is likely the reason that $La_2Si_2O_7$ began to form in larger quantities as opposed to $La_2SiO_5$, which is commonly detected in the

synthesis of La$_{10}$(SiO$_4$)$_6$O$_3$. These synthetic outcomes conflict with the report by Kim and Lee,[20] who claim to have synthesised materials at 1300 °C and obtained pure samples. However, at 2$\theta$ ≈ 26, 29° in their pattern for La$_8$Bi$_2$(SiO$_4$)$_6$O$_3$, there are two peaks that do not arise from the apatite structure, suggesting that their product was in fact not pure.

In order to remain consistent and provide different measurements on the same sample batch, powder patterns with 10 ° ≤ 2$\theta$ ≤ 120° in 0.2° steps with a scan time per step of 6 s step$^{-1}$ were obtained from the sample used in impedance spectroscopy (see Section 5.3.2). This resulted in a small amount of Pt impurity due to the Pt paste used to make electrode contact. In the Rietveld refinement, Bi was placed on the A2 site with an occupancy of 1/3 based on the results for the germanate analogue.[22] The rest of the A2 site was 2/3 La and the A1 site was exclusively occupied by La. This model resulted in $R_{wp}$ = 4.107%. Attempts were made to freely refine the Bi occupancy by also introducing Bi on the A1 site. Whilst the total amount of La and Bi per formula unit refined to approximately 8 and 2 respectively, the occupancies of the A1 and A2 sites varied depending on the starting values and had large errors with the standard uncertainties. Therefore, it was not possible to determine the occupancies of the A1 and A2 site reliably from laboratory powder X-ray diffraction. Given the occupancies found in the germanate analogue[22] and that ions with lone pairs tend to occupy the A2 site,[24] (*e.g.* Ca$_4$Pb$_6$(AsO$_4$)$_6$Cl$_2$ and Cd$_6$Pb$_9$(Si$_2$O$_7$)$_3$(SiO$_4$)$_3$), the model with Bi$^{3+}$ only on the A2 site was adopted. La$_2$Si$_2$O$_7$ was detected and included in the refinement, giving $R_{wp}$ = 3.694%. As there is doubt to the existence of oxygen-excess lanthanum silicate apatites, another refinement was performed where a scale factor of 0.933 was applied to the constrained La and Bi occupancies so that the total A site cations per formula unit = 9.33 and so that the La : Bi ratio of 8 : 2 is maintained. This resulted in a fit with R$_{wp}$ = 3.676%. As the free refinement of the Bi and La occupancies resulted in large standard uncertainties, the refinement of "La$_{10}$(SiO$_4$)$_6$O$_3$" resulted in a formula of La$_{9.29(5)}$(SiO$_4$)$_6$O$_2$ and the R$_{wp}$ is slightly lower (3.694% vs. 3.676%), the model with a formula of La$_{7.464}$Bi$_{1.866}$(SiO$_4$)$_6$O$_2$ was adopted. The weight percentages of each phase determined from this refinement are 92.3(4)% La$_{7.464}$Bi$_{1.866}$(SiO$_4$)$_6$O$_2$, 7.5(4)% La$_2$Si$_2$O$_7$ and 0.19(5)% Pt. This Rietveld plot is shown in Figure 5.4. There are still three, weak, unaccounted for peaks (marked with black arrows in Figure 5.4). We estimate that these represent < 1.5 % weight percentage of the sample. Henceforth, this report shall refer to MSC050 as La$_{7.464}$Bi$_{1.866}$(SiO$_4$)$_6$O$_2$.
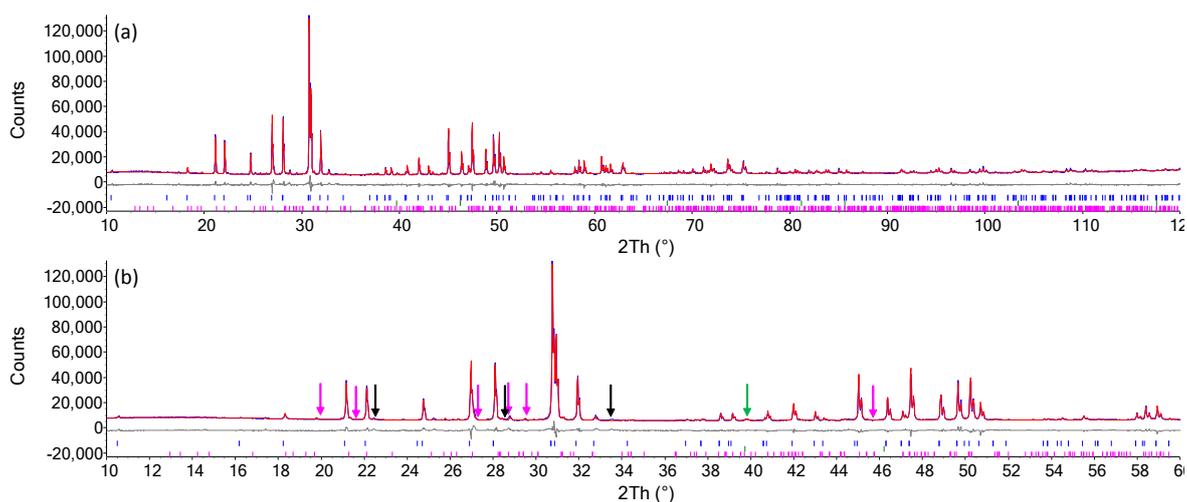
**Figure 5.4 –** The Rietveld plot of La$_{7.464}$Bi$_{1.866}$(SiO$_4$)$_6$O$_2$ (a) over the range of 10 ≤ 2θ ≤ 120° and (b) 10 ≤ 2θ ≤ 60°; $R_{wp}$ = 3.694%. The black arrows highlight the unaccounted for peaks, the green arrow highlights the most prominent peak from the Pt and the pink arrows highlight prominent peaks from La$_2$Si$_2$O$_7$.

The cell parameters of La$_{7.464}$Bi$_{1.866}$(SiO$_4$)$_6$O$_2$ are $a$ = 9.71917(5); $c$ = 7.20434(5) Å; V = 589.364(7) Å$^3$: a relative increase of 0.2701(8)% for the $c$ cell parameter and a relative increase of 0.0123(6)% for the $a$ cell parameter in comparison to the cell parameters of La$_{9.29(5)}$(SiO$_4$)$_6$O$_2$. An increase in cell parameters also occurs in the germanate analogues[22] when Bi$^{3+}$ is doped in place of La$^{3+}$ (see Chapter 4.3.1). This means that the $c$ cell parameter has a relative increase that is 22(1) times larger than the relative increase for the $a$ cell parameter. The cause of large difference in change in cell parameters may be due to the anisotropic shape and orientation of the lone pairs of Bi$^{3+}$. Table 5.9 gives the crystallographic parameters obtained from the refinement shown in Figure 5.4. The resultant model has no short La–O bond distances, but it does have a Si–O bond distance of 1.55(2) Å, which is ~0.07 Å less than the $R_{SiO}$ value of ~1.62 Å.[23] Whilst this is a very small Si–O bond length, this bond length was determined from X-ray data. The distribution of the O atoms is therefore not highly accurate, as the phase also consists of a large proportion of La and Bi atoms. It would be difficult to obtain more accurate Si–O bond lengths without employing neutron diffraction.

**Table 5.9 – Crystallographic parameters from the refinement of La$_{7.464}$Bi$_{1.866}$(SiO$_4$)$_6$O$_2$. Space group = $P6_3/m$; $a$ = 9.71917(5) Å; $c$ = 7.20434(5) Å; α = 90°; γ = 120°; V = 589.364(7) Å$^3$.**

| Site label | Wyckoff site | $x$ | $y$ | $z$ | Occupancy | B (Å)$^2$ |
|---|---|---|---|---|---|---|
| La1 | 4$f$ | ⅔ | ⅓ | −0.0077(7) | 0.933 | 3.24(5) |
| La2 | 6$h$ | 0.0076(4) | 0.2387(2) | ¼ | 0.622 | 2.76(3) |
| Bi2 | 6$h$ | 0.0076(4) | 0.2387(2) | ¼ | 0.311 | 2.76(3) |
| Si1 | 6$h$ | 0.401(1) | 0.367(1) | ¼ | 1 | 3.1(2) |
| O1 | 6$h$ | 0.329(2) | 0.488(2) | ¼ | 1 | 4.6(2) |
| O2 | 6$h$ | 0.533(2) | 0.118(2) | ¼ | 1 | 4.6(2) |
| O3 | 12$i$ | 0.342(1) | 0.254(1) | 0.0680(1) | 1 | 4.6(2) |
| O4 | 2$a$ | 0 | 0 | ¼ | 1 | 4.6(2) |

The ADPs on the Si and O sites are large, indicating a large amount of disorder in the crystal structure.

### 5.3.1.2 SEM-EDX

Chemical analyses of the apatite silicates have not yet been reported to this author's knowledge. SEM-EDX were performed and the data were analysed by comparing the molar ratios of La : Bi : Si in La$_{7.464}$Bi$_{1.866}$(SiO$_4$)$_6$O$_2$ and La : Si for La$_{9.29(5)}$(SiO$_4$)$_6$O$_2$, "La$_{10}$(SiO$_4$)$_6$O$_3$" and La$_{9.33}$(SiO$_4$)$_6$O$_2$ (see table 5.6), where the oxygen content was calculated by balancing the charge of the resulting formulae. Figure 5.5 shows the ratios of La : Bi : Si obtained for La$_{7.464}$Bi$_{1.866}$(SiO$_4$)$_6$O$_2$ (MSC050) plotted on a ternary phase diagram. The mean formula obtained by using all spectra normalised to Si is La$_{7.5(3)}$Bi$_{1.4(2)}$Si$_6$O$_{25.4(5)}$, but ignoring three of the outliers, where the La molar ratio in La : Bi : Si < 0.49, the formula is La$_{7.7(3)}$Bi$_{1.4(2)}$Si$_6$O$_{25.6(5)}$. The formula is within 1σ of the nominal La content and the content used in Rietveld analysis, but is 4σ from the nominal Bi content and ~3σ from the Bi content used in Rietveld analysis. In addition, there were no spectra that matched the ratio of La$_2$Si$_2$O$_7$, despite it being clearly visible in the Rietveld refinement. It is possible that the La$_2$Si$_2$O$_7$ phase is mixed with the apatite phase, resulting in less Bi in the La : Bi : Si ratio than expected. If the apatite phase had a formula of La$_{7.464}$Bi$_{1.866}$(SiO$_4$)$_6$O$_2$, using the weight percentages obtained from the Rietveld refinement, the average formula normalised to Si would be La$_{7.3(6)}$Bi$_{1.7(2)}$Si$_6$O$_{26(1)}$.
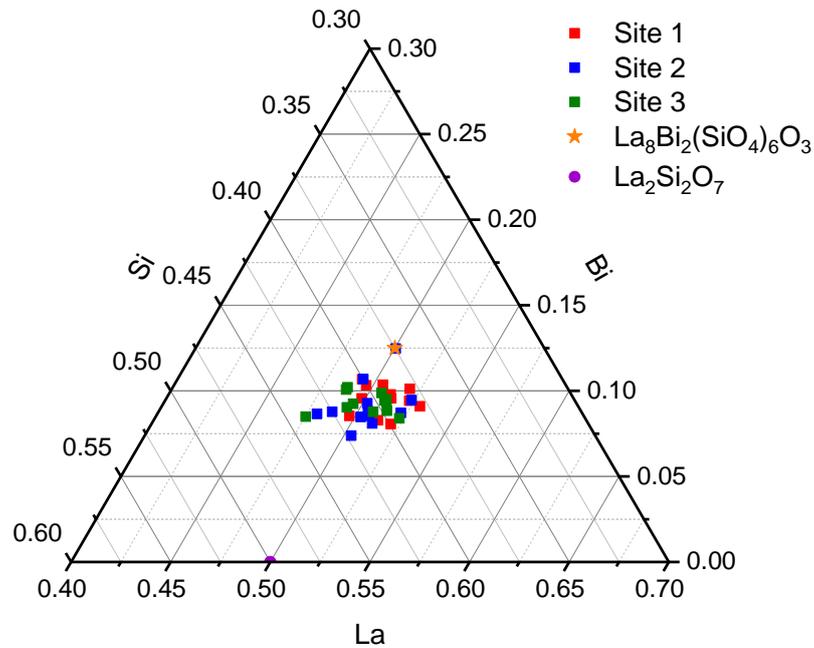
**Figure 5.5** – The La : Bi : Si molar ratios determined from each spectrum from SEM-EDX analysis of La$_{7.464}$Bi$_{1.866}$O$_{26}$ plotted as a ternary phase diagram.

This is very close to the composition obtained from EDX; the La content is within 1σ and the Bi content is within 1.8σ. The sample areas used in EDX have an approximate range of 240 – 520 μm$^2$. These areas are large enough to contain crystallites from both phases. The Bi may be under-calculated as some of the outgoing X-rays are absorbed by the Bi in the sample due to its high X-ray attenuation. Therefore, the observed La : Bi : Si ratio in the spectra is likely due to the presence of La$_2$Si$_2$O$_7$ or due to a systematic error in the technique.

Figure 5.6 shows the binary phase diagrams of La : Si ratios found in the nominal compositions of "La$_{10}$(SiO$_4$)$_6$O$_3$" (MSC047, CAF012, CAF015) and La$_{9.33}$(SiO$_4$)$_6$O$_2$. The spectra obtained for MSC047, shown in Figure 5.6a, resulted in an average formula of La$_{9.8(3)}$Si$_6$O$_{26.8(5)}$, which is only 1 σ from the nominal composition. Whilst the Rietveld refinement showed 3.8(2)% La$_2$SiO$_5$, that phase is not clearly distinguishable in the EDX data. The Rietveld refinement also suggested that the formula of the apatite phase is La$_{9.29(5)}$(SiO$_4$)$_6$O$_2$, which is a lower La : Si ratio. Assuming that the apatite phase has a formula of La$_{9.33}$(SiO$_4$)$_6$O$_2$, from these weight percentages, the expected average formula normalised to Si would be La$_{9.4(8)}$Si$_6$O$_{26\ (1)}$ if the phases were mixed. This formula is within 1.3σ of the formula as observed from EDX. Furthermore, the areas that were scanned range from approximately 105 μm$^2$ to 1370 μm$^2$. These areas contain many crystallites and could easily contain mixtures of the apatite phase and La$_2$SiO$_5$ phase. Therefore, it is highly likely that the La$_2$SiO$_5$ impurity phase was measured at the same time as the apatite phase.
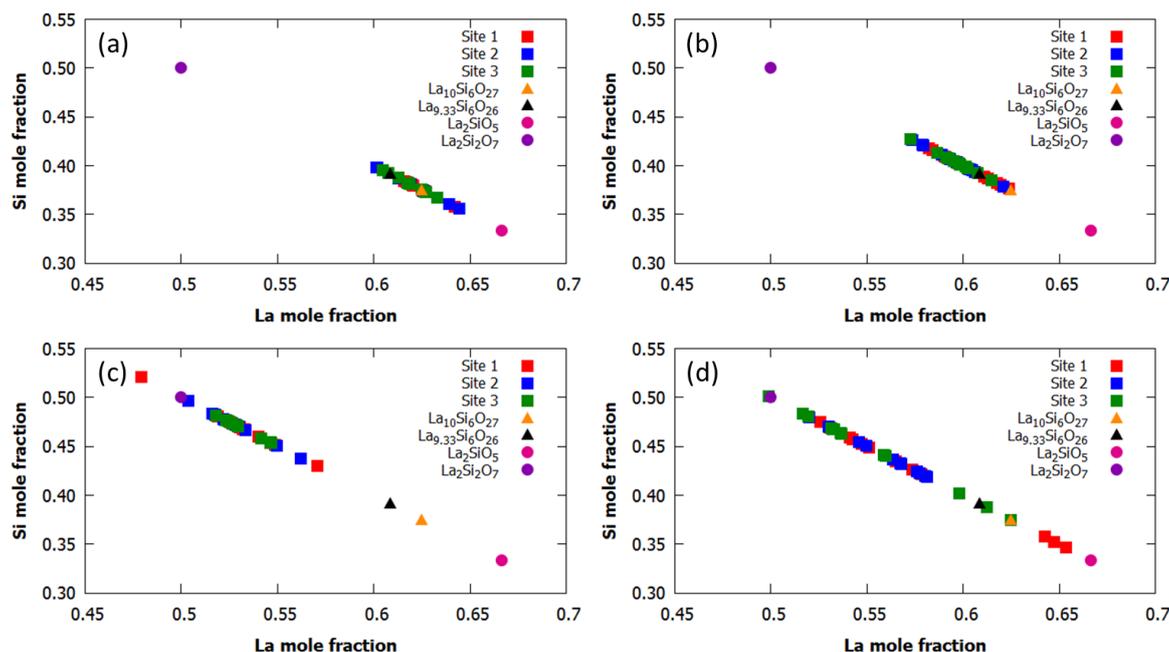
**Figure 5.6 –** The binary phase diagrams showing the La : Si ratios for the samples measured here (see Table 5.6): (a) MSC047 (La$_{9.29(5)}$(SiO$_4$)$_6$O$_2$), (b) CAF012 ("La$_{10}$(SiO$_4$)$_6$O$_3$"), (c) CAF013 (La$_{9.33}$(SiO$_4$)$_6$O$_2$) and (d) CAF015 ("La$_{10}$(SiO$_4$)$_6$O$_3$"). One outlying point in (c) has been excluded.

CAF012 (Figure 5.6b), which is also nominally La$_{10}$(SiO$_4$)$_6$O$_3$ and is phase pure from Rietveld refinements, was found to have a mean formula of La$_{8.9(3)}$Si$_6$O$_{25.4(5)}$ when all spectra were used. Excluding points where the La content in the La : Si ratio is < 0.59, the resulting formula is La$_{9.1(3)}$Si$_6$O$_{25.7(4)}$, which is still La-deficient. There are no obvious secondary phases, but it is possible that there is La$_2$Si$_2$O$_7$ present that is not found in Rietveld refinement. The spectra shown in Figure 5.6d for the other nominal composition of La$_{10}$(SiO$_4$)$_6$O$_3$ (CAF015) show a large deviation from the apatite phase. This sample was made using solid state synthesis and contains 7.6(4)% La$_2$SiO$_5$ and 2.8(2)% La$_2$O$_3$ from Rietveld refinement. From these spectra, the phase of La$_2$SiO$_5$ was clearly distinguished, with a formula of La$_{1.84(3)}$SiO$_{4.76(4)}$. It also seemingly has La$_2$Si$_2$O$_7$, as a phase with a formula of La$_{2.1(2)}$Si$_2$O$_{7.1(3)}$ was observed, however the apatite phase was not clearly distinguished, even though it is the major phase in Rietveld refinement. There are only 4 points that would fit in the La ratio range of 0.58 < $x$ < 0.63, giving a formula of La$_{8.7(3)}$Si$_6$O$_{25.1(5)}$. The spectra obtained for the nominal composition of La$_{9.33}$(SiO$_4$)$_6$O$_2$ (CAF013), shown in figure 5.6c, also did not clearly show the apatite phase, despite it once again being the major phase in Rietveld refinement. The mean formula obtained from all spectra, except for the outlier (La ratio ≈ 0.34), is La$_{2.2(2)}$Si$_2$O$_{7.3(3)}$; closer to La$_2$Si$_2$O$_7$ than La$_{9.33}$(SiO$_4$)$_6$O$_2$.

All but one of the spectra showed La : Si ratios that are within the range of known lanthanum silicate phases. For MSC047, the obtained formula is within 1σ from La$_{10}$(SiO$_4$)$_6$O$_3$, but also only

1.6σ from La$_{9.33}$(SiO$_4$)$_6$O$_2$. For CAF012, the obtained formula of La$_{9.1(3)}$Si$_6$O$_{25.7(4)}$ is 3σ from La$_{10}$(SiO$_4$)$_6$O$_3$, but only 1σ from La$_{9.33}$(SiO$_4$)$_6$O$_2$.

## 5.3.2 Conductivity

After synthesising La$_{9.29(5)}$(SiO$_4$)$_6$O$_2$ and La$_{7.464}$Bi$_{1.866}$(SiO$_4$)$_6$O$_2$, the electrical properties were investigated with impedance spectroscopy. Figure 5.7 shows the Nyquist plots of La$_{7.464}$Bi$_{1.866}$(SiO$_4$)$_6$O$_2$ (MSC050) and La$_{9.29(5)}$(SiO$_4$)$_6$O$_2$ (MSC047).
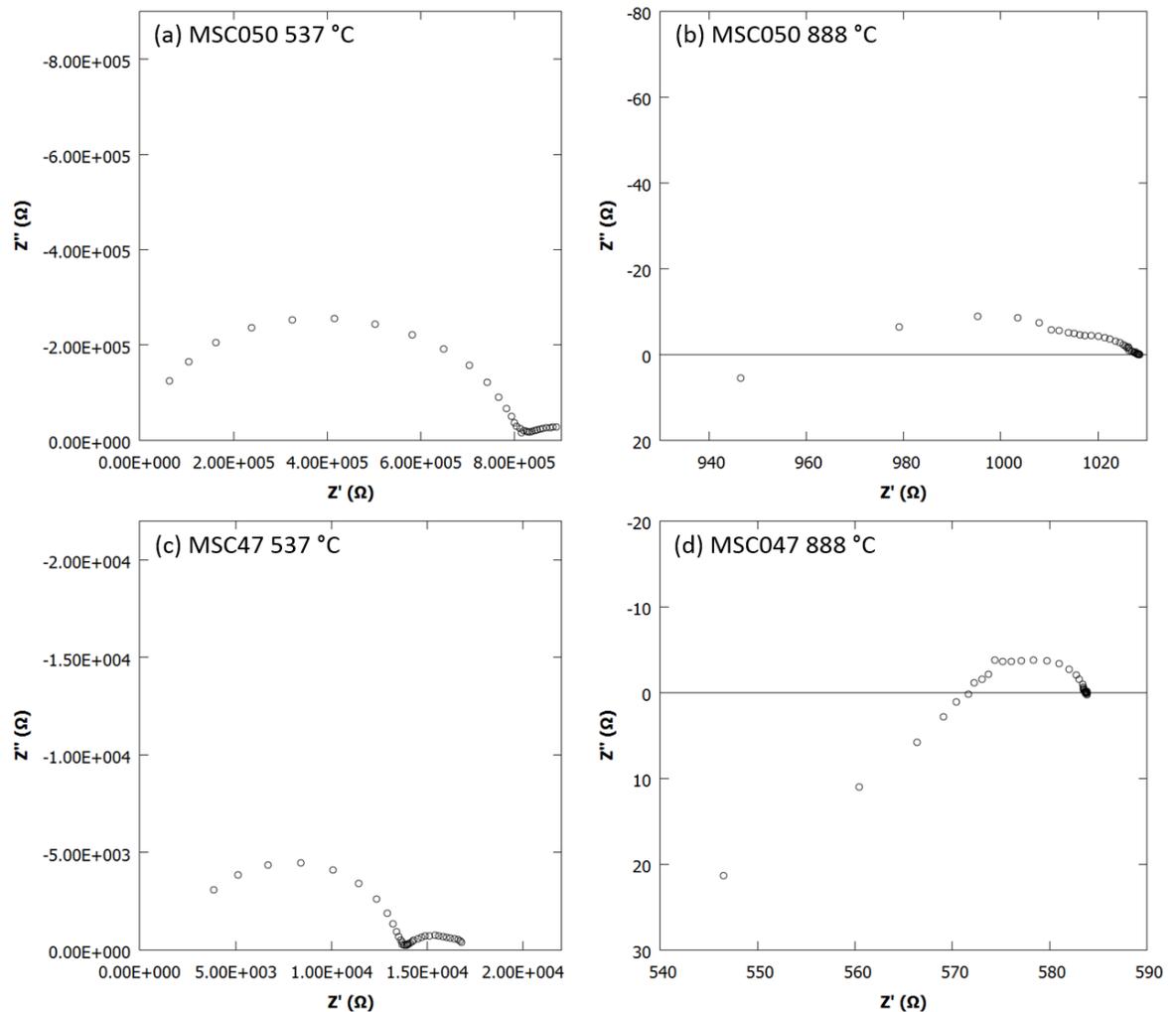
**Figure 5.7** – The Nyquist plots of La$_{7.464}$Bi$_{1.866}$(SiO$_4$)$_6$O$_2$ (MSC050) at (a) 537 °C and (b) 888 °C and of La$_{9.29(5)}$(SiO$_4$)$_6$O$_2$ (MSC047) at (c) 537 °C and (d) 888 °C. There is an overlap of the bulk and grain boundary responses in all samples.

The capacitance of the large semicircle seen in Figure 5.7a is 1.92 × 10$^{-11}$ F, which corresponds to an overlap of the bulk and grain boundary responses.[25] A second semicircle is also present in the low frequency region with a capacitance of 7.10 × 10$^{-7}$ F, corresponding to the sample-electrode interface. In the plot in Figure 5.7b, first semicircle has a capacitance of 4.17 × 10$^{-10}$ F, which indicates an overlap of the grain boundary and bulk responses. There is a second semicircle that overlaps with the first, which has a capacitance of 2.45 × 10$^{-8}$ F, which could correspond to the

grain boundary response. The semicircle at the high frequency region in the impedance plot shown in Figure 5.7c has a capacitance of $4.59 \times 10^{-11}$ F, corresponding to an overlap of the bulk and grain boundary. The semicircle in the low frequency region has a capacitance of $2.37 \times 10^{-6}$ F, which can be attributed to the sample-electrode interface. For the impedance plot shown in Figure 5.5d, there is only one visible semicircle in the high frequency region with a capacitance of $2.78 \times 10^{-9}$ F. A similar pattern was observed in all measured samples, so only the total conductivities could be extracted. Both samples exhibited similar impedance responses, indicating that La$_{7.464}$Bi$_{1.866}$(SiO$_4$)$_6$O$_2$ is an ionic conductor.

The primary purpose of measuring the La$_{9.29(5)}$(SiO$_4$)$_6$O$_2$ sample was to provide a Bi-free benchmark in order to compare the conductivity of La$_{7.464}$Bi$_{1.866}$(SiO$_4$)$_6$O$_2$. The conductivity obtained for La$_{9.29(5)}$(SiO$_4$)$_6$O$_2$ (MSC047) (see Table 5.5) is σ ≈ $3.6 \times 10^{-4}$ S cm$^{-1}$ at 888 °C. This was nearly an order of magnitude lower than the conductivity found by Tao and Irvine for "La$_{10}$(SiO$_4$)$_6$O$_3$",[9] which was σ ≈ $9.6 \times 10^{-3}$ S cm$^{-1}$. It is also lower than the conductivity observed by Nakayama *et al.*[1] at 900 °C ($2.9 \times 10^{-3}$ S cm$^{-1}$). The relative density of the pellet used for La$_{7.464}$Bi$_{1.866}$(SiO$_4$)$_6$O$_2$ was 75%, whilst for "La$_{10}$(SiO$_4$)$_6$O$_3$" (MSC047) the relative density was 70%. These values are similar to the densities obtained by Tao & Irvine,[9] who also reported difficulty in synthesising dense pellets. In order to check the reproducibility of the measurements, two samples of nominal composition "La$_{10}$(SiO$_4$)$_6$O$_3$", CAF012 and CAF015 (see Table 5.5), were measured, giving similar results at 888 °C of σ ≈ $2.6 \times 10^{-4}$ S cm$^{-1}$ and σ ≈ $2.9 \times 10^{-4}$ S cm$^{-1}$ respectively. Figure 5.8 shows the total conductivity plots of the samples measured and Table 5.10 gives the activation energies, with the relative densities of MSC047 and MSC050 updated to reflect the composition as determined by Rietveld refinement. The error quoted for the activation energies is derived from the error of the line least squares fit.
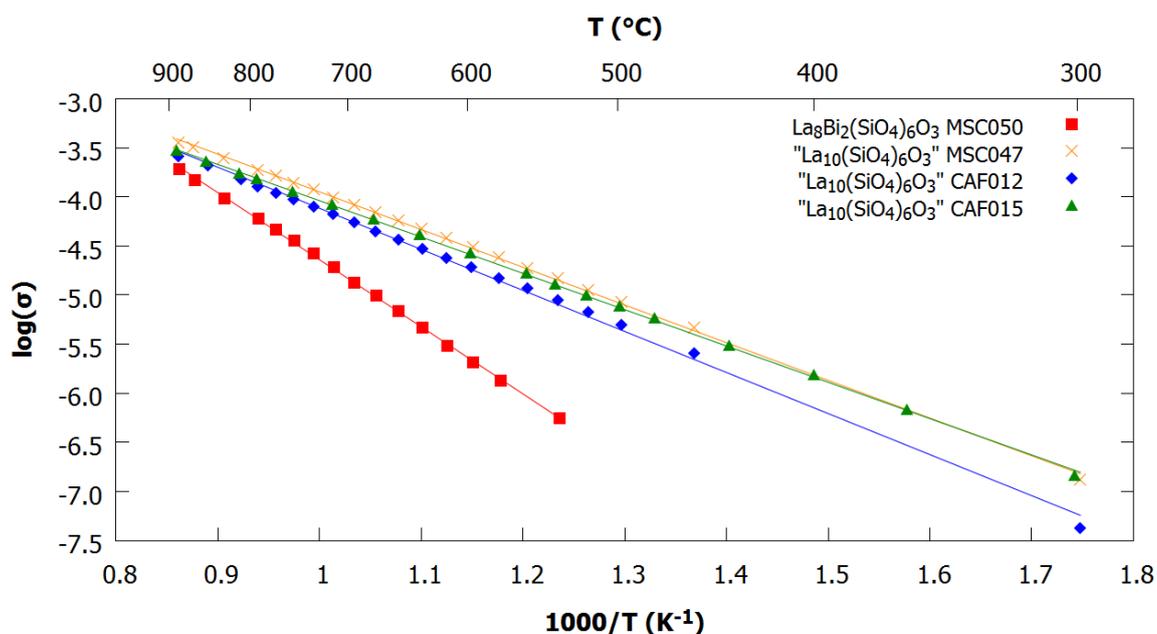
**Figure 5.8** – The total conductivities of La$_{7.464}$Bi$_{1.866}$(SiO$_4$)O$_2$, La$_{9.29(5)}$(SiO$_4$)$_6$O$_2$ and "La$_{10}$(SiO$_4$)$_6$O$_3$" samples measured here (Table 5.5).

It is unknown why the conductivity of the samples measured here is much lower than previously reported. The conductivity from La$_{7.464}$Bi$_{1.866}$(SiO$_4$)$_6$O$_2$ is lower than the samples of "La$_{10}$(SiO$_4$)$_6$O$_3$" measured here; La$_{7.464}$Bi$_{1.866}$(SiO$_4$)$_6$O$_2$ only possesses a conductivity of σ ≈ 1.9 × 10$^{-4}$ S cm$^{-1}$ at 888 °C. It is possible that the La$_2$Si$_2$O$_7$ impurity is hindering the conductivity of the La$_{7.464}$Bi$_{1.866}$(SiO$_4$)$_6$O$_2$ sample, although it is unlikely that an impurity that is 7.5(4)% by mass would affect conductivity significantly.

**Table 5.10 – Activation energies, conductivities at 888 °C and relative densities of La$_{9.29(5)}$(SiO$_4$)$_6$O$_2$, "La$_{10}$(SiO$_4$)$_6$O$_3$" and La$_{7.464}$Bi$_{1.866}$(SiO$_4$)$_6$O$_2$ samples. The relative densities of CAF012 and CAF015 were calculated using the nominal compositions.**

| Sample code | Formula | $E_a$ (eV) | σ (S cm$^{-1}$) | Relative density (%) |
|---|---|---|---|---|
| MSC047 | La$_{9.29(5)}$(SiO$_4$)$_6$O$_2$ | 0.833(3) | 3.6 × 10$^{-4}$ | 70 |
| CAF012 | "La$_{10}$(SiO$_4$)$_6$O$_3$" | 0.9000(7) | 2.6 × 10$^{-4}$ | 65 |
| CAF015 | "La$_{10}$(SiO$_4$)$_6$O$_3$" | 0.8040(6) | 2.9 × 10$^{-4}$ | 64 |
| MSC050 | La$_{7.464}$Bi$_{1.866}$(SiO$_4$)$_6$O$_2$ | 1.439(8) | 1.9 × 10$^{-4}$ | 75 |

The activation energy for La$_{7.464}$Bi$_{1.866}$(SiO$_4$)$_6$O$_2$ is much higher than that determined for La$_{9.29(5)}$(SiO$_4$)$_6$O$_2$. The conductivity observed here for La$_{7.464}$Bi$_{1.866}$(SiO$_4$)$_6$O$_2$ is also lower than that of "La$_8$Bi$_2$(SiO$_4$)$_6$O$_3$" found by Kim and Lee,[20] who determined the conductivity to be σ ≈ 2.4 × 10$^{-4}$ S cm$^{-1}$ at 700 °C. Their value is very similar to the conductivity of the "La$_{10}$(SiO$_4$)$_6$O$_3$" samples presented here at 888 °C. They did not give the conductivity of the "La$_{10}$(SiO$_4$)$_6$O$_3$" sample that

they made, though they claim that "La$_8$Bi$_2$(SiO$_4$)$_6$O$_3$" has a superior ionic conductivity. The activation energy they report is 0.72 eV. Additionally, they qualitatively describe the activation energy of their samples and suggest that the "La$_8$Bi$_2$(SiO$_4$)$_6$O$_3$" sample would have superior conductivity at lower temperatures. As they did not give any conductivity measurements for "La$_{10}$(SiO$_4$)$_6$O$_3$", these results can only be compared to those found previously in the literature and here. The activation energy of "La$_8$Bi$_2$(SiO$_4$)$_6$O$_3$" is slightly lower than that observed for the "La$_{10}$(SiO$_4$)$_6$O$_3$" samples in this work (0.8040(6) – 0.9000(7) eV), but equal to or slightly higher than the values[1-2, 9] given in Table 5.2. This suggests that it would likely still have a lower conductivity at lower temperatures. Furthermore, they conclude that there is likely some sort of order-disorder transition in the "oxygen vacancy structure", but their Arrhenius plot has no change in gradient and they show no measurements that support this conclusion.

Despite Bi$^{3+}$ improving conductivity in the germanate apatites,[14-15, 22] these results indicate that Bi$^{3+}$ doping in the silicate analogues decreases conductivity at the operating temperatures for SOFCs.

### 5.3.3 SSNMR

MAS-SSNMR was performed on La$_{7.464}$Bi$_{1.866}$(SiO$_4$)$_6$O$_2$ in order to probe the local environment around Si$^{4+}$. Additionally, samples of nominal compositions of "La$_{10}$(SiO$_4$)$_6$O$_3$" (MSC047, CAF012 and CAF015) and La$_{9.33}$(SiO$_4$)$_6$O$_2$ were also measured in order to compare the local environments. Figure 5.9 shows the spectra. La$_{9.33}$(SiO$_4$)$_6$O$_2$, La$_8$M$_2$(SiO$_4$)$_6$O$_2$, La$_{8.67}$M(SiO$_4$)$_6$O$_2$, La$_9$M(SiO$_4$)$_6$O$_{2.5}$ (M = Ca, Sr, Ba) and La$_{10}$(TiO$_4$)$_x$(SiO$_4$)$_{6-x}$O$_3$ (0.25 ≤ $x$ ≤ 2.0) have previously been studied with $^{29}$Si SSNMR.[17, 26] Table 5.11 summarises the peaks seen in the $^{29}$Si SSNMR spectra of these materials. All of the spectra were measured using TMS as the standard, so the chemical shifts can be directly compared. Table 5.11 shows that all the apatite silicate samples have a peak at $-\delta$ = 77–78 ppm. The samples that nominally have excess oxygen (La$_9$M(SiO$_4$)$_6$O$_{2.5}$, La$_{10}$(TiO$_4$)(SiO$_4$)$_5$O$_3$) have peaks at $-\delta$ = 77–78, and at 81 ppm. The samples that nominally have cation vacancies and/or excess oxygen (La$_{9.33}$(SiO$_4$)$_6$O$_2$, La$_{9.67}$(SiO$_4$)$_6$O$_{2.5}$, La$_{9.6}$(SiO$_4$)$_6$O$_{2.4}$) have all three peaks at $-\delta$ = 77–78, 81 and 83–85 ppm. Peaks in the $-\delta$ = 77 − 78 ppm region are typically attributed to isolated SiO$_4$ tetrahedra.[12, 26-28]
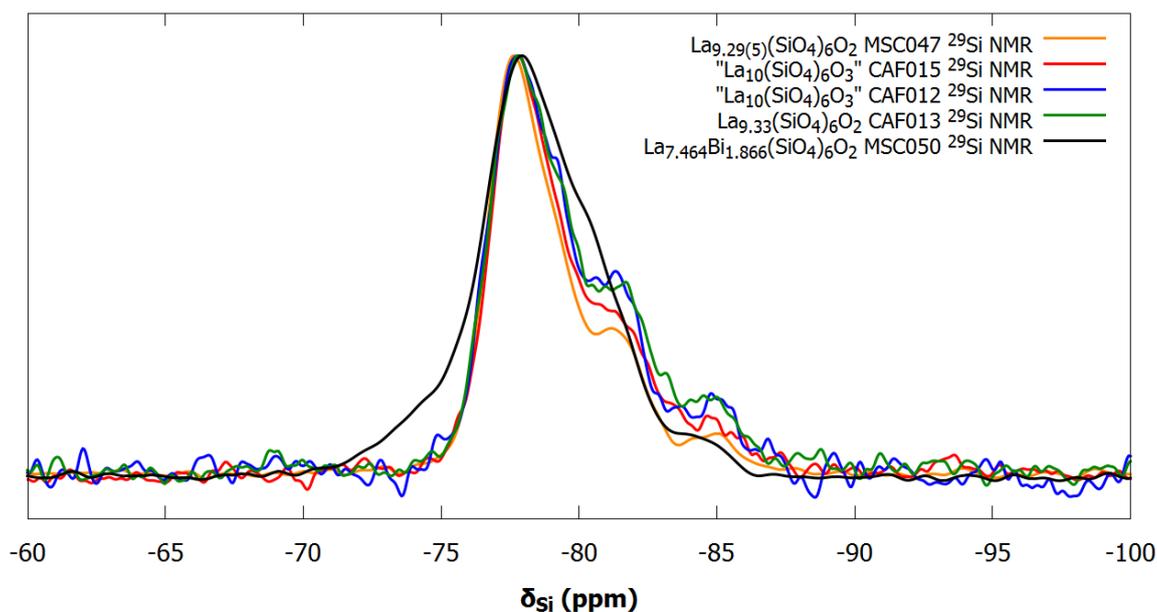
**Figure 5.9 –**$^{29}$Si MAS-NMR spectra of La$_{9.29(5)}$(SiO$_4$)$_6$O$_2$, "La$_{10}$(SiO$_4$)$_6$O$_3$", La$_{9.33}$(SiO$_4$)$_6$O$_2$ and La$_{7.464}$Bi$_{1.866}$(SiO$_4$)$_6$O$_2$.

In the literature, the peak at $-\delta$ = 81 ppm has been attributed to both "SiO$_5$" units and SiO$_4$ tetrahedra that have been distorted by the La$^{3+}$ cation vacancies.[12, 26, 28] While Ge is known to readily adopt five-fold and six-fold coordination under standard conditions as discussed in Chapter 4, for Si this is far less common, though it has been reported. For example, silicon phosphates, such as SiP$_2$O$_7$, Si$_5$(PO$_4$)$_6$O and the Si(PO$_4$)$_6$(SiO$_4$Et$_2$)$_6^-$ anion are known to have SiO$_6$ octahedra.[29-31] Si$_5$(PO$_4$)$_6$O was determined to have SiO$_6$ octahedra through single crystal X-ray diffraction.[29] Si atoms with five-fold coordination have also been observed in hydroxyl silicates[32] through single crystal X-ray diffraction, where the backbone is considered as SiO$_5$ units. Furthermore, SSNMR has indicated that 0.06(2)% (slow cooled) to 0.10(2)% (quenched) Si atoms are present as SiO$_5$ in K$_2$Si$_4$O$_9$ glasses at atmospheric pressure, although in order to detect these features $^{29}$Si-enriched samples were used.[33] This suggests that it is possible for SiO$_5$ to exist at standard conditions, though it has not been demonstrated by crystallography in apatite-type materials.

**Table 5.11 – The peaks previously found in the $^{29}$Si SSNMR spectra of different silicate apatite-type materials reported in the literature. A green fill means that the peak is present at that chemical shift in the spectrum of the material(s) and a grey fill means that there is no peak present at that chemical shift.**

| −δ (ppm) Attributed to: | 77–78 SiO$_4$ tetrahedra | 81 "SiO$_5$"/cation vacancies (distorted SiO$_4$) | 83–85 Si$_2$O$_7$ group | Reference |
|---|---|---|---|---|
| La$_8$M$_2$(SiO$_4$)$_6$O$_2$ (M = Ca, Sr, Ba) | green | grey | grey | Samson et al.[17] |
| La$_9$M(SiO$_4$)$_6$O$_{2.5}$ (M = Ca, Sr, Ba) | green | green | grey | Samson et al.[17] |
| La$_{8.67}$M(SiO$_4$)$_6$O$_2$ (M = Ca, Sr, Ba) | green | green | grey | Samson et al.[17] |
| La$_{9.33}$(SiO$_4$)$_6$O$_2$ | green | green | green | Samson et al.[17] |
| La$_{9.67}$(SiO$_4$)$_6$O$_{2.5}$ | green | green | green | Samson et al.[17] |
| La$_{10}$(TiO$_4$)$_2$(SiO$_4$)$_4$O$_3$ | green | grey | grey | Al-Yasari et al.[26] |
| La$_{10}$(TiO$_4$)(SiO$_4$)$_5$O$_3$ | green | green | grey | Al-Yasari et al.[26] |
| La$_{9.6}$(SiO$_4$)$_6$O$_{2.4}$ | green | green | green | Corrie et al.[12] |
| La$_{9.33}$(SiO$_4$)$_6$O$_2$ | green | green | grey | Dupree et al.[27] |

The peaks at −δ = 83 − 85 ppm have previously been attributed to the formation of Si$_2$O$_7$ units through condensation of SiO$_4$ tetrahedra.[17] However, the shortest Si–Si distance[10] in La$_{9.33}$(SiO$_4$)$_6$O$_2$ is 4.231 Å, whilst in La$_2$Si$_2$O$_7$, the Si–Si distances within the Si$_2$O$_7$ are 2.988 and 3.026 Å,[34] and the Si–Si distance within the Si$_2$O$_7$ units in Si$_5$(PO$_4$)$_6$O is 3.186 Å.[29] The shortest Si–Si distance between Si$_2$O$_7$ units is 3.892 Å, which is still shorter than the shortest distance between adjacent Si atoms found in La$_{9.33}$(SiO$_4$)$_6$O$_2$. It is therefore not likely that a Si$_2$O$_7$ unit could form in the apatites. It may be possible that the La$^{3+}$ cation vacancy allows the Si$^{4+}$ to attract the coordinated O$^{2-}$ more strongly, resulting in a contracted SiO$_4$ unit; i.e. a SiO$_4$ unit with short Si–O bonds. For example, the shortest Si–O distance found in this report for La$_{9.29(5)}$(SiO$_4$)$_6$O$_2$ is 1.59(2) Å. SiO$_4$ units have been attributed to chemical shifts in the range of −δ = 77 − 85 ppm.[35]

In La$_{8.67}$M(SiO$_4$)$_6$O$_2$ apatites, there are no excess oxides, but there is still a peak at −δ = 81 ppm, indicating that this peak could be attributed to distorted SiO$_4$ groups by introducing cation vacancies. There are no peaks at −δ = 83–85 ppm. The increased size of the Sr$^{2+}$ and Ba$^{2+}$

compared to La$^{3+}$ may prevent SiO$_4$ contraction, but Ca$^{2+}$ is smaller[21] than La$^{3+}$, which makes this reason seem unlikely.

The apatite material La$_{10}$(TiO$_4$)(SiO$_4$)$_5$O$_3$ only has the peak at $-\delta$ = 77 – 78 ppm, corresponding to typical SiO$_4$ units, which can be explained[26] by the excess oxygen coordinating only with the Ti$^{4+}$. On the other hand, La$_{10}$(TiO$_4$)$_2$(SiO$_4$)$_4$O$_3$ has fewer Ti$^{4+}$ cations, so the small shoulder observed at – 80.5 ppm has been attributed to SiO$_5$ units. The SiO$_5$ units were not demonstrated crystallographically, however, and the shoulder could arise from short Si–O distances within SiO$_4$ tetrahedra.

The peak at $-\delta$ = 83–85 ppm only appears in apatites with cation vacancies, so it is reasonable to assume that the cation vacancies are the reason for its presence in apatites, possibly caused by allowing the contraction of SiO$_4$ tetrahedra.[17, 35] Table 5.12 gives a summary of the peaks that are present in the samples measured and shown in Figure 5.9.

**Table 5.12 – Summary of the approximate chemical shifts of the peaks present in the $^{29}$Si NMR spectra shown in Figure 5.9, where a green X means that the peak is present.**

|  |  | $-\delta$ (ppm) | | |
| --- | --- | --- | --- | --- |
| Sample code | Nominal Formula | 77–78 | 80.5 | 85 |
| MSC047 | La$_{10}$(SiO$_4$)$_6$O$_3$ | X | X | X |
| CAF015 | La$_{10}$(SiO$_4$)$_6$O$_3$ | X | X | X |
| CAF012 | La$_{10}$(SiO$_4$)$_6$O$_3$ | X | X | X |
| CAF013 | La$_{9.33}$(SiO$_4$)$_6$O$_2$ | X | X | X |
| MSC050 | La$_8$Bi$_2$(SiO$_4$)$_6$O$_3$ | X | X | |

The La$_{9.33}$(SiO$_4$)$_6$O$_2$ sample (CAF013) has all three peaks, agreeing with the previous literature.[17] On the other hand, the nominally "La$_{10}$(SiO$_4$)$_6$O$_3$" samples (MSC047, CAF012, CAF015) all have three peaks. It has been shown through Rietveld refinement and SEM-EDX that these three samples most likely do not correspond to the formula "La$_{10}$(SiO$_4$)$_6$O$_3$", but are more likely La$_{9.33}$(SiO$_4$)$_6$O$_2$. The weak feature could correspond to the Si$_2$O$_7$ units found in La$_2$Si$_2$O$_7$. The SEM-EDX results indicated the existence of La$_2$Si$_2$O$_7$ in CAF013 and CAF015, but there is no evidence of this phase existing in MSC047, which suggests that this feature arises due to the apatite phase. The presence of these three peaks would be accounted for if all samples are La-deficient, leading to a range of Si environments.

Examining La$_{7.464}$Bi$_{1.866}$(SiO$_4$)$_6$O$_2$ (MSC050), there is a peak at $-\delta$ = 78 ppm that is very broad. This most likely arises from SiO$_4$ tetrahedra, with the broadening due to the additional disorder

created by introducing Bi$^{3+}$ into the cation sublattice. The broadening of this peak has been observed with Sr$^{2+}$ doping previously.[12] This first peak is wide enough to overlap with the region at $-\delta \approx 80.5$ with a larger relative intensity than the La$_{9.33+x}$(SiO$_4$)$_6$O$_{2+1.5x}$ ($x$ = 0, 0.67) samples, which may also be as a result of the additional disorder induced by Bi$^{3+}$. There is a weak feature at $-\delta$ = 85 ppm, which could be due to the Si$_2$O$_7$ groups in the La$_2$Si$_2$O$_7$ impurity or from short Si–O distances in the apatite caused by cation vacancies. It is difficult to determine how much the impurity contributes to the intensity seen at this chemical shift and how much, if at all, the apatite phase contributes to it. Due to the broadening of the peaks, it is highly probable that Bi$^{3+}$ has been doped into the lanthanum silicate apatite.

There was an attempt at a quantum-filtered experiment in order to determine if the feature at $-\delta$ = 85 ppm arose from Si$_2$O$_7$ or SiO$_4$ units, but no signal was obtained. It is not known if no signal were obtained because there are no Si$_2$O$_7$ units, or because of the low natural abundance of $^{29}$Si.

## 5.4 Conclusions

The results described here lead us to the following conclusions:

1. In the attempt to synthesise "La$_8$Bi$_2$(SiO$_4$)$_6$O$_3$", a Bi-doped apatite silicate has been formed. SEM-EDX results a formula that does not correspond to "La$_8$Bi$_2$(SiO$_4$)$_6$O$_3$", but whilst Bi-containing, is cation-deficient and therefore has no excess oxygen.

2. The $^{29}$Si SSNMR spectra provide more evidence that Bi$^{3+}$ has been doped into the apatite structure, as there is a large broadening of the SiO$_4$ peak compared to that of La$_{9.33+x}$(SiO$_4$)$_6$O$_{2+1.5x}$ ($x$ = 0, "0.67").

3. The results cast further doubt on the existence of "La$_{10}$(SiO$_4$)$_6$O$_3$", as Rietveld refinements show a stoichiometry of La$_{9.29(5)}$(SiO$_4$)$_6$O$_2$ for MSC047 (see Table 5.3), which was nominally "La$_{10}$(SiO$_4$)$_6$O$_3$". SEM-EDX also suggests that all "La$_{10}$(SiO$_4$)$_6$O$_3$" samples are in fact La-deficient.

4. $^{29}$Si-SSNMR spectra show two different samples of "La$_{10}$(SiO$_4$)$_6$O$_3$" (CAF012 and CAF015) containing a peak that possibly arises from contracted SiO$_4$ units (see Table 5.12). This was also seen in the La$_{9.33}$(SiO$_4$)$_6$O$_2$ sample (CAF013). This peak is seen in apatite silicates with La$^{3+}$ vacancies, but not in silicate apatites with apparently fully occupied A sites[12, 17, 26] (see Table 5.11). The peak most likely arises due to the contraction of SiO$_4$ tetrahedra so that the Si–O bonds are of a similar length to the Si–O bonds in a Si$_2$O$_7$ unit.

5. Based on the evidence suggesting "La$_{10}$(SiO$_4$)$_6$O$_3$" does not exist, the Rietveld refinement for the Bi-doped phase was performed with a total A cation content per formula unit of 9.33, corresponding to a formula of La$_{7.464}$Bi$_{1.866}$(SiO$_4$)$_6$O$_2$. This resulted in a slightly better fit than when the total A site content was 10.

6. These results indicate that it could be impossible to form an oxygen-excess lanthanum silicate apatite.

7. The conductivity of $La_{7.464}Bi_{1.866}(SiO_4)_6O_2$ was found to be lower than $La_{9.29(5)}(SiO_4)_6O_2$ and "$La_{10}(SiO_4)_6O_3$", with $\sigma = 6.04 \times 10^{-5}$ S cm$^{-1}$ and $\sigma = 1.88 \times 10^{-4}$ S cm$^{-1}$ respectively at 800 °C. This is the opposite of the effect observed in the germanate analogues.[14-15]

It is unknown why the conductivity is lower in $La_{7.464}Bi_{1.866}(SiO_4)_6O_2$ compared to the Bi-free analogues, but this is likely to be due to different conduction mechanisms arising from different distributions of the key defects. Further investigations into the conductivity are warranted, ideally involving single crystal neutron diffraction and computational dynamics studies. Quantum-filtered SSNMR experiments on $^{29}$Si-enriched samples could also determine definitively if the feature at $-\delta = 85$ ppm is caused by $Si_2O_7$ units or $SiO_4$ units.

## 5.5 References

1. Nakayama, S.; Kageyama, T.; Aono, H.; Sadaoka, Y., Ionic conductivity of lanthanoid silicates, $Ln_{10}(SiO_4)_6O_3$ (Ln= La, Nd, Sm, Gd, Dy, Y, Ho, Er and Yb). *Journal of Materials Chemistry* **1995,** *5* (11), 1801-1805.
2. Arikawa, H.; Nishiguchi, H.; Ishihara, T.; Takita, Y., Oxide ion conductivity in Sr-doped $La_{10}Ge_6O_{27}$ apatite oxide. *Solid State Ionics* **2000,** *136*, 31-37.
3. Kendrick, E.; Islam, M. S.; Slater, P. R., Developing apatites for solid oxide fuel cells: insight into structural, transport and doping properties. *Journal of Materials Chemistry* **2007,** *17* (30), 3104-3111.
4. Abram, E. J.; Kirk, C. A.; Sinclair, D. C.; West, A. R., Synthesis and characterisation of lanthanum germanate-based apatite phases. *Solid State Ionics* **2005,** *176* (23), 1941-1947.
5. Orera, A.; Slater, P. R., New Chemical Systems for Solid Oxide Fuel Cells. *Chemistry of Materials* **2009,** *22* (3), 675-690.
6. León-Reina, L.; Losilla, E. R.; Martínez-Lara, M.; Bruque, S.; Aranda, M. A. G., Interstitial oxygen conduction in lanthanum oxy-apatite electrolytes. *Journal of Materials Chemistry* **2004,** *14* (7), 1142-1149.
7. An, T.; Baikie, T.; Orera, A.; Piltz, R. O.; Meven, M.; Slater, P. R.; Wei, J.; Sanjuán, M. L.; White, T. J., Interstitial Oxide Ion Distribution and Transport Mechanism in Aluminum-Doped Neodymium Silicate Apatite Electrolytes. *Journal of the American Chemical Society* **2016,** *138* (13), 4468-4483.
8. Fujii, K.; Yashima, M.; Hibino, K.; Shiraiwa, M.; Fukuda, K.; Nakayama, S.; Ishizawa, N.; Hanashima, T.; Ohhara, T., High oxide-ion conductivity in Si-deficient $La_{9.565}(Si_{5.826}\square_{0.174})O_{26}$ apatite without interstitial oxygens due to the overbonded channel oxygens. *Journal of Materials Chemistry A* **2018,** *6* (23), 10835-10846.
9. Tao, S.; Irvine, J. T. S., Preparation and characterisation of apatite-type lanthanum silicates by a sol-gel process. *Materials Research Bulletin* **2001,** *36* (7), 1245-1258.
10. Okudera, H.; Masubuchi, Y.; Kikkawa, S.; Yoshiasa, A., Structure of oxide ion-conducting lanthanum oxyapatite, $La_{9.33}(SiO_4)_6O_2$. *Solid State Ionics* **2005,** *176* (15), 1473-1478.
11. Nakayama, S.; Sakamoto, M., Preparation of apatite-type $La_{9.33}Ge_6O_{26}$ single-crystal from sintered ceramics by a seeding method and its oxide ionic conduction. *Solid State Ionics* **2013,** *253*, 47-52.
12. Corrie, B. J.; Shin, J. F.; Hull, S.; Knight, K. S.; Vlachou, M. C.; Hanna, J. V.; Slater, P. R., Neutron diffraction and multinuclear solid state NMR investigation into the structures of oxide ion conducting $La_{9.6}Si_6O_{26.4}$ and $La_8Sr_2Si_6O_{26}$, and their hydrated phases. *Dalton Transactions* **2016,** *45* (1), 121-133.
13. Peet, J. R.; Piovano, A.; Johnson, M. R.; Evans, I. R., Location and orientation of lone pairs in apatite-type materials: a computational study. *Dalton Transactions* **2017,** *46* (46), 15996-15999.
14. Tate, M. L.; Fuller, C. A.; Avdeev, M.; Brand, H. E. A.; McIntyre, G. J.; Radosavljevic Evans, I., Synthesis and characterisation of new Bi(iii)-containing apatite-type oxide ion conductors: the influence of lone pairs. *Dalton Transactions* **2017,** *46* (37), 12494-12499.
15. Peet, J. R.; Chambers, M. S.; Piovano, A.; Johnson, M. R.; Evans, I. R., Dynamics in Bi(iii)-containing apatite-type oxide ion conductors: a combined computational and experimental study. *Journal of Materials Chemistry A* **2018,** *6* (12), 5129-5135.
16. Tolchard, J. R.; Sansom, J. E. H.; Slater, P. R.; Islam, M. S., Effect of Ba and Bi doping on the synthesis and sintering of Ge-based apatite phases. *Journal of Solid State Electrochemistry* **2004,** *8* (9), 668-673.
17. Sansom, J. E. H.; Tolchard, J. R.; Islam, M. S.; Apperley, D.; Slater, P. R., Solid state $^{29}$Si NMR studies of apatite-type oxide ion conductors. *Journal of Materials Chemistry* **2006,** *16* (15), 1410-1413.
18. Liu, W.; Tsuchiya, T.; Miyoshi, S.; Yamaguchi, S.; Kobayashi, K.; Pan, W., The effect of local structure on ionic conductivity of apatite-type $La_{9.5}Si_6O_{26.25}$. *Journal of Power Sources* **2014,** *248*, 685-689.

19.     Matsunaga, K.; Imaizumi, K.; Nakamura, A.; Toyoura, K., Physical Origin of Unusual Anisotropic Motion of Columnar Oxygen Ions in Apatite-Type Fast Ionic Conductor of Lanthanum Silicate. *Journal of Physical Chemistry C* **2017,** *121* (38), 20621-20628.

20.     Kim, D.-Y.; Lee, S.-G., Fabrication and electrical properties of Si-based La$_{10-x}$Bi$_x$(SiO$_4$)$_6$O$_3$ apatite ionic conductor. *Materials Research Bulletin* **2012,** *47* (10), 2856-2858.

21.     Shannon, R. D.; Prewitt, C. T., Effective Ionic Radii in Oxides and Fluorides. *Acta Crystallographica Section B: Structural Crystallography and Crystal Chemistry* **1969**, 925-946.

22.     Tate, M. L.; Blom, D. A.; Avdeev, M.; Brand, H. E. A.; McIntyre, G. J.; Vogt, T.; Evans, I. R., New Apatite-Type Oxide Ion Conductor, Bi$_2$La$_8$[(GeO$_4$)$_6$]O$_3$: Structure, Properties, and Direct Imaging of Low-Level Interstitial Oxygen Atoms Using Aberration-Corrected Scanning Transmission Electron Microscopy. *Advanced Functional Materials* **2017,** *27* (8), 1605625.

23.     Brown, I. D.; Altermatt, D., Bond-valence parameters obtained from a systematic analysis of the Inorganic Crystal Structure Database. *Acta Crystallographica Section B: Structural Crystallography and Crystal Chemistry* **1985,** *41* (4), 244-247.

24.     Baikie, T.; Pramana, S. S.; Ferraris, C.; Huang, Y.; Kendrick, E.; Knight, K. S.; Ahmad, Z.; White, T. J., Polysomatic apatites. *Acta Crystallographica Section B: Structural Crystallography and Crystal Chemistry* **2010,** *66* (1), 1-16.

25.     Irvine, J. T. S.; Sinclair, D. C.; West, A. R., Electroceramics: Characterization by Impedance Spectroscopy. *Adv. Mater.* **1990,** *2* (3), 132-138.

26.     Al-Yasari, A.; Jones, A.; Orera, A.; Apperley, D. C.; Driscoll, D.; Islam, M. S.; Slater, P. R., Preparation of high-oxygen-content apatite silicates through Ti-doping: effect of Ti-doping on the oxide ion conductivity. *Journal of Materials Chemistry* **2009,** *19* (28), 5003-5008.

27.     Dupree, R.; Lewis, M. H.; Smith, M. E., A high-resolution NMR study of the lanthanum-silicon-aluminum-oxygen-nitrogen system. *Journal of the American Chemical Society* **1989,** *111* (14), 5125-5132.

28.     Sansom, J. E. H.; Slater, P. R., Oxide ion conductivity in the mixed Si/Ge apatite-type phases La$_{9.33}$Si$_{6-x}$Ge$_x$O$_{26}$. *Solid State Ionics* **2004,** *167* (1), 23-27.

29.     Mayer, H., Die Kristallstruktur von Si$_5$O[PO$_4$]$_6$. *Monatshefte für Chemie* **1974,** *105*, 46-54.

30.     Poojary, D. M.; Borade, R. B.; Clearfield, A., Structural characterisation of silicon orthophosphate. *Inorganica Chimica Acta* **1993,** *208*, 23-29.

31.     Jähnigen, S.; Brendler, E.; Böhme, U.; Heide, G.; Kroke, E., Silicophosphates containing SiO$_6$ octahedra – anhydrous synthesis under ambient conditions. *New Journal of Chemistry* **2014,** *38*, 744-751.

32.     Tacke, R.; Burschka, C.; Richter, I.; Wagner, B.; Willeke, R., Pentacoordinate Silicon Compounds with SiO$_5$ Skeletons Containing SiOH or SiOSi Groups: Derivatives of the Pentahydroxosilicate(1–) Anion [Si(OH)$_5$]$^-$ and Its Anhydride [(HO)$_4$Si–O–Si(OH)$_4$]$^{2-}$. *Journal of the American Chemical Society* **2000,** *122* (35), 8480-8485.

33.     Stebbins, J. F., NMR evidence for five-coordinated silicon in a silicate glass at atmospheric pressure. *Nature* **1991,** *351*, 638.

34.     Dago, A. M.; Pushcharovskij, D. Y.; Strelkova, E. E.; Pobedimskaya, E. A.; Belov, N. V., La$_2$Si$_2$O$_7$ Hydrothermal synthesis and crystal structure. *Doklady Akademii Nauk SSSR* **1980,** *252* (5), 1117-1121.

35.     Magi, M.; Lippmaa, E.; Samoson, A.; Engelhardt, G.; Grimmer, A. R., Solid-state high-resolution silicon-29 chemical shifts in silicates. *The Journal of Physical Chemistry* **1984,** *88* (8), 1518-1522.

# 6. Local and Long Range Structure of Hexagonal Perovskite-like Ba₃NbMoO₈.₅

## 6.1 Introduction

### 6.1.1 Background

The perovskite-type oxides, $ABO_3$, are a highly functional family of materials. One of their properties is high oxide-ion conductivity as shown, for example, by $Na_{0.5}Bi_{0.5}TiO_{3-\delta}$.[1] The cubic perovskite structure can be thought of as close packed $AO_3$ layers stacked in a cubic manner, where the B cations fill the octahedral holes. The $AO_3$ layers can also stack in a hexagonal manner with various A:B ratios, leading to a wide range of related structures and stoichiometries. Examples include the 9R polytypes, such as $BaRuO_3$ ($Ba_3Ru_3O_9$)[2] and cation-deficient $Ba_3Re_2O_9$[3] ($A_3B_2O_9$). The 9R polytype consists of face-sharing $BO_6$ octahedra, creating B1–B2–B1 trimers that connect to other B1–B2–B1 trimers along the rhombohedral $c$ axis. $Ba_3Re_2O_9$ adopts a similar structure with the middle octahedral site vacant, resulting in only corner-sharing $BO_6$ octahedra. In addition, anion-deficient compositions of $A_3B_2O_8$ are found, adopting the palmierite structure.[4] This structure is similar to the 9R polytype, but stacks alternatively with $AO_2$ layers and $A_2O_6$ layers.

Ba₃NbMoO₈.₅ crystallises with a novel structure in $R$-$3m$ symmetry that has been described as a hybrid of the palmierite and 9R structures. Table 6.1 gives some previously reported[5] crystallographic parameters for Ba₃NbMoO₈.₅ and Figure 6.1 shows the 9R polytype, the hybrid Ba₃NbMoO₈.₅ and $Ba_3Nb_2O_8$ palmierite.

**Table 6.1 – The structural parameters of Ba₃NbMoO₈.₅ as reported by Fop *et al*.[5] The 'M1' and 'M2' sites are equally occupied by Nb and Mo, *i.e.* M1 is 0.463 Nb and 0.463 Mo. Space group = *R*-3*m* (hexagonal axes); *a* = 5.92744(3) Å; *c* = 21.0995(2) Å; *V* = 642.003(9)**

| Site | Wyckoff position | x | y | z | Occupancy |
|------|------------------|---|---|---|-----------|
| Ba1 | 3*a* | 0 | 0 | 0 | 1 |
| Ba2 | 6*c* | 0 | 0 | 0.20629(8) | 1 |
| M1 | 6*c* | 0 | 0 | 0.39936(6) | 0.926(1) |
| M2 | 3*b* | 0 | 0 | 0.5 | 0.148(1) |
| O1 | 18*h* | 0.17212(5) | 0.82788(5) | 0.10343(2) | 1 |
| O2 | 9*e* | 0.5 | 0 | 0 | 0.449(2) |
| O3 | 36*i* | 0.0850(9) | 0.0933(7) | 0.3195(2) | 0.096(1) |
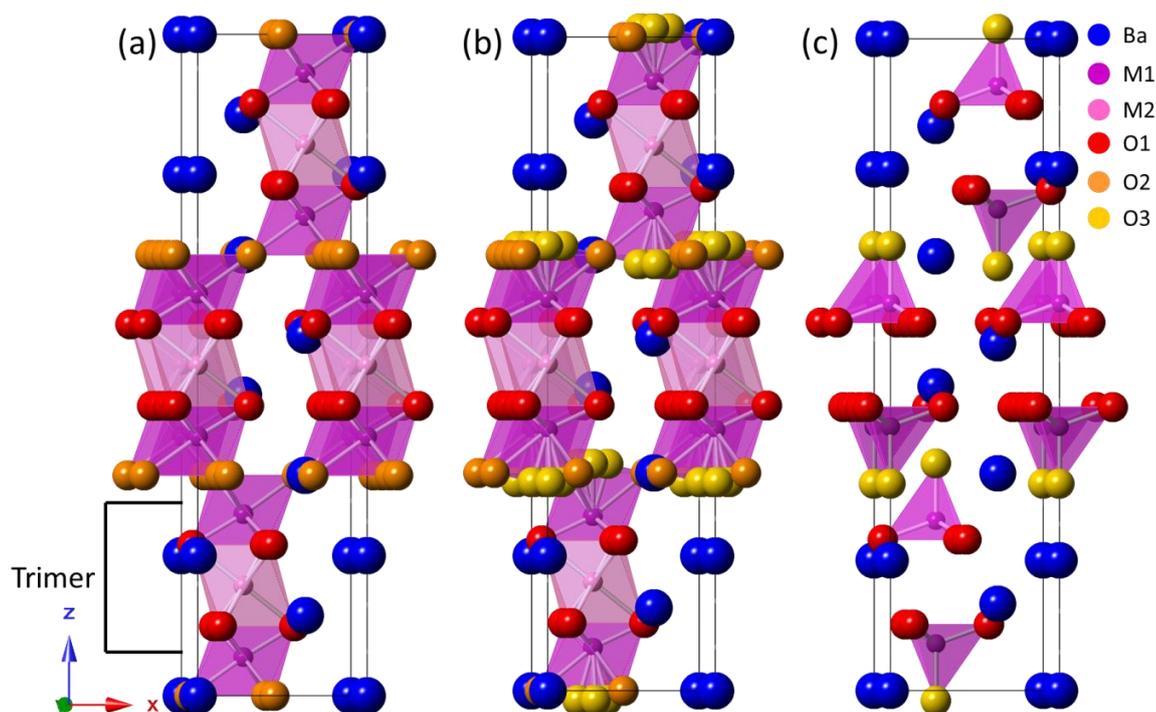
**Figure 6.1** – The crystal structures of (a) 9R perovskite, (b) Ba$_3$NbMoO$_{8.5}$ and (c) Ba$_3$Nb$_2$O$_8$ (palmierite).

The three possible B sites (two symmetrically related M1 sites and one M2 site) in the trimer are populated by two cations and the oxygen deficiency allows the terminal B sites (M1) to have a variable coordination number. It is thought that M1 polyhedra either exist as octahedra (when the O2 sites are occupied) or as tetrahedra (when an O3 site is occupied).[5-11] These models make the assumption that if an O2 site is occupied, all three neighbouring O2 sites must be occupied, and if an O3 site is occupied, the adjacent O2 sites must all be unoccupied.

Ba$_3$NbMoO$_{8.5}$ was recently found to be a good oxide-ion conductor,[5] with a conductivity of 2.2 × 10$^{-3}$ S cm$^{-1}$ at 600 °C and a change in the gradient of the Arrhenius plot between 300 and 400 °C. Authors of a high-resolution powder neutron diffraction study[6] connected the change in the conductivity with an increase in the $a$ and $c$ cell parameters, which is not accounted for by thermal expansion alone. Additionally, the M1 and O3 occupancies increase, whilst the M2 and O2 occupancies decrease in the temperature range where the $a$ and $c$ cell parameters increase (300 – 400 °C).

Fop *et al.*[6] claim that if an O3 site is occupied, the O2 sites cannot be occupied due to the short O2–O3 distances, which means the Mo/Nb in the M1 site are present exclusively as either tetrahedra or octahedra, whilst the Mo/Nb in the M2 site are always present as octahedra. These observations led the authors to hypothesise that the oxide-ion conductivity is related to the ratio of M1O$_4$ tetrahedra to M1O$_6$ octahedra. They suggest that there are approximately 50% tetrahedra at 300 °C, but at 600 °C there are ~65% tetrahedra. The oxygen stoichiometry is

believed to be maintained. A study[7] into the conductivity of Ba$_3$Mo$_{1-x}$Nb$_{1+x}$O$_{8.5-x/2}$ ($x$ = 0, 0.1, 0.2, 0.3) revealed that increasing the Nb:Mo ratio decreased the bulk conductivity at 300 °C from 1.3 × 10$^{-6}$ S cm$^{-1}$ for $x$ = 0 to 1.1 × 10$^{-7}$ S cm$^{-1}$ for $x$ = 0.3. This was attributed to Nb$^{5+}$ preferentially adopting an octahedral environment. As a result, the M2 occupancy increases and the O3 occupancy decreases. Upon heating to 600 °C, the conductivities converge, which the authors attribute to a rearrangement to a more similar structure throughout the series.

A similar study[9] was undertaken with Ba$_3$Mo$_{1-x}$W$_x$NbO$_{8.5}$ ($x$ = 0, 0.25, 0.5, 0.75, 1). The conductivity was not heavily affected above 600 °C by W doping: at ~620 °C, the total conductivities of $x$ = 0, 0.5 and 1 were σ ≈ 6.7 × 10$^{-4}$, 3.0 × 10$^{-4}$ and 2.4 × 10$^{-4}$ S cm$^{-1}$ respectively. These results agree with the study by McCombie et al.[10], who also found that the number of M1O$_4$ tetrahedra is reduced in Ba$_3$NbWO$_{8.5}$ to ~15% at room temperature compared to the ~49.9% in Ba$_3$NbMoO$_{8.5}$ at the same temperature. They found that the conductivity of the W-containing sample is an order of magnitude lower at 450 °C than the Mo analogue, but by 600 °C they are of a similar magnitude (σ = 1.7 × 10$^{-3}$ S cm$^{-1}$ for Ba$_3$NbWO$_{8.5}$). Table 6.2 gives a summary of the reported conductivities for the various compositions and Figure 6.2 shows a plot of the bulk conductivities (or total conductivity, as available) of these compositions.

**Table 6.2 – Reported conductivities for Ba$_3$Mo$_{1-x}$W$_x$NbO$_{8.5}$ ($x$ = 0, 0.5, 1), Ba$_3$Mo$_{0.7}$Nb$_{1.3}$O$_{8.35}$ and Ba$_3$W$_{1.2}$Nb$_{0.8}$O$_{8.6}$**

| Composition | Temperature (°C) | σ (S cm$^{-1}$) | Reference | Notes |
|---|---|---|---|---|
| Ba$_3$NbMoO$_{8.5}$ | 600 | 2.2 × 10$^{-3}$ | Fop et al.[5] | Bulk conductivity |
| Ba$_3$Mo$_{0.7}$Nb$_{1.3}$O$_{8.35}$ | 600 | 1.8 × 10$^{-3}$ | Fop et al.[7] | Bulk conductivity |
| BaNbWO$_{8.5}$ | 600 | 1.7 × 10$^{-3}$ | McCombie et al.[10] | Bulk conductivity |
| BaMo$_{0.5}$W$_{0.5}$NbO$_{8.5}$ | 600 | 1.61 × 10$^{-4}$ | Bernasconi et al.[9] | Total conductivity |

A synchrotron variable temperature experiment[8] indicated that there is a change in the M1 and M2 occupancies in W-doped samples and that the cell volumes of Ba$_3$NbMo$_{1-x}$W$_x$O$_{8.5}$ ($x$ = 0, 0.5, 1) converge at ~630 °C. Furthermore, the authors calculate an increase in M1O$_4$ tetrahedra to ~61% at ~630 °C and a corresponding decrease in M1O$_6$ octahedra to ~39% at the same temperature in all samples. It should be noted that the number of octahedra are calculated from oxygen occupancies obtained from X-ray diffraction, which may not be as accurate as those derived from neutron studies. These values agree with the previous results found by Fop et al.[6] Doping to create excess O made little difference to the conductivity in Ba$_3$Nb$_{0.8}$ W$_{1.2}$O$_{8.6}$, resulting in bulk conductivity of σ = 1.6 × 10$^{-3}$ S cm$^{-1}$ at 600 °C compared to 1.7 × 10$^{-3}$ S cm$^{-1}$ in Ba$_3$NbWO$_{8.5}$.[10-11]
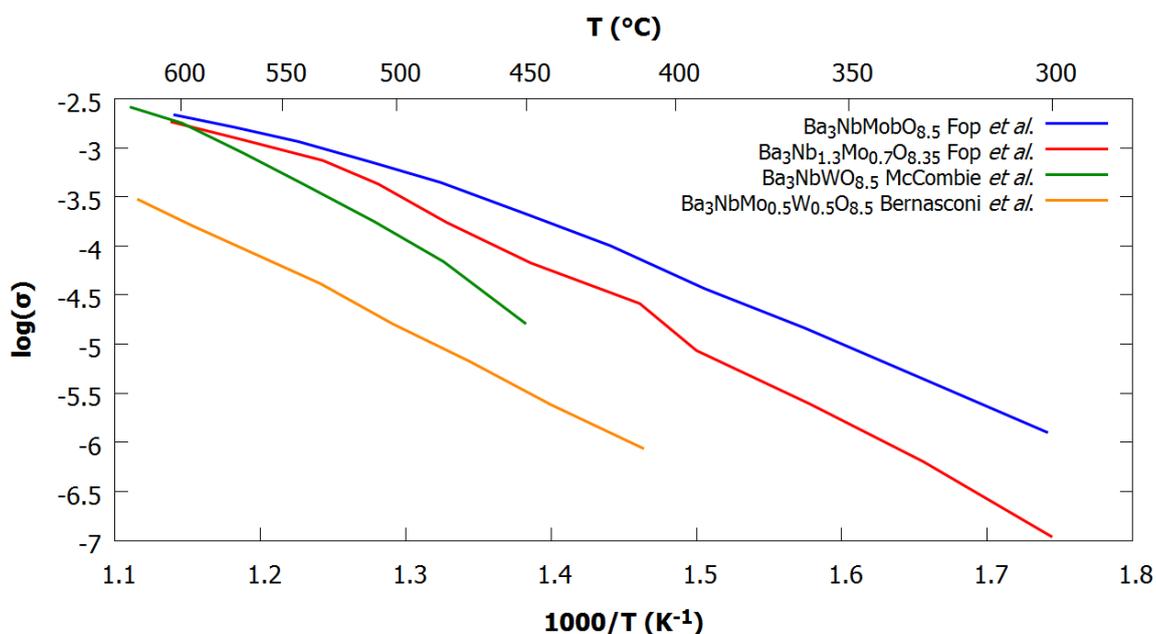
**Figure 6.2** – Conductivity plots of the compositions shown in Table 6.2.

There are, however, several problems with the proposed structural models.[5-11] Firstly, the M1–M2 distance is only ~2.1 Å. A dimer with one M1 site and M2 site occupied could not exist without either site moving significantly off centre of its ideal position. Furthermore, when the M1 and M2 anisotropic ADPs were refined freely, the M2 ADPs show an unphysical elongation along the *c* axis.[10] A recent (and to date the only) X-ray single crystal study[12] revealed that the M2 site is in fact more accurately modelled as split along the *c*-axis (on a 6*c* position) in both Ba$_3$NbMoO$_{8.5}$ and Ba$_3$NbWO$_{8.5}$. In this model, the single M2 site in the middle of a trimer is split into two, where each of the two sites are further from one of the M1 sites. This is consistent with the off-centring frequently observed for d$^0$ transition metals.[13] The longer of the two M1–M2 distances is ~2.7 Å, which is similar in magnitude to the Mo–Mo metallic bond length.[14] The authors suggested[12] that when an M2 site is occupied, the nearest M1 site is vacant, removing any short M1–M2 distances. Figure 6.3 shows a comparison between the previous models (based on powder diffraction) and the latest model (based on single crystal X-ray diffraction).
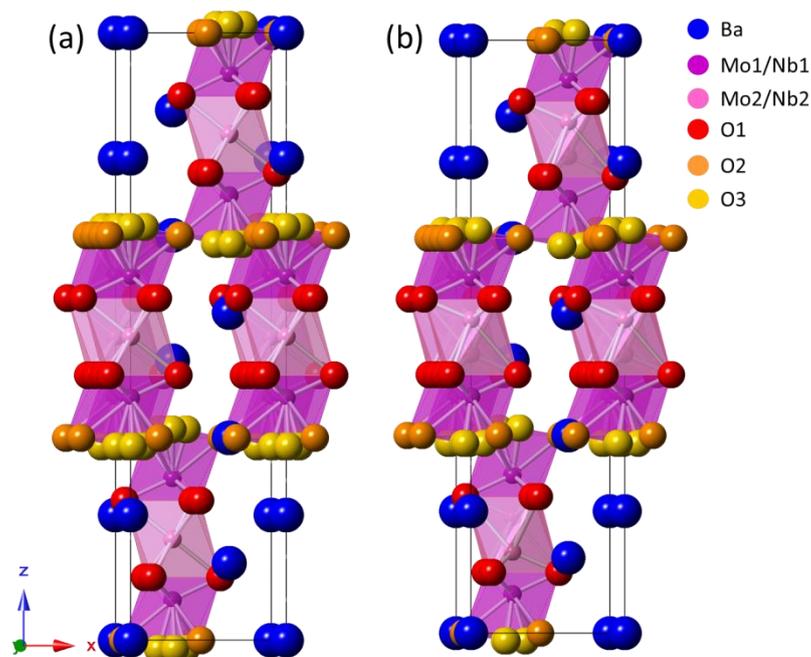
**Figure 6.3 –** Two models of Ba₃NbMoO₈.₅ with (a) a single M2 site on the 3*b* Wyckoff position[5] at room temperature and (b) the split M2 site on the 6*c* position[12] at 200 °C.

A further problem with the previous average structure models derived from powder data is the heavy emphasis placed on the octahedra : tetrahedra ratio.[5-11] There is no reason to assume that all adjacent O2 sites must be occupied if one is occupied, nor that all O2 sites are unoccupied if an adjacent O3 site is occupied. These models imply that there are no five-coordinate M1 atoms. The recent single-crystal study[12] points out that the absence of five-coordinate M1 atoms is unlikely. It was recently proposed[15] that consecutive vacancies between the boundaries of palmierite and 9R polytype domains may result in five-fold coordination of M1 atoms at the domain boundaries, but there is no experimental or computational evidence given to support this statement.

### 6.1.2 Purpose of study

Ba₃NbMoO₈.₅ is a highly disordered phase, which cannot be accurately described by the average structure alone. Variable temperature neutron total scattering analysis was performed in order to gain further insights into this phase. This allows the local coordination environment of the M1 and M2 sites to be determined and the distribution of the O2 and O3 atoms to be examined. The single-crystal X-ray study[12] revealed that the anisotropic displacement parameters of the O2 atoms suggest a hexagonal 'network' in the *ab* plane in each of the layers. Similar results were obtained from bond-valence energy landscape calculations. Neutron total scattering analysis will allow a more detailed investigation into the oxygen sublattice.

## 6.2 Experimental Procedure

### 6.2.1 Synthesis

The following synthesis was performed by Kirstie McCombie, a PhD student under the supervision of Dr Abbie McLaughlin at the University of Aberdeen. Ba$_3$NbMoO$_{8.5}$ was synthesised by grinding stoichiometric amounts of BaCO$_3$ (Aldrich, 99.98%), MoO$_3$ (Aldrich, 99.5+%) and Nb$_2$O$_5$ (Aldrich, 99.99%) together and pressing them into ten 1 g pellets. The pellets were calcined in an alumina crucible at 900 °C for 10 h. The pellets were reground, repelletised and heated at 1100 °C for 48 h and cooled to room temperature at a rate of 5 °C min$^{-1}$. The latter heating was repeated until a phase-pure product was obtained, as determined by powder X-ray diffraction. Once a phase-pure sample was deemed to have been obtained, the pellets were ground together to make one sample. The sample colour was pale beige.

### 6.2.2 Neutron analysis methodology

6.69322 g of Ba$_3$NbMoO$_{8.5}$ were loaded into an 8 mm diameter V can, filled to a depth of 5.1 cm. Neutron scattering data were collected on the POLARIS instrument at the ISIS Neutron and Muon Source. PDF-quality data were obtained at room temperature, 200 °C, 300 °C, 400 °C, 500 °C and 600 °C, by collecting eight 1 h datasets at each temperature, which were subsequently merged. Rietveld-quality data were obtained using ten minute data collections from 50 − 575 °C in 25 °C intervals. To obtain Bragg scattering data, the data were processed using routines within Mantid software.[16] Rietveld refinements were performed against the room-temperature data by refining the cell parameters, atomic coordinates, the site occupancies of the Mo, Nb and O atoms, anisotropic atomic displacement parameters (ADPs) and peak shapes. An isotropic ADP was used for the O3 site. The Mo and Nb occupancies were equated due to small difference in neutron scattering lengths ($b_{Mo}$ = 6.715 fm; $b_{Nb}$ = 7.054 fm). The background was fitted using a 12$^{th}$-order Chebyshev polynomial. The model[5] in Table 6.1 was used as a starting point. Data collected from three detector banks were used: bank 3 ($2\theta$ = 52.2461°), bank 4 ($2\theta$ = 91.5081°) and bank 5 ($2\theta$ = 146.942°). The final model obtained at room temperature was used as starting point for refinement of the higher temperature data. The procedure applied for the variable temperature refinements is discussed in Section 6.3.1.1. At 600 °C, isotropic ADPs were used and the M1 and M2 ADPs were equated.

For total scattering analysis, PDF-quality data were processed using GudrunN version 5[17] to produce $S(Q)$ data as defined in Chapter 2.3. The $S(Q)$ data produced by GudrunN were processed with the STOG software to produce $G(r)$ and $F(Q)$ files. The $G(r)$ data were produced using $Q_{max}$ = 35 Å$^{-1}$ and a Soper-Lorch correction was applied to both room temperature and 600 °C data to remove Fourier ripples resulting from Fourier transform over a limited $Q_{max}$. A low-$r$ Fourier filter was applied with a cut-off of 1.6 Å.

Total scattering analysis was performed using TOPAS v6[18] for small box refinements, where the $G(r)$ were converted into $D(r)$ data normalised by the sum of the scattering from all pairs. RMCProfile[19] was employed for big box refinements. A more detailed description of the big box refinements is given in Section 6.3.2.

### 6.2.3 Synchrotron X-ray powder diffraction

High resolution synchrotron X-ray diffraction data were collected on the I11 beamline at Diamond Light Source (DLS). In addition to collecting data on the sample as synthesised in 6.2.1 (henceforth referred to as MSC053_pre, colour = pale beige), data were also collected on the sample that was used in the neutron total scattering experiment, which underwent heating as described in Section 6.2.2 (henceforth referred to as MSC053_post, colour = pale grey). The data were collected using a wavelength of $\lambda$ = 0.824681 Å and the high resolution multi-analysing crystal (MAC) detector. Both samples were loaded into 0.3 mm diameter quartz capillaries. A hot hair blower (HAB) was used to control the temperature for variable temperature data collection. The data collection summary for the samples is given in Table 6.3.

The temperature of the hot air blower was calibrated using an $Al_2O_3$/Si standard, where $Al_2O_3$ was used to determine the calibration curve and Si was used to confirm that the calibration curve is correct. The resulting calibration equations are:

$$\Delta T = -2.607 \times 10^{-7}T^3 + 5.102 \times 10^{-4}T^2 + 0.3764T + 84.09 \qquad (6.1a)$$

$$T_{\text{corrected}} = T + \Delta T \qquad (6.1b)$$

Where $T$ is the nominal temperature and $\Delta T$ is the difference between the nominal temperature and true temperature. Rietveld refinements were performed against all datasets. The cell parameters, atomic coordinates (except for oxygen sites), Mo and Nb occupancies and ADPs were refined. The Mo and Nb occupancies were equated due to the equivalent X-ray scattering power of Mo and Nb ($Z_{\text{Mo(VI)}}$ = 36; $Z_{\text{Nb(V)}}$ = 36). The background was fitted using a 12th-order Chebyshev polynomial, and a peak to describe the scattering from the quartz capillary was inserted at $2\theta$ = 11.52 ° and its position, width and intensity were allowed to refine. The peak shapes were modelled using a fixed Thompsons-Cox-Hastings pseudo-Voigt peak shape based on the Si standard peak shape, in combination with refined crystallite size and strain dependent peak terms. The absorption coefficient, $\mu r$, was calculated based on a packing factor of 40% and fixed at 1.46.

**Table 6.3 – Data collection parameters used for Ba$_3$NbMoO$_{8.5}$ samples on the I11 beamline at Diamond Light Source.**

| Sample | *T* range (°C) | *T* steps (°C) | Scan time (min) | Notes |
|---|---|---|---|---|
| MSC053_pre | 30 | N/A | 4 × 15 | No HAB used. |
| MSC053_pre | 400 | N/A | 4 × 15 | |
| MSC053_pre | 600 | N/A | 4 × 15 | |
| MSC053_pre | 30 | N/A | 4 × 15 | Removed HAB at 600 °C and waited 5 minutes for temperature equilibration. |
| MSC053_post | 30 | N/A | 4 × 15 | No HAB used. |
| MSC053_post | 30 – 600 | 30 | 10 | First heating on MSC053_post sample. |
| MSC053_post | 570 – 315 | 30 | 10 | Cooled with HAB. |
| MSC053_post | 30 | N/A | 3 | Removed HAB at ~ 315 °C. Collected after heating. |

### 6.2.4 Solid-state NMR (SSNMR)

Samples were submitted to the SSNMR service at Durham University Chemistry Department. $^1$H-magic angle spinning (MAS) SSNMR spectra were collected on MSC053_pre and MSC053_post. Spectra were collected at room temperature using a 400 MHz Varian VNMRS spectrometer using tetramethylsilane (TMS) as the reference. Data were deconvoluted using a Gaussian peak shape, only varying the height and width between samples. Due to the weak signal, the spectra were run with a background suppression pulse sequence and the residual empty rotor signal was subtracted. The results are presented in Appendix B.

### 6.2.5 Thermogravimetric analysis

MSC053_pre and MSC053_post were submitted to the thermogravimetric analysis (TGA) service at Durham University Chemistry Department. The samples were heated from 30 °C to 600 °C at a rate of 5 °C min$^{-1}$. The analyses were performed on a Perkin Elmer TGA 8000 with a Hiden mass spectrometer attached, which monitored the signal from water (18 g mol$^{-1}$) and O$_2$ (32 g mol$^{-1}$) throughout the experiment. The results are presented in Appendix B.

## 6.3 Results and Discussion

### 6.3.1 Long range average structure

#### 6.3.1.1 Neutron diffraction

The starting model was based on the one given in Table 6.1. The M2 site was moved from the 3*b* site onto the 6*c* site[12] and the M1 and M2 occupancies were refined in addition to the atomic coordinates. This resulted in occupancies of Mo1 = 0.451(1) and Mo2 = 0.043(1), summing to a total of 0.989(5) Mo/Nb content per formula unit. This fit gave a value of R$_{wp}$ = 3.066%. The O2 and O3 occupancies were refined freely, which resulted in a total O content per formula unit of

8.38(2) and R$_{wp}$ = 3.058%. The Mo/Nb occupancies were multiplied by 1.01 so that the total Mo/Nb content per formula unit = 1.0 and the oxygen occupancies were refined again, resulting in a total O content per formula unit of 8.40(2) and R$_{wp}$ = 3.061%. This fit is close to the fit obtained when O is constrained to 8.5 per formula unit, suggesting that there is little sensitivity to small differences in total oxygen content per formula unit. The crystallographic parameters from this fit are given in Table 6.4 and the Rietveld plots are given in Figure 6.4 and Appendix B, showing a good fit. The anisotropic ADPs of the M2 sites are very small, which is likely caused by the low site occupancy, creating difficulties in obtaining the precise value. In addition, a refinement was performed where all the ADPs were isotropic and the M1 and M2 APDs were equated. This resulted in a total O content of 8.52(2) and a worse fit with R$_{wp}$ = 3.332%.
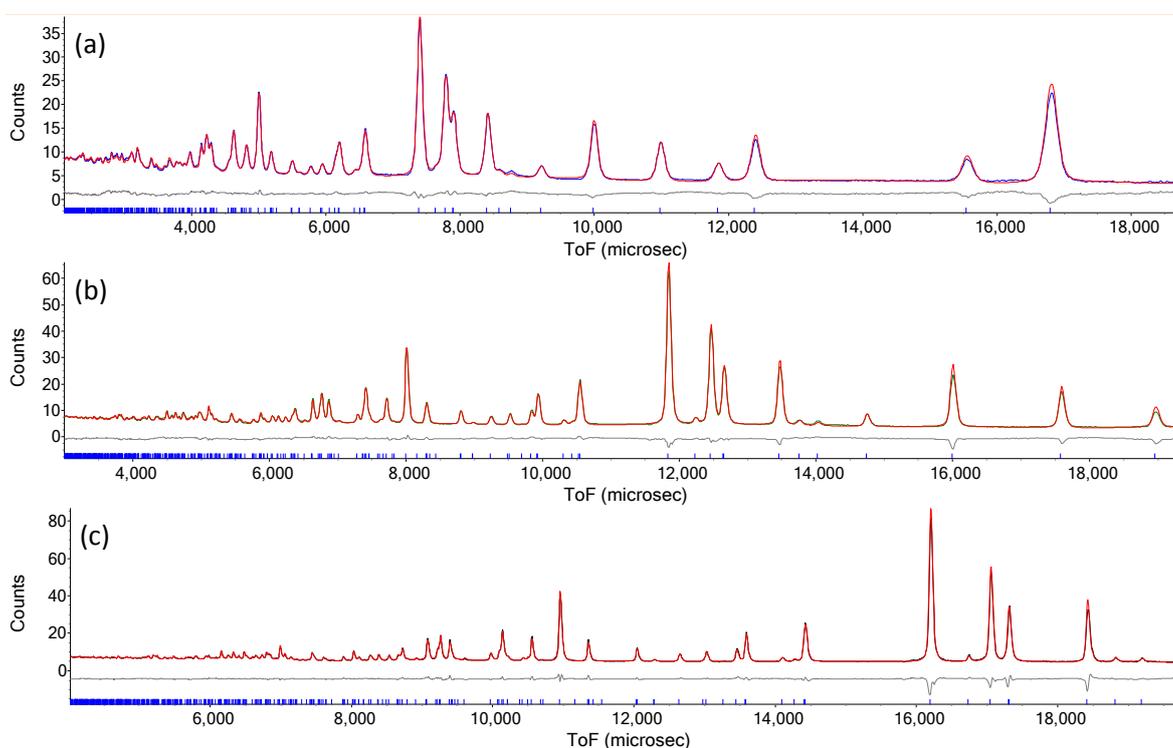


**Figure 6.4 –** The Rietveld plots of Ba$_3$NbMoO$_{8.5}$ at room temperature from POLARIS (a) bank 3, R$_{wp}$ = 3.111%, χ$^2$ = 6.863; (b) bank 4, R$_{wp}$ = 3.324%, χ$^2$ = 10.167; (c) bank 5, R$_{wp}$ = 2.491%, χ$^2$ = 4.465. Blue tick marks correspond to reflections arising from Ba$_3$NbMoO$_{8.5}$.

**Table 6.4 – Crystallographic parameters obtained from neutron diffraction Rietveld refinement of Ba$_3$NbMoO$_{8.40(2)}$ at room temperature. Space group = *R*-3*m* (hexagonal axes); *a* = 5.92805(5) Å; *c* = 21.0910(3) Å; *V* = 641.88(2) Å$^3$.**

| Site | Wyckoff | x | y | z | Occupancy | $U_{11}=U_{22}$ (Å$^2$) | $U_{12}$ (Å$^2$) | $U_{33}$ (Å$^2$) | B (Å$^2$) |
|------|---------|---|---|---|-----------|-------------------------|------------------|------------------|-----------|
| Ba1 | 3*a* | 0 | 0 | 0 | 1 | 0.0061(9) | 0.0031(5) | 0.0009(1) | – |
| Ba2 | 6*c* | 0 | 0 | 0.2074(1) | 1 | 0.0137(7) | 0.0069(3) | 0.025(1) | – |
| Mo1 | 6*c* | 0 | 0 | 0.39788(9) | 0.4563 | 0.0063(4) | 0.0031(2) | 0.035(1) | – |
| Nb1 | 6*c* | 0 | 0 | 0.39788(9) | 0.4563 | 0.0063(4) | 0.0031(2) | 0.035(1) | – |
| Mo2 | 6*c* | 0 | 0 | 0.5228(5) | 0.0437 | 0.000(3) | 0.000(2) | 0.000(5) | – |
| Nb2 | 6*c* | 0 | 0 | 0.5228(5) | 0.0437 | 0.000(3) | 0.000(2) | 0.000(5) | – |
| O1 | 18*h* | 0.17203(9) | 0.82797(9) | 0.10393(4) | 1 | 0.0166(3) | 0.0083(1) | 0.0154(6) | – |
| O2 | 9*e* | 0.5 | 0 | 0 | 0.444(4) | 0.022(1) | 0.0111(6) | 0.012(2) | – |
| O3 | 36*i* | 0.0900(1) | 0.092(1) | 0.3209(3) | 0.089(2) | N/A | N/A | N/A | 2.49(2) |

**Table 6.5 – Crystallographic parameters obtained from neutron diffraction Rietveld refinement of Ba$_3$NbMoO$_{8.42(2)}$ at 600 °C. Space group = *R*-3*m* (hexagonal axes); *a* = 6.00651(6) Å; *c* = 21.2490(4) Å; *V* = 663.92(2) Å$^3$.**

| Site | Wyckoff | x | y | z | Occupancy | B (Å$^2$) |
|------|---------|---|---|---|-----------|-----------|
| Ba1 | 3*a* | 0 | 0 | 0 | 1 | 1.40(6) |
| Ba2 | 6*c* | 0 | 0 | 0.2057(2) | 1 | 3.27(6) |
| Mo1 | 6*c* | 0 | 0 | 0.39931(9) | 0.485 | 1.80(3) |
| Nb1 | 6*c* | 0 | 0 | 0.39931(9) | 0.485 | 1.80(3) |
| Mo2 | 6*c* | 0 | 0 | 0.526(2) | 0.015(2) | 1.80(3) |
| Nb2 | 6*c* | 0 | 0 | 0.526(2) | 0.015(2) | 1.80(3) |
| O1 | 18*h* | 0.1734(1) | 0.8266(1) | 0.10198(5) | 1 | 2.63(3) |
| O2 | 9*e* | 0.5 | 0 | 0 | 0.374(5) | 3.6(2) |
| O3 | 36*i* | 0.088(1) | 0.089(1) | 0.3205(2) | 0.1095(2) | 2.57(2) |

The average structure at 600 °C was also obtained through Rietveld refinement. A free refinement of the Mo/Nb occupancies and O occupancies (all ADPs isotropic) resulted in a total Mo/Nb content per formula unit of 0.985(6), total O content per formula unit of 8.38(3) and $R_{wp}$ = 3.821%. A scale factor of 1.017 was applied to the Mo/Nb occupancies to force the total Mo/Nb content per formula unit to equal unity, and the O occupancies were refined again. This resulted in a total O content of 8.42(2) and $R_{wp}$= 3.832%. The crystallographic parameters of this fit are presented in Table 6.5 and the Rietveld plots are in Figure 6.5 and Appendix B, showing a good fit.
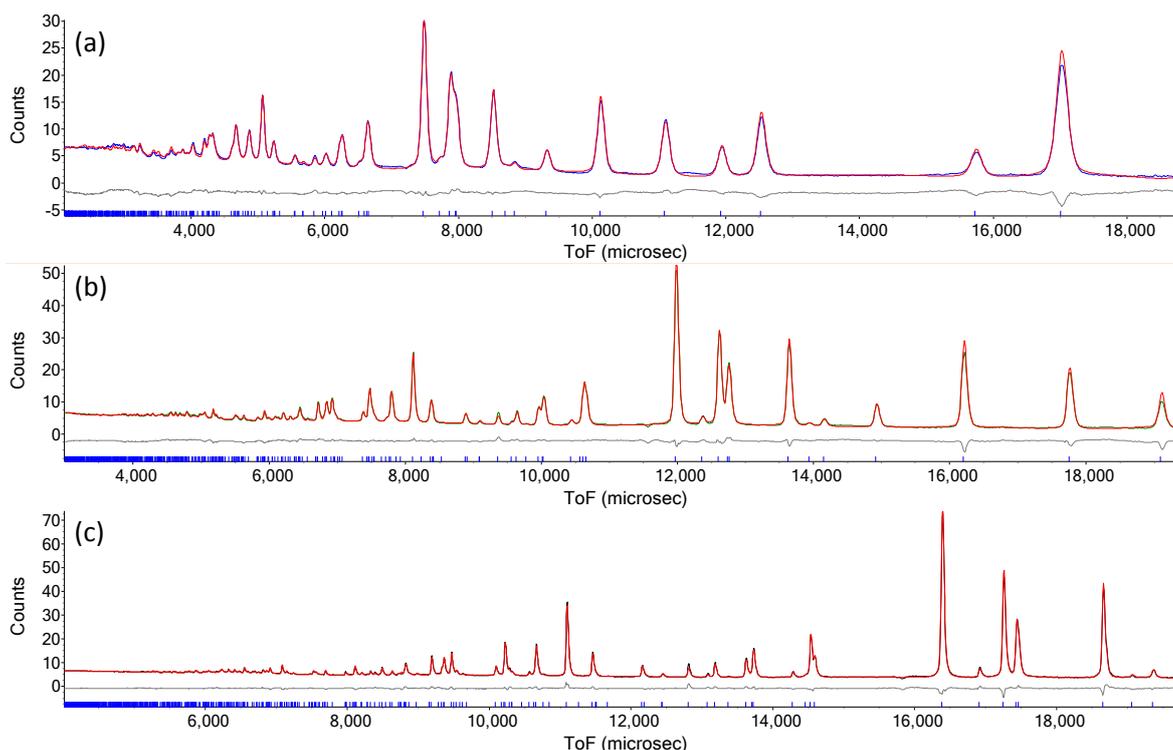


**Figure 6.5 –** The Rietveld plots of $Ba_3NbMoO_{8.5}$ at 600 °C from POLARIS (a) bank 3, $R_{wp}$ = 4.841%, $\chi^2$ = 9.247; (b) bank 4, $R_{wp}$ = 4.028%, $\chi^2$ = 11.123; (c) bank 5, $R_{wp}$ = 2.188%, $\chi^2$ = 3.711. Blue tick marks correspond to reflections that fit $Ba_3NbMoO_{8.5}$.

At 600 °C, the occupancy of Mo1 has increased by 0.029 relative to the room temperature structure, whilst the occupancy of Mo2 has decreased by the same amount. The occupancy of O2 has also decreased by 0.070(6) whilst the occupancy of O3 has increased by 0.019(2). These changes in site occupancies are in agreement with previous literature, corresponding to a trend towards $M1O_4$ at higher temperature.[6, 8]
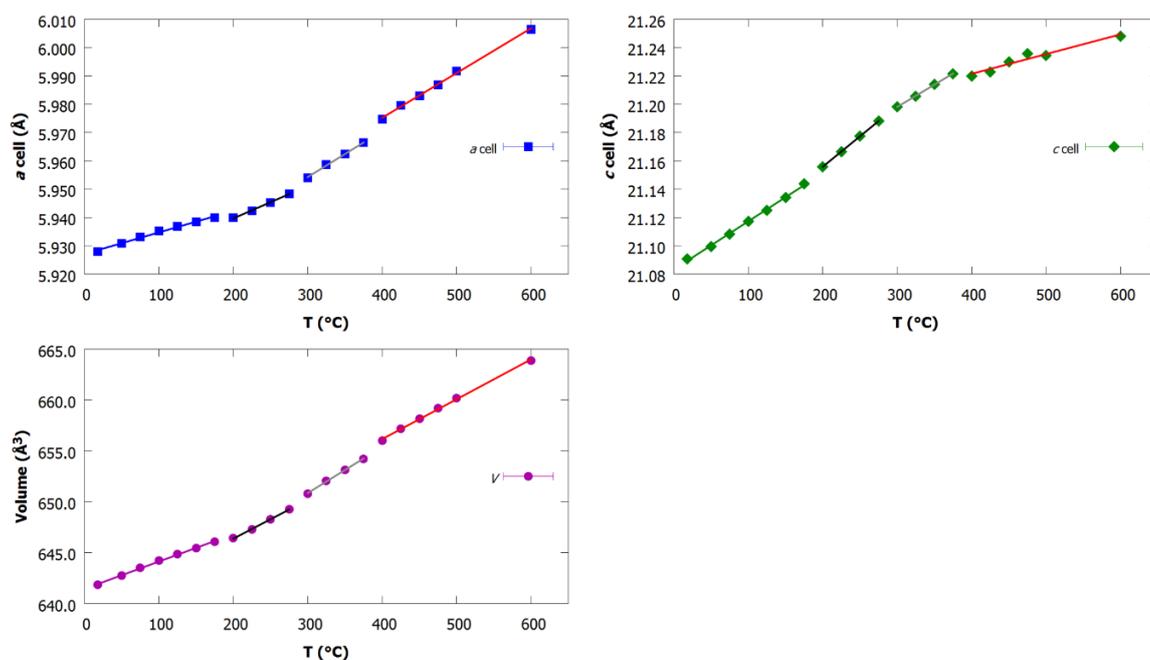
**Figure 6.6** – The thermal evolution of the cell parameters of Ba₃NbMoO₈.₅ obtained from neutron diffraction. Lines of best fit for each of the different gradients of thermal expansion have been plotted in different colours.

Analysis of the temperature-dependent behaviour of the cell parameters was performed using Rietveld analysis of variable temperature data, the results of which are presented in Figure 6.6. The cell parameters appear to show four distinctly different gradients of thermal expansion. The origins of this phenomenon are discussed in Section 6.3.1.2.

Additionally, the dependence of the Mo1, Mo2, O2 and O3 occupancies on the temperature was also analysed. For this analysis, the occupancies were refined with the total Mo/Nb content restrained to 1.0 to mimic the analysis performed above and with two restraints: the Mo/Nb content restraint and the total O content per formula unit restrained to 8.5.  In addition, ADPs were isotropic and the M1 and M2 ADPs were equated.

Figure 6.7 shows the resulting $R_{wp}$ values and occupancies from this analysis, where the data used at $T$ = 18, 200, 300, 400, 500 and 600 °C had better statistics (see Section 6.2.2). The total O content per formula unit (Figure 6.e) reduced to 8.39(2) when a restraint was absent, whilst applying the restraint resulted in a total O content of 8.47(3). We cannot exclude a small loss of oxygen on heating, which is charge balanced by reduction of $Mo^{6+}$ to $Mo^{5+}$, but the fact that the $R_{wp}$ values (Figure 6.7a) are almost identical between the two models at all temperatures indicates that there is a lack of sensitivity for such a small difference in total oxygen content. Figure 6.7b shows that the Mo1 occupancy increases with temperature and the Mo2 decreases simultaneously. There is a slight discontinuity at ~200 °C. Similarly, the O2 occupancy decreases

with temperature as the O3 occupancy increases with temperature. This trend was previously reported by Fop *et al*.[6]
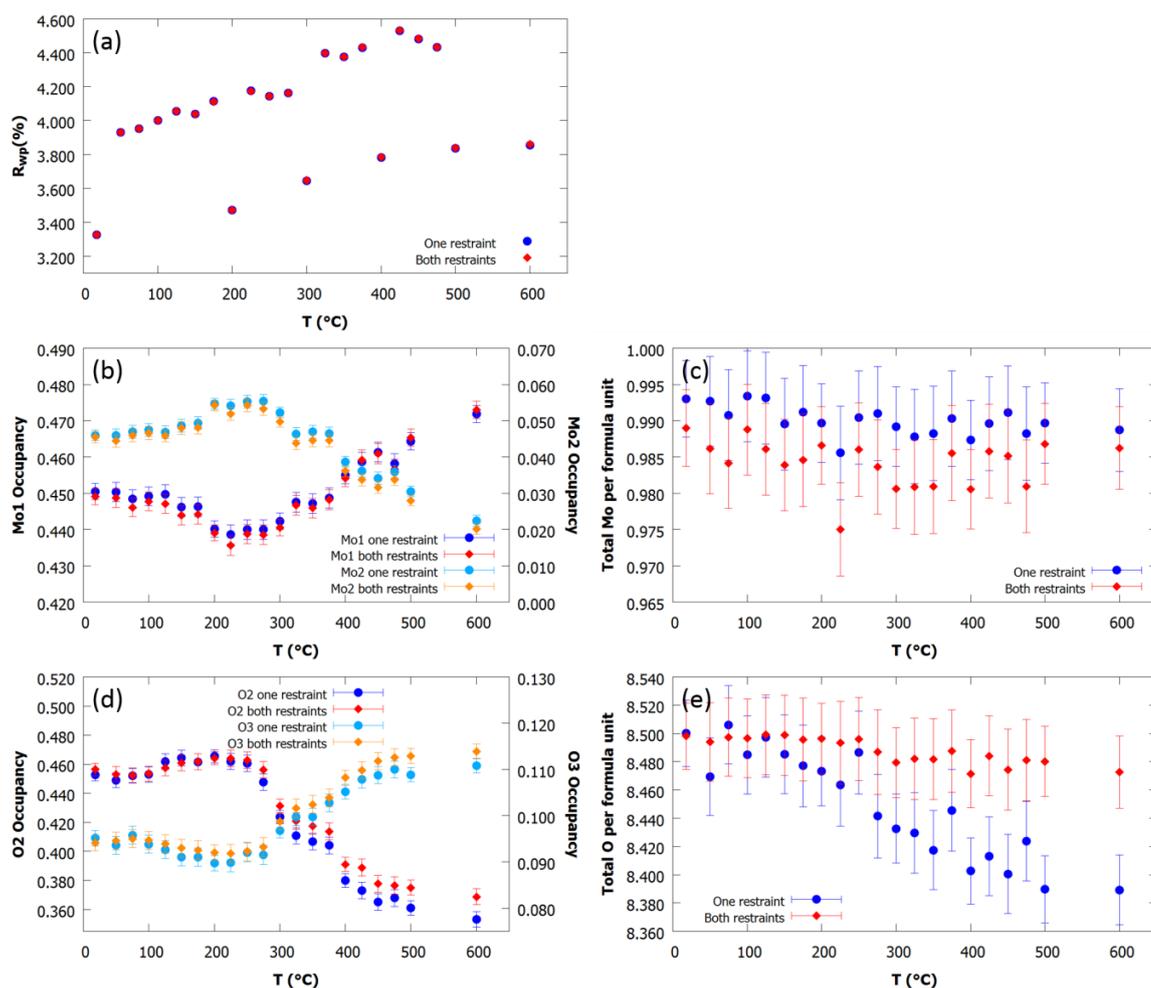


**Figure 6.7 –** The thermal evolution of multiple parameters of Ba₃NbMoO₈.₅ obtained from neutron diffraction. The parameters are: (a) The $R_{wp}$ obtained for each of the fits at different temperatures; (b) The Mo1 and Mo2 occupancies (Nb1 = Mo1, Nb2 = Mo2); (c) The total Mo content per formula unit; (d) The O2 and O3 occupancies; (e) the total O content per formula unit.

### 6.3.1.2 Phase evolution with temperature

Rietveld analysis was performed using high-resolution powder synchrotron X-ray diffraction on two samples of Ba₃NbMoO₈.₅: the as-made sample (MSC053_pre) and the same sample that had been heated at 600 °C under vacuum for 8 h on the POLARIS instrument (MS053_post).

Figure 6.8 shows the Rietveld plots of MSC053_pre and MSC053_post, zoomed in on the (2 −1 0) peak. Several peaks in these diffraction data showed shoulders, which have not been reported previously. These shoulders were particularly prominent in the initial room-temperature measurement of the MSC053_pre sample. For example, Figure 6.8a shows two distinct peaks: a sharp, less intense peak at lower 2$\theta$ (peak **A**), and a broad, more intense peak at higher 2$\theta$ (peak **B**). The shoulders could be fitted with a second Ba₃NbMoO₈.₅-related phase, which shared the

same atomic coordinates and ADPs, but with different cell parameters. The peak shape of the phase with the smaller $a$ cell parameter (peak **B**) was modelled with a function that accounts for anisotropic strain.[20]

Upon heating to 600 °C, a single sharp (2 −1 0) reflection is observed (Figure 6.8b, peak **C**). Upon rapid cooling to room temperature (Figure 6.8c), **A** became the strongest peak and **B** became less intense.

In contrast, the MSC053_post sample, which had been heated to 600 °C under vacuum, shows a single peak at **A** at room temperature (Figure 6.8d). At 600 °C (Figure 6.8e), a single, sharp peak is observed at **C**, corresponding to a very similar $a$ cell parameter to that of MSC053_pre at the same temperature ($a_{pre}$ = 6.00016(1) Å; $a_{post}$ = 5.99939(2) Å). When MSC053_post was cooled slowly from 600 °C to ~315 °C, and then rapidly to room temperature, a single peak formed which corresponded to cell parameters that are intermediate to those that give rise to peaks **A** and **B** (Figure 6.8f).
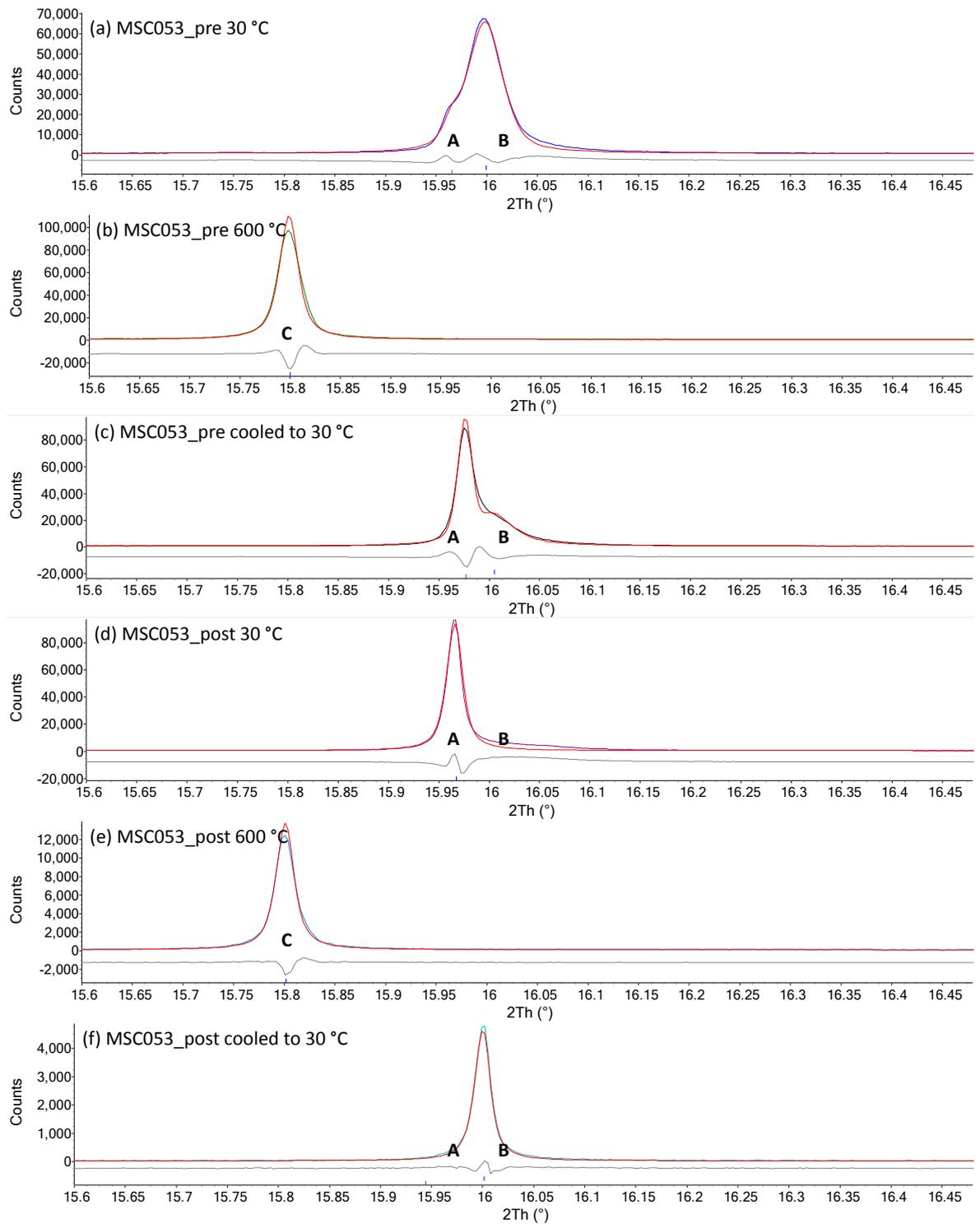
**Figure 6.8 –** The Rietveld plots from high resolution powder synchrotron X-ray diffraction of Ba₃NbMoO₈.₅. Peak **A** corresponds to phases with larger *a* cell parameters; peak **B** to phases with smaller *a* cell parameters and peak **C** to the 600 °C phase. (a)–(c) represent the as-made sample, without prior heating in a vacuum; (d)–(f) represents the sample which had been heated in a vacuum during the neutron total scattering experiment.

These results show that the thermal history is clearly important for the structure of BaNbMoO$_{8.5}$, as different heating and cooling rates produce phases with noticeably different cell parameters. Table 6.6 reports the cell parameters obtained from these refinements.

**Table 6.6 – The cell parameters of the different Ba₃NbMoO₈.₅ phases obtained from high-resolution powder synchrotron X-ray diffraction at different temperatures (*T*). The colours correspond to phases at the different positions shown in Figure 6.8. Green = A; blue = B; red = C and turquoise = middle of A and B.**

| Sample | *T* (°C) | *a* (Å) | *c* (Å) | *V* (Å³) | Notes |
|---|---|---|---|---|---|
| MSC053_pre **A** | 30 | 5.93820(5) | 21.0221(2) | 641.97(1) | First scan at room temperature |
| MSC053_pre **B** | 30 | 5.92583(2) | 21.0894(6) | 641.347(5) | First scan at room temperature |
| MSC053_pre | 600 | 6.00016(1) | 21.25490(6) | 662.729(4) | Single phase |
| MSC053_pre **A** | 30 | 5.93409(1) | 21.09126(5) | 643.194(3) | Post I11 heating |
| MSC053_pre **B** | 30 | 5.92370(7) | 21.1003(2) | 641.22(2) | Post I11 heating |
| MSC053_post | 30 | 5.93764(1) | 21.04918(5) | 642.677(3) | First scan at room temperature, single phase |
| MSC053_post | 600 | 5.99939(2) | 21.26002(9) | 662.687(5) | Single phase |
| MSC053_post | 30 | 5.92494(2) | 21.10784(9) | 641.714(5) | Post I11 heating, single phase |

To gain additional insight, a multi-temperature experiment was performed on the MSC053_post sample. Figure 6.9a shows clear evidence of a first-order phase transition on heating, with several peaks showing a marked discontinuity on heating to ~150 °C. At temperatures around 150 – 370 °C (Figure 6.9e), two phases are observed, which relate to the **A/B** peaks discussed above.

The thermal evolution of the cell parameters is shown in Figure 6.9b–d. At the beginning of the refinement, there is a single phase (corresponding to peak **A** of Figure 6.8d). However, at ~150 °C, a second phase begins to form with a smaller *a* cell parameter (Figure 6.9b) and a larger *c* cell parameter (Figure 6.9c), with an overall smaller unit cell volume (Figure 6.9d). In neutron variable temperature refinements, there is a change in the gradient of thermal expansion (Figure 6.6), which corresponds to this phase transition. The phase with the smaller *a* cell parameter gradually increases in abundance (Figure 6.9e) until ~370 °C, where only a single phase is present. As this phase becomes dominant at high temperature, it shall be referred to as the "high-temperature" phase, whilst the other phase shall be referred to as the "low-temperature" phase. The temperature when a single phase forms corresponds to the temperature when the Mo1 occupancies apparently increase and the Mo2 occupancies apparently decrease, as observed in neutron refinements (see Section 6.3.1.1). It is also within the temperature range of the unusual structural rearrangement in Ba$_3$NbMoO$_{8.5}$ proposed by Fop *et al.*[6] (300 – 400 °C), where Mo$^{6+}$ and

Nb$^{5+}$ ions move from M2 to M1 sites. When the sample was slowly cooled to ~315 °C, then quenched, only the high-temperature phase remained. This explains why there is a single peak in between positions **A** and **B** in Figure 6.8f. These experiments also explain why there are multiple phases depending on the sample's thermal history and why there are apparently complex changes in the temperature dependence of the cell parameters in Figure 6.6.
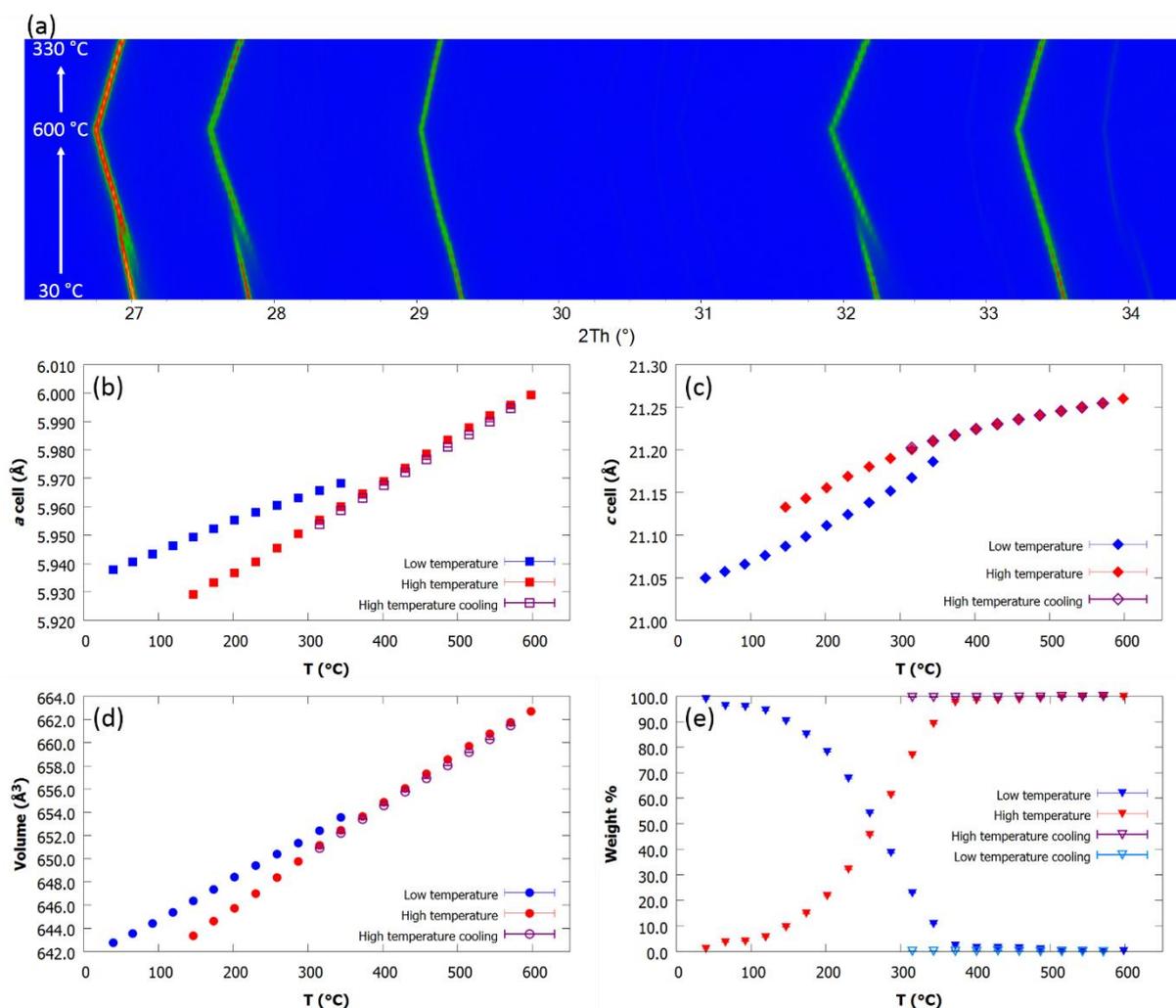


**Figure 6.9** – The thermal evolution of MSC053_post refined against I11 data using two Ba₃NbMoO₈.₅-like phases. (a) plan view surface plot of the raw patterns on heating and cooling (30 – 600 – 330 °C); (b) *a* cell parameters; (c) *c* cell parameters; (d) unit cell volumes; (e) phase weight percentages.

## 6.3.2 Local structure
### 6.3.2.1 Starting configurations

[8 8 4] supercells were produced using the data2config program. Initial models were based on the crystallographic parameters obtained from neutron Rietveld refinement. The atomic coordinates and occupancies used were the same as those shown in Table 6.4, but with some exceptions. The M2 atoms started on the 3*b* site instead of the nearby 6*c* site and O3 atoms were started on a nearby 6*c* site instead of the 36*i* site. This allows for more efficient RMCProfile modelling as there

are significantly fewer atomic positions to refine and the crystallographically split sites are free to move off the high symmetry sites during the refinement. [8 8 4] supercell dimensions were necessary so that the distance (~16 Å) from the bottom of one M1–M2–M1 trimer to the top of the corner-connected M1–M2–M1 trimer (see Figure 6.3) could be modelled.

Four different starting configurations were explored: two for room temperature refinements (**SC1** and **SC2**) and two for 600 °C (**SC3** and **SC4**). As Mo and Nb cannot be readily distinguished with neutrons, they were modelled as 'Mo' atoms for convenience, with a mean neutron scattering length of $b_M$ = 6.8845 fm. The O2 and O3 atoms were labelled as 'Te' atoms and were given the same scattering length as oxygen to distinguish them from the O1 atoms. Vacancies on the M1/M2 sites were labelled as 'Ta' and on O2/O3 sites as 'Va'; both were given a scattering length of zero. The O2 and O3 atoms were randomised using RMCProfile with a minimum distance constraint of O2–O2/O3–O3 > 1.6 Å to produce sensible starting configurations.

As the M1 and M2 cationic sublattice appears to be crucial to the conduction mechanism, starting configurations with different M1 and M2 site occupancies were studied. All four starting configurations have a total of 13056 atoms, including the dummy 'Ta' and 'Va' atoms. Table 6.7 gives a summary of the four supercells used. The cell parameters for the room temperature configurations (**SC1** and **SC2**) were: $a = b$ = 47.424400 Å; $c$ = 84.363840 Å; $\alpha = \beta$ = 90°; $\gamma$ = 120°. The cell parameters for 600 °C were: $a = b$ = 48.052080 Å; $c$ = 84.996120 Å; $\alpha = \beta$ = 90°; $\gamma$ = 120°.

**Table 6.7 – The different [8 8 4] supercell starting configurations and temperatures ($T$) used for total scattering analysis of Ba$_3$NbMoO$_{8.5}$**

| $T$ (°C) | Name | Mo1 | Mo2 | O2 | O3 | Notes |
|---|---|---|---|---|---|---|
| 18 | SC1 | 1422 | 114 | 1034 | 885 | Average room temperature structure. |
| 18 | SC2 | 1536 | 0 | 1034 | 885 | M1 100% occupied, M2 0% occupied. |
| 600 | SC3 | 1502 | 34 | 896 | 1023 | Average 600 °C structure. |
| 600 | SC4 | 1422 | 114 | 1034 | 885 | Uses the cell parameters of **SC3**, but atomic coordinates and occupancies of **SC1**. |

### 6.3.2.2 Refinement methodology

It was determined from preliminary refinements with a [5 5 4] supercell (similar to **SC1**) that the dataset weightings for the PDF : $F(Q)$ : Bragg that achieved the lowest $\chi^2_{dof}$ values are 0.01 : 0.02 : 0.05. This weighting ratio was applied in all of the successive refinements that are described here.

The same procedure **P1** was applied to all models, with minimum distance constraints, bond valence sums (BVS) and weightings as summarised in Tables 6.9 – 6.11. The 'Mo' atoms (Mo and Nb) were permitted to swap with 'Ta' atoms (cation vacancies) and simultaneously the 'Te' atoms (O2 and O3) were allowed to swap with 'Va' atoms (O vacancies) at a rate of 10% for each pair.

**Table 6.8 – The minimum distance constraints applied in procedure** P1 **for Ba₃NbMoO₈.₅ where 'Mo' represents Mo and Nb atoms, 'Ta' represents M1 and M2 vacancies, 'Te' represents O2 and O3 atoms and 'Va' represents O2 and O3 vacancies. "–" mean no constraint was applied.**

| Ba | 'Mo' | 'Ta' | O | 'Te' | 'Va' | |
|---|---|---|---|---|---|---|
| >1.6 Å | >1.6 Å | – | >2.2 Å | >2.2 Å | – | Ba |
| | >2.2 Å | – | >1.6 Å | >1.6 Å | – | 'Mo' |
| | | – | – | – | – | 'Ta' |
| | | | >2.2 Å | >2.2 Å | – | O |
| | | | | >2.2 Å | – | 'Te' |
| | | | | | – | 'Va' |

**Table 6.9 – The $R_{ij}$ values applied in BVS restraints used in Ba₃NbMoO₈.₅ refinement procedure** P1**.**

| Ba | 'Mo' | 'Ta' | O | 'Te' | 'Va' | |
|---|---|---|---|---|---|---|
| – | – | – | 2.285 Å | 2.285 Å | – | Ba |
| | – | – | 1.909 Å | 1.909 Å | – | 'Mo' |
| | | – | – | – | – | 'Ta' |
| | | | – | – | – | O |
| | | | | – | – | 'Te' |
| | | | | | – | 'Va' |

**Table 6.10 – The BVS restraint weightings applied in Ba₃NbMoO₈.₅ refinement procedure** P1**. Lower numbers mean a higher weighting. Setting 'Ta' and 'Va' to a weighting of 5000 means these BVS restraints are effectively ignored.**

| Ba | 'Mo' | 'Ta' | O | 'Te' | 'Va' |
|---|---|---|---|---|---|
| 2 | 1 | 5000 | 1 | 1 | 5000 |

Mo and Nb in Ba₃NbMoO₈.₅ have the oxidation states of +6 and +5 respectively. Separate refinements were performed where the valence applied to the 'Mo' was +5 and +6, as RMCProfile 6.7.0 cannot model BVS restraints with non-integer oxidation states. The refined configurations were then combined for analysis. Overall, each model consists of eight refined configurations: four where 'Mo' oxidation state = +5 and four where the 'Mo' oxidation state = +6. The primary difference is that the BVS restraints will attempt to make the charge of the 'Mo' atoms either be +5 or +6, based on its coordination to 'Te' and O atoms. However, as the BVS restraints have a weak weighting, there are no significant differences between the models so they can be averaged during the analysis.

After convergence of the RMC refinements, it became evident that the scaling of the $F(Q)$ data was not optimal; a final 10 min refinement was performed to fit the scale of the $F(Q)$ data which significantly improved the $\chi^2_{F(Q)}$ value and visual fit for the $F(Q)$ data, but will not have caused substantive changes to the atomistic models.

When referring to the refined models, abbreviations will be used in square brackets as in Chapter 4. Python scripts were employed to analyse the geometries of the local structural models. Full details of these scripts are in Appendix B. RMCProfile .dat control files are also included.

### 6.3.2.3 Small box modelling of Ba$_3$NbMoO$_{8.5}$

A small box refinement was performed against the PDF expressed as $D(r)$ obtained from neutron total scattering on the POLARIS instrument at room temperature and 600 °C. For the purpose of this analysis, a 9R perovskite model and a palmierite model were produced in space group $R$-$3m$. The 9R model was produced by taking the crystallographic parameters from Tables 6.4 and 6.5 at room temperature and 600 °C respectively, deleting the M2 and O3 sites and setting the occupancy of the O2 site to 1.00. The palmierite was produced in a similar manner, but by deleting the O2 site instead of O3. In addition, the O3 was moved onto the nearby 6$c$ site in order to avoid unphysical O3–O3 distances and the occupancy was set to 100%. The two phases were included in the refinement simultaneously with an equal scale factor. The cell parameters, fractional coordinates and ADPs of the two models were refined but equated to mimic a 'single' phase. The two-phases used produces an approximate model with no unphysical O–O distances caused by the partially occupied sites.  Figure 6.10 shows the resulting PDF fits. The small box refinements show that the long-range, average structure is insufficient to describe the local structure ($r \leq 8$ Å) at both room temperature and 600 °C.
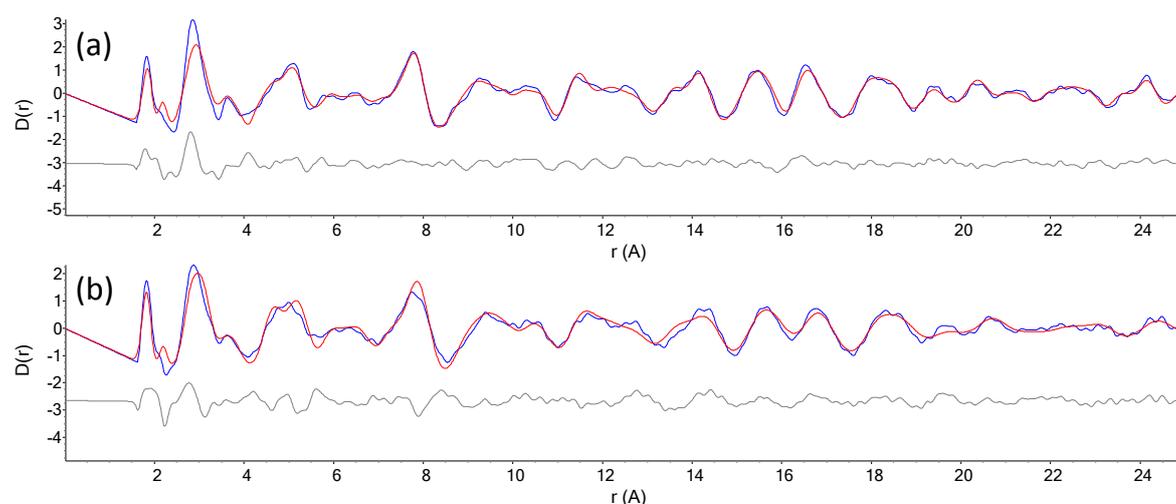


**Figure 6.10 –** The small box neutron PDF fit of Ba$_3$NbMoO$_{8.5}$ showing $0 \leq r \leq 25.0$ Å at (a) room temperature; R$_{wp}$ = 26.712%; $\chi^2$ = 0.102 and (b) 600 °C; R$_{wp}$ = 31.732%; $\chi^2$ = 0.106.

### 6.3.2.4 Room temperature big box modelling of Ba₃NbMoO₈.₅

In order to determine the local structure, big box modelling using RMC calculations was employed. Figure 6.11 shows representative PDF and Bragg fits of the room temperature models **[SC1, P1]** and **[SC2, P2]** and Table 6.11 gives the average goodness of fit values obtained from these models. An excellent fit is obtained to all data sets and the misfits in the small box fitting to the $D(r)$ (Figure 6.10a) have been eliminated. We find that the models converge to similar fits regardless of the initial Mo1/Mo2 distributions. This similarity is shown in each of the analyses of the local structure discussed below. Representative $F(Q)$ fits are in Appendix B.

**Table 6.11 – The goodness of fit values obtained for models** [SC1–SC4, P1] **of Ba₃NbMoO₈.₅. The** $\chi^2_{F(Q)}$ **reported were obtained from the final fits with the $F(Q)$ data rescaled.**

| $T$ (°C) | Model | $\chi^2_{dof}$ | $\chi^2_{PDF}$ | $\chi^2_{Bragg}$ | $\chi^2_{F(Q)}$ |
|---|---|---|---|---|---|
| 18 | [SC1, P1] | 8.69(4) | 18.6(2) | 24.7(1) | 0.228(2) |
| 18 | [SC2, P1] | 8.8(3) | 19.1(9) | 25.0(6) | 0.232(5) |
| 600 | [SC3, P1] | 5.44(7) | 6.2(2) | 18.2(2) | 0.134(2) |
| 600 | [SC4, P1] | 5.42(4) | 6.04(5) | 18.25(1) | 0.132(1) |
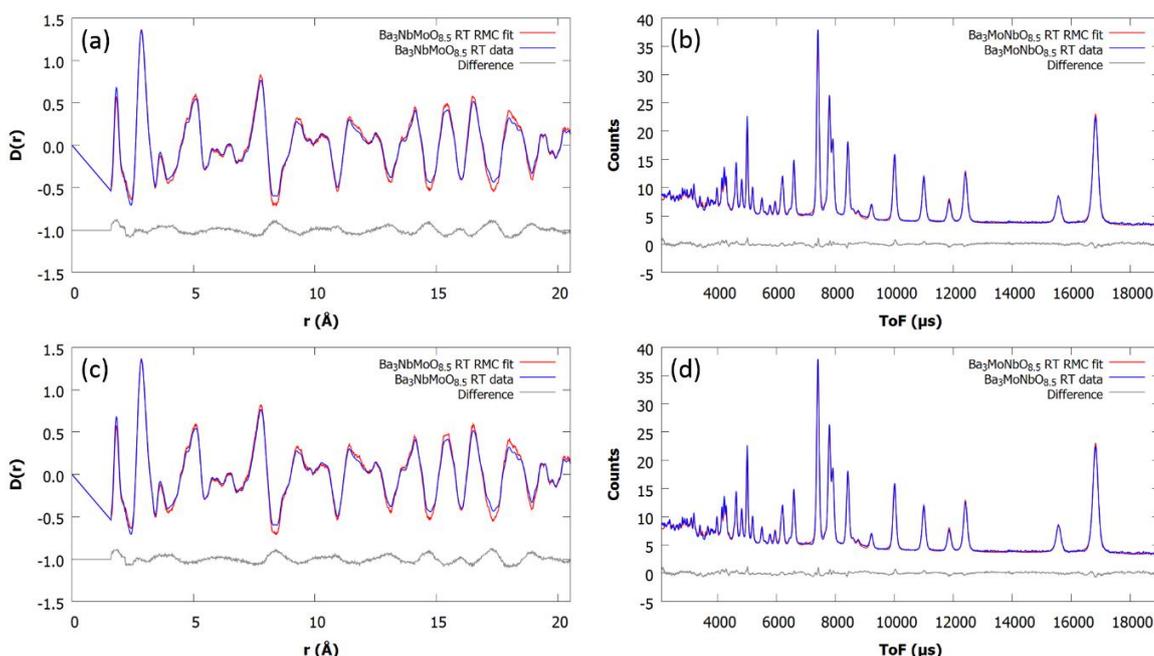


**Figure 6.11 –** Representative fits obtained from RMC analysis of room temperature Ba₃NbMoO₈.₅ models (a) **[SC1, P1]** PDF, $\chi^2_{PDF}$ = 18.60; (b) **[SC1, P1]** Bragg, $\chi^2_{Bragg}$ = 24.75; (c) **[SC2, P1]** PDF, $\chi^2_{PDF}$ = 18.83; (d) **[SC2, P1]** Bragg, $\chi^2_{Bragg}$ = 24.68.

One of the critical aspects of Ba₃NbMoO₈.₅ is its distribution of Mo/Nb cations on the M1 and M2 sites and the details of their local coordination. Previously, the structure had been modelled with the M2 site situated on the 3*b* position,[4-11] but a recent single-crystal X-ray diffraction study[12] determined that the M atoms are displaced along the *c* axis onto a nearby 6*c* Wyckoff position.

Consideration of the local environment means that all three sites cannot be occupied simultaneously in a given trimer. Therefore the local environment of the M1 and M2 sites was investigated and the numbers of Mo1 atoms and Mo2 atoms were counted.

Figure 6.12 shows the atomic density maps around the M1–M2–M1 trimers in the room temperature models **[SC1&SC2, P1]**. From these maps, it can be seen that the density distribution is quite diffuse. The occupancy of these sites is more like a continuous column along the *c* axis rather than 3 distinct sites, as previous average structure models have suggested.[5-11] This confirms that the average structure model found from single crystal diffraction is more accurate,[12] but is still an under-representation of the amount of disorder within the structure. Additionally, the atomic density maps perhaps reveal that there is some displacement of the M2 atoms in the *ab* plane, which is attributed to the proximity of the M1 sites.
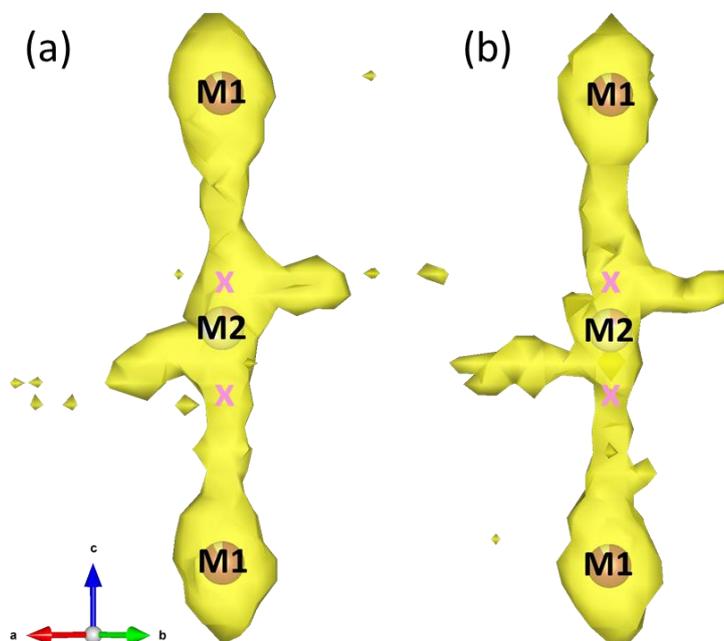


**Figure 6.12 –** The atomic density maps of the M1 and M2 sites in room temperature Ba$_3$NbMoO$_{8.5}$ models (a) **[SC1, P1]** and (b) **[SC2, P1]** superimposed on the average structure at room temperature, where M2 is on the 3*b* site. Yellow clouds = 0.2 × 0.2 × 0.2 Å$^3$ voxel with at least 1.5 atoms. The isolated voxels likely represent atoms that have been moved out of a sensible position during RMC runs. Pink crosses mark the position of the M2 in the split model (Table 6.3).

The observation that the density maps from **[SC1, P1]** and **[SC2, P1]** are the same is important. The starting configurations in [**SC2, P1**] had the M1 sites 100% occupied and the M2 sites completely empty. Despite the fact that a trimer with only the M1 sites occupied has no short distances, the atomic density map produced at the end of the refinement is the same as when the M2 sites were occupied in the starting configuration. This demonstrates that the columns are in

fact a real part of the local structure and that this result is data-driven, rather than a result of the starting configuration.

The number of atoms in the M1 and M2 sites was counted in each of the models. One difficulty is that that there is a significant overlap between the M1 and M2 atoms (Figure 6.12). It is therefore difficult to precisely assign an atom as Mo1 or Mo2. In our analysis, a search is first made around the ideal M1 sites. If a Mo atom is within 1.1 Å of an M1 site, it is counted as a Mo1 atom. Next, a search is made around the ideal M2 sites and if an unassigned Mo atom is within 1.2 Å, it is counted as Mo2. This form of counting slightly biases the number of M1 sites, but some biasing cannot be avoided due to the large overlap of the sites. In order to demonstrate that the current definitions of Mo1 and Mo2 are reasonable, the distances from the Mo atoms to the crystallographic M1 and M2 (3$b$) sites were calculated before any assignments were made. Figure 6.13a shows these histograms from a representative configuration from **[SC1, P1]**. The Mo atoms were then labelled as Mo1 and Mo2 atoms, and the Mo1–M1 and Mo2–M2 distances were calculated, shown in Figure 6.13b. There is very little change between Figure 6.13a and Figure 6.13b. Therefore the definitions of Mo1 and Mo2 atoms are suitable and a small amount of 'unassigned' atoms are an inherent part of the refined configurations. In addition, Figure 6.13b reveals that many of the assigned 'Mo2' atoms are ~1.0 Å from the ideal site, which further suggests the split site model[12] is more accurate.
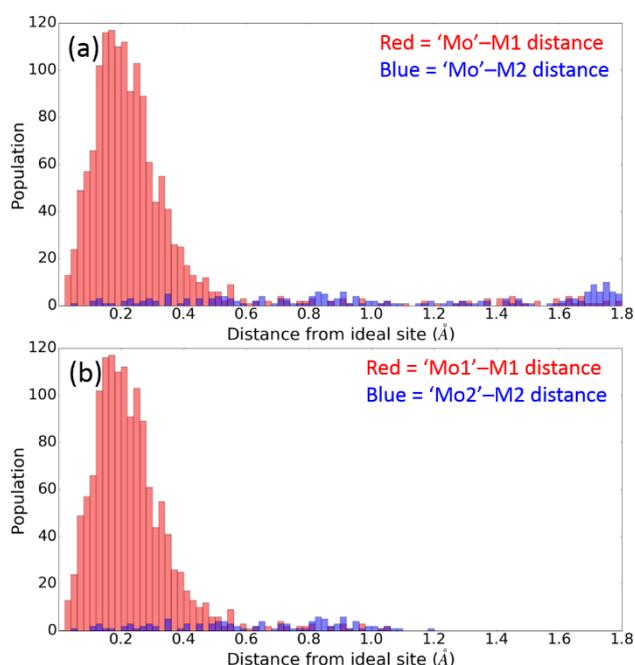


**Figure 6.13** – Histograms from a representative room temperature configuration of **[SC1, P1]** of (a)'Mo'–M1 and 'Mo'–M2 distances before assigning the M1 and M2 positions and (b) 'Mo1'–M1 and 'Mo2'–M2 distances after assigning them.

**Table 6.12 – The number of Mo atoms in the M1 and M2 sites in room temperature Ba₃NbMoO₈.₅ models** [SC1, P1] **and** [SC2, P1]**. 'Unassigned' Mo atoms refer to atoms that have moved further from the ideal sites than the definitions of Mo1 and Mo2 atoms allow.**

|            | [SC1, P1] | [SC2, P1] |
|------------|-----------|-----------|
| **Unassigned** | 21(1)   | 13(4)     |
| **Mo1**    | 1410(2)   | 1416(4)   |
| **Mo2**    | 105(3)    | 107(3)    |

The number of atoms in the Mo1/Mo2 sites is given in Table 6.12. We see that the occupancies in the different models **[SC1, P1]** and **[SC2, P1]** have converged, where occupancies of M1 = 0.919(3), M2 = 0.068(2) were obtained in **[SC1, P1]** and M1 = 0.922(5), M2 = 0.069(2) in **[SC2, P1]**. They are also very similar to the occupancies found in the average structure by Fop *et al.*[5] [M1 = 0.926(1), M2 = 2 × 0.074 = 0.148(1); M2 is on 3*b* site].
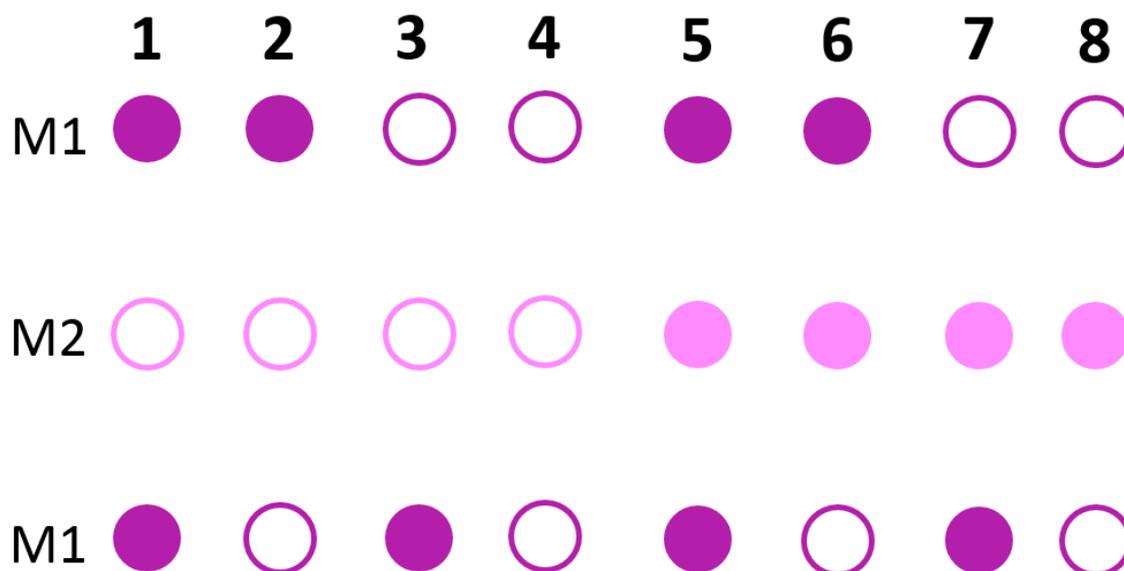


**Figure 6.14 –** The possible arrangement of 'Mo' atoms in a single M1–M2–M1 trimer in Ba₃NbMoO₈.₅, drawn with the M2 site on the 3*b* Wyckoff position. Filled circles = occupied; empty circles = vacant.

The average structure model from single crystal X-ray diffraction[12] suggested that the off-centring of the M2 atoms along the *c*-axis means that when one of the two M2 sites in the trimer is occupied, the nearest M1 must be unoccupied, and when an M1 is occupied, the nearest M2 must be unoccupied. We can probe this hypothesis from our refined configurations. Figure 6.14 shows the possible occupation patterns for an individual M1–M2–M1 trimer, where trimer **5** should never be found due to the close M–M distances involved. Table 6.13 gives the numbers of each of these trimers found in models **[SC1&SC2, P1]**, the expected numbers based on statistical occupancies alone and the numbers in the starting configurations. As there are slight ambiguities

in labelling due to a few sites moving to unphysical positions, a small number of trimers cannot be assigned. The unassigned M1 atoms most likely correspond to M1 atoms with a M2 vacancy (trimers **1**, **2** and **3**).

It can be seen that the numbers found in **SC1** correspond with the expected trimers based on statistics alone, indicating that the algorithm for determining the trimer arrangement is valid. Trimer **5**, which has M1 atoms above and below an occupied M2 site becomes far less populated in the refined models than pure statistics would suggest. Furthermore, trimers **1**, **6, 7** have become more populated. This agrees with the previous hypothesis made by Auckett *et al.*[12] However, the RMC models do contain some trimers with all three sites occupied simultaneously [47(3) and 51(2)]. This could occur because the M2 sites can move in the *ab* plane to alleviate short contacts. However, it may also be permitted because of the relatively small (Mo–Mo > 2.2 Å) minimum distance constraints applied and the natural tendency of the RMC algorithm to favour random configurations. We note again that **[SC1, P1]** and **[SC2, P1]** converged to give similar site distribution pictures. The presence of trimers **1**, **6** and **7** helps explain the extended cloud plots of Figure 6.11: local shifts of the individual sites in each will lead to a smeared out atomic density.

**Table 6.13 – The number of each of the trimers illustrated in Figure 6.14 expected from statistics alone, the numbers found in starting configurations** SC1–SC2 **and the numbers found in the refined models** [SC1–SC2, P1]**. The expected number of** SC2 **is not included as M1 is 100% occupied.**

| Description | Timer type (Fig 6.15) | Statistically expected | SC1 | [SC1, P1] | SC2 | [SC2, P1] |
|---|---|---|---|---|---|---|
| M2 Va with M1 above AND below | 1 | 560.8 | 561 | 599(3) | 768 | 602(6) |
| M2 Va with M1 above OR below | 2+3 | 89.6 | 87 | 51(3) | 0 | 54(6) |
| M2 Va with M1 Va above AND below | 4 | 3.6 | 6 | 0.6(7) | 0 | 1.0(7) |
| M2 atoms with M1 above AND below | 5 | 97.8 | 99 | 47(3) | 0 | 51(2) |
| M2 atoms with Va above OR below | 6+7 | 15.6 | 15 | 49(4) | 0 | 51(5) |
| M2 atoms with Va above AND below | 8 | 0.6 | 0 | 9(2) | 0 | 6(2) |
| Unassigned 'Mo' atoms | N/A | 0 | 0 | 21(1) | 0 | 11(4) |
| Unassigned M1 atoms | N/A | 0 | 0 | 18(3) | 0 | 6(3) |

Another important aspect of the structure in Ba$_3$NbMoO$_{8.5}$ is the coordination number of the M sites. The variable coordination numbers of Mo$^{6+}$ in La$_2$Mo$_2$O$_9$ and V$^{5+}$ in Bi$_{1-x}$V$_x$O$_{1.5+x}$ ($x$ = 0.087, 0.095) have been shown to be critical to high oxide-ion conductivity.[21-22] In Ba$_3$NbMoO$_{8.5}$, the high oxide-ion conductivity is also attributed to the variable coordination numbers of Mo$^{6+}$ and Nb$^{5+}$,[5] and links have been made between the ratio of MO$_4$ tetrahedra to MO$_6$ octahedra and the conductivity.[6-11] However, the average structural view that the M cations exist as either MO$_4$ or MO$_6$ is limited and MO$_5$ polyhedra are highly likely to be present.

In order to determine a sensible cut-off distance for the coordination sphere of a Mo atom, the Mo1–O and Mo2–O distances were examined, as shown in Figure 6.15. The small number of unassigned Mo atoms have been excluded from these analyses as they have moved into non-physical positions. We note that both models produce very similar histograms of bond distances and angles. The majority of Mo1–O distances (Figure 6.15a) are close to $r \approx 1.85$ Å, with a cut off at $r \approx 2.2$ Å. There is a second maximum seen at $r \approx 2.5$ Å with a broad distribution, which is also seen in the Mo2–O histogram and is explained below. There is another large population at $r \approx 3.5$ Å, which we attribute to the second coordination sphere. On the other hand, the Mo2–O distance histogram (Figure 6.15b) shows that after the cut off at $r \approx 2.2$ Å, there is a second maximum at $r \approx 2.7$ Å. This maximum extends beyond 3.0 Å. This bond distribution occurs because the Mo2 atoms are displaced off centre of the 3$b$ position, which results in three shorter Mo2–O1 distances and three longer Mo2–O1 distances. If the Mo2 atoms were in 3$b$ position, there would be a single maximum at $r \approx 2.1$ Å rather than the two distinct maxima seen in Figure 6.15b.Therefore, in order to include the longer Mo2–O1 distances in the coordination sphere of Mo atoms, a distance of $r < 3.05$ Å was selected for both Mo1 and Mo2 atoms.
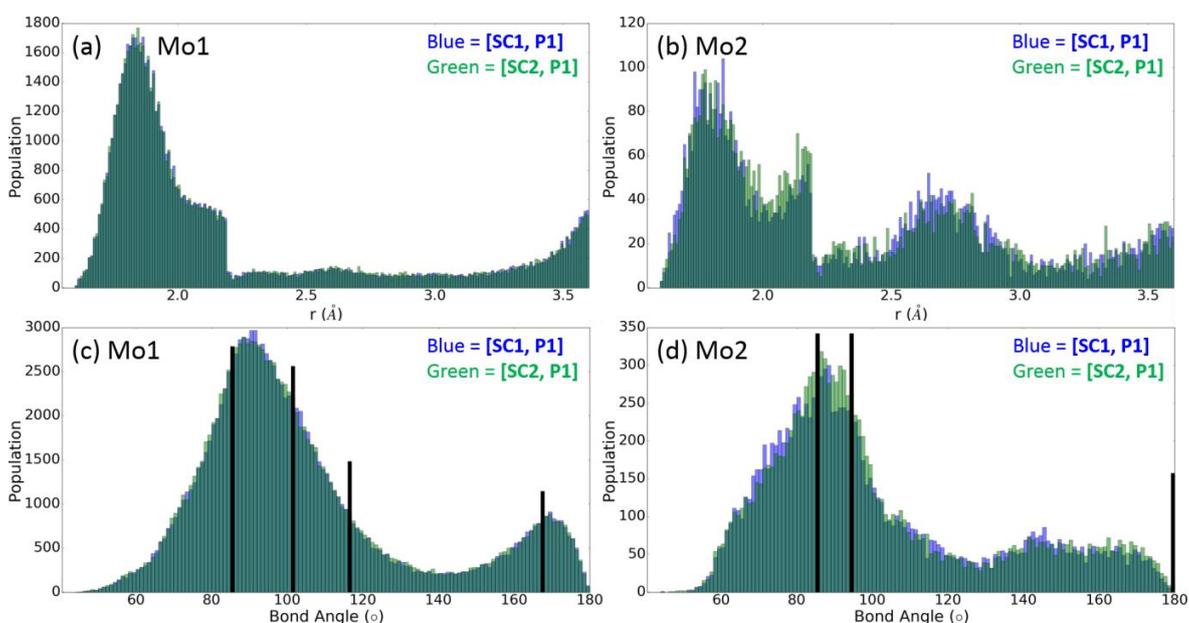
**Figure 6.15** – Histograms of room temperature Ba₃NbMoO₈.₅ refined models of (a) Mo1–O distances; (b) Mo2–O distances; (c) O–Mo1–O bond angles; (d) O–Mo2–O. The bond angles from the average configurations (black) have been superimposed on (c) and (d).

Tables 6.14 and 6.15 give the coordination numbers for the Mo1 atoms and Mo2 atoms respectively from models **[SC1&SC2, P1]**. Refinements that used no experimental data but the same constraints and restraints (see Tables 6.9 and 6.10) were also performed and their coordination numbers are included in Tables 6.14 and 6.15. These used four configurations from **SC1**. This was done to determine if the results obtained were data-driven, or merely caused by the constraints and restraints applied.

**Table 6.14** – **The average coordination numbers (CNs) of Mo1 atoms from room temperature Ba₃NbMoO₈.₅ models** [SC1&SC2, P1] **and with no data, where a Mo1 atom is coordinated with an O atom if Mo1–O < 3.05 Å.**

|  | [SC1, P1] | [SC1, P1] % | [SC2, P1] | [SC2, P1] % | No data | No data % |
|---|---|---|---|---|---|---|
| CN < 4 | 1.1(8) | 0.08(6) | 2(10) | 0.11(9) | 15(3) | 3(2) |
| CN = 4 | 293(8) | 20.8(5) | 280(10) | 20(1) | 80(60) | 20(20) |
| CN = 5 | 630(20) | 45(1) | 662(20) | 47(1) | 200(200) | 40(50) |
| CN = 6 | 460(10) | 33(1) | 450(10) | 31.8(8) | 200(200) | 40(50) |
| CN > 6 | 21(4) | 1.5(3) | 24(4) | 1.7(3) | 50(40) | 10(10) |
| Average | 5.149(7) |  | 5.155(6) |  | 5.1(3) |  |
| Total | 1410(2) |  | 1416(4) |  | 500(500) |  |

In both experimental models **[SC1&SC2, P1]**, the most common coordination number is 5, with ~45% of Mo1 atoms in this environment. The refinements with no data also resulted CN = 5 as the most common coordination number, but the standard deviation is much larger and there is an almost equal number of Mo1 atoms with CN = 6. This demonstrates that the coordination

numbers are a result of the data and not merely a result of the minimum distance constraints and BVS restraints that were applied in the refinements. The numbers shown in Table 6.14 indicate that the previous hypotheses[5-11] that $Mo^{6+}$ and $Nb^{5+}$ ions exist as either tetrahedra or octahedra is incorrect. They also reveal that the recent suggestion[15] that there are only Mo and Nb atoms with CN = 5 at boundaries of domains of palmierite and 9R hybrid perovskite does not fully describe the local structure. If the structure were arranged in this manner, fivefold coordination would be less common than the fourfold and six-fold coordination numbers.

**Table 6.15 – The average coordination numbers (CNs) of 'Mo2' atoms from room temperature Ba₃NbMoO₈.₅ models** [SC1&SC2, P1] **and with no data, where a 'Mo2' atom is coordinated with an O atom if 'Mo2'–O < 3.05 Å.**

|          | [SC1, P1] | [SC1, P1] % | [SC2, P1] | [SC2, P1] % | No data | No data % |
|----------|-----------|-------------|-----------|-------------|---------|-----------|
| **CN < 4** | 0.1(3) | 0.1(3) | 0(0) | 0(0) | 16(9) | 20(10) |
| **CN = 4** | 0.9(9) | 8(9) | 0.5(9) | 0.5(8) | 21(8) | 20(10) |
| **CN = 5** | 5(1) | 4(1) | 6(2) | 6(2) | 20(8) | 20(10) |
| **CN = 6** | 93(3) | 89(4) | 92(4) | 86(5) | 20(20) | 20(20) |
| **CN > 6** | 6(1) | 6(1) | 8(3) | 8(3) | 11(4) | 13(6) |
| **Average** | 6.00(3) | | 6.03(5) | | 4.7(6) | |
| **Total** | 105(3) | | 107(3) | | 80(20) | |

Table 6.15 shows that the coordination number of the Mo2 atoms is overwhelmingly six-fold. It is expected that the Mo2 atoms would have a coordination number of CN = 6, as they are surrounded by six of the fully occupied O1 sites. The few deviations from this coordination number are likely a result of a small number of Mo2 or O1 atoms moving beyond the search range during the RMC run.

The O–Mo1–O bond angle distributions around all Mo1 sites are shown in Figure 6.15c. There are two maxima at ~90° and ~170°. However, as the Mo1 atoms adopt different coordination numbers, there will be different bond angle distributions corresponding to each environment. Figure 6.16 shows the bond angle histograms that arise from each of the different coordination environments of Mo1 in **[SC1, P1]**. It should be noted that the histogram of all angles includes those from Mo1 atoms with CN > 6 and CN < 3, but as they are a small proportion of the total they are statistically insignificant.
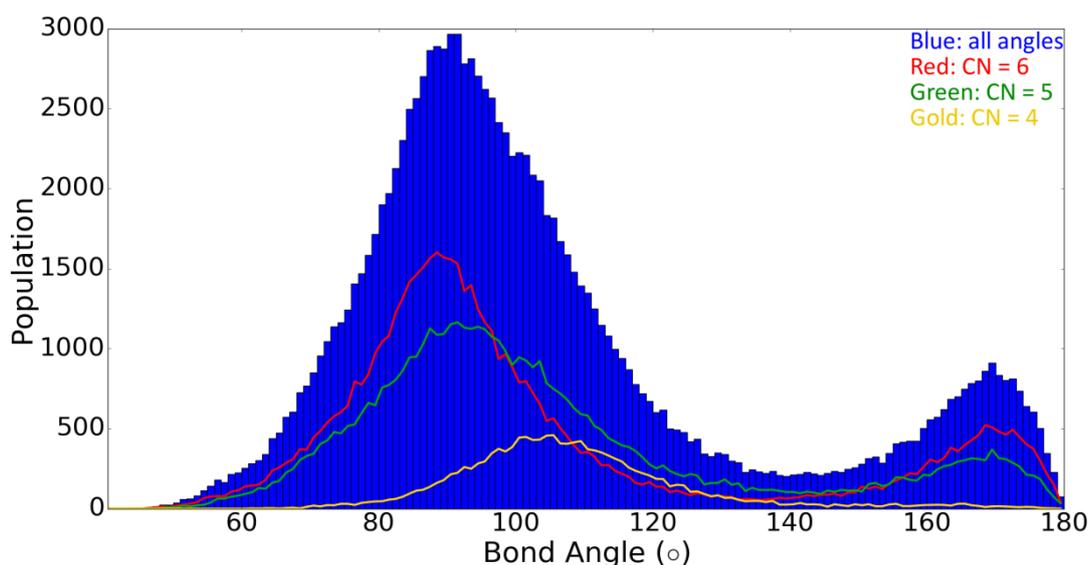
**Figure 6.16** – The O–Mo1–O bond angle histograms of room temperature Ba₃NbMoO₈.₅ model **[SC1, P1]** with the different coordination environments distinguished.

Figure 6.16 shows that the Mo1 polyhedra with CN = 4 follow a very broad distribution with the mean at ~105°, indicating that they are in a distorted tetrahedral geometry. We note that the distribution width is similar to those of the GeO₄ tetrahedra at high temperature discussed in Chapter 4 (FWHM ≈ 30°). The Mo1 polyhedra with CN = 6 follow an octahedral distribution with the two peaks at ~89° and ~170°. The Mo1 polyhedra with CN =5 have a broad distribution with two peaks at ~92° and ~170°, which suggests that square pyramids are the most common coordination geometry adopted. The $\tau$ values[23] of the polyhedra with CN = 5 were investigated and shown in Figure 6.17.
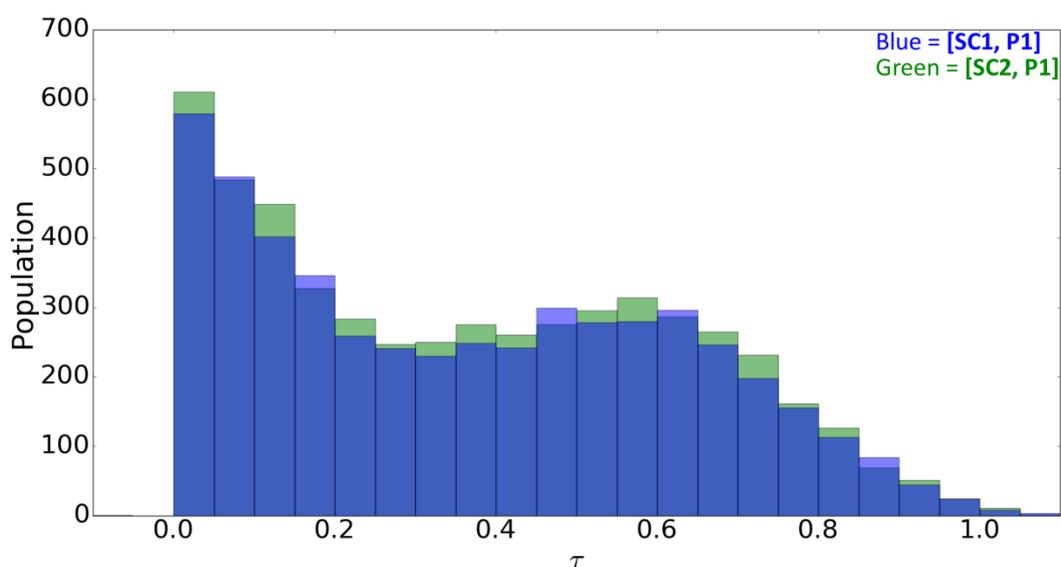


**Figure 6.17** – Histograms of tau values in room temperature Ba₃NbMoO₈.₅.

The $\tau$ histograms again show that the two different starting configurations give similar refined models. They also reveal that the Mo1O₅ polyhedra adopt a mostly square pyramidal geometry ($\tau$

= 0 for square pyramid and $\tau$ = 1 for trigonal biypyramid). This is unsurprising, as the arrangement of the fully occupied O1 atoms means that if a single O2 atom is missing, a square pyramidal geometry would be adopted. However, the significant population at higher $\tau$ shows that many of the polyhedra adopt an intermediate geometry between square pyramids and trigonal bipyramids, which explains the broad angle distribution seen in Figure 6.16. This could be caused by polyhedra where O3 atoms are present, resulting in a less regular geometry. There is a very small population (~0.2%) at $\tau > 1.0$; this is a result of a flaw in the definition of $\tau$, where "umbrella" configurations are not properly accounted for.[24] The population at these values is statistically insignificant, however. The O–Mo2–O bond angle distributions (Figure 6.15d) show that the Mo2 polyhedra are in a distorted octahedral environment. This distorted distribution is a result of the displacement of the Mo2 atoms from the octahedral centre, leading to a range of angles.
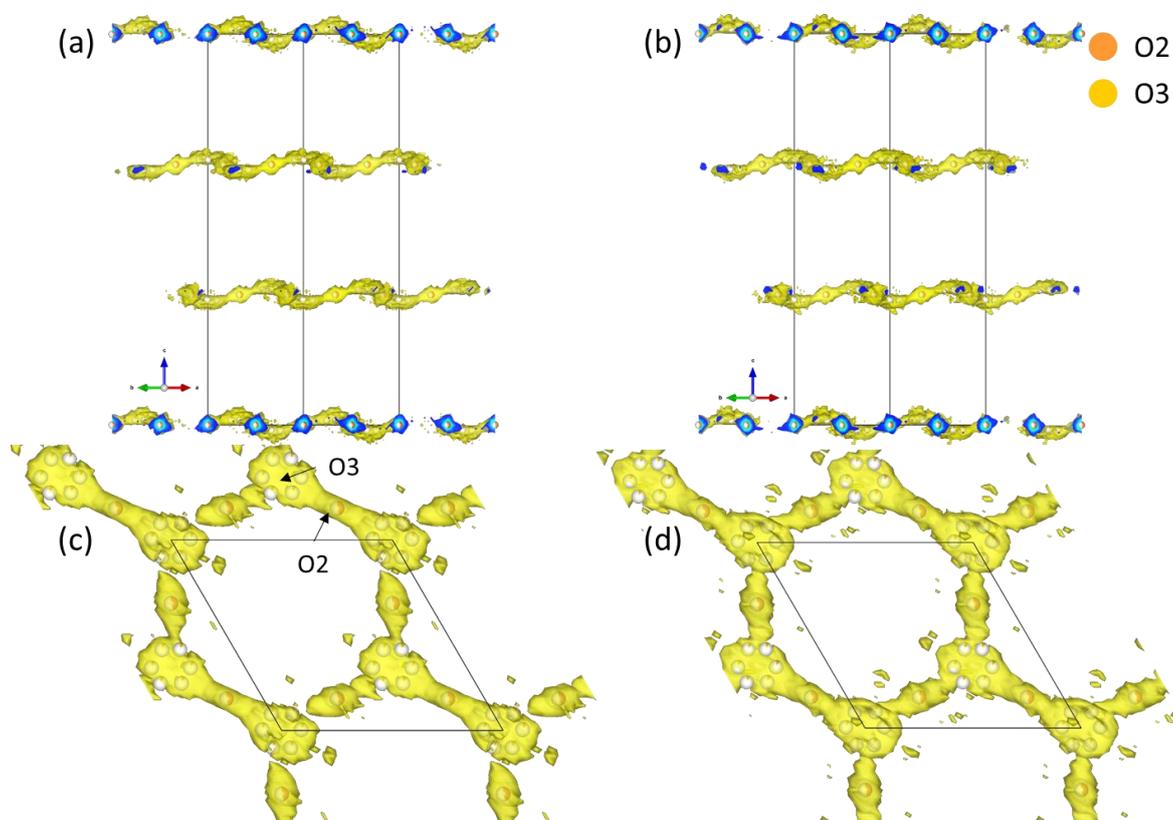


**Figure 6.18 –** The atomic density maps created from the O2 and O3 atom distributions in room temperature Ba₃NbMoO₈.₅ superimposed on the average room temperature structure showing the layers in (a) **[SC1, P1]** (b) **[SC2, P1]** and an individual layer viewed down the *c* axis in (c) **[SC1, P1]** and (d) **[SC2, P1]**. Yellow clouds represent 0.2 × 0.2 × 0.2 Å³ voxels where at least 1.5 atoms are present. The cross sections show the density of atoms from 1.5 to 108 atoms (blue – green – red).

Finally, we will discuss the overall oxygen distribution observed using the atomic density plots shown in Figure 6.18. Figure 6.18a–b shows that O2 and O3 atomic density maps in models **[SC1, P1]** and **[SC2, P1]** viewed down [1 1 0]. Figure 6.18c–d shows one of these layers viewed

perpendicular to the *c* axis. It can be seen that there is significant overlap between the O2 and O3 sites, producing hexagonal sheets that are layered along the *c* axis. It is unusual to see such large oxygen disorder at room temperature. As these models were derived using room temperature data, the disorder here is most likely static. The atomic density maps highly resemble the shape of the O2 and O3 anisotropic ADPs and the bond valence energy landscape in the *ab* plane reported by Auckett *et al.*[12] This large disorder explains why the average structure is insufficient to describe the local structure (see Figure 6.10) and it is likely to be a significant contributor to the oxide-ion conductivity.

### 6.3.2.5 600 °C big box modelling of Ba$_3$NbMoO$_{8.5}$

600 °C data were again analysed based on the extreme models **[SC3, P1]** and **[SC4, P1]** with starting configurations from the average 600 °C structure and the room temperature structure respectively with high temperature cell parameters. As discussed below, both models converged to essentially identical configurations and give excellent fits to the data. We therefore focus on model **[SC3, P1]** and its comparison to the room temperature model (**[SC1, P1]**). Figure 6.19 presents the PDF and Bragg fits of the 600 °C whilst the average goodness of fit values obtained are in Table 6.11. Representative *F*(*Q*) fits are in Appendix B.
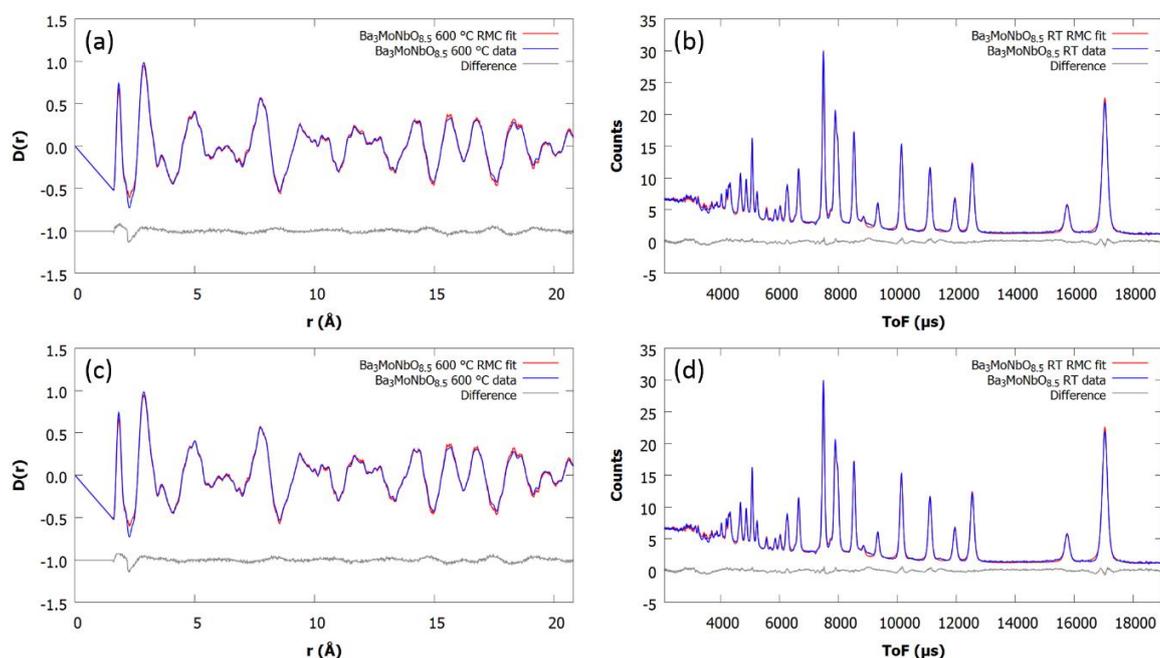


**Figure 6.19 –** Representative fits obtained from RMC analysis of 600 °C Ba$_3$NbMoO$_{8.5}$ models **[SC3, P1]** (a) PDF, $\chi^2_{PDF}$ = 6.028; (b) Bragg, $\chi^2_{Bragg}$ = 17.85 and **[SC4, P1]** (c) PDF, $\chi^2_{PDF}$ = 6.116; (d) Bragg, $\chi^2_{Bragg}$ = 18.04.

Figure 6.20 compares the atomic density maps for the M1–M2–M1 trimers for both models with the room temperature plots from Figure 6.12. The fact that the starting models with different M2 occupancies converged to similar atomic density maps indicates that this occupancy change can be extracted readily from the PDF data analysis. At room temperature, the trimer atomic density

maps formed columns going from one M1 site to the next. At 600 °C, the two M1 sites are isolated, with the atomic density maps as diffuse "spheres", though there is some elongation towards the M2 site. The 600 °C trimers appear less disordered than the room temperature trimers.
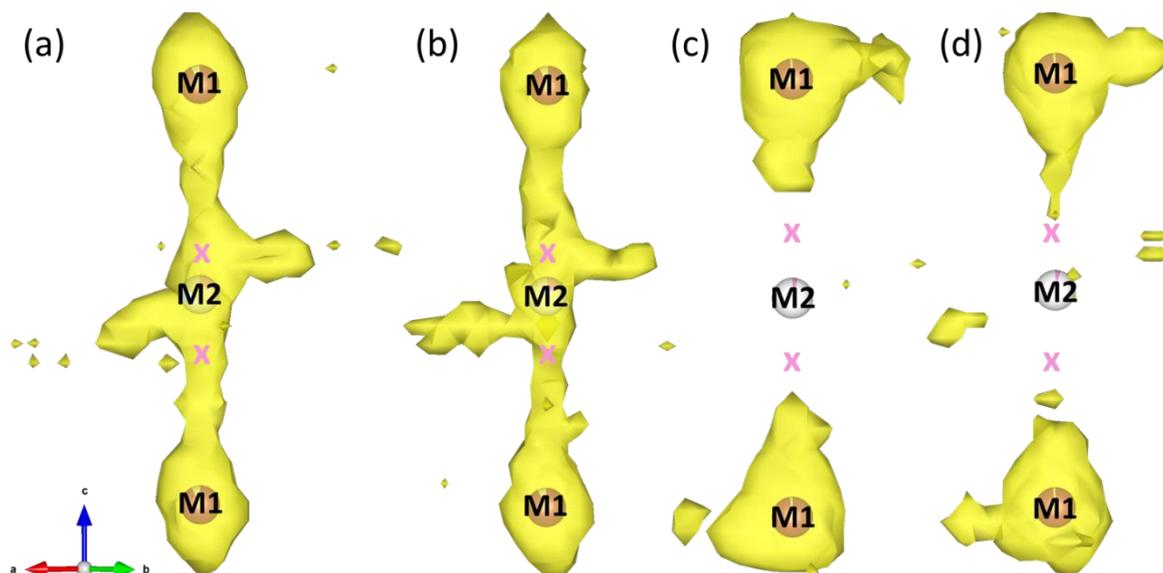


**Figure 6.20** – The atomic density maps obtained from RMC refinements of Ba₃NbMoO₈.₅ at room temperature (a) **[SC1, P1]** and (b) **[SC2, P1]**. 600 °C around the M sites of models (c) **[SC3, P1]** and (d) **[SC4, P1]** superimposed onto the average structure at 600 °C with the M2 atom modelled on the 3*b* position. Pink crosses mark the M2 position in the split model (Tables 6.3 and 6.4).

**Table 6.16** – **The number of 'Mo atoms in the M1 and M2 sites in 600 °C Ba₃NbMoO₈.₅ models** [SC3&SC4, P1]. **'Unassigned' Mo atoms refer to atoms that have moved beyond the definitions of Mo1 and Mo2 atoms.**

|  | [SC3, P1] | [SC4, P1] |
|---|---|---|
| **Unassigned** | 17(2) | 21(3) |
| **Mo1** | 1497(3) | 1490(3) |
| **Mo2** | 22(3) | 26(2) |

Table 6.16 gives the M site occupancies in the models **[SC3&SC4, P1]**. Both models have similar M1 site occupancies to the starting configuration **SC3** (number of M1 = 1502/1536). Despite starting with a larger M2 site occupancy, the Mo atoms originally on the M2 site still moved onto the M1 site in **[SC4, P1]**. The models now closely resemble an oxygen-deficient Ba₃Re₂O₉ structure, as the M1 sites are nearly fully occupied and the M2 sites are nearly completely vacant.

**Table 6.17** – **The number of each of the trimers outlined in Figure 6.14 expected from statistics alone in the room temperature starting configuration** SC3**, the numbers found in starting configurations** SC3&SC4 **and the numbers found in the refined models** [SC3, P1]**.**

| Description | Trimer type (Fig 6.15) | Statistically expected | SC3 | [SC3, P1] |
|---|---|---|---|---|
| M2 Va with M1 above AND below | 1 | 702.1 | 701 | 708(4) |
| M2 Va with M1 above OR below | 2+3 | 31.6 | 33 | 25(2) |
| M2 Va with M1 Va above AND below | 4 | 0.4 | 0 | 0.1(3) |
| M2 atoms with M1 above AND below | 5 | 32.5 | 33 | 11(3) |
| M2 atoms with Va above OR below | 6+7 | 1.4 | 1 | 10(3) |
| M2 atoms with Va above AND below | 8 | 0.02 | 0 | 0.4(7) |
| Unassigned 'Mo' atoms | N/A | 0 | 0 | 16.9(5) |
| Unassigned M1 atoms | N/A | 0 | 0 | 23(4) |

Despite the relatively low number of M2 sites, for completeness the arrangements of the Mo1–Mo2–Mo1 trimers in model **[SC3, P1]** are given in Table 6.17. The result is similar to the result obtained for the room temperature models, where Mo2 atoms have preferentially moved onto sites where there is at least one adjacent M1 vacancy (*i.e* trimers **6** and **7**, not **5**). The bond distances and angles of **[SC3, P1]** are shown in Figure 6.21. The Mo1–O distances (Figure 6.21a) at 600 °C show a similar trend to the room temperature distances, though there is a small minimum at $r \approx 2.6$ Å. There are very few Mo2 atoms, so there are low populations in the Mo2–O distances (Figure 6.21b) and O–Mo2–O bond angles (Figure 6.21d).

As there are very few Mo2 atoms, the coordination numbers shall not be reported. Table 6.18 gives the coordination numbers of the Mo1 polyhedra. The most common coordination number for Mo1 atoms is still CN = 5 (47%), as opposed to CN = 4 as has been previously suggested.[6] On the other hand, the proportion of Mo1 atoms with CN = 4 has increased by a small amount, whilst the proportion of CN = 6 has decreased, when compared to the room temperature results (Table 6.14 and reproduced in Table 6.18).
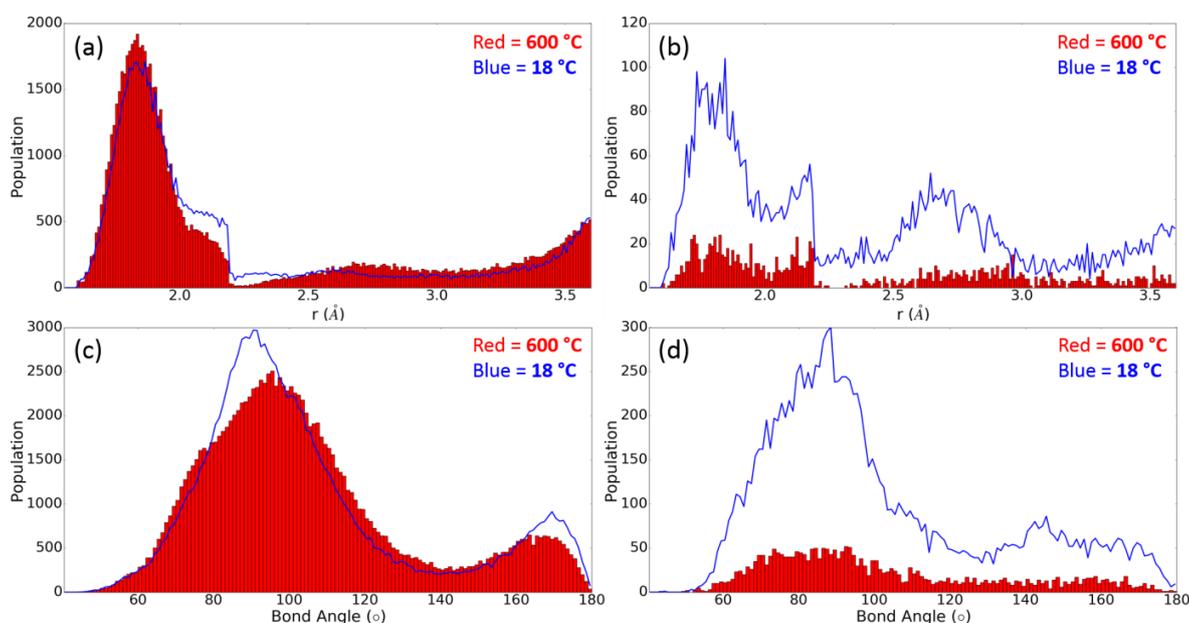
**Figure 6.21** – Histograms of Ba₃NbMoO₈.₅ at 600 °C with the room temperature histograms superimposed: (a) Mo1–O distances; (b) Mo2–O distances; (c) O–Mo1–O bond angles; (d) O–Mo2–O bond angles.

**Table 6.18 – The average coordination numbers (CNs) of Mo1 atoms from 600 °C Ba₃NbMoO₈.₅ models** [SC3&SC4, P1] **and with no data from** SC3**, where a Mo1 atom is coordinate with an O atom if Mo1–O < 3.05 Å.**

|  | [SC3, P1] | [SC3, P1] % | No data | No data % | [SC1, P1] | [SC1, P1] % |
|---|---|---|---|---|---|---|
| **CN < 4** | 3(2) | 0.2(1) | 26(4) | 4(2) | 1.1(8) | 0.08(6) |
| **CN = 4** | 382(7) | 25.5(5) | 130(70) | 20(10) | 293(8) | 20.8(5) |
| **CN = 5** | 710(20) | 47(1) | 300(200) | 40(30) | 630(20) | 45(1) |
| **CN = 6** | 390(20) | 26(1) | 200(100) | 30(20) | 460(10) | 33(1) |
| **CN > 6** | 16(3) | 1.1(2) | 60(30) | 9(6) | 21(4) | 1.5(3) |
| **Average** | 5.02(1) |  | 5.1(2) |  | 5.149(7) |  |
| **Total** | 1497(3) |  | 700(400) |  | 1410(2) |  |

The O–Mo1–O bond angle distribution (Figure 6.21c) at 600 °C has broadened and the mean has moved towards a higher angle (~95°). Figure 6.22 shows the O–Mo1–O bond angles of **[SC3, P1]** separated into the different coordination number environments.
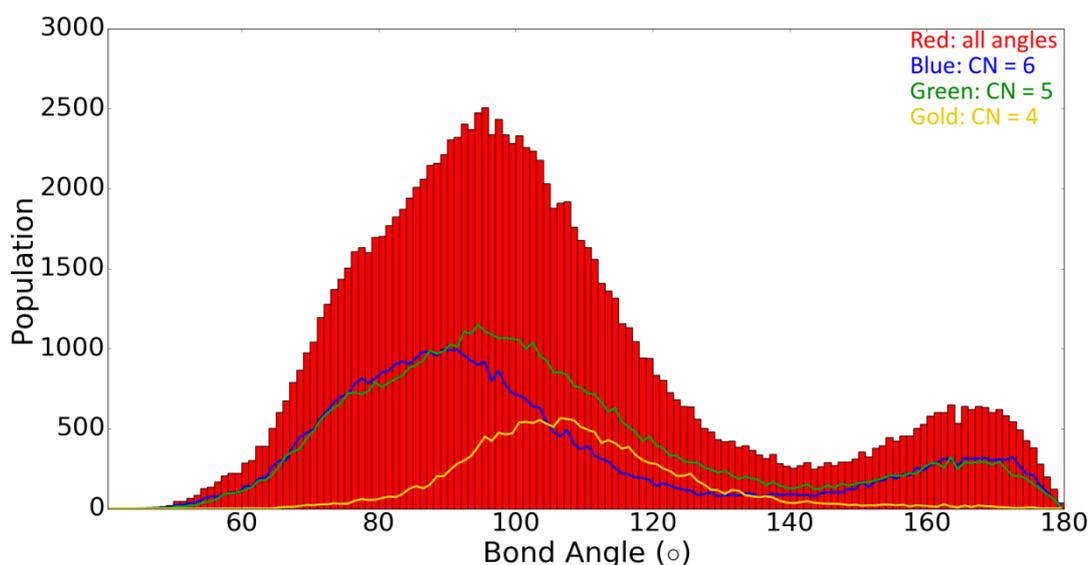
**Figure 6.22** – The O–Mo1–O bond angle histograms of 600 °C Ba₃NbMoO₈.₅ model **[SC3, P1]** with the different coordination environments distinguished.

The O–Mo1–O bond angle distributions of all coordination environments except for CN = 4 have broadened compared to room temperature (Figure 6.16), but are otherwise similar. The mean angle of the CN = 6 polyhedra is the same as in the room temperature configuration (~89°), as is the mean angle of the CN = 4 polyhedra (~105°). The mean of the bond angle distributions of the fivefold coordination environments have moved from ~92° to ~95° in addition to broadening.
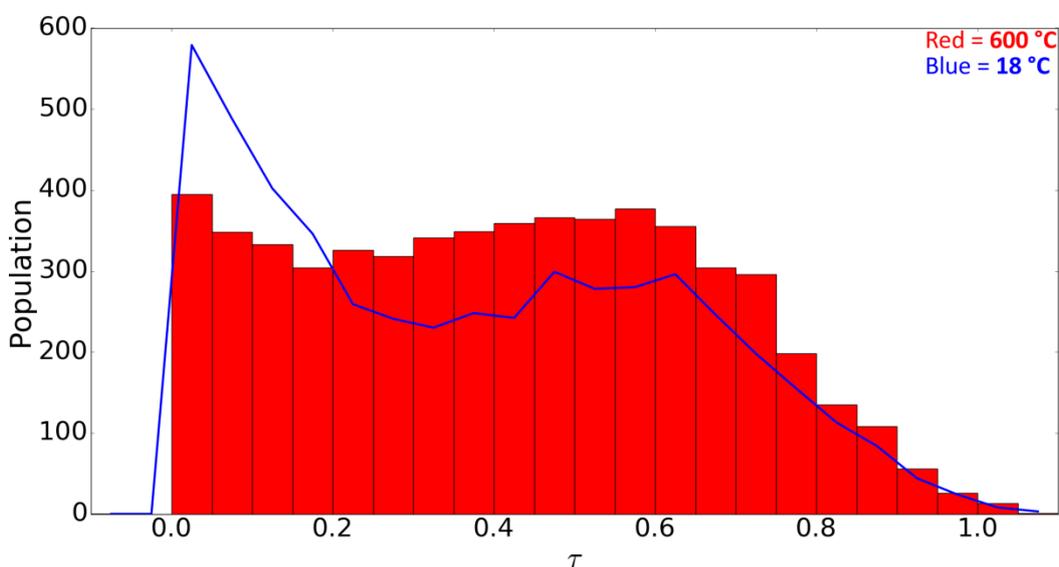


**Figure 6.23** – Histogram of $\tau$ values obtained in Ba₃NbMoO₈.₅ 600 °C model with the room temperature histogram superimposed.

Figure 6.23 shows the $\tau$ values obtained at 600 °C compared with values from room temperature. Whilst there is still a large population that adopts a square pyramidal geometry, the population has shifted towards an intermediate geometry between square pyramid and trigonal bipyramid.

This shows that the Mo1O$_5$ polyhedral environments have become more distorted, which could be caused by the large oxide-ion mobility at high temperature.
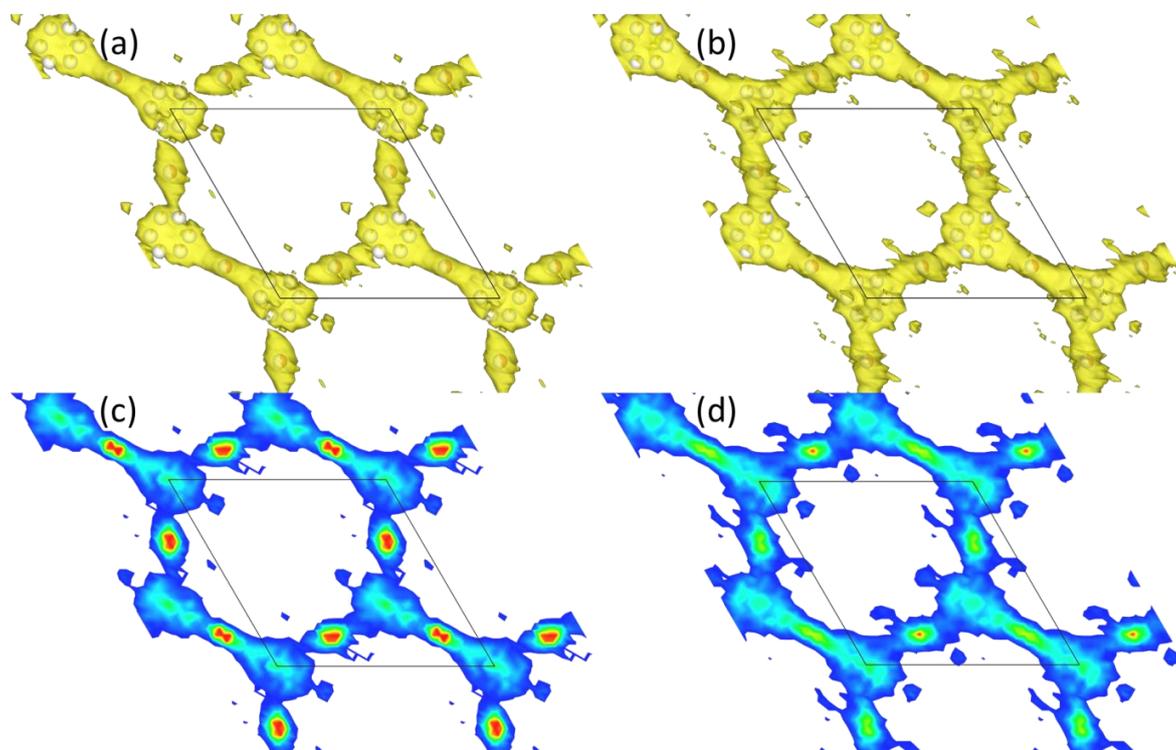


**Figure 6.24 –** The atomic density maps created from the O2 and O3 distributions in Ba$_3$NbMoO$_{8.5}$ superimposed on the average structures at (a) room temperature (**[SC1, P1]**) and (b) 600 °C (**[SC3, P1]**). Cross sections of the atomic density in the same single layers at (c) room temperature and (d) 600 °C models. Blue–green–red = 1.5–96+ atoms.

Figure 6.24 compares the atomic density maps produced from the O2 and O3 atoms at room temperature and high temperature. It can be seen that the high temperature atomic density map is more diffuse than the room temperature map, though with the same general shape. In order to further investigate the differences, the atoms from those single layers were placed onto a single plane and the cross section of the single layers shown in Figure 6.24 were examined. Figure 6.24c shows that at room temperature, whilst there is a spread of atoms, the majority of the O2 atoms remain close to the crystallographic sites and the atomic density of the O3 atoms is evenly distributed around the 6$c$ site, resembling the crystallographic split to the 36$i$ site previously reported.[5] Figure 6.24d shows that at 600 °C, the O2 and O3 atoms are more evenly distributed around the hexagonal sheets, showing the increase in disorder likely caused by the large oxide-ion mobility.

It was previously suggested[5] that the increase in the O3 occupancy and decrease in the O2 occupancy is one of the reasons that the conductivity increases at $T \geq 400$ °C. However, the atomic density maps (Figure 6.24) reveal that there is a very large overlap of the O2 and O3 sites.

It is highly likely that the apparent increase in O3 occupancy as O2 decreases is an artefact of the large amount of disorder in the O2 and O3 sublattice. Therefore, the apparent change in the crystallographic occupancy is an effect of the oxide-ion mobility as opposed to the cause.

## 6.4 Conclusions

The work described in this chapter leads us to the following conclusions:

1.  The long-range average structure of Ba$_3$MoNbO$_{8.5}$ is best described with the M2 atoms on a 6*c* site, as opposed to the 3*b* site previously used.

2.  Variable temperature experiments reveal through the change in the cell parameters that there is a phase transition beginning at ~150 °C and completed at ~370 °C. The high-temperature phase is stable at lower temperatures when quenched, but when cooled slowly the low temperature phase can reform. The difference in the cell parameters of the two phases is subtle and high-resolution diffraction must be employed to resolve it. This explains the unusual behaviour in the thermal evolution of the cell parameters observed with lower-resolution instruments.

3.  Total scattering experiments show that the long-range average structure does not reproduce experimental PDFs below 8 Å, but they can be fitted using big box modelling.

4.  The atomic density maps, Mo–O and O–Mo–O bond angle distributions derived from different starting configurations both at room temperature and 600 °C are very similar. This strongly suggests that the results are data-driven, as opposed to a result of a bias in the starting configurations.

5.  The local structure analysis shows that the atomic density within the M1–M2–M1 trimers at room temperature is more like a column, as opposed to three separate sites. This is related to static distortions of different trimer occupancy patterns. At 600 °C the atoms have mostly moved into the M1 position and as a result the high temperature configuration, counter intuitively, appears less disordered.

6.  The most common coordination number of the M1 sites is CN = 5 at both room temperature and 600 °C. This is contrary to previous reports,[5-11] where it was suggested that the coordination number is either CN = 4 or CN = 6. It also shows that the recent suggestion[15] that Ba$_3$NbMoO$_{8.5}$ exists with domains of palmierite and 9R perovskite falls short of identifying that CN = 5 is the most common environment. The clear preference for this environment is only revealed through local structure studies such as this; crystallographic studies favour the more ordered tetrahedral and octahedral geometries because on average the atomic density will tend to fall towards these higher symmetry sites.

7. The O–Mo1–O bond angle distributions show that the polyhedra with CN = 4 adopt a tetrahedral geometry and the polyhedra with CN = 6 adopt an octahedral geometry at both room temperature and 600°C, with the distributions broadened at 600 °C. For the CN = 5 polyhedra, the bond angle distributions and $\tau$ values indicate that at room temperature they are mostly in a square pyramidal geometry, but a large proportion are in an intermediate geometry between square pyramid and trigonal bipyramid. At 600 °C, the geometry shifts more towards the intermediate geometry. This shift is likely caused by the large oxide-ion movement.

8. The O2 and O3 sites are extremely disordered at room temperature and this disorder increases at 600 °C. There is a significant overlap of the O2 and O3 sites, making it difficult to determine whether an oxide ion is in an O2 position or O3 position. Therefore, the change in the O3 occupancy observed both in the literature[6] and in this study at high temperature is likely to be an effect of the oxide-ion mobility, rather than the cause.

9. The atomic density maps of the O2 and O3 sites suggest that the oxide-ion mobility is largely in the *ab* plane.

Single-crystal impedance spectroscopy experiments could determine if the conduction mechanism is anisotropic, providing evidence for the hypothesis that the oxide-ion mobility would be largely in the *ab* plane. Furthermore, studies on the dynamics of the oxide ion mobility are highly warranted, such as DFT calculations and quasielastic neutron scattering. These studies will provide an insight into the dynamic disorder, which will supplement the static disorder revealed in this study. In addition, doping Ba$_3$Re$_2$O$_9$ with aliovalent cations to create Ba$_3$Re$_{2-x}$M$_x$O$_{8.5-y}$ phases with oxygen vacancies may also yield more good oxide-ion conductors, though the variable oxidation state of Re may produce mixed conductors.

## 6.5 References

1. Li, M.; Pietrowski, M. J.; De Souza, R. A.; Zhang, H.; Reaney, I. M.; Cook, S. N.; Kilner, J. A.; Sinclair, D. C., A family of oxide ion conductors based on the ferroelectric perovskite Na$_{0.5}$Bi$_{0.5}$TiO$_3$. *Nature Materials* **2014,** *13* (1), 31-35.
2. Donohue, P. C.; Katz, L.; Ward, R., The Crystal Structure of Barium Ruthenium Oxide and Related Compounds. *Inorganic Chemistry* **1965,** *4* (3), 306-310.
3. Calvo, C.; Ng, H. N.; Chamberland, B. L., Preparation and structure of a ternary oxide of barium and rhenium, Ba$_3$Re$_{2-x}$O$_9$. *Inorganic Chemistry* **1978,** *17* (3), 699-701.
4. García-González, E.; Parras, M.; González-Calbet, J. M., Electron Microscopy Study of a New Cation Deficient Perovskite-like Oxide: Ba$_3$MoNbO$_{8.5}$. *Chemistry of Materials* **1998,** *10* (6), 1576-1581.
5. Fop, S.; Skakle, J. M. S.; McLaughlin, A. C.; Connor, P. A.; Irvine, J. T. S.; Smith, R. I.; Wildman, E. J., Oxide Ion Conductivity in the Hexagonal Perovskite Derivative Ba$_3$MoNbO$_{8.5}$. *Journal of the American Chemical Society* **2016,** *138* (51), 16764-16769.
6. Fop, S.; Wildman, E. J.; Irvine, J. T. S.; Connor, P. A.; Skakle, J. M. S.; Ritter, C.; McLaughlin, A. C., Investigation of the Relationship between the Structure and Conductivity of the Novel Oxide Ionic Conductor Ba$_3$MoNbO$_{8.5}$. *Chemistry of Materials* **2017,** *29* (9), 4146-4152.
7. Fop, S.; Wildman, E. J.; Skakle, J. M. S.; Ritter, C.; McLaughlin, A. C., Electrical and Structural Characterization of Ba$_3$Mo$_{1-x}$Nb$_{1+x}$O$_{8.5-x/2}$: The Relationship between Mixed Coordination, Polyhedral Distortion and the Ionic Conductivity of Ba$_3$MoNbO$_{8.5}$. *Inorganic Chemistry* **2017,** *56* (17), 10505-10512.
8. Bernasconi, A.; Tealdi, C.; Malavasi, L., High-Temperature Structural Evolution in the Ba$_3$Mo$_{(1-x)}$W$_x$NbO$_{8.5}$ System and Correlation with Ionic Transport Properties. *Inorganic Chemistry* **2018,** *57* (11), 6746-6752.

9.      Bernasconi, A.; Tealdi, C.; Mühlbauer, M.; Malavasi, L., Synthesis, crystal structure and ionic conductivity of the Ba$_3$Mo$_{1-x}$W$_x$NbO$_{8.5}$ solid solution. *Journal of Solid State Chemistry* **2018,** *258*, 628-633.

10.     McCombie, K. S.; Wildman, E. J.; Fop, S.; Smith, R. I.; Skakle, J. M. S.; McLaughlin, A. C., The crystal structure and electrical properties of the oxide ion conductor Ba$_3$WNbO$_{8.5}$. *Journal of Materials Chemistry A* **2018,** *6* (13), 5290-5295.

11.     McCombie, K. S.; Wildman, E. J.; Ritter, C.; Smith, R. I.; Skakle, J. M. S.; McLaughlin, A. C., Relationship between the Crystal Structure and Electrical Properties of Oxide Ion Conducting Ba$_3$W$_{1.2}$Nb$_{0.8}$O$_{8.6}$. *Inorganic Chemistry* **2018,** *57* (19), 11942-11947.

12.     Auckett, J. E.; Milton, K. L.; Evans, I. R., Cation distributions and anion disorder in Ba$_3$NbMO$_{8.5}$ (M = Mo, W) materials: Implications for oxide ion conductivity. *Chemistry of Materials* **2019,** *31* (5), 1715-1719.

13.     Halasyamani, P. S., Asymmetric Cation Coordination in Oxide Materials:  Influence of Lone-Pair Cations on the Intra-octahedral Distortion in d0 Transition Metals. *Chemistry of Materials* **2004,** *16* (19), 3586-3592.

14.     Edwards, J. W.; Speiser, R.; Johnston, H. L., High temperature structure and thermal expansion of some metals as determined by X-ray diffraction data. I. Platinum, tantalum, niobium, and molybdenum. *Journal of Applied Physics* **1951,** *22* (4), 424-428.

15.     Fop, S.; McCombie, K. S.; Wildman, E. J.; Skakle, J. M. S.; McLaughlin, A. C., Hexagonal perovskite derivatives: a new direction in the design of oxide ion conducting materials. *Chemical Communications* **2019,** *55* (15), 2127-2137.

16.     Project, M. https://www.mantidproject.org/Main_Page (accessed 11/04/2019).

17.     Soper, A. K. *GudrunN and GudrunX*, 5; 2012.

18.     Coelho, A. A.; Chater, P. A.; Kern, A., Fast synthesis and refinement of the atomic pair distribution function. *Journal of Applied Crystallography* **2015,** *48* (3), 869-875.

19.     Tucker, M. G.; Keen, D. A.; Dove, M. T.; Goodwin, A. L.; Hui, Q., RMCProfile: reverse Monte Carlo for polycrystalline materials. *Journal of Physics: Condensed Matter* **2007,** *19* (33), 335218.

20.     Stephens, P., Phenomenological model of anisotropic peak broadening in powder diffraction. *Journal of Applied Crystallography* **1999,** *32* (2), 281-289.

21.     Evans, I. R.; Howard, J. A. K.; Evans, J. S. O., The crystal structure of $\alpha$-La$_2$Mo$_2$O$_9$ and the structural origin of the oxide ion migration pathway. *Chemistry of Materials* **2005,** *17* (16), 4074-4077.

22.     Kuang, X.; Payne, J. L.; Johnson, M. R.; Evans, I. R., Remarkably High Oxide Ion Conductivity at Low Temperature in an Ordered Fluorite-Type Superstructure. *Angewandte Chemie International Edition* **2012,** *51* (3), 690-694.

23.     Addison, A. W.; Rao, T. N.; Reedijk, J.; van Rijn, J.; Verschoor, G. C., Synthesis, structure, and spectroscopic properties of copper(II) compounds containing nitrogen–sulphur donor ligands; the crystal and molecular structure of aqua[1,7-bis(N-methylbenzimidazol-2'-yl)-2,6-dithiaheptane]copper(II) perchlorate. *Journal of the Chemical Society, Dalton Transactions* **1984,** (7), 1349-1356.

24.     Alvarez, S.; Alemany, P.; Casanova, D.; Cirera, J.; Llunell, M.; Avnir, D., Shape maps and polyhedral interconversion paths in transition metal chemistry. *Coordination Chemistry Reviews* **2005,** *249* (17), 1693-1708.

# 7. Bi$_{0.775}$Ln$_{0.225}$O$_{1.5}$ (Ln = La, Dy) Oxide-Ion Conductors

## 7.1 Introduction

### 7.1.1 Background

One of the materials with the highest oxide-ion conductivity known is $\delta$-Bi$_2$O$_3$,[1-3] which has a conductivity of ~1 S cm$^{-1}$ at 750 °C.[4] The high oxide-ion conductivity is attributed to the fact that its structure is that of an oxygen-deficient fluorite, with 25% intrinsic oxygen vacancies. However, the highly conductive phase is only stable between 730 °C and 825 °C,[5] where it melts. Attempts have been made to stabilise the high-temperature phase by doping with various oxides, such as the rare-earth sesquioxides and Y$_2$O$_3$,[3, 6-9] transition metals[4, 7, 10-17] such as W$^{6+}$, Nb$^{5+}$, Ta$^{5+}$, Re$^{7+}$, Mo$^{6+}$, Zr$^{4+}$ and V$^{5+}$, alkaline earths[6, 18] and even group 15 elements.[19-20] Many of the "stabilised" cubic phases are in fact only metastable and can transition back into phases with lower conductivities.[8, 17] When doping with alkaline earths Sr$^{2+}$ and Ca$^{2+}$, rare earths and Y$_2$O$_3$ such that Bi$_2$O$_3$ is still the majority of the solid solution, a rhombohedral phase is formed instead of a cubic phase.[5-6, 18, 21] This rhombohedral phase is still a good oxide-ion conductor: Bi$_{0.8}$Sr$_{0.1}$O$_{1.3}$ has a conductivity of 0.025 S cm$^{-1}$ at 600 °C in air,[6] whilst Bi$_{0.75}$Y$_{0.25}$O$_{1.5}$ has a conductivity[3] of 0.012 S cm$^{-1}$ at 500 °C. These families of materials will henceforth be referred to as Bi–Sr–O and Bi–Y–O respectively. The materials with composition Bi$_{0.775}$Ln$_{0.225}$O$_{1.5}$ (Ln = La, Pr, Nd, Sm, Eu, Gd, Tb, Dy) have shown good ionic conductivity: Bi$_{0.775}$La$_{0.225}$O$_{1.5}$, the best conductor of the series, has a conductivity[21-22] of ~0.01 S cm$^{-1}$ at 550 °C and even Bi$_{0.775}$Dy$_{0.225}$O$_{1.5}$, the worst conductor in the series, has a conductivity of ~0.01 S cm$^{-1}$ at 700 °C. This latter phase can also form from the decomposition of cubic WO$_3$–Dy$_2$O$_3$-Bi$_2$O$_3$ phases.[23] The conductivity decreases with a decreasing Ln$^{3+}$ ionic radius. Additionally, Bi$_{0.775}$La$_{0.225}$O$_{1.5}$ has a higher oxygen diffusivity than yttria-stabilized zirconia (YSZ) and gadolinium-doped ceria (GDC).[22] Table 7.1 summarises the conductivities of various materials and Figure 7.1 shows the thermal evolution of the conductivities. As suggested by Figure 7.1, the Bi$_{0.775}$Ln$_{0.225}$O$_{1.5}$ and Bi–Sr–O rhombohedral phases show an increase in conductivity associated with a phase transition at high temperature.[3, 5-6, 18, 21]

**Table 7.1 – The conductivities of Bi$_2$O$_3$ and rhombohedral doped bismuth oxides.**
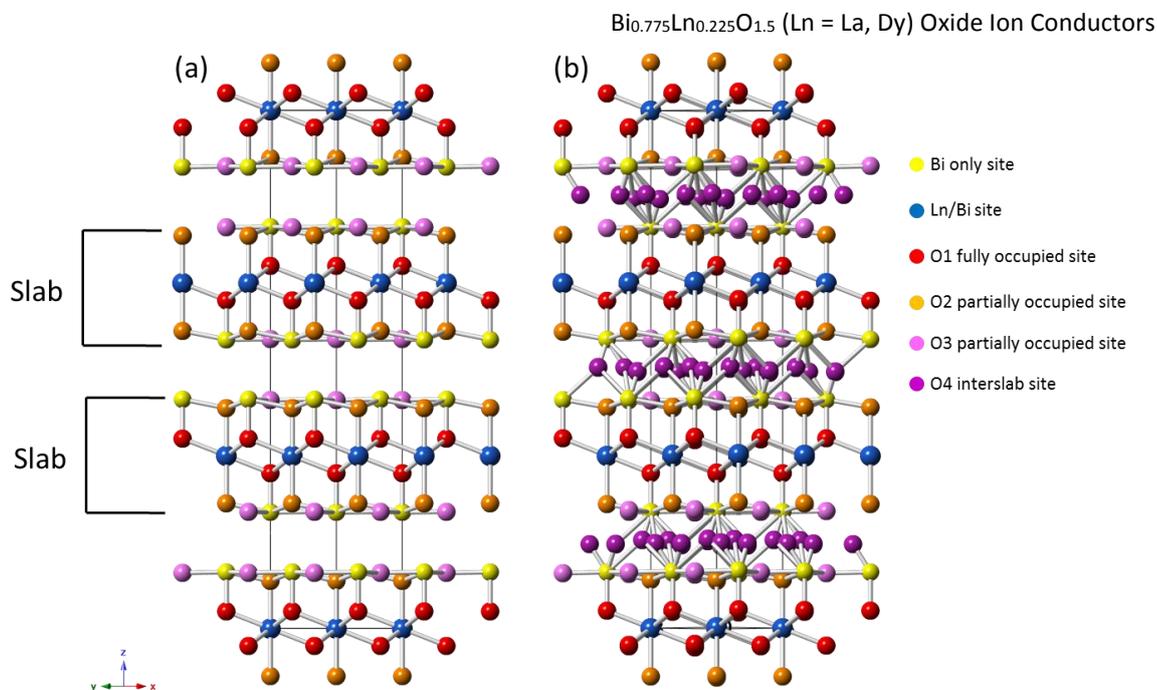
| Reference | Composition | Temperature (°C) | σ (S cm$^{-1}$) |
|---|---|---|---|
| Takahashi *et al.*[6] | Bi$_2$O$_3$ | 550 | 7.70 × 10$^{-4}$ |
| Takahashi *et al.*[6] | Bi$_{0.8}$Sr$_{0.1}$O$_{1.3}$ | 540 | 1.0 × 10$^{-2}$ |
| Drache *et al.*[21] | Bi$_{0.775}$La$_{0.225}$O$_{1.5}$ | 540 | 9.18 × 10$^{-3}$ |
| Drache *et al.*[21] | Bi$_{0.775}$Dy$_{0.225}$O$_{1.5}$ | 540 | 3.59 × 10$^{-4}$ |
| Watanabe & Kikuchi[5] | Bi$_{0.775}$Y$_{0.225}$O$_{1.5}$ | 540 | 8.39 × 10$^{-4}$ |
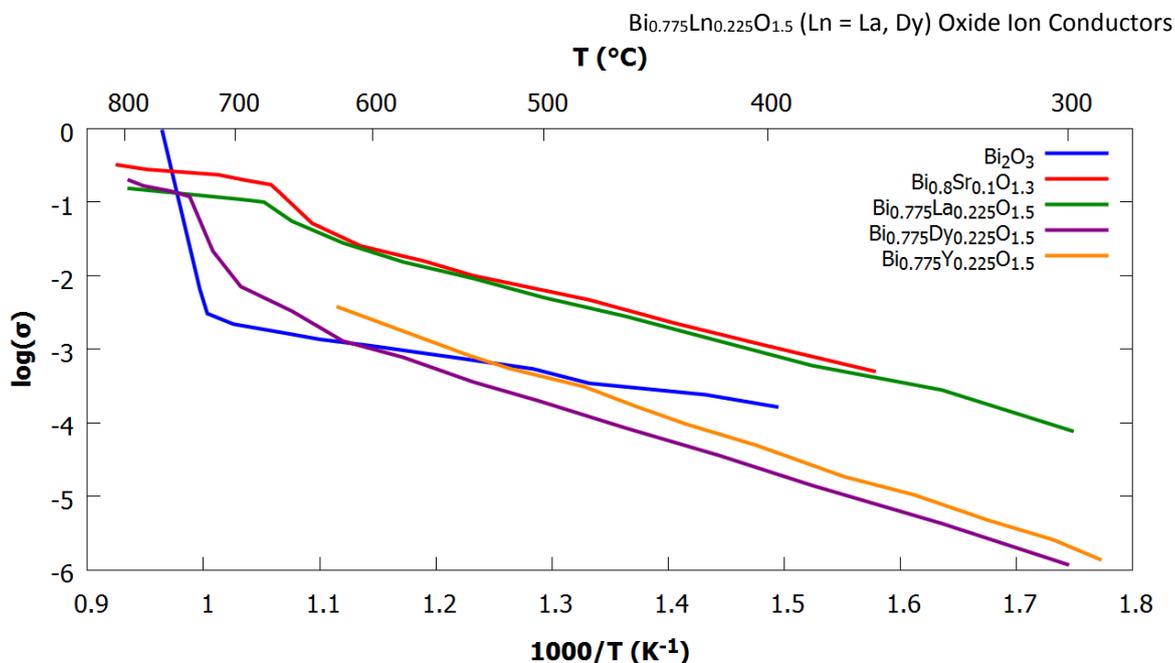
**Figure 7.1** – The conductivities of Bi$_2$O$_3$ and the rhombohedral doped phases: Bi$_2$O$_3$ and Bi$_{0.8}$Sr$_{0.1}$O$_{1.3}$;[6] Bi$_{0.775}$Ln$_{0.225}$O$_{1.5}$ (Ln = La, Dy);[21] hexagonal polymorph of Bi$_{0.775}$Y$_{0.225}$O$_{1.5}$.[5]

**Table 7.2 – Site labels, Wyckoff positions, fractional coordinates and occupancies in Bi$_{0.775}$La$_{0.225}$O$_{1.5}$ at room temperature reported by Obbade *et al.*[24] Space group = *R*-3*m* (hexagonal axes); *a* = 4.0253(1) Å; *c* = 27.6004(9) Å; *V* = 387.29(1) Å³.**

| Site | Wyckoff site | x | y | z | Occupancy |
|------|--------------|-----|-----|-----------|-----------|
| Bi1 | 3*a* | 0 | 0 | 0 | 0.325 |
| La1 | 3*a* | 0 | 0 | 0 | 0.675 |
| Bi2 | 6*c* | 0 | 0 | 0.22475(7) | 1.0 |
| O1 | 6*c* | 0 | 0 | 0.2997(1) | 1.0 |
| O2 | 6*c* | 0 | 0 | 0.0934(2) | 0.742(8) |
| O3 | 6*c* | 0 | 0 | 0.4400(9) | 0.297(8) |
| O4 | 18*h* | 0.201(7) | 0.402(7) | 0.496(1) | 0.071(3) |

(a)

(b)



Slab

Slab

- Bi only site
- Ln/Bi site
- O1 fully occupied site
- O2 partially occupied site
- O3 partially occupied site
- O4 interslab site

**Figure 7.2** – The room temperature $\beta_2$ structure of Bi$_{0.775}$Ln$_{0.225}$O$_{.15}$ (Ln = La, Dy) (a) Without interslab O4 atoms and (b) with interslab O4 atoms.

The room temperature structure ($\beta_2$) of Bi$_{0.775}$Ln$_{0.225}$O$_{1.5}$ is shown in Figure 7.2 and the site labels and atomic coordinates of Bi$_{0.775}$La$_{0.225}$O$_{1.5}$ are given in Table 7.2. The $\beta_2$ structure adopts the $R$-$3m$ space group and consists of layers of fully occupied Bi$^{3+}$ (Bi2) sites and layers of mixed Ln$^{3+}$/Bi$^{3+}$ sites (Ln1/Bi1), organised into slabs that that stack along the $c$ axis. The cationic layers stack in both a hexagonal ($h$) and cubic ($c$) manner following a ($hhc$)$_3$ pattern, but the slabs stack in a cubic manner. Each slab contains a 2:1 ratio of Bi-only to mixed Ln$^{3+}$/Bi$^{3+}$ layers. Within each slab, there are fully occupied O1 sites and partially occupied O2 and O3 sites. The Bi$^{3+}$-only sites are mostly coordinated to the partially occupied O2 and O3 sites, whilst the mixed Bi1/Ln1 cation sites mostly coordinate to the fully occupied O1 site. A neutron diffraction study[24] revealed the possible existence of a fourth oxygen site, O4, which is present in the interslab space and highly disordered. On the other hand, the existence of the interslab O4 has been questioned, as at 10 K the O4 atom was found by powder neutron diffraction to have a very large isotropic atomic displacement parameter (ADP) of $B$ = 9.0 Å$^2$.[25]

The exact nature of the high-temperature phase transition is complex and depends on the rare-earth dopant. There are two different phase transitions: $\beta_2 \rightarrow \beta_1$, where the $\beta_1$ phase still adopts a rhombohedral unit cell, and $\beta_2 \rightarrow$ cubic $\delta$-Bi$_2$O$_3$ structure type. The Bi$_{0.775}$Ln$_{0.225}$O$_{1.5}$ compositions shall be described as belonging to the $\beta_2/\beta_1$ category or the $\beta_2/\delta$ for simplicity. Bi$_{0.775}$Ln$_{0.225}$O$_{1.5}$ (Ln = La – Sm) belong to the $\beta_2/\beta_1$ category,[21, 24] but compositions with the smaller Ln = Gd – Dy cations belong to the $\beta_2/\delta$ category. The cubic phase is metastable at lower temperatures. Bi$_{0.775}$Eu$_{0.225}$O$_{1.5}$ possesses qualities of both categories; it adopts the $\beta_1$ phase at high temperature but the occupancy of the O3 anions is more similar to those seen in Bi$_{0.775}$Ln$_{0.225}$O$_{1.5}$ (Ln = Gd – Dy).

The Bi–Sr–O family belongs to the $\beta_2/\beta_1$ group.[6, 18] The Bi–Y–O compositions belong to the $\beta_2/\delta$ category.[3, 5]

It appears that there is some correlation between the phase transition to the cubic structure and the size of the dopant cation, where the smaller cation dopants favour the cubic phase at high temperatures. The origin of the $\beta_2 \rightarrow \beta_1$ phase transition is attributed to the migration of O2 and O3 anions into the interslab space, allowing the oxide ions to be more mobile. This migration is believed to be the reason for the sudden increase in cell parameters.[18, 24] The evidence that the increase in cell parameters and conductivity is due to the migration is provided in the thermal evolution of the occupancies of O2 and O3 sites in Bi$_{0.775}$La$_{0.225}$O$_{1.5}$ and Bi$_{0.75}$Sr$_{0.25}$O$_{1.375}$. The increase in conductivity and cell parameters is less severe in the Bi$_{0.7}$La$_{0.3}$O$_{1.5}$ material than in Bi$_{0.75}$Sr$_{0.25}$O$_{1.375}$ as some oxide anions already populate the interslab space.[18] The O2 and O3 sites have been suggested to partially occupy 18$h$ sites (as opposed to the 6$c$ sites) in both Bi$_{0.75}$Sr$_{0.25}$O$_{1.375}$ and Bi$_{0.775}$La$_{0.225}$O$_{1.5}$, further suggesting a large amount of intrinsic disorder in these phases.[18, 25]

In addition, there is an $\varepsilon$ monoclinic phase with $P2/c$ symmetry that is adopted by Bi$_{4.86}$La$_{1.14}$O$_9$ (Bi$_{0.81}$La$_{0.19}$O$_{1.5}$), which is a member of the Bi$_{1-x}$La$_x$O$_{1.5}$ ($0.15 \leq x \leq 0.325$) solid solution.[26] This phase is obtained by annealing a liquid nitrogen-quenched $\beta_1$ sample at 300 °C. This structure is also arranged in cationic slabs, but the slabs stack along the monoclinic axis and there are no interslab oxide ions. It is unusual that there are no interslab oxide ions as the $\beta_1$ phase allegedly has a high O4 interslab oxide occupancy. The O4 ions would have to move into the slabs during the $\beta_1$(quenched) $\rightarrow \varepsilon$ transition at $T \approx 300$ °C, then move back into the interslab space during the $\varepsilon \rightarrow \beta_2$ transition, which occurs at $T \approx 420$ °C. The phase transitions of $\beta_1$(quenched) $\rightarrow \varepsilon \rightarrow \beta_2 \rightarrow \beta_1$ were observed from changes in the unit cell volume per formula unit as well as through differential thermal analysis (DTA). Whilst $\beta_2 \rightarrow \beta_1$ is a reversible phase transition, the $\beta_1 \rightarrow \varepsilon \rightarrow \beta_2$ phase transitions are not. The $\varepsilon$-phase has a conductivity approximately ten times lower than the $\beta_2$ phase, which may be due to the lack of interslab oxide ions.

TEM studies have also shown the existence of a superstructure in Bi$_{0.775}$Ln$_{0.225}$O$_{1.5}$ (Ln = La, Pr, Nd, Tb, Dy).[24] The entire Bi$_{0.775}$Ln$_{0.225}$O$_{1.5}$ family, Bi–Sr–O and Bi–Ba–O phases exhibit one modulation vector for [-111] ED patterns of $q^* = \frac{1}{7}(3a^* - 2b^* + 5c^*)$, except for the La phase. The La phase has a modulation vector of $q^* = \frac{1}{12}(3a^* - 2b^* + 5c^*)$. The superstructure may arise due to ordering between different cations in the mixed layer, but it is unknown why the La sample has a unique superstructure.

Diffuse scattering has been found in these samples at scattering vector $Q = 3.0$ Å$^{-1}$, which has led to total scattering and RMC analysis of Bi$_{0.775}$La$_{0.225}$O$_{1.5}$.[25] In addition to the diffuse scattering, a

further motivation for Ahi *et al.*[25] to employ RMC calculations was that the results of their Rietveld refinements were affected by the background function employed. Their results showed that there was a concentration of oxygen atoms around the O2 and O3 sites, but never around the O4 site. The O2 and O3 atomic density distributions adopted a triangular shape, which was maintained from 10 K to 1013 K. The distribution was consistent with the calculated bond valence sum (BVS) distributions of the O$^{2-}$ anions. The RMC results from Ahi *et al.*[25] suggested that the M1 (Bi1/La1) site is also split, and when they introduced M1' sites into their Rietveld refinements, an improvement was obtained, particularly in regards to the [110] reflection intensity. In addition, they found that cation–cation and anion–anion partial PDFs corresponded to the average structure, but there was local ordering revealed by M2–O partials. However, there is a problem with this analysis of the local structure. The authors used neutron powder diffraction data where the neutrons had a wavelength of $\lambda$ = 1.48 Å and a maximum $2\theta$ = 139.92°. This means that their $Q$ range had a maximum of $Q_{max}$ = 7.977 Å$^{-1}$. This $Q$ range is dominated by the Bragg diffraction[27] and results in a low resolution ($\Delta r \approx 0.8$ Å) in the PDF.

### 7.1.2 Purpose of study

There are several questions still surrounding these phases. Firstly, the nature of the phase transition is not fully understood. It is unknown why Bi$_{0.775}$Ln$_{0.225}$O$_{1.5}$ (Ln = La − Sm) fall into the $\beta_2/\beta_1$ category, but Ln = Gd − Dy are in the $\beta_2/\delta$ category. Secondly, it is still unclear whether the interslab O4 oxide ions exist and what their role is in oxide-ion conductivity, as there conflicting reports.[24-25] Finally, there is potentially a complex superstructure,[24] where Bi$_{0.775}$La$_{0.225}$O$_{1.5}$ adopts a different superstructure than the rest of the series. Furthermore, the structure of these compounds is layered, which introduces the possibility of stacking faults being present. No studies regarding stacking faults have been performed on these compositions.

In order to explore these questions, neutron total scattering, X-ray total scattering and high-resolution synchrotron X-ray powder diffraction data were collected on Bi$_{0.775}$Ln$_{0.225}$O$_{1.5}$ (Ln = La, Dy), the two extremes of the family in terms of conductivity. Neutron total scattering will allow the local structure to be probed through PDF analysis and variable temperature data could elucidate the origin of the phase transition and improve our understanding of the conduction mechanism. The neutron Bragg data can be used to determine whether the O4 ions are really present. The high resolution synchrotron powder X-ray diffraction data will be used to examine the cation ordering and to investigate the possible superstructure. Additionally, high-resolution diffraction could reveal stacking faults from the experimental peak shapes.

## 7.2 Experimental Procedure

### 7.2.1 Synthesis

The following syntheses were performed by a previous IRE group member[28] specifically to enable this study. Bi$_{0.775}$La$_{0.225}$O$_{1.5}$ was synthesised by grinding stoichiometric amounts of Bi$_2$O$_3$ (Acros, 99.9%) and La$_2$O$_3$ (Acros, 99.9%) with an agate pestle and mortar. Bi$_2$O$_3$ and La$_2$O$_3$ were calcined at 700 and 1000 °C respectively for 10 hours beforehand. The sample was pelletised and sealed in a silica tube at $< 8 \times 10^{-3}$ mbar. The tube was fired to 750 °C for 15 h with a heating rate of 2 °C min$^{-1}$ and a cooling rate of 5 °C min$^{-1}$. The final product was yellow.

Bi$_{0.775}$Dy$_{0.225}$O$_{1.5}$ was synthesised by grinding stoichiometric amounts of Bi$_2$O$_3$ (Acros, 99.9%) and Dy$_2$O$_3$ (Aldrich, 99.9%) with an agate pestle and mortar. Bi$_2$O$_3$ and Dy$_2$O$_3$ were calcined at 700 and 1000 °C respectively before the synthesis. The sample was pelletised and sealed in a silica tube at $< 8 \times 10^{-3}$ mbar. The tube was fired to 750 °C for 15 h with a heating rate of 2 °C min$^{-1}$ and a cooling rate of 5 °C min$^{-1}$. The sample was reground and pelletised, sealed in a quartz tube and heated to 900 °C for 45 h with a heating rate of 2 °C min$^{-1}$ and a cooling rate of 0.1 °C min$^{-1}$. The sample was reground and pelletised and then calcined at 615 °C for 60 h with a heating rate of 2 °C min$^{-1}$ and cooling rate of 0.1 °C min$^{-1}$. The last step was repeated, but with a heating time of 10 h. Table 7.3 gives the sample codes and nominal formulae. The final product was orange. For the purpose of this report, the sample codes were renamed to MSC043 and MSC044.

**Table 7.3 – Sample codes and nominal formulae of Bi$_{0.775}$Ln$_{0.225}$O$_{1.5}$ (Ln = La, Dy) used in this work.**

| Original code | New code | Nominal formula | Colour |
|---|---|---|---|
| ZMD014 | MSC043 | Bi$_{0.775}$La$_{0.225}$O$_{1.5}$ | Yellow |
| ZMD015 | MSC044 | Bi$_{0.775}$Dy$_{0.225}$O$_{1.5}$ | Orange |

### 7.2.2 Laboratory powder X-ray diffraction

Powder X-ray diffraction patterns were obtained by the same IRE group member who performed the syntheses[28] using a D8 Bruker Advance with a Cu target and Ni filter. The emitted wavelength is a mixture of Cu K$\alpha_1$ (1.54051 Å) and Cu K$\alpha_2$ (1.54433 Å). Patterns were collected using Si slides with a range of $10 \leq 2\theta \leq 70°$ in 0.02° steps with a scan time of 0.6 s step$^{-1}$ for Bi$_{0.775}$La$_{0.225}$O$_{1.5}$ and with a scan time of 0.4 s step$^{-1}$. The purpose of these powder patterns was to check phase purity.

### 7.2.3 SEM-EDX

SEM-EDX was performed on Bi$_{0.775}$Ln$_{0.225}$O$_{1.5}$ (Ln = La, Dy) in order to confirm the composition and purity of the phases at the Research Complex at Harwell (RCaH) by James Gilchrist on a JEOL SEM 6610LV with an Oxford instruments EDS detector. The data were analysed using INCA by Oxford Instruments. INCA reports weight percentage values calculated using a theoretical library of EDX spectra. The compositional data reported herein are values from INCA without any additional

processing or calibration using standards; the accuracy of these compositions is therefore approximately to be ±10%. A small amount of both samples was attached to carbon paper and multiple scans were taken from different positions on different crystallites.

### 7.2.4 Neutron total scattering

Neutron total scattering data were collected on $Bi_{0.775}Ln_{0.225}O_{1.5}$ (Ln = La, Dy) samples in an 8 mm (Ln = La) or 6 mm (Ln = Dy) vanadium can on the POLARIS instrument at the ISIS Neutron and Muon Source. PDF-quality data were collected at room temperature and 800 °C for a total of 6 h at two temperatures for each sample (6 × 10 min + 5 × 1 h for $Bi_{0.775}La_{0.225}O_{1.5}$; 6 × 1 h for $Bi_{0.775}Dy_{0.225}O_{1.5}$). For $Bi_{0.775}La_{0.225}O_{1.5}$, Rietveld-quality data were collected with a scan time of 1 hour (6 × 10 min scans) in the range of 100 – 800 °C in 50 °C steps, whilst for $Bi_{0.775}Dy_{0.225}O_{1.5}$ Rietveld-quality data with a scan time of 1 hour (6 × 10 min scans) were collected from 200 – 800 °C in 200 °C steps. Table 7.4 summarises the sample masses.

**Table 7.4 – Experimental details of the $Bi_{0.775}Ln_{0.225}O_{1.5}$ (Ln = La, Dy) samples used for neutron total scattering.**

| Sample code | Ln | Mass (g) | Can diameter (mm) | Height (cm) | Temperature steps (°C) | Time per step (h) |
|---|---|---|---|---|---|---|
| MSC043 | La | 7.411 | 8 | 4.7 | 50 | 1 |
| MSC044 | Dy | 5.716 | 6 | 4.2 | 200 | 1 |

The data were processed for Rietveld refinement using an in-house python script. Rietveld refinements were performed against the room temperature data by refining the cell parameters, fractional coordinates, the site occupancies of the O atoms and peak shapes. The background was fitted using a 12th-order Chebyshev polynomial. Two starting models were used: one[21] with no O4 and one[24] with the O4 sites (see Table 7.2) included. Data collected from three banks were used: bank 3 ($2\theta$ = 52.2461°), bank 4 ($2\theta$ = 91.5081°) and bank 5 ($2\theta$ = 146.942°).

The PDF-quality data were processed using GudrunN version 5[29] to produce $S(Q)$, $F(Q)$, $G(r)$ and $D(r)$ as defined in Chapter 2.3. The $S(Q)$ data were processed with the STOG software, creating $G(r)$ and $F(Q)$ files. The $G(r)$ data were produced using $Q_{max}$ = 35 Å$^{-1}$ and a Soper-Lorch correction was applied to remove Fourier ripples produced by using a Fourier transform to a limited $Q_{max}$. Data for $r \leq 1.7$ Å were Fourier filtered. Small box PDF analysis was performed using TOPAS v6[30-31] with the $G(r)$ converted into $D(r)$ normalised to the sum of the scattering from all pairs (the native PDF of TOPAS).

### 7.2.5 Synchrotron X-ray powder diffraction

Synchrotron X-ray powder diffraction data were collected on the I11 high resolution powder diffraction beamline at Diamond Light Source using a wavelength of $\lambda$ = 0.82576530(8) Å, determined from a Si calibration. The samples were loaded into 0.3 mm diameter quartz

capillaries. A hot air blower was used to control the temperature ($T$) for variable-temperature data collection. The temperature and scan times for both samples are given in Table 7.5.

**Table 7.5 – Data collection parameters used on Bi$_{0.775}$Ln$_{0.225}$O$_{1.5}$ (Ln = La, Dy) samples on the I11 beam line at Diamond Light Source.**

| Run code | Ln | Nominal $T$ (°C) | $T$ steps (°C) | Scan time (min) |
|---|---|---|---|---|
| 576490 | La | 30 | – | 60 |
| 576491 – 576537 | La | 30 – 950 | 20 | 3 |
| 576538 | La | 950 | – | 60 |
| 576539 | Dy | 30 | – | 60 |
| 576540 – 576586 | Dy | 30 – 950 | 20 | 3 |
| 576587 | Dy | 950 | – | 60 |

The temperature of the hot air blower was calibrated using an Al$_2$O$_2$/Si standard. The cell parameters of Al$_2$O$_3$ and Si were determined through Rietveld refinement over a nominal range of 30 – 950 °C, where Al$_2$O$_3$ was used to determine the calibration curve and Si was used to determine that the calibration curve was correct. The difference between the true temperature and nominal temperature, $\Delta T$, is given in equation 7.1a:

$$\Delta T = -1.12104 \times 10^{-4}T^2 + 0.0780586T - 13.9107 \qquad (7.1a)$$

$$T_{\text{corrected}} = T + \Delta T \qquad (7.1b)$$

Where $T$ is the nominal temperature. Rietveld refinements were performed using the 1 h room temperature data refining the cell parameters, atomic coordinates, atomic occupancies of the Bi/Ln (Ln = La, Dy), ADPs and peak shapes. The model obtained from the POLARIS refinement was used as a starting model, where the O4 were included. The background was fitted using a 12$^{\text{th}}$-order Chebyshev polynomial. A peak corresponding to scattering from the quartz capillary was inserted at $2\theta$ = 11.52° and its position, width and intensity were allowed to refine. The absorption coefficient, $\mu r$, was calculated based on a packing factor of 20% and then fixed at 2.08. Stacking faults were also modelled using the same background functions. The details of the stacking fault modelling are in Section 7.3.4.

Total scattering data were also collected on the I15-1 beamline at Diamond Light Source using a wavelength of $\lambda$ = 0.16169 Å. The temperature was calibrated using an Al$_2$O$_3$/Si standard and the difference between the true temperature and the nominal temperature, $\Delta T$, is given in equation 7.2a:

$$\Delta T = -2.65630 \times 10^{-4}T^2 + 0.27519T - 64.5127 \qquad (7.2a)$$

$$T_{\text{corrected}} = T + \Delta T \qquad (7.2b)$$

# 7.3 Results and Discussion

## 7.3.1 Synthesis and phase purity

Bi$_{0.775}$Ln$_{0.225}$O$_{1.5}$ (Ln = La, Dy) were successfully synthesised using the method employed above. The phase purity was first determined using powder X-ray diffraction.

There were no unaccounted for peaks in either sample. The sample purity was also examined with SEM-EDX. For nominal composition Bi$_{0.775}$La$_{0.225}$O$_{1.5}$, a Bi-normalised formula of Bi$_{0.775}$La$_{0.252(11)}$O$_{1.541(16)}$ was obtained, where the oxygen content was determined from charge balancing. This formula has a normalised Bi : La ratio of 0.754(10) : 0.246(10), which is 2.1σ from the nominal ratio of 0.775 : 0.225 and well within the compositional uncertainty from the EDX data (estimated to be ±10%). As Rietveld refinement indicated the presence of one phase, this strongly suggests that the phase with the correct nominal composition had been formed. For nominal composition Bi$_{0.775}$Dy$_{0.225}$O$_{1.5}$, a formula of Bi$_{0.775}$Dy$_{0.232(13)}$O$_{1.510(13)}$ was obtained, which corresponds to a normalised Bi : Dy ratio of 0.767(12) : 0.230(12). The Bi : Dy ratio is less than 1σ from the nominal composition, showing that the correct phase had again been synthesised.

## 7.3.2 Average structure

### 7.3.2.1 Bi$_{0.775}$La$_{0.225}$O$_{1.5}$

Rietveld refinements were performed on Bi$_{0.775}$La$_{0.225}$O$_{1.5}$ initially using the model suggested by Drache *et al.*,[21] where no O4 atoms are present. This model uses the same site labels and Wyckoff positions as the model in Table 7.2, although there are slight differences in the coordinates of some of the sites. The cation distribution from the starting model,[21] which was assumed to be the same as the distribution found in Bi$_{0.775}$Pr$_{0.225}$O$_{1.5}$ from neutron diffraction, was maintained. This is because the neutron scattering lengths for Bi and La are similar ($b_{La}$ = 8.24 fm; $b_{Bi}$ = 8.532 fm), meaning that the exact distribution would not affect the neutron scattering. Preliminary refinements against the neutron data were performed, refining the O2, O3 and (upon introduction) O4 occupancies, with a single ADP for all O sites (including fully occupied O1). Introducing the O4 site marginally improved the fit ($R_{wp}$ = 3.521% lowered to 3.473%).

High resolution Bragg synchrotron data were used in order to refine the cation site occupancies and Bi2/La2 coordinates and to obtain more accurate cell parameters. To refine the cation occupancies, La2 was introduced onto the same site as Bi2 with an initial occupancy of 0.5, and the fractional occupancies were refined with the constraint that the total site occupancies = 1.0. The La2 site occupancy refined to 0.08(9), which indicates that the M2 site is purely occupied by Bi$^{3+}$, agreeing with previous refinements for this phase and related rhombohedral phases.[18, 21, 24, 32] The La2 site was removed and the Bi2 occupancy was fixed at 1.0, which resulted in a total Bi and La content of 0.789(4) and 0.211(4) respectively, with a fit of $R_{wp}$ = 7.578%. A restraint was applied so that the total content would match the formula. This resulted in a total Bi and La content of 0.775(4) and 0.225(4) and an essentially identical fit with $R_{wp}$ = 7.579%.

The occupancies of the O sites were further investigated by introducing individual isotropic ADPs for the O2, O3 and O4 sites. Refining the oxygen occupancies freely with individual ADPs resulted in an oxygen content per formula unit of 1.82(2) and R$_{wp}$ = 3.086%, whilst applying a restraint so that the total O per formula unit should be 1.5 resulted in a total content of 1.604(18) and R$_{wp}$ = 3.109%. Increasing the weighting of that restraint so that the total content = 1.504(15) resulted in R$_{wp}$= 3.155%, indicating that there is a lack of sensitivity to the total oxygen content in these data. As the oxidation state of both cations will remain as +3, it is justified to use the more heavily restrained model in order to obtain a charge-balanced formula. The ADPs of O2, O3 and O4 were very large, so they were equated, giving a fit with R$_{wp}$ = 3.192%. Finally, refinement was performed against the neutron and synchrotron data simultaneously, giving the final model in Table 7.6 (R$_{wp}$ = 5.136%, $\chi^2$ = 2.886). The Rietveld plots are given in Figure 7.3. The (0 0 $l$) reflections, two of which are highlighted in Figure 7.3, do not fit the observed data well, and reflections where the $l$ is large are also poorly fitted. As the reflections that are poorly fitted all had the large $l$ value in common, stacking faults were investigated; this is discussed in Section 7.3.4.

**Table 7.6 – Crystallographic parameters obtained from combined neutron and synchrotron refinement of Bi$_{0.775}$La$_{0.225}$O$_{1.5}$. Space group = $R$-3$m$ (hexagonal axes); cell parameters: $a$ = 4.02884(3) Å; $c$ = 27.6052(3) Å; $\alpha$ = 90°; $\gamma$= 120°; $V$ = 388.043(7) Å$^3$. Errors for Bi1, La1 O2, O3 and O4 occupancies are not included as restraints were applied.**

| Site label | Wyckoff site | X | y | z | Occupancy | B (Å$^2$) |
|---|---|---|---|---|---|---|
| Bi1 | 3$a$ | 0 | 0 | 0 | 0.326 | 2.00(3) |
| La1 | 3$a$ | 0 | 0 | 0 | 0.674 | 2.00(3) |
| Bi2 | 6$c$ | 0 | 0 | 0.22455(3) | 1.0 | 1.90(2) |
| O1 | 6$c$ | 0 | 0 | 0.30057(8) | 1.0 | 2.53(4) |
| O2 | 6$c$ | 0 | 0 | 0.0931(1) | 0.795 | 6.5(2) |
| O3 | 6$c$ | 0 | 0 | 0.4414(4) | 0.356 | 6.5(2) |
| O4 | 18$h$ | 0.162(6) | 0.32(1) | 0.493(2) | 0.034 | 6.5(2) |
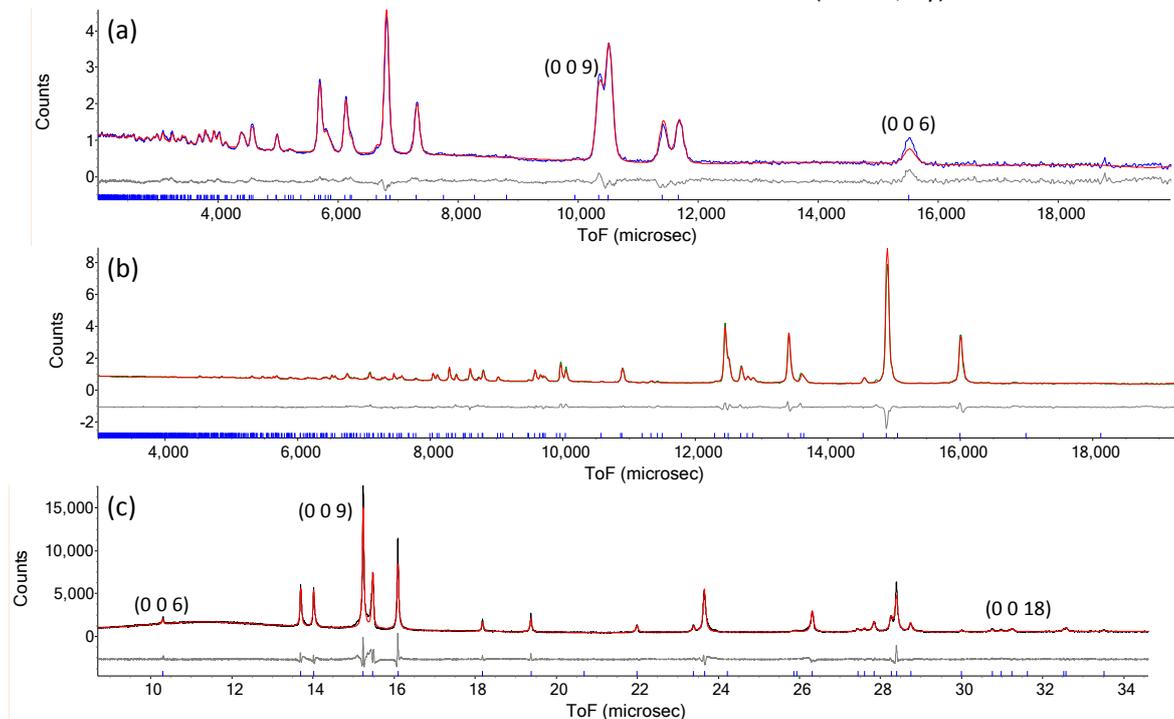
**Figure 7.3** – Combined neutron and synchrotron Rietveld refinement of $Bi_{0.775(4)}La_{0.225(4)}O_{1.5}$. (a) POLARIS bank 3, $R_{wp}$ = 3.773, $\chi^2$ = 1.848; (b) POLARIS bank 5, $R_{wp}$ = 2.738, $\chi^2$ = 2.547; (c) I11, $R_{wp}$ = 7.716, $\chi^2$ = 2.851. Blue tick marks represent reflections arising from $Bi_{0.775(4)}La_{0.225(4)}O_{1.5}$.
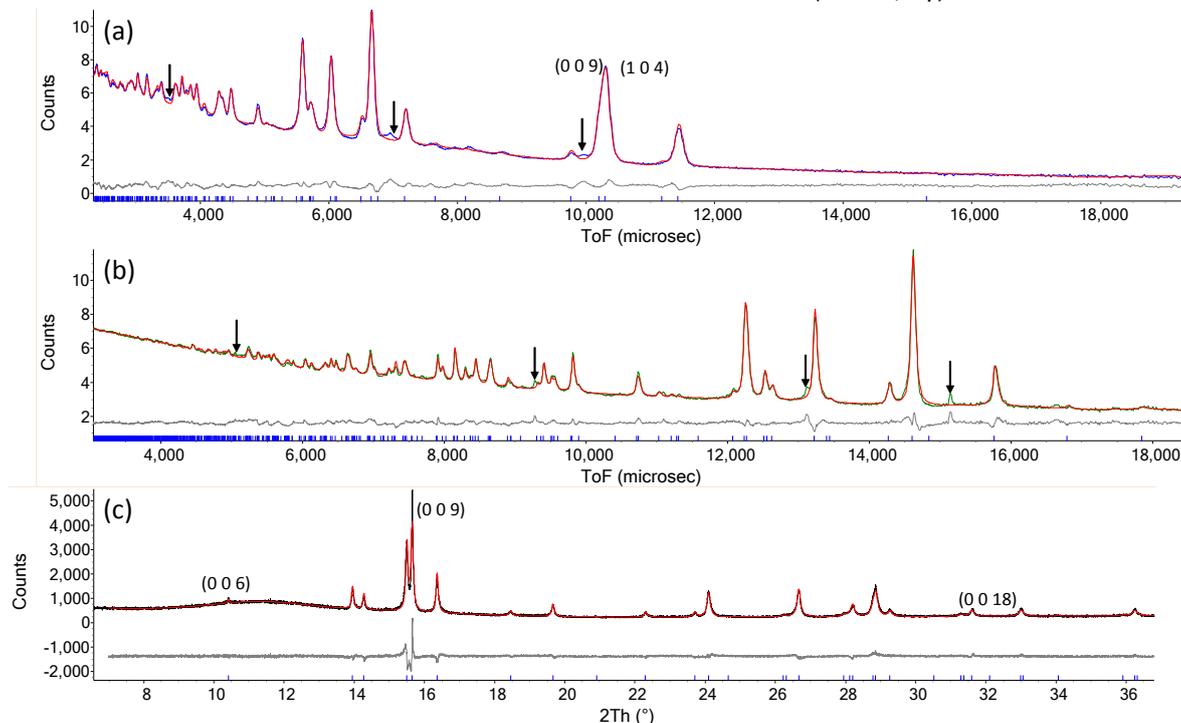
### 7.3.2.2 $Bi_{0.775}Dy_{0.225}O_{1.5}$

Rietveld refinements were also performed against neutron and synchrotron data of $Bi_{0.775}Dy_{0.225}O_{1.5}$. The starting model[21] contained only three oxygen sites in the same positions as those given in Table 7.2. Due to the different neutron scattering lengths of Bi and Dy, attempts were made to refine Bi and Dy occupancies on both M1 and M2 sites. With freely refined occupancies, a total Bi content per formula unit of 0.349(7) and a total Dy content per formula unit of 0.512(13) was obtained. A constraint was added such that the occupancy on the Bi1/Dy1 and Bi2/Dy2 sites each summed to 1 each, which gave a total Bi content of 0.646(14) and Dy content of 0.354(14). The fits of these two models were almost identical; the former gave a fit with $R_{wp}$= 2.228% and the latter fit gave $R_{wp}$ = 2.229%. This indicates that there is not enough sensitivity in the data to determine the exact cation distribution. In the constrained model, the Dy2 occupancy refined to 0.039(16), so the expected cation distribution of Bi1 = 0.325, Dy1 = 0.675 and Bi2 = 1.0 was adopted. A free refinement of the O2 and O3 oxygen occupancies with all O ADPs equated (including fully occupied O1) against the neutron data resulted in a fit with $R_{wp}$ = 2.109 % and a total oxygen content per formula unit of 1.276(9), suggesting that O4 atoms could be present in this sample. When the O4 site was introduced, a fit of $R_{wp}$ = 2.086% was obtained with a restraint applied so that the total O content per formula unit = 1.5. The resulting total oxygen content was 1.460(14).

Refinements against synchrotron data were also unable to resolve the cation distribution, so the occupancies were constrained to those in Table 7.2. The atomic coordinates and cell parameters were also refined against the synchrotron data.

The O occupancies were again refined against neutron data only, using independent ADPs on O2, O3 O4, with a restraint that the total O content per formula unit = 1.5. Refinements were also performed with the O2, O3 and O4 ADPs equated. Similarly to Bi$_{0.775}$La$_{0.225}$O$_{1.5}$, it was found that there is a lack of sensitivity with the O content. It was decided that the best approach is to equate the O2, O3 and O4 ADPs and refine with restraint to keep the total O content per formula unit to 1.5, which resulted in a fit with R$_{wp}$= 2.012% (compared to 1.992% for a free refinement and 1.999% for weaker restraint). The refinement was performed against the synchrotron data simultaneously with a spherical harmonic function used to account for preferred orientation in the synchrotron dataset, resulting in a fit with R$_{wp}$ = 2.362%, $\chi^2$ = 3.164. The crystallographic parameters obtained from this refinement are in Table 7.7 and the Rietveld plots are presented in Figure 7.4.

**Table 7.7 – Crystallographic parameters obtained from combined neutron and synchrotron refinement of Bi$_{0.775}$Dy$_{0.225}$O$_{1.5}$. Space group = *R*-3*m* (hexagonal axes); cell parameters: *a* = 3.95654(4) Å; *c* = 27.3053(5) Å; $\alpha$ = 90°; $\lambda$ = 120°; *V* = 370.18(1) Å$^3$. Errors for O2, O3 and O4 occupancies are not included as restraints were applied to fix the composition.**

| Site label | Wyckoff site | *x* | *y* | *z* | Occupancy | B (Å$^2$) |
|---|---|---|---|---|---|---|
| Bi1 | 3*a* | 0 | 0 | 0 | 0.325 | 1.05(3) |
| Dy1 | 3*a* | 0 | 0 | 0 | 0.675 | 1.05(3) |
| Bi2 | 6*c* | 0 | 0 | 0.22543(4) | 1.0 | 1.20(3) |
| O1 | 6*c* | 0 | 0 | 0.3050(1) | 1.0 | 2.74(5) |
| O2 | 6*c* | 0 | 0 | 0.0855(1) | 0.684 | 3.3(1) |
| O3 | 6*c* | 0 | 0 | 0.4419(3) | 0.309 | 3.3(1) |
| O4 | 18*h* | 0.217(2) | 0.434(4) | 0.5113(6) | 0.085 | 3.3(1) |

**Figure 7.4 –** Combined neutron and synchrotron Rietveld refinement of Bi$_{0.775}$Dy$_{0.225}$O$_{1.5}$. (a) POLARIS bank 3, R$_{wp}$ = 2.253, χ$^2$ = 4.866; (b) POLARIS bank 5, R$_{wp}$ = 1.463, χ$^2$ = 3.207; (c) I11, R$_{wp}$ = 7.404, χ$^2$ =1.975. Blue tick marks represent reflections arising from Bi$_{0.775}$Dy$_{0.225}$O$_{1.5}$. The black arrows highlight the unaccounted for peaks.

In the neutron data, there are three unaccounted for peaks, which do not correspond to a δ-Bi$_2$O$_3$-type phase. These peaks are not visible in the synchrotron refinements. This implies that they may arise due to some sort of ordering in the oxygen sublattice. In a similar manner to the Bi$_{0.775}$La$_{0.225}$O$_{1.5}$ sample, the (0 0 *l*) peaks, and any reflection with high *l* values, are poorly fitted. It is highly likely that the cause of the poor fit in these peaks in this sample is the same as in the Bi$_{0.775}$La$_{0.225}$O$_{1.5}$ sample.

### 7.3.3 Analysis of variable temperature data obtained on Bi$_{0.775}$Ln$_{0.225}$O$_{1.5}$ (Ln = La, Dy)

#### 7.3.3.1 Bi$_{0.775}$La$_{0.225}$O$_{1.5}$

Variable temperature refinements were performed using the neutron diffraction data obtained on POLARIS, the high resolution synchrotron data obtained on I11 and additionally the Bragg data obtained from the synchrotron total scattering data on I15-1. Refinements with each data set were not performed simultaneously. Figure 7.5 shows the thermal evolution of the cell parameters from the refinements using POLARIS data and I15-1 data.
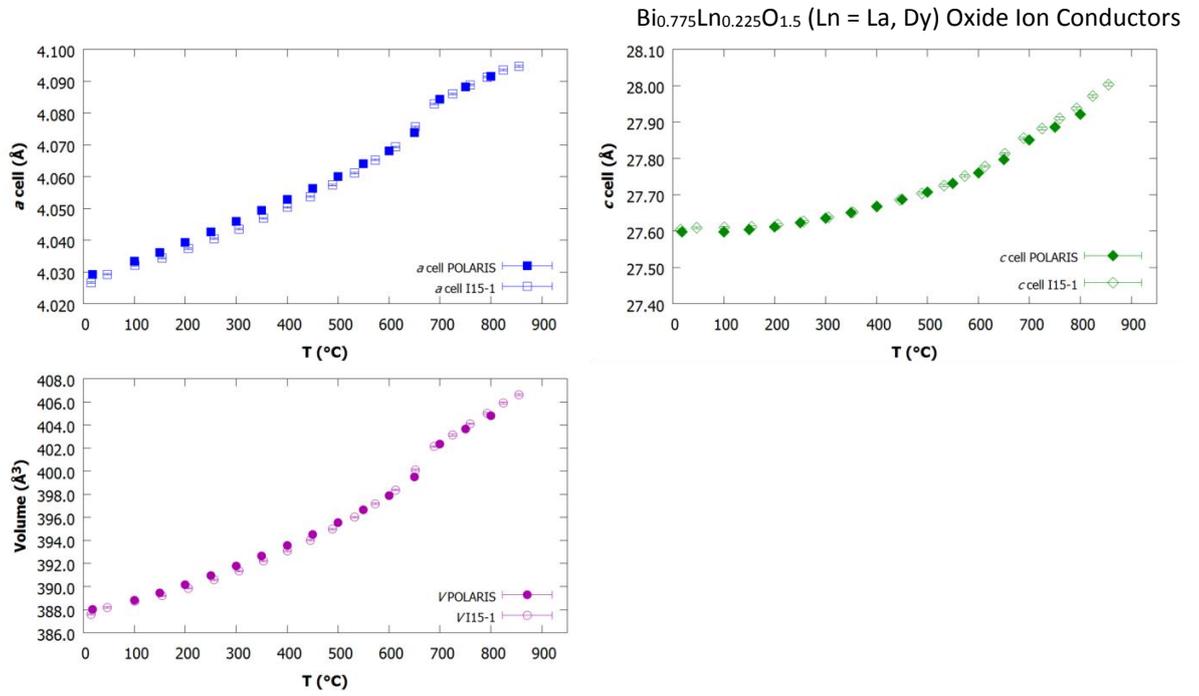
**Figure 7.5** – The thermal evolution of the cell parameters and cell volume of Bi$_{0.775}$La$_{0.225}$O$_{1.5}$ obtained from POLARIS and I15-1 data.

The thermal expansion coefficient of the *a* cell parameter over the temperature range of 293 – 923 K (20 – 650 °C) can be approximately represented by the equation:

$$a(T) = a_0[1 + 1.219 \times 10^{-5}T + 7.916 \times 10^{-9}T^2] \qquad (7.3)$$

With $a_0$ = 4.02927(4) Å. The thermal expansion coefficient over the temperature range of 973 – 1073 K (700 – 800 °C) is $\alpha_a$ = 18(1) × 10$^{-6}$ K$^{-1}$. The *c* cell parameter follows non-linear thermal expansion over the temperature range of 293 – 923 K that can be approximately represented by the equation:

$$c(T) = c_0[1 - 3.110 \times 10^{-7}T + 1.822 \times 10^{-8}T^2] \qquad (7.4)$$

With $c_0$ = 27.5975(6) Å. The thermal expansion coefficient over the temperature range of 973 – 1073 K is $\alpha_c$ = 25.52(2) × 10$^{-6}$ K$^{-1}$. The thermal expansion of the volume over the temperature range of 293 – 923 K can be approximated by the equation:

$$V(T) = V_0[1 + 2.382 \times 10^{-5}T + 3.506 \times 10^{-8}T^2] \qquad (7.5)$$

With $V_0$ = 388.02(1) Å$^3$. The thermal expansion coefficient over the temperature range of 973 – 1073 K is $\alpha_V$ = 63.3(2) K$^{-1}$. The trend for the sudden increase in both cell parameters not accounted for by thermal expansion alone was observed previously in the literature.[21]
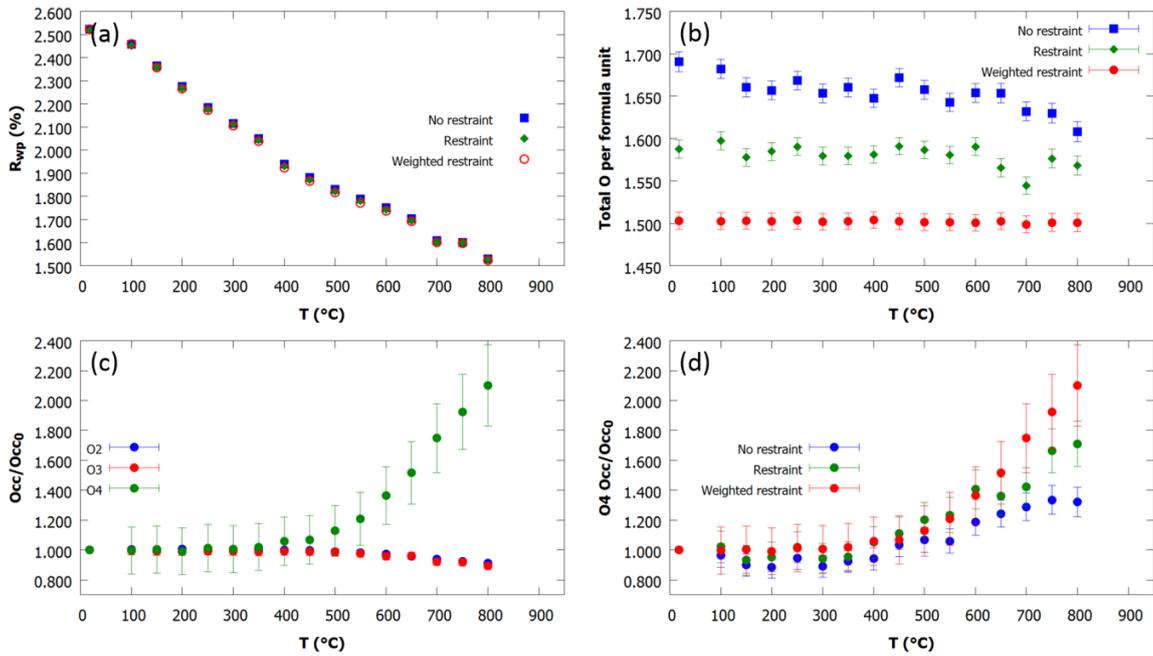
**Figure 7.6 –** The thermal evolution of parameters of Bi$_{0.775}$La$_{0.225}$O$_{1.5}$ (a) R$_{wp}$ of unrestrained, restrained, and weighted restrained from bank 5; (b) total O content per formula unit in the three models; (c) the Occ/Occ$_0$ ratio of the O2, O3 and O4 occupancies in the restrained model with increased weighting; (d) O4 Occ/Occ$_0$ ratio obtained in all three models.

In addition to the cell parameters, analysis of the variable temperature data was performed using three different models: 1) refining the O2, O3 and O4 occupancies freely; 2) refining the occupancies with a weak restraint that the total O content is 1.5 per formula unit; and 3) increasing the weighting on that restraint to force the O content to 1.5 per formula unit. Figure 7.6 presents the results of this analysis. Figure 7.6a shows that the R$_{wp}$ is essentially the same in all models at all temperatures despite the fact that Figure 7.6b shows that the total O per formula unit is quite different between the three models. This agrees with the room temperature refinements and shows that there is not enough sensitivity to determine the exact oxygen content. As there is no reason to believe that there is an excess of 1.5 O per formula unit, the weighted restrained model is taken as the best model and is examined further. As the absolute value of the O4 fractional occupancy is small compared to the fractional occupancies of O2 and O3, in order to compare the changes in occupancies, the ratio of the occupancy at temperature $T$ (Occ) to the occupancy at temperature $T_0$ ( Occ$_0$; $T_0$ = 18 °C) was plotted and is shown in Figure 7.6c–d. Figure 7.6c shows that in the weighted restrained model, the occupancy of the O2 and O3 sites is reduced, whilst the occupancy of the O4 site begins to increase at ~650 °C, which is the same temperature that the cell parameters increase beyond normal thermal expansion (Figure 7.5). This phase transition has been attributed to an increase to the interslab O4 oxide ions previously.[24] Whilst Figure 7.6d shows that the magnitude of the increase in O4 might be exaggerated by the restraint that was applied, the O4 occupancy increases in all three models.

The results from the variable temperature analysis using data obtained from the I11 beamline were unusual. Figure 7.7 shows the surface plot of the raw data obtained in this experiment. At ~695 °C, peaks from an unaccounted for phase begin to form and at ~874 °C it is the major phase, revealed by the sharp peaks that form at $2\theta \approx$ 11.2, 12.5, 17.2, 18.4, 22.5 and 23.5°. It is unknown why this phase formed during the I11 experiment, but not during the POLARIS or I15-1 experiments. It is possible that the small amount of sample in the I11 experiment facilitated a reaction, or that the reaction was with the quartz capillary.

Figure 7.8 shows the thermal evolution of the cell parameters, which do not follow the same behaviour as seen in POLARIS and I15-1 (Figure 7.5). It is unknown why the thermal evolution from the I11 data set is different from the I15-1 and POLARIS data sets, as the same batch of sample was used in all three experiments.
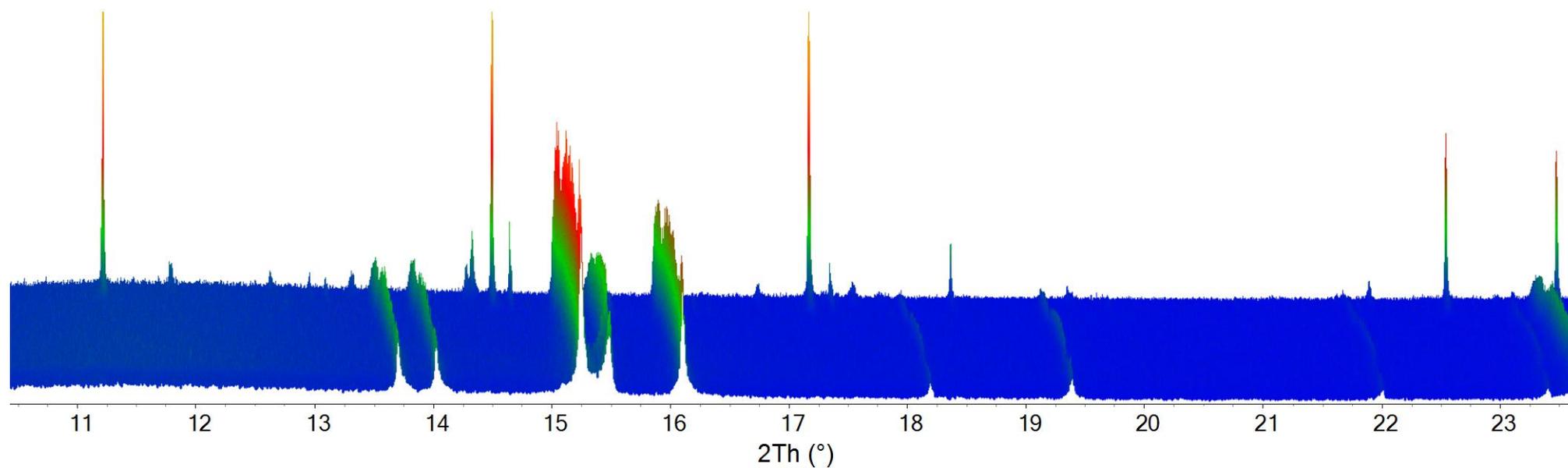
**Figure 7.7 –** Surface plot of the raw synchrotron powder X-ray diffraction data obtained for Bi$_{0.775}$La$_{0.225}$O$_{1.5}$ from 18 °C (front) to 909 °C (back). The colours of blue – green – red represent the relative intensities.
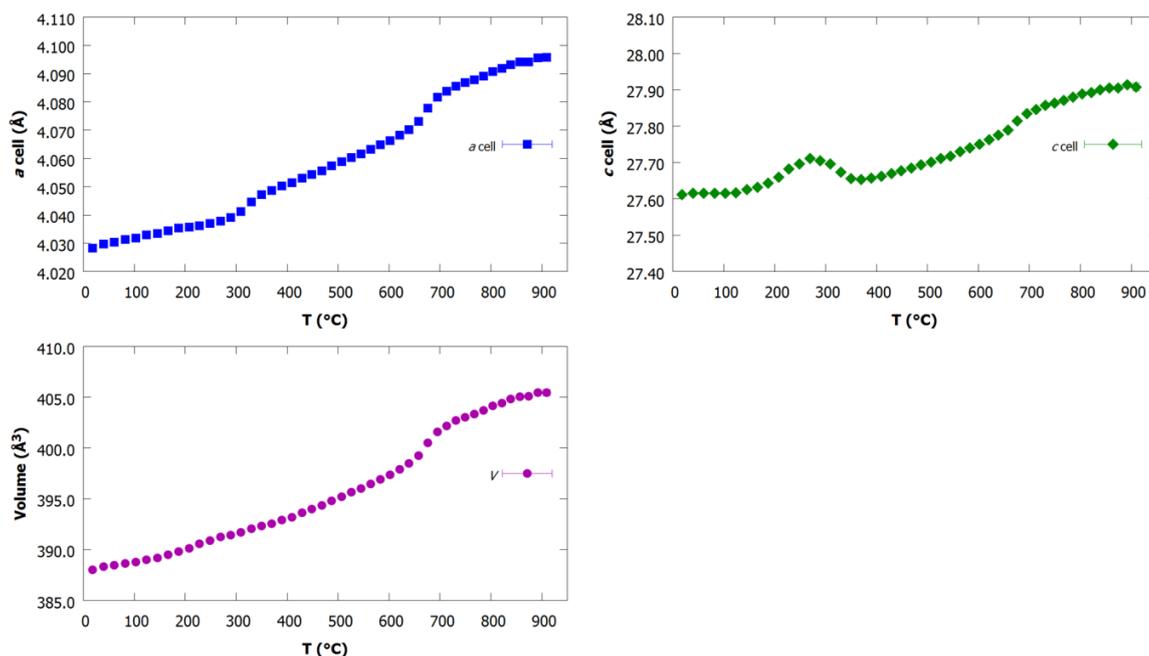
**Figure 7.8 –** The thermal evolution of cell parameters and cell volume of Bi$_{0.775}$La$_{0.225}$O$_{1.5}$ refined againstI11 data.

### 7.3.3.2 Bi$_{0.775}$Dy$_{0.225}$O$_{1.5}$

Analysis of the variable temperature data was performed on Bi$_{0.775}$Dy$_{0.225}$O$_{1.5}$. This sample undergoes the $\beta_2 \rightarrow \delta$-Bi$_2$O$_3$-type transition. In order to model this, the cubic phase was included as a second phase throughout all of the refinements. In addition, the O2, O3 and O4 occupancies of the $\beta_2$ phase were fixed during this analysis. Figure 7.9 shows the results of the variable temperature refinement using POLARIS and I15-1.

The POLARIS and I15-1 results agree well with each other. Figure 7.9a shows that both the rhombohedral and cubic phases show essentially linear thermal expansion whilst they are present. Figure 7.9d shows that only the rhombohedral phase is present until $T \approx 725$ °C, at which point both the cubic and the rhombohedral phases exist simultaneously, where the cubic phase accounts for ~70% of the mass of the sample. This indicates that a first order phase transition occurs. The volume per formula unit (Figure 7.9c) increases sharply when the cubic phase forms.
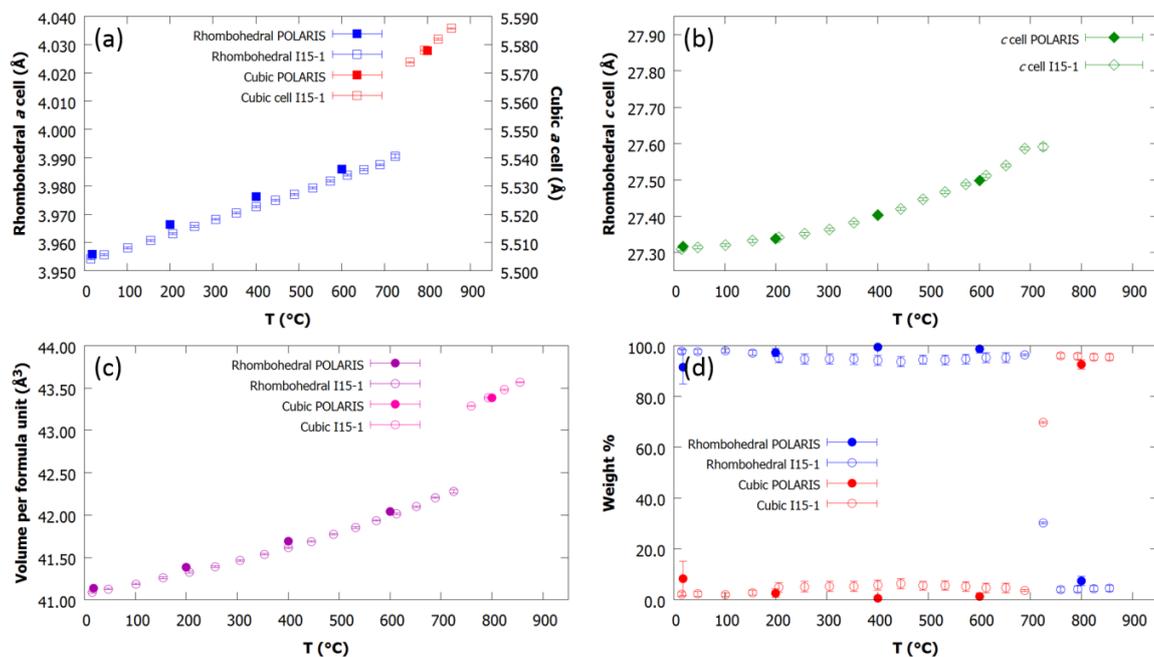
**Figure 7.9 –** The thermal evolution of the (a) *a* cell parameters, (b) rhombohedral *c* cell parameter, (c) unit cell volume per formula unit and (e) weight percentages of the rhombohedral and cubic phases of Bi$_{0.775}$Dy$_{0.225}$O$_{1.5}$.

The results from the I11 variable temperature analysis were similar to those obtained in Bi$_{0.775}$La$_{0.225}$O$_{1.5}$. Peaks that are not accounted by $\delta$–Bi$_{0.775}$Dy$_{0.225}$O$_{1.5}$ begin to form at $T \approx 713$ °C and at ~804 °C, this unaccounted for phase appears to be the major phase. This phase is likely related to the phase that formed with Bi$_{0.775}$La$_{0.225}$O$_{1.5}$, as the peaks appear at similar $2\theta$ values. Figure 7.10 shows the observed patterns of Bi$_{0.775}$La$_{0.225}$O$_{1.5}$ and Bi$_{0.775}$Dy$_{0.225}$O$_{1.5}$ at ~909 °C.
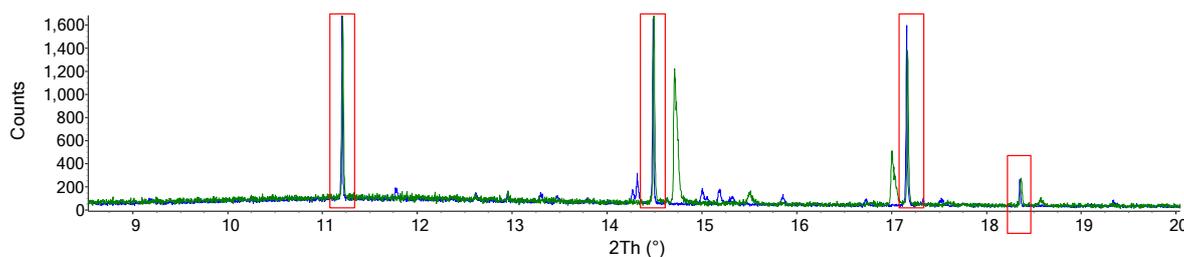


**Figure 7.10 –** The observed patterns of Bi$_{0.775}$La$_{0.225}$O$_{1.5}$ (blue curve) and Bi$_{0.775}$Dy$_{0.225}$O$_{1.5}$ (green curve) at 909 °C with normalised intensities. The red boxes highlight the peaks with very similar $2\theta$ values.

### 7.3.4 Stacking fault investigations in Bi$_{0.775}$La$_{0.225}$O$_{1.5}$

As discussed in Section 7.3.2.1, the calculated pattern of Bi$_{0.775}$La$_{0.225}$O$_{1.5}$ did not match the intensities of peaks with *hkl* values of (0 0 *l*) or those with high *l* values (Figure 7.3c). To try to explain these discrepancies, stacking fault modelling was applied. $\beta_2$-Bi$_{0.775}$La$_{0.225}$O$_{1.5}$ has a layered structure, where oxide ions can potentially populate the space between the slabs (see Figure 7.2), so it is not unreasonable that stacking faults could be present. The individual cationic layers stack both hexagonally (*h*) and cubically (*c*) with (*hhc*)$_3$ stacking. As a result of this (*hhc*) stacking, if the

layers in Slab 1 stack as (*abc*), Slab 2 will stack as (*bca*), and Slab 3 will stack as (*cab*). If the whole slab is treated as an individual layer, the stacking is cubic: the first layer in Slab 1 is *a*, whilst the first layer is Slab 2 is *b* and the first layer in Slab 3 is *c*. We will denote the slab layering as (*xyz*). This is illustrated in Figure 7.11.
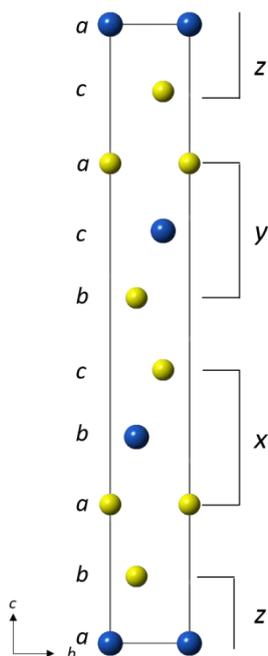


**Figure 7.11** – The layering of the Bi$^{3+}$/La$^{3+}$ cations in a unit cell of Bi$_{0.775}$La$_{0.225}$O$_{1.5}$, where *abc* describes the individual cationic layers and *xyz* describes the stacking of the slabs.

In order to model the stacking faults, three models were used. In all models, the slabs of Figure 7.2 were treated as the layers that would exhibit the stacking fault as opposed to modelling stacking of individual atom layers. In model **1**, the stacking produces a cubic *xyz* layering with a probability of *P*, but has a chance to change to hexagonal *xyx* layering with a probability of $(1 - P)$ and vice versa. This is analogous to the type of stacking faults found in diamond.[33] In model **2**, the layers were stacked with a constant height, $h_1$, between slabs as observed in the average structure with a probability of *P*, but they could also stack with a shorter distance of $h_2$ with a probability of $(1 - P)$. Once a layer stacks with a distance of $h_2$, there is a probability of *P* for the next slab to stack with distance $h_1$. Model **3** is similar to model **2**, but once the fault occurs, it continues to stack with a distance of $h_2$ with a probability of *P* until it stacks with a distance of $h_1$ (probability of $1 - P$). These three models are illustrated in Figure 7.12. The input files are in Appendix C.
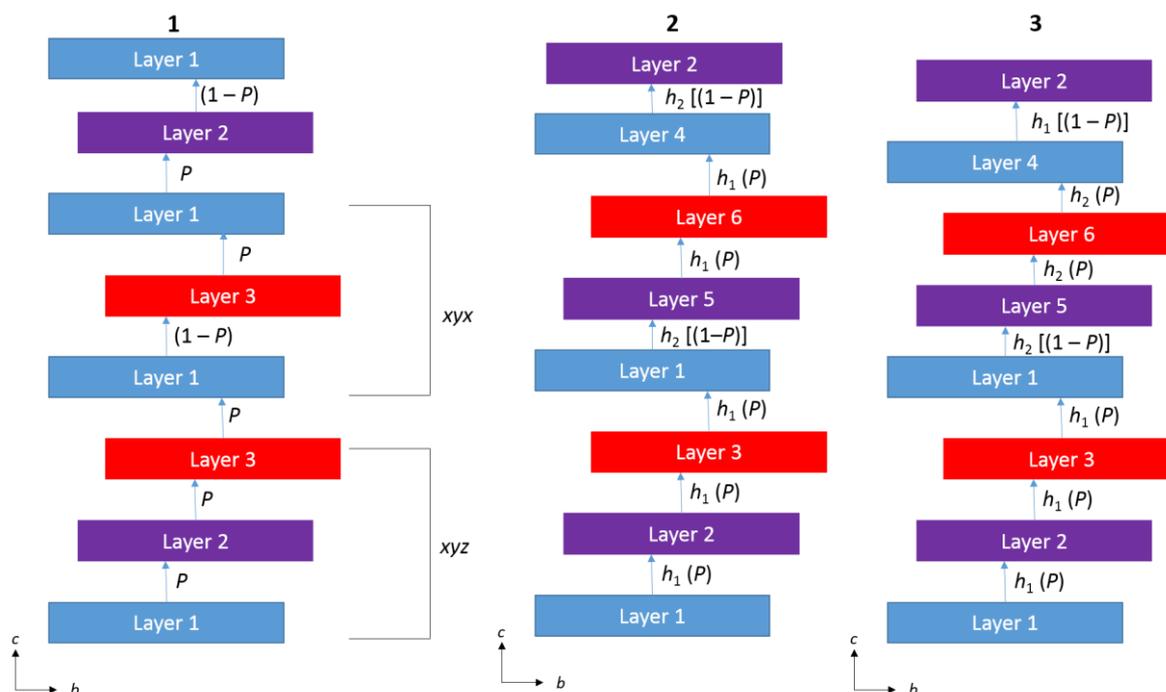
**Figure 7.12** – Illustration of the three models employed for stacking faults of Bi$_{0.775}$La$_{0.225}$O$_{1.5}$, where each layer corresponds to a slab as shown in Figure 7.2. The blue, purple and red colours indicate which relative position a slab is in, *i.e.* *x*, *y* or *z*. In models **2** and **3**, the layers are separated by distances $h_1$ and $h_2$. The probability of a 'normal' stacking is *P* and the probability of a fault occurring is (1 − *P*) in all three models.

Models **2** and **3** were introduced as the presence of the O4 oxide ions in the interslab space could increase the distance between slabs. This would lead to subtle changes in the *c* cell, which could be why the (0 0 *l*) reflections were poorly fitted. The stacking faults were modelled using TOPAS version 6.[34] In each case the diffraction was simulated by stacking $N_v$ layers to produce a "sequence". The scattering from $N_{str}$ sequences were then averaged. The $N_v$ and $N_{str}$ values used were as follows: in model **1**, $N_v$ = 333, $N_{str}$ = 300; in model **2**, $N_v$ = 684, $N_{str}$ = 144; in model **3**, $N_v$ = 432, $N_{str}$ = 432. The refinements were performed with a range of *P* values successively. Figure 7.13 shows the $R_{wp}$ values obtained from all three models with various probabilities of a fault occurring. In all models, a range of 7 ≤ 2$\theta$ ≤ 30° was utilised.

Model **1** (Figure 7.12a) shows a linear increase in the R$_{wp}$ as the probability of a fault occurring increases. Even a 5% chance for a fault occurring results in a fit with R$_{wp}$ ≈ 18%. This conclusively shows that there is a low number of hexagonal/cubic slab stacking faults in this sample. For models **2** and **3** (Figure 7.13b and 7.13c respectively), the distance between each stack centre when no fault occurs, $h_1$, is 1/3 of the *c* cell. The distance between a stack when there is a fault, $h_2$, was determined by refining models with (1 − *P*) = 0.02 with multiple values for the difference between $h_1$ and $h_2$, Δ*h*, which was determined to be 0.007 Å. This difference was used in the refinements presented in Figure 7.13.
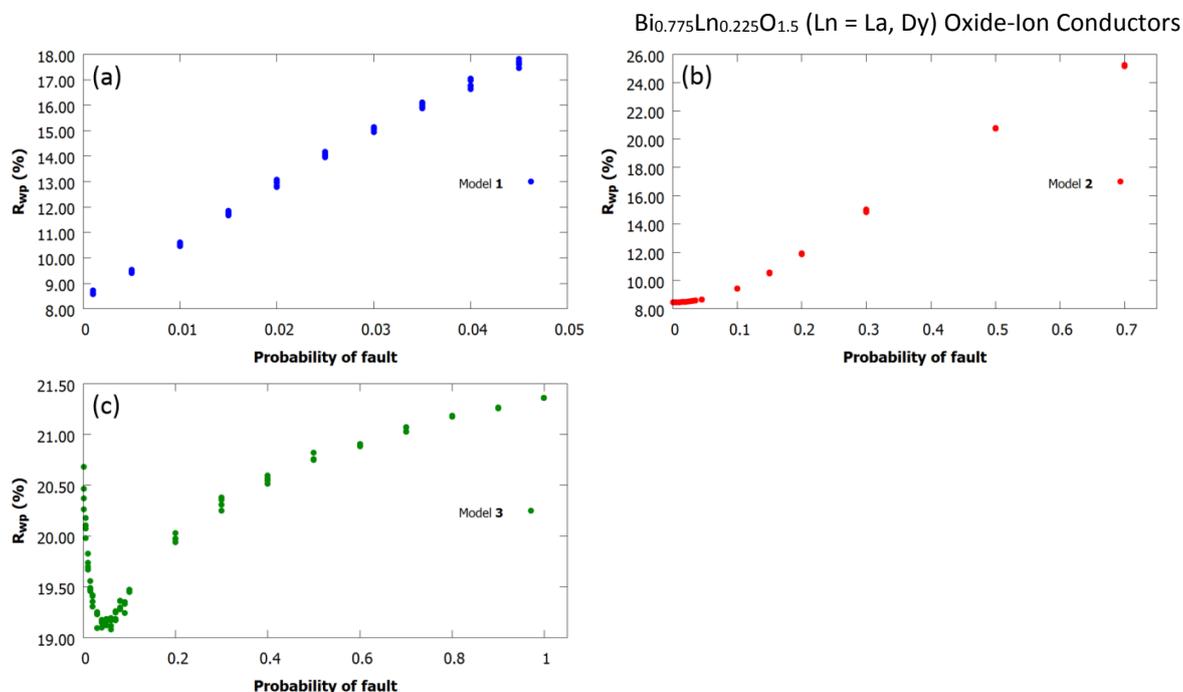
**Figure 7.13** – The R$_{wp}$ obtained from refinements as a function of the probability of a stacking fault occurring of (a) model **1**; (b) model **2**; (c) model **3**.

In model **2**, the R$_{wp}$ again increases with the probability of the fault occurring. Therefore, this stacking fault does not occur in this sample. The R$_{wp}$ found for model **3**, also increases for high probabilities of the fault occurring, but initially it decreases, reaching a minimum at (1–$P$) = 0.05. It is unknown why the initial R$_{wp}$ of 8.7% was not obtained in this model. It is clear, however, that model **3** does not represent the stacking faults, if there are any, in Bi$_{0.775}$La$_{0.225}$O$_{1.5}$.

All three models failed to improve the fits to the data. There is still a possibility that stacking faults exist, but if present, they do not appear to follow the models tested here.

### 7.3.5 Local structure analysis – small box PDF refinements

Small box PDF analysis was performed using the average structure obtained for Bi$_{0.775}$La$_{0.225}$O$_{1.5}$ and the neutron total scattering data. As the O4 sites create false short O–O distances when partial occupancy is not accounted for, a $P1$ 2 × 1 × 1 supercell was created where the total oxygen content per formula unit was maintained, but any atoms that would create unphysical distances were removed. As the neutron scattering lengths of La and Bi are similar, to allow a small supercell the M1 sites were set to 100% La, which results in a compound with stoichiometry of Bi$_{0.667}$La$_{0.333}$O$_{1.5}$. The O2, O3 and O4 site occupancies were also appropriately adjusted. The numbers of each atom (and relative occupancies) are presented in Table 7.8. The cell parameters (with $a$ = 2$b$ as a constraint) and ADPs (equated for each atom type) were refined, but the coordinates remained fixed. The resultant fit (Figure 7.14a) shows that the average structural model is inadequate to fit the local structure at $r \leq 10$ Å. There seems to be a local ordering of La/Bi–O distances (2.0 $\leq r \leq$ 3.0 Å) that is not seen from the average structure, as the data

contains a sharp peak overlapping with a broader peak, whereas the fit predicts a single broad peak in that region. The coordinates were then allowed to refine. A distance restraint was applied to one Bi–O pair, as when the coordinates were freely refined that single Bi–O pair resulted in a distance of $r \approx 1.6$ Å. Figure 7.14b shows this fit.  We see that allowing the coordinates to refine gives a much better agreement with the experimental data.

**Table 7.8 – Number of atoms and fractional occupancies in the 2 × 1 × 1 supercell of Bi$_{0.667}$La$_{0.333}$O$_{1.5}$.**

| Site label | Number | Occupancy |
|---|---|---|
| La1 | 6 | 1.0 |
| Bi2 | 12 | 1.0 |
| O1 | 12 | 1.0 |
| O2 | 10 | $^5/_6$ |
| O3 | 4 | $^1/_3$ |
| O4 | 1 | $^1/_{36}$ |
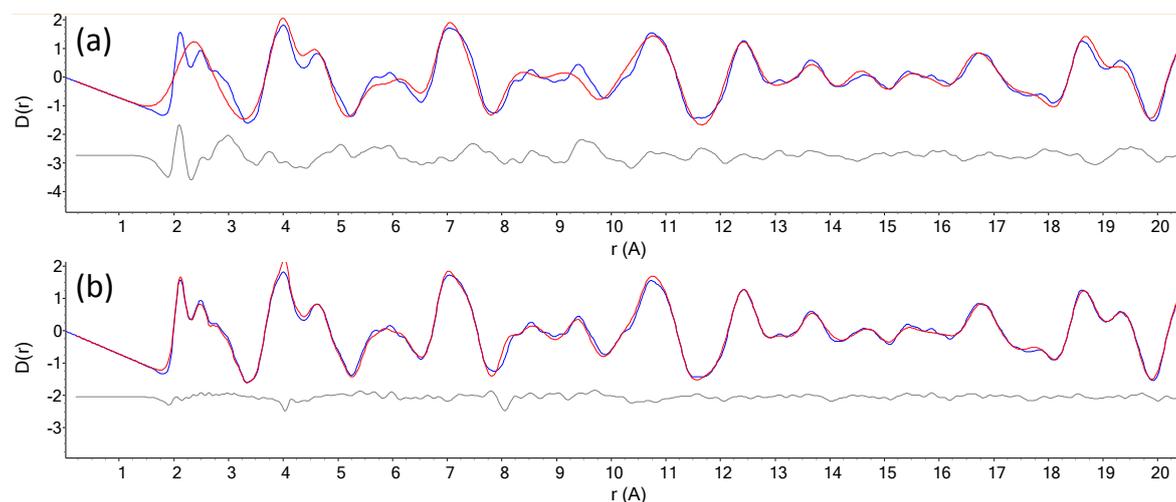


**Figure 7.14 –** Small box PDF refinements of Bi$_{0.667}$La$_{0.333}$O$_{1.5}$ at room temperature with (a) atomic coordinates fixed, R$_{wp}$ = 27.153; (b) atomic coordinates refined, R$_{wp}$ = 14.182%.

Figure 7.15 compares the small box starting configuration to the refined small box configuration. It can be seen that the small box refinement did not drastically distort the structure, suggesting that it is a reasonable approximation of the local structure. In particular, there are no unphysically short O–O distances ($r < 2.2$ Å) in the refined structure. The primary difference between the average structure (Figure 7.15a) and the refined structure (Figure 7.15b) is that the slabs have distorted slightly in order to fit the more ordered local structure. Whilst it is clear that PDF data do contain valuable information on the local structure of these materials, their complexity and the difficulty in obtaining a good fit to the Bragg data suggested that obtaining more information using big box modelling was likely to be unsuccessful.
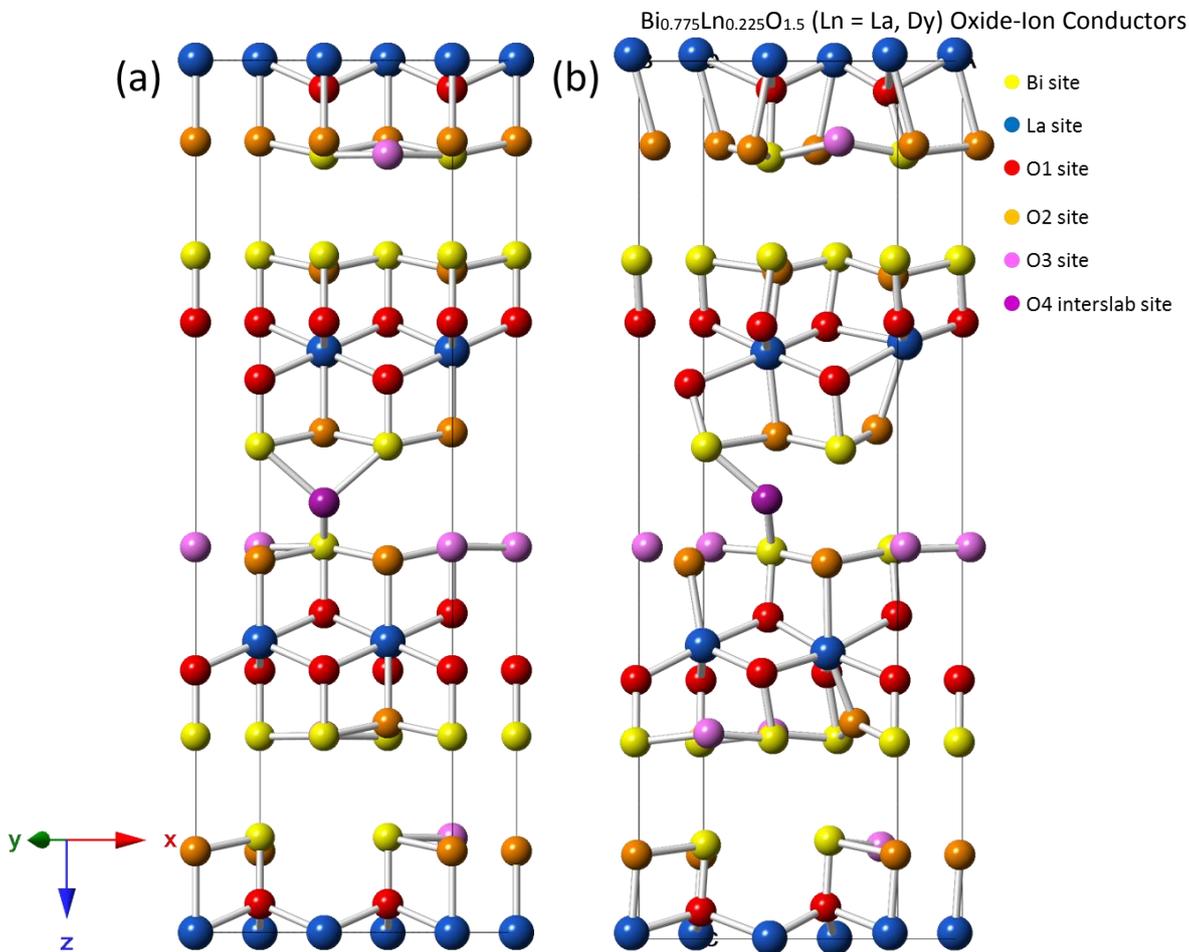
**Figure 7.15** – The 2 × 1 × 1 small box configurations of $Bi_{0.775}La_{0.225}O_{1.5}$ at room temperature. (a) Average structure configuration; (b) refined configuration.

## 7.4 Conclusions and Further Work

From the analysis carried out in this work, the following conclusions can be made:

1. The interslab O4 oxides are likely present in $Bi_{0.775}La_{0.225}O_{1.5}$ and $Bi_{0.775}Dy_{0.225}O_{1.5}$, as their introduction improved the quality of the Rietveld fit.

2. There is a lack of sensitivity to the exact oxygen stoichiometry in the data collected on both samples, as applying a weighted restraint so that the total O content per unit formula = 1.5 resulted in very similar $R_{wp}$ values as freely refining O occupancies.

3. The O2, O3 and O4 sites have large isotropic ADPs when refined independently, indicating a large amount of disorder within these sites. Therefore, a single ADP was used for these three sites.

4. The (0 0 $l$) peaks did not fit well in the data collected on both samples, which is most easily seen in the high-resolution powder synchrotron refinements. This could be a result of stacking faults, but none of the models tested here were able to produce satisfactory fits.

5. There is an apparent increase in the O4 occupancies and a concurrent decrease in the O2 and O3 occupancies at $T$ > 650 °C in Bi$_{0.775}$La$_{0.225}$O$_{1.5}$, though the exact magnitude of these changes is not clear due to the lack of sensitivity to the overall oxygen content.

6. Bi$_{0.775}$Dy$_{0.225}$O$_{1.5}$ undergoes the $\beta_2 \rightarrow \delta$-Bi$_2$O$_3$-type transition at ~725 °C as previously reported,[21] where there is also a sharp increase in the unit cell volume per formula unit.

7. The small box PDF refinement revealed that the average structure model is insufficient to describe the local structure of Bi$_{0.775}$La$_{0.225}$O$_{1.5}$. Instead, the slabs show a distortion on the local scale.

8. Whilst weak evidence for redistribution of O atoms in the $\beta_2$ structure relative to $\beta_1$ has been obtained, more work and other analytical/theoretical methods will be needed to fully understand this material.

Further investigation into stacking faults is warranted. It is possible that a kind of stacking fault not employed here is the result for the discrepancy between the fit and the observed data. Furthermore, big box modelling could be attempted in order to determine the nature of the local structure, but the complexity of the long range structure would cause complications.

## 7.5 References

1. Jacobson, A. J., Materials for solid oxide fuel cells. *Chemistry of Materials* **2009,** *22* (3), 660-674.
2. Orera, A.; Slater, P. R., New Chemical Systems for Solid Oxide Fuel Cells. *Chemistry of Materials* **2009,** *22* (3), 675-690.
3. Takahashi, T.; Iwahara, H.; Arao, T., High oxide ion conduction in sintered oxides of the system Bi$_2$O$_3$-Y$_2$O$_3$. *Journal of Applied Electrochemistry* **1975,** *5* (3), 187-195.
4. Payne, J. L.; Farrell, J. D.; Linsell, A. M.; Johnson, M. R.; Evans, I. R., The mechanism of oxide ion conductivity in bismuth rhenium oxide, Bi$_{28}$Re$_2$O$_{49}$. *Solid State Ionics* **2013,** *244*, 35-39.
5. Watanabe, A.; Kikuchi, T., Cubic-hexagonal transformation of yttria-stabilized δ-bismuth sesquioxide, Bi$_{2-2x}$Y$_{2x}$O$_3$ ($x$ = 0.215 − 0.235). *Solid State Ionics* **1986,** *21* (4), 287-291.
6. Takahashi, T.; Iwahara, H.; Nagai, Y., High oxide ion conduction in sintered Bi$_2$O$_3$ containing SrO, CaO or La$_2$O$_3$. *Journal of Applied Electrochemistry* **1972,** *2* (2), 97-104.
7. Orlova, E. I.; Kharitonova, E. P.; Gorshkov, N. V.; Goffman, V. G.; Voronkova, V. I., Phase formation and electrical properties of Bi$_2$O$_3$-based compounds in the Bi$_2$O$_3$–La$_2$O$_3$–MoO$_3$ system. *Solid State Ionics* **2017,** *302*, 158-164.
8. Shitara, K.; Moriasa, T.; Sumitani, A.; Seko, A.; Hayashi, H.; Koyama, Y.; Huang, R.; Han, D.; Moriwake, H.; Tanaka, I., First-Principles Selection of Solute Elements for Er-Stabilized Bi$_2$O$_3$ Oxide-Ion Conductor with Improved Long-Term Stability at Moderate Temperatures. *Chemistry of Materials* **2017,** *29* (8), 3763-3768.
9. Sanna, S.; Esposito, V.; Andreasen, J. W.; Hjelm, J.; Zhang, W.; Kasama, T.; Simonsen, S. B.; Christensen, M.; Linderoth, S.; Pryds, N., Enhancement of the chemical stability in confined δ-Bi$_2$O$_3$. *Nature Materials* **2015,** *14* (5), 500-504.
10. Wind, J.; Auckett, J. E.; Withers, R. L.; Piltz, R. O.; Maljuk, A.; Ling, C. D., Type II Bi$_{1-x}$W$_x$O$_{1.5 + 1.5x}$: a (3+3)-dimensional commensurate modulation that stabilizes the fast-ion conducting delta phase of bismuth oxide. *Acta Crystallographica Section B: Structural Science Crystal Engineering and Materials* **2015,** *71* (6), 679-687.
11. Wind, J.; Kayser, P.; Zhang, Z.; Radosavljevic Evans, I.; Ling, C. D., Stability and range of the type II Bi$_{1-x}$W$_x$O$_{1.5+1.5x}$ solid solution. *Solid State Ionics* **2017,** *308* (Supplement C), 173-180.
12. Borowska-Centkowska, A.; Leszczynska, M.; Krok, F.; Malys, M.; Wrobel, W.; Hull, S.; Abrahams, I., Local structure and conductivity behaviour in Bi$_7$WO$_{13.5}$. *Journal of Materials Chemistry A* **2018,** *6* (13), 5407-5418.
13. Tate, M. L.; Hack, J.; Kuang, X.; McIntyre, G. J.; Withers, R. L.; Johnson, M. R.; Evans, I. R., Bi$_{1-x}$NbxO$_{1.5+x}$ ($x$=0.0625, 0.12) fast ion conductors: Structures, stability and oxide ion migration pathways. *Journal of Solid State Chemistry* **2015,** *225*, 383-390.
14. Gambino, M.; Giannici, F.; Longo, A.; Di Tommaso, S.; Labat, F.; Martorana, A., Dopant Clusterization and Oxygen Coordination in Ta-Doped Bismuth Oxide: A Structural and Computational Insight into the Mechanism of Anion Conduction. *Journal of Physical Chemistry C* **2015,** *119* (47), 26367-26373.
15. Firman, K.; Tan, K. B.; Khaw, C. C.; Zainal, Z.; Tan, Y. P.; Chen, S. K., Doping mechanisms and electrical properties of bismuth tantalate fluorites. *Journal of Materials Science* **2017,** *52* (17), 10106-10118.

16.      Pandey, J.; Shrivastava, V.; Nagarajan, R., Metastable Bi$_2$Zr$_2$O$_7$ with Pyrochlore-like Structure: Stabilization, Oxygen Ion Conductivity, and Catalytic Properties. *Inorganic Chemistry* **2018,** *57* (21), 13667-13678.

17.      Kuang, X.; Payne, J. L.; Johnson, M. R.; Evans, I. R., Remarkably High Oxide Ion Conductivity at Low Temperature in an Ordered Fluorite-Type Superstructure. *Angewandte Chemie International Edition* **2012,** *51* (3), 690-694.

18.      Mercurio, D.; Champarnaud-Mesjard, J. C.; Frit, B.; Conflant, P.; Boivin, J. C.; Vogt, T., Thermal Evolution of the Crystal Structure of the Rhombohedral Bi0.75Sr0.25O1.375 Phase: A Single Crystal Neutron Diffraction Study. *Journal of Solid State Chemistry* **1994,** *112* (1), 1-8.

19.      Darriet, J.; Launay, J. C.; Zúniga, F. J., Crystal structures of the ionic conductors Bi$_{46}$M$_8$O$_{89}$ (M=P, V) related to the fluorite-type structure. *Journal of Solid State Chemistry* **2005,** *178* (6), 1753-1764.

20.      Mauvy, F.; Launay, J. C.; Darriet, J., Synthesis, crystal structures and ionic conductivities of Bi$_{14}$P$_4$O$_{31}$ and Bi$_{50}$V$_4$O$_{85}$. Two members of the series Bi$_{18-4m}$M$_{4m}$O$_{27+4m}$ (M=P, V) related to the fluorite-type structure. *Journal of Solid State Chemistry* **2005,** *178* (6), 2015-2023.

21.      Drache, M.; Obbade, S.; Wignacourt, J. P.; Conflant, P., Structural and Conductivity Properties of Bi$_{0.775}$Ln$_{0.225}$O$_{1.5}$Oxide Conductors (Ln=La, Pr, Nd, Sm, Eu, Gd, Tb, Dy) with Rhombohedral Bi–Sr–O Type. *Journal of Solid State Chemistry* **1999,** *142* (2), 349-359.

22.      Kotsantonis, S.; Kilner, J. A., Oxygen ion diffusion measurements in Bi$_{0.775}$La$_{0.225}$O$_{1.5}$. *Solid State Ionics* **2011,** *192* (1), 168-171.

23.      Jung, D. W.; Nino, J. C.; Duncan, K. L.; Bishop, S. R.; Wachsman, E. D., Enhanced long-term stability of bismuth oxide-based electrolytes for operation at 500 °C. *Ionics* **2010,** *16* (2), 97-103.

24.      Obbade, S.; Huve, M.; Suard, E.; Drache, M.; Conflant, P., Powder Neutron Diffraction and TEM Investigations of Bi$_{0.775}$Ln$_{0.225}$O$_{1.5}$ Oxide Conductors (Ln=La, Pr, Nd, Sm, Tb, Dy) with Rhombohedral Bi–Sr–O type: Structural Relationships with Monoclinic ε-Bi$_{4.86}$La$_{1.14}$O$_9$ Form. *Journal of Solid State Chemistry* **2002,** *168* (1), 91-99.

25.      Ahi, A.; Mellergard, A.; Eriksson, S. G., Local and average atomic order of ion-conducting Bi$_{0.775}$La$_{0.225}$O$_{1.5}$ studied by neutron scattering and reverse Monte Carlo simulations. *Solid State Ionics* **2006,** *177* (3-4), 289-297.

26.      Obbade, S.; Drache, M.; Conflant, P.; Suard, E., Ab Initio Determination of Bi$_{4.86}$La$_{1.14}$O$_9$ Monoclinic Structure from Powder Neutron Diffraction Data. Characterization of the Related Solid Solution. *Journal of Solid State Chemistry* **2001,** *162* (1), 10-19.

27.      Dove, M. T.; Tucker, M. G.; Keen, D. A., Neutron total scattering method simultaneous determination of long-range and short-range order in disordered materials. *European Journal of Mineralogy* **2002,** *14* (2), 331-348.

28.      Duncan, Z. Synthesis and characterisation of oxides for energy applications: new ionic and mixed conductors. Durham University, Durham University, 2017.

29.      Soper, A. K. *GudrunN and GudrunX*, 5; 2012.

30.      Coelho, A. A.; Chater, P. A.; Kern, A., Fast synthesis and refinement of the atomic pair distribution function. *Journal of Applied Crystallography* **2015,** *48* (3), 869-875.

31.      Coelho, A. *TOPAS Academic Version 6 Computer Software*, 6; Coelho Software: Brisbane, 2016.

32.      Mercurio, D.; Farissi, M. E.; Champarnaud-Mesjard, J. C.; Frit, B.; Conflant, P.; Roult, G.; Vogt, T., Etude structurale par diffraction X sur monocristal et diffraction neutronique sur poudre de l'oxyde mixte Bi$_{0.7}$La$_{0.3}$O$_{1.5}$. *Journal of Solid State Chemistry* **1989,** *80* (1), 133-143.

33.      Treacy, M. M. J.; Newsam, J. M.; Deem, M. W., A general recursion method for calculating diffracted intensities from crystals containing planar faults. *Proceedings of the Royal Society of London. Series A: Mathematical and Physical Sciences* **1991,** *433* (1889), 499-520.

34.      Coelho, A. A.; Evans, J. S. O.; Lewis, J. W., Averaging the intensity of many-layered structures for accurate stacking-fault analysis using Rietveld refinement. *Journal of Applied Crystallography* **2016,** *49* (5), 1740-1749.

# Appendix A

## Supplementary Data for Chapter 4
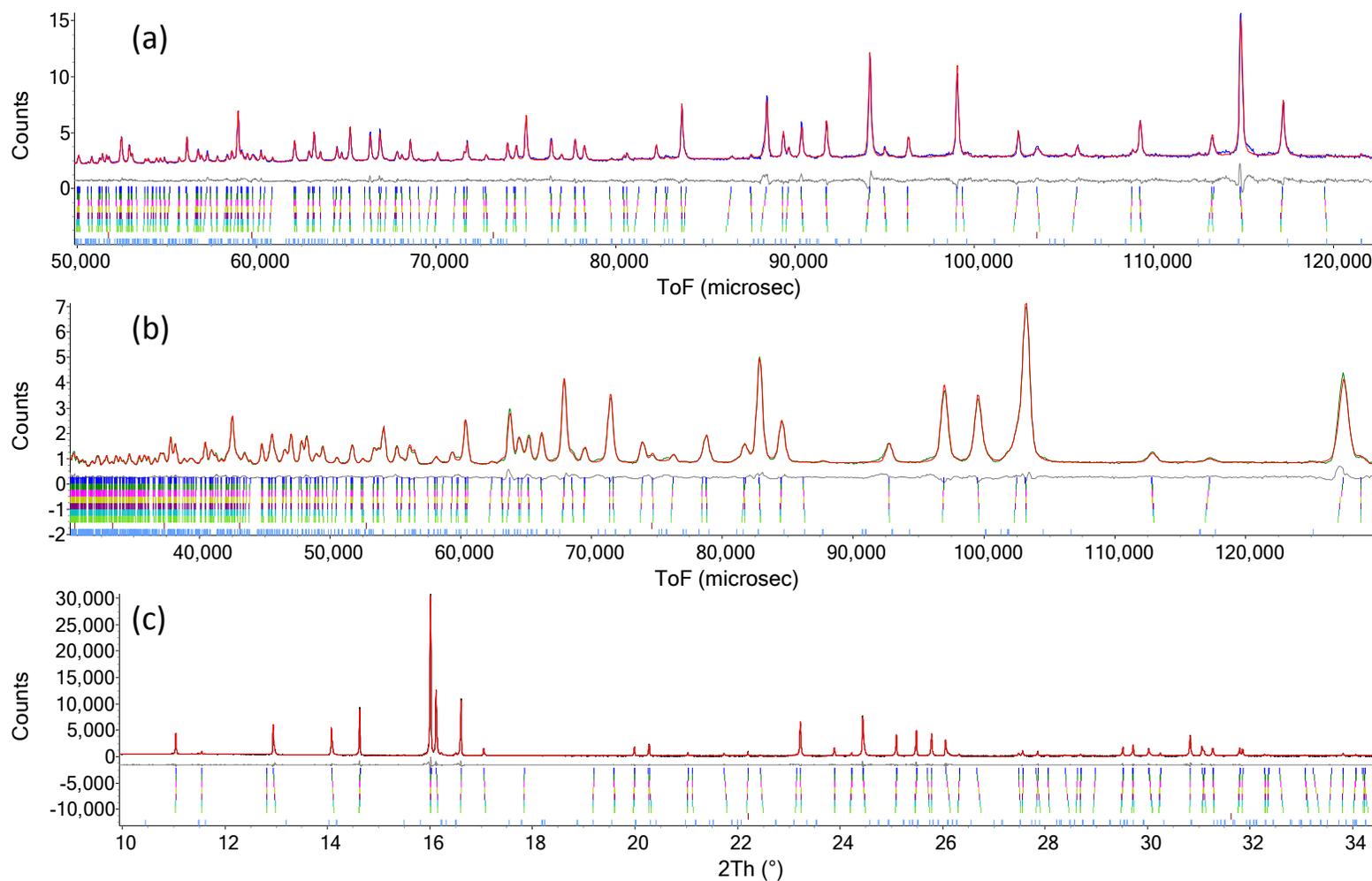
**Figure A.1 –** The combined Rietveld plots for $La_8Sr_2(GeO_4)_6O_2$ at room temperature; (a) HRPD bank 1, $R_{wp}$ = 2.567% and $\chi^2$ = 1.960; (b) HRPD bank 2, $R_{wp}$ = 3.884% and $\chi^2$ = 4.272; (c) I11,

$R_{wp}$ = 8.394%; $\chi^2$ = 1.888.
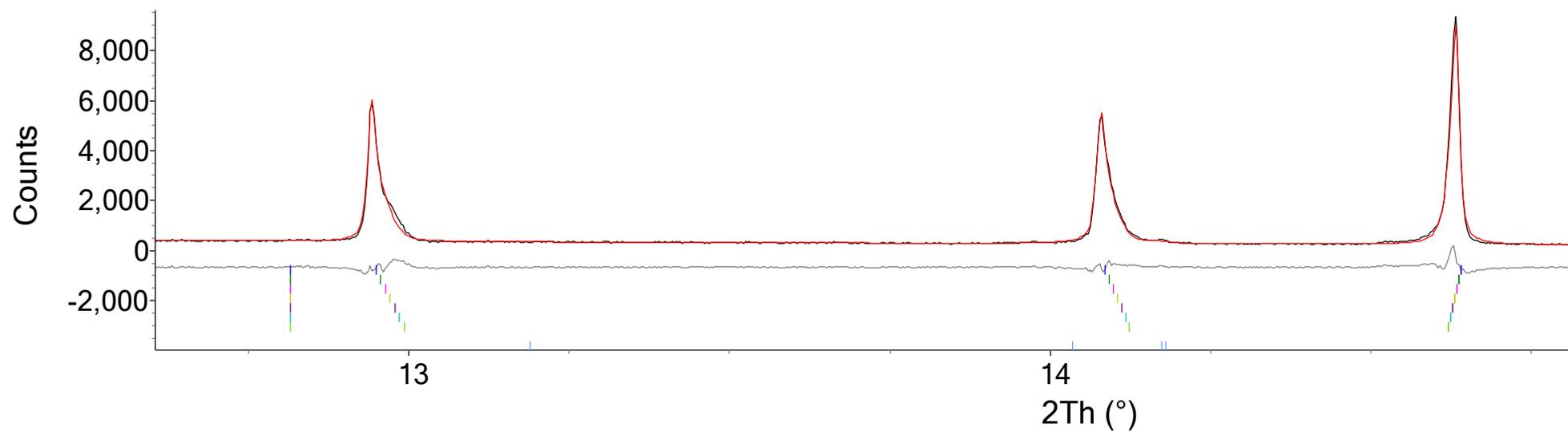
**Figure A.2 –** Rietveld plot for $La_8Sr_2(GeO_4)O_2$ using I11 data, showing the asymmetry of the peaks. The left hand peak is the (002) reflection, where this is particularly noticeable.
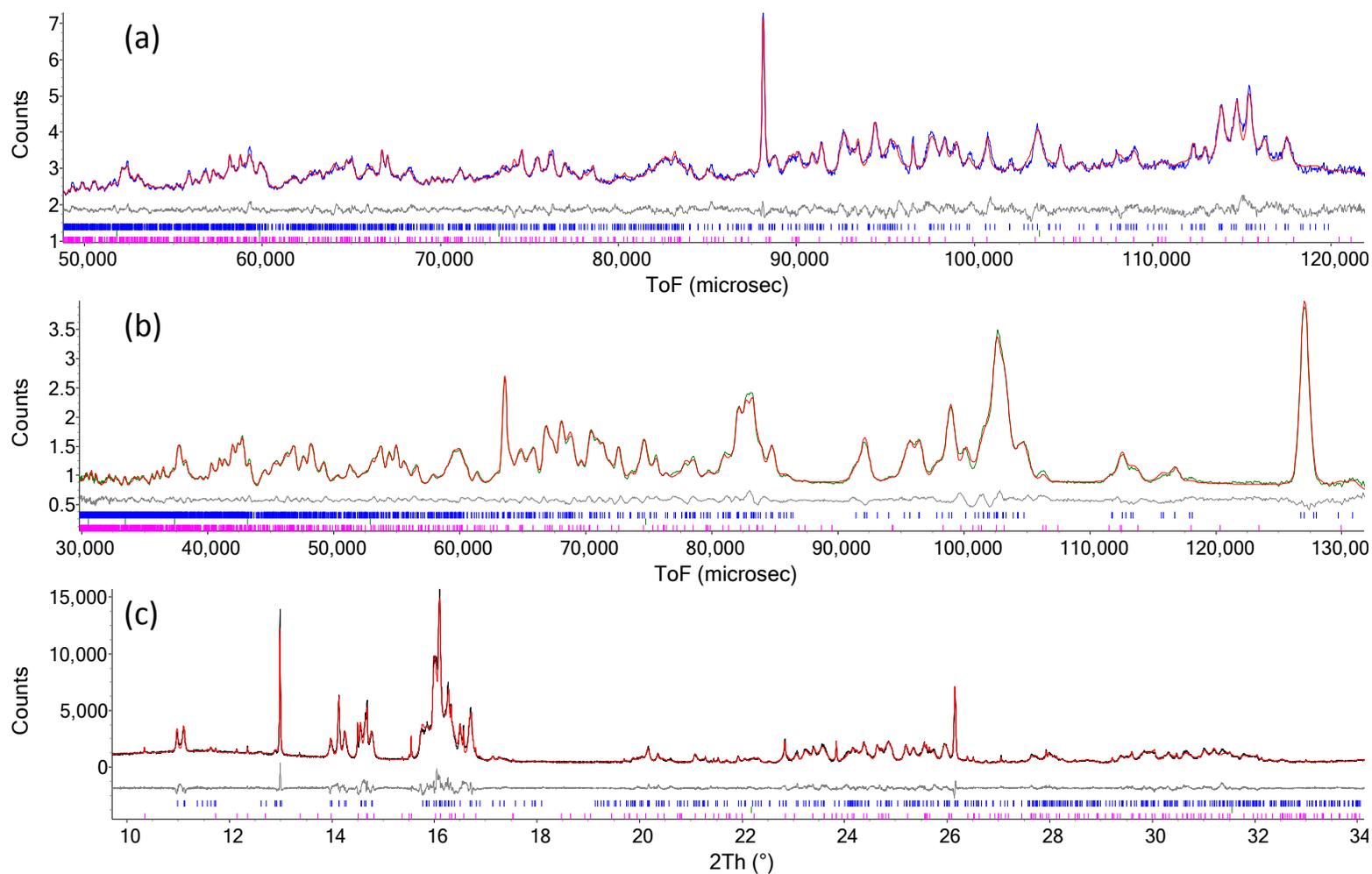
**Figure A.3 –** The combined Rietveld plots of $La_{10}(GeO_4)_6O_3$ from: (a) HRPD bank 1, $R_{wp}$ = 1.973%, $\chi^2$ = 1.839; (b) HRPD bank 2, $R_{wp}$ = 2.273%, $\chi^2$ = 3.509%; (c) I11 , $R_{wp}$ = 7.557%, $\chi^2$ = 2.986.
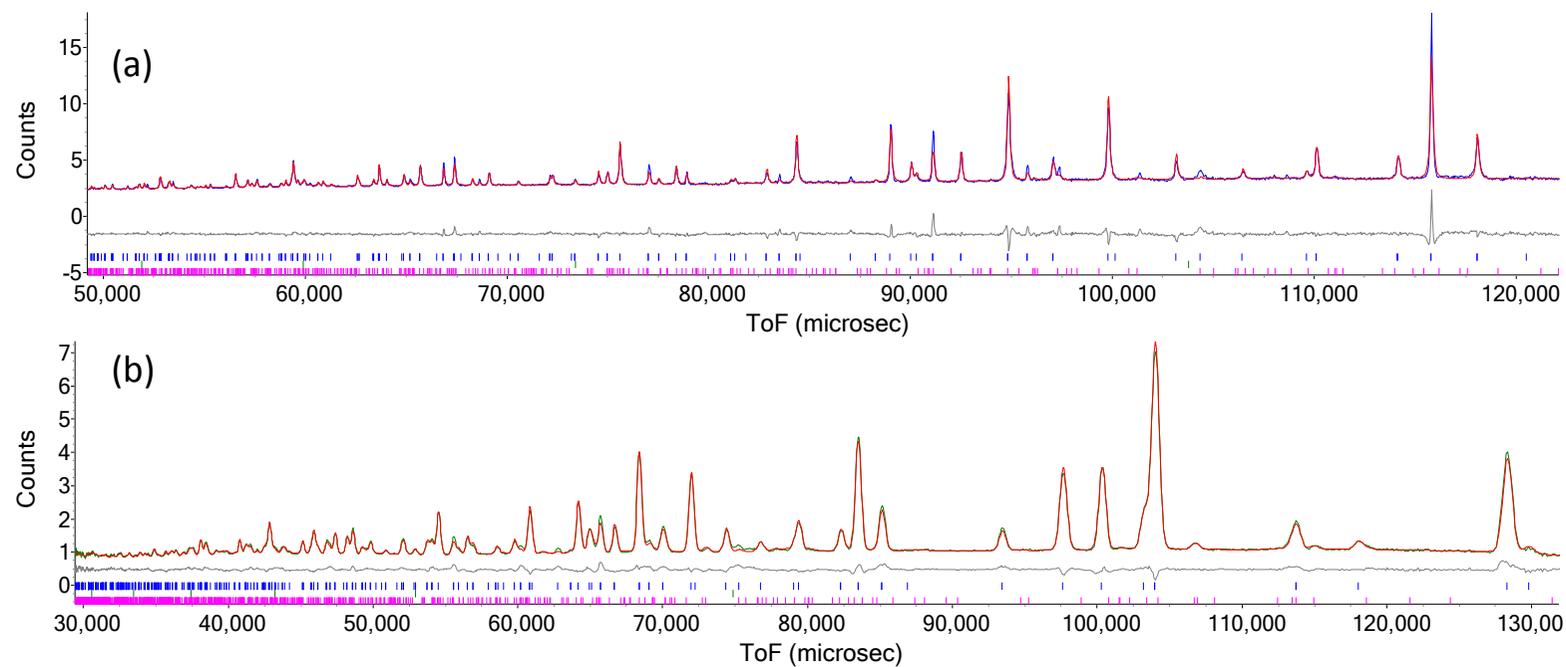
**Figure A.4** – The Rietveld plots of $La_{10}(GeO_4)_6O_3$ at 850 °C using HRPD data. (a) bank 1, $R_{wp}$ = 2.679%, $\chi^2$ = 2.417 ; (b) bank 2, $R_{wp}$ = 3.166%, $\chi^2$ = 4.879.
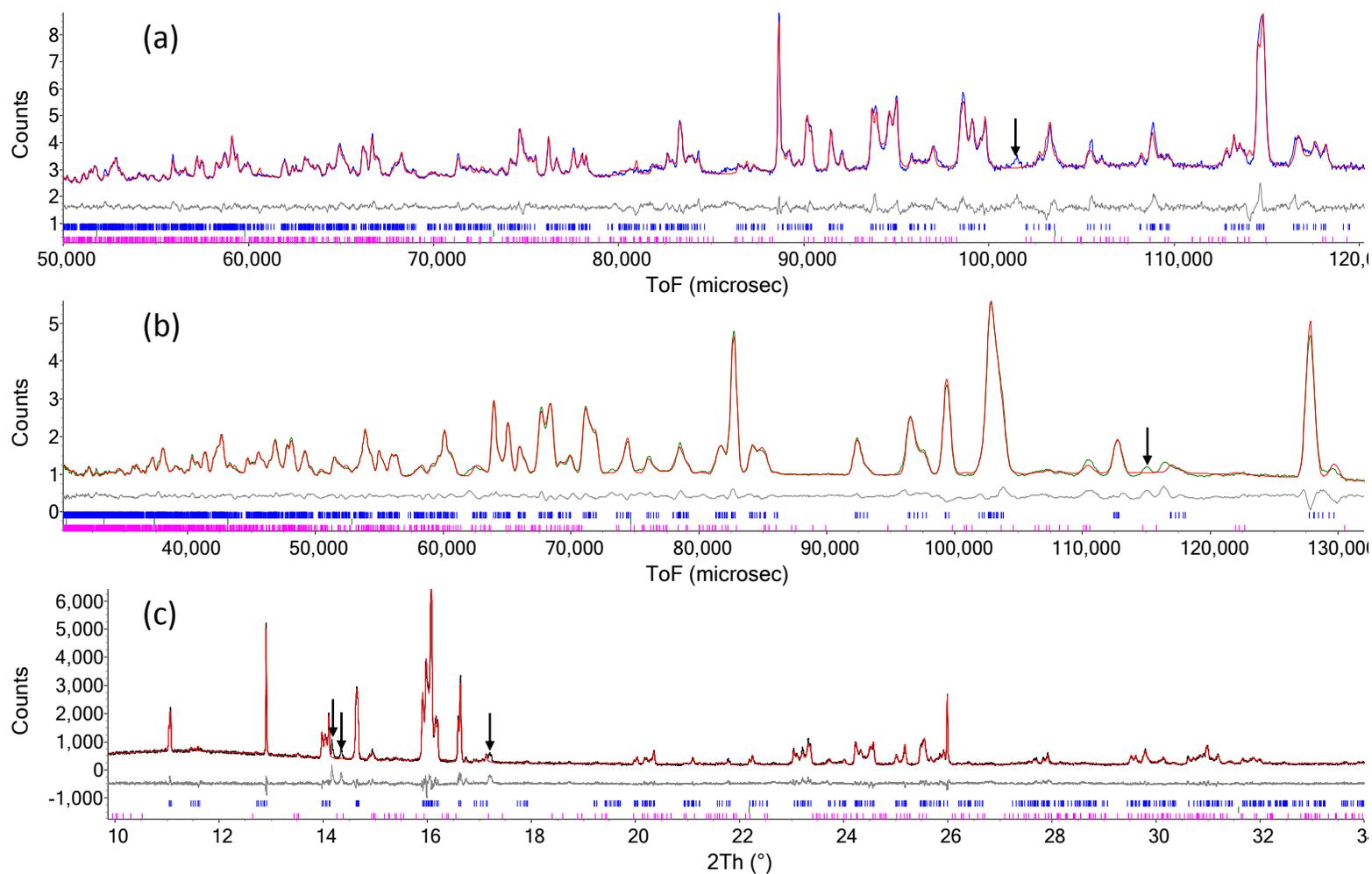
**Figure A.5 –** The combined Rietveld plots of La$_8$Bi$_2$(GeO$_4$)$_6$O$_3$ from: (a) HRPD bank 1, R$_{wp}$ = 2.291%, χ$^2$ = 2.233; (b) HRPD bank 2, R$_{wp}$ = 2.983%, χ$^2$ = 4.808; (c) I11, R$_{wp}$ = 8.407%, χ$^2$ = 1.955.

The black arrows highlight the unaccounted for peaks.
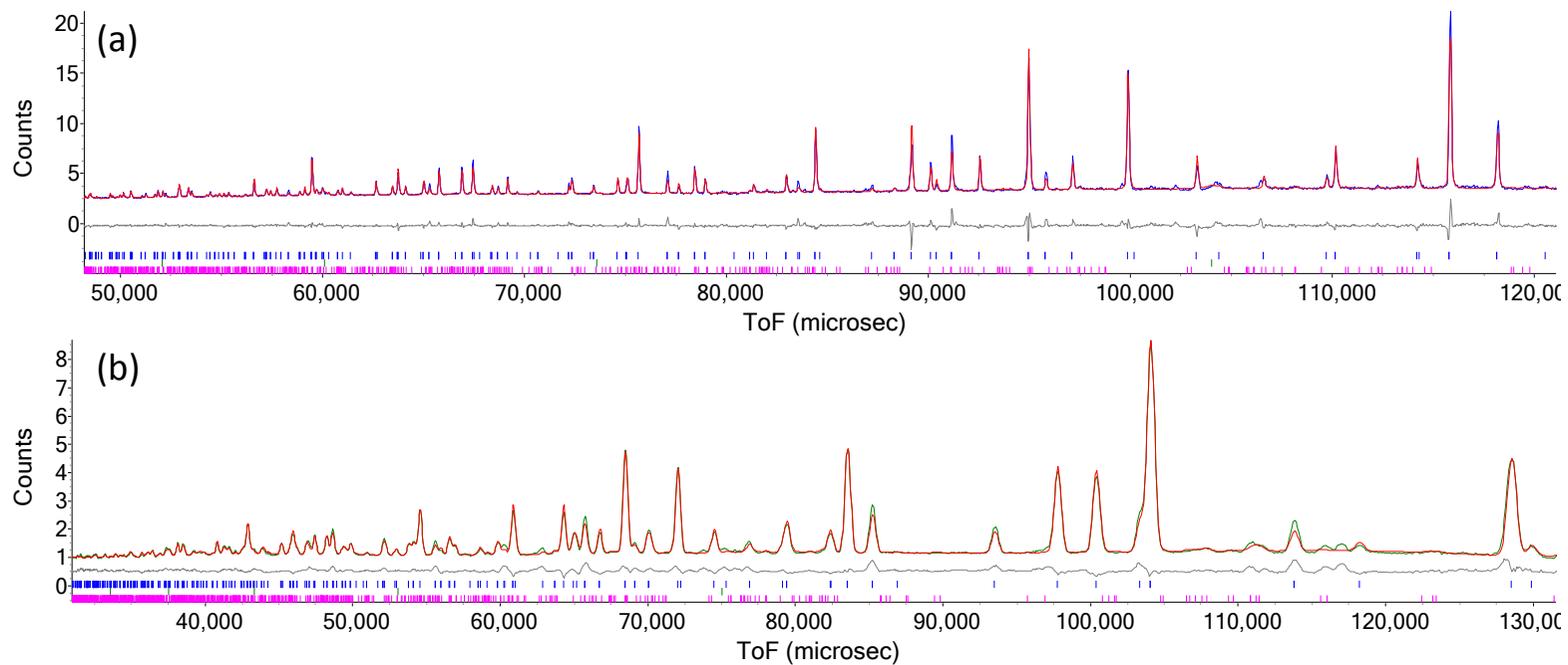
**Figure A.6** – The Rietveld plots of La$_8$Bi$_2$(GeO$_4$)$_6$O$_3$ at 850 °C using HRPD data. (a) Bank 1, R$_{wp}$ = 2.677%, $\chi^2$ = 2.639 ; (b) bank 2, R$_{wp}$ = 3.844%, $\chi^2$ = 6.231.
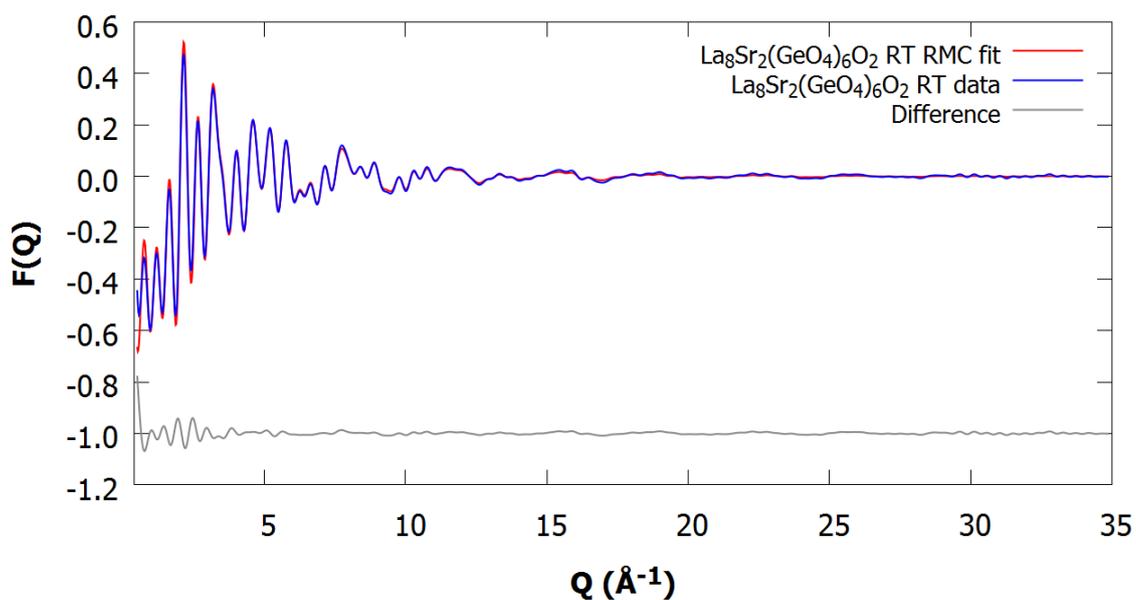
**Figure A.7 –** Representative $F(Q)$ fit of La$_8$Sr$_2$(GeO$_4$)$_6$O$_3$ model **[SC1, P2]** obtained from RMCProfile; $\chi^2_{F(Q)}$ = 0.4278.
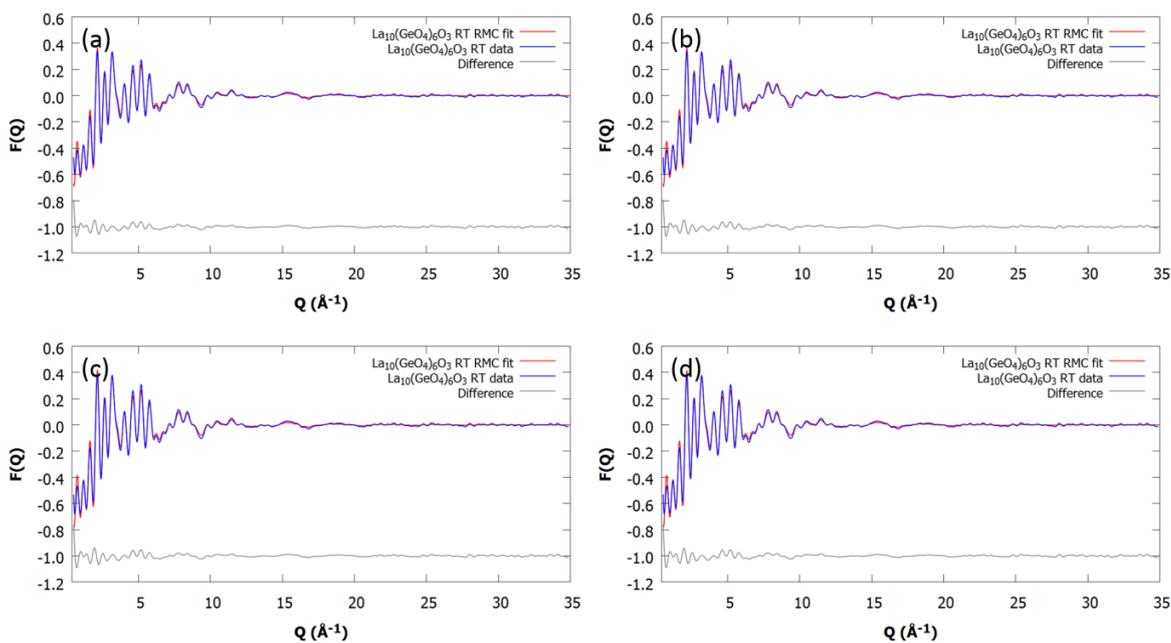


**Figure A.8 –** Representative $F(Q)$ fits of La$_{10}$(GeO$_4$)$_6$O$_3$ at room temperature obtained from the final configurations with the scale fitted. (a) **[SC1, P1]**, $\chi^2_{F(Q)}$ = 0.2947; (b) **[SC2, P1]**, $\chi^2_{F(Q)}$ = 0.2943; (c) **[SC3, P1]**, $\chi^2_{F(Q)}$ = 0.3161; (d) $\chi^2_{F(Q)}$ = 0.3115.
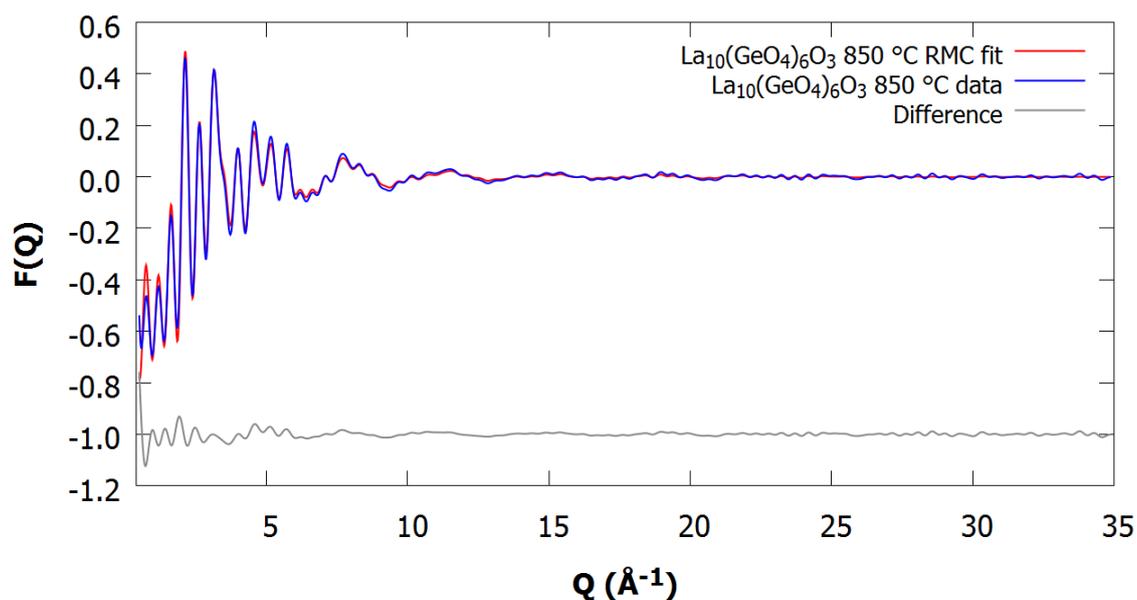
**Figure A.9 –** Representative $F(Q)$ fit of $La_{10}(GeO_4)_6O_3$ at 850 °C model **[SC5, P2]** obtained from the final configuration with the scale fitted; $\chi^2_{F(Q)} = 0.3221$.
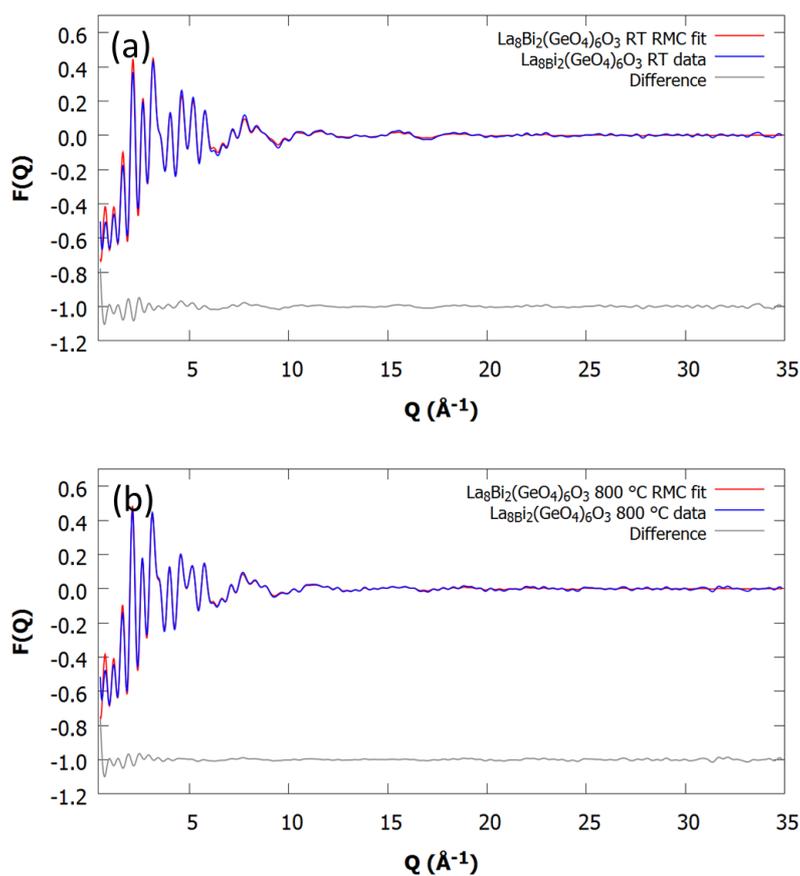


**Figure A.10 –** Representative $F(Q)$ fits of $La_8Bi_2(GeO_4)_6O_3$ obtained from the final configuration with the scale fitted. (a) Room temperature **[SC4, P1]**, $\chi^2_{F(Q)} = 0.3193$; (b) 800 °C **[SC5, P2]**, $\chi^2_{F(Q)} = 0.2645$.
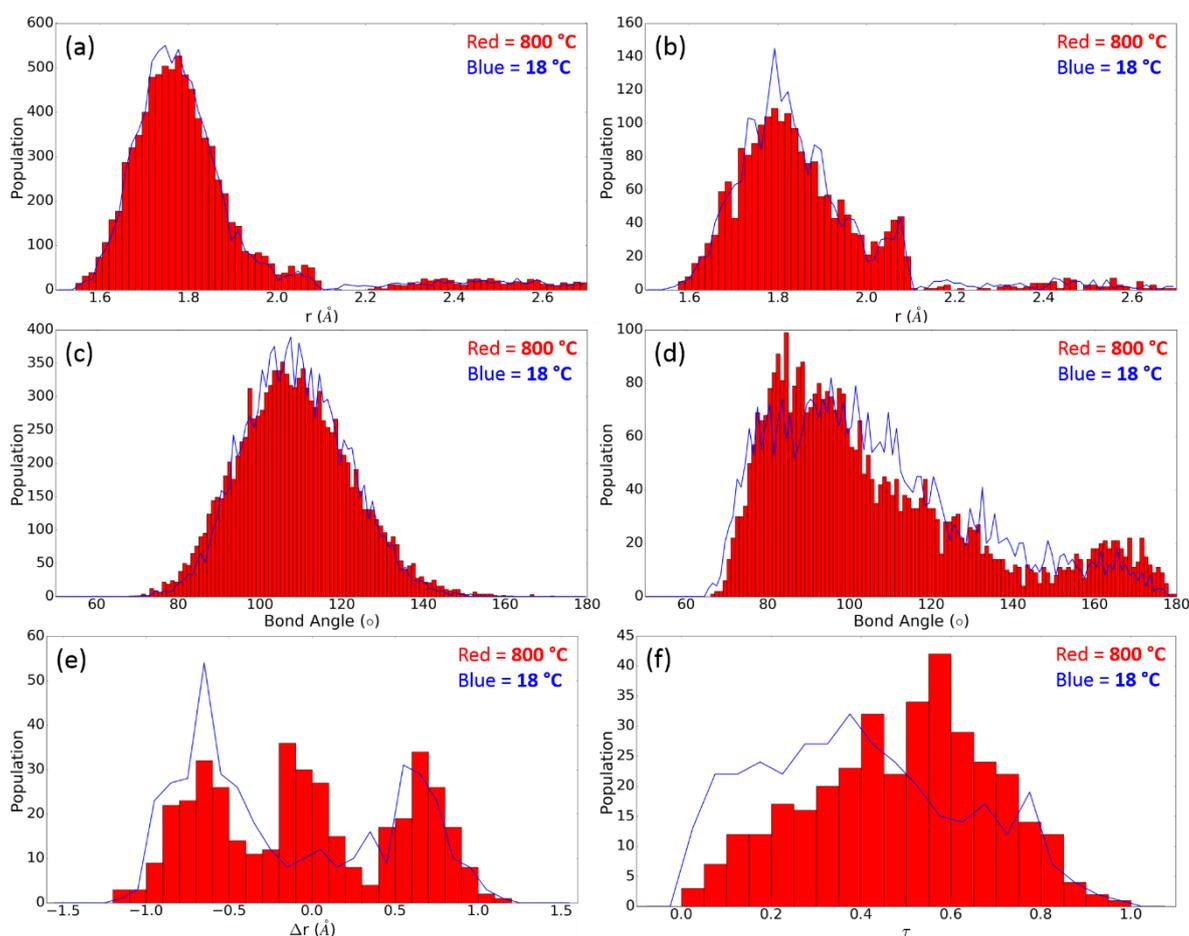
**Figure A.11** – Histograms from La$_8$Bi$_2$(GeO$_4$)$_6$O$_3$ at 800 °C from model **[SC8, P2]** (red bars) with the room temperature model **[SC4, P1]** (blue line) superimposed: (a) Ge–O bond distances in GeO$_4$; (b) Ge–O bond distances in GeO$_5$; (c) O–Ge–O bond angles in GeO$_4$; (d) O–Ge–O bond distances in GeO$_5$; (e) ΔGe–O$_{int}$ distances; (f) τ values.

## Appendix A.1 Python script details

- *rmc_oint_count.py*
    - Labels 'Te' (O$_{int}$) atoms as being in the A, B, C, D, E or F site and then counts the number of each.

- *rmc_Ge_oint_label.py*
    - Labels any 'Ge' atom that has a 'Te' atom within a distance of $r < 2.2$ Å as 'Ga'. This allows the Ge atoms with no neighbouring O$_{int}$ atoms and those with nearby O$_{int}$ atoms to be analysed separately.
    - A related script, *rmc_Ge_oint_label_pos_X.py*, combines *rmc_Ge_oint_label.py* with *rmc_oint_count.py* so that atomic density maps can be made (using *rmc2cgrds.py*) considering the occupancy of one type of O$_{int}$ site.

- *rmc_Ga_O_label.py*
    - Labels any 'O' within a distance of $r < 2.2$ Å of 'Ga' atoms (after using *rmc_Ge_oint_label.py*) as 'F' to distinguish them from O atoms near 'Ge'. This was

used so that separate atomic density maps could be made for situations when a 'Te' atom is or is not present.

- o A related script, *rmc_Ga_O_label _pos_X.py*, combines *rmc_Ge_oint_label.py* with *rmc_oint_count.py* so that atomic density maps can be made (using *rmc2cgrds.py*) considering the occupancy of one type of $O_{int}$ site.

- *rmc_GeO4_only.py*

  - o Removes atoms except for 'Ge' atoms and 'O' atoms after using *rmc_Ga_O_label.py* to obtain atomic density maps for the '$GeO_4$' tetrahedra only.

- *rmc2cgrds.py*

  - o Collapses a given number of supercell configurations into a single cell and then creates *.grd* files, which can be read by VESTA as an isosurface. The *.grd* files consist of voxels of a given dimension ($0.2 \times 0.2 \times 0.2$ $\text{Å}^3$ for all analyses in this work) and the number of atoms within each. This was also utilised in Chapter 6.

- *rmc_GaO_CN.py*

  - o Counts the number of 'O' and 'Te' atoms around 'Ga' atoms (after using *rmc_Ge_oint_label.py*) within a given radius ($r < 2.2$ Å in this work).

- *rmc_Te-Ge_dist.py*

  - o Calculates the distance between 'Te' atoms and the two closest 'Ge' atoms (in this case, all 'Ge' atoms within $r < 3.3$ Å from each 'Te' atom), then calculates the difference between those two distances, $\Delta Ge–O_{int}$, appending the $\Delta Ge–O_{int}$ values to a histogram. Also counts the number of instances where $0 \leq \Delta Ge–O_{int} \leq 0.25$.

- *rmc_GeO_bonds.py*

  - o Calculates the Ge–O and 'Ga'–O/'Te' distances (after using *rmc_Ge_oint_label.py*) within a given radius ($r < 2.7$ Å in this work), appending the Ge–O distances to one histogram and the 'Ga'–O/'Te' distances to another histogram.

- *rmc_GeO_angles.py*

  - o Calculates the O–Ge–O and O/'Te'–'Ga'–O/'Te' angles within a given radius of Ge/'Ga' atoms ($r < 2.2$ Å in this work) and appends the O–Ge–O angles to one histogram and the O/'Te'–'Ga'–O/'Te' angles to another.

  - o Also calculates the τ value for 'Ga' atoms with five-fold coordination.

# Appendix B

## Supplementary Data for Chapter 6
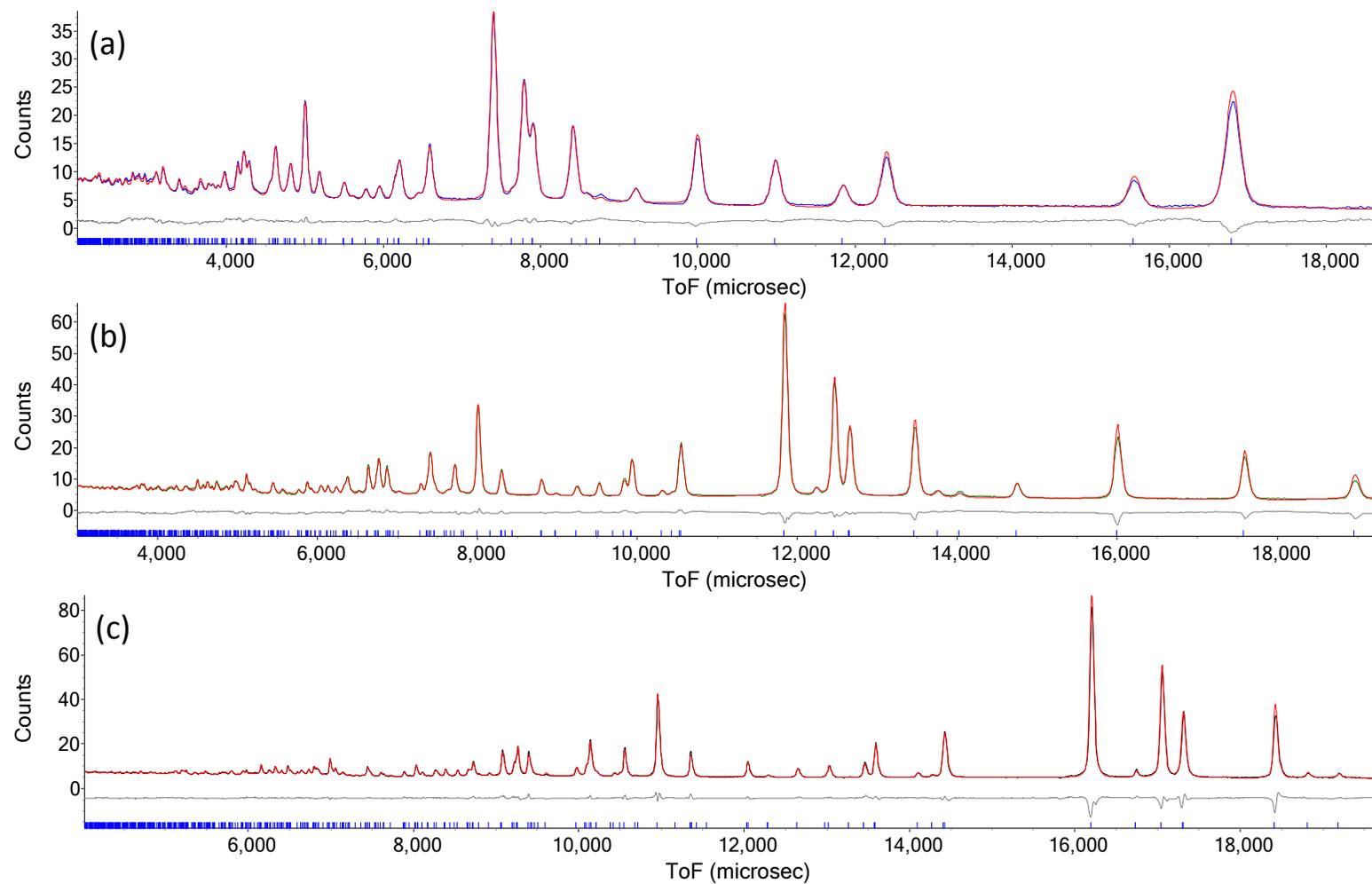
**Figure B.1 –** The Rietveld plots of $Ba_3NbMoO_{8.5}$ at room temperature from POLARIS (a) bank 3, $R_{wp}$ = 3.111%, $\chi^2$ = 6.863; (b) bank 4, $R_{wp}$ = 3.324%, $\chi^2$ = 10.167; (c) bank 5, $R_{wp}$ = 2.491%, $\chi^2$ = 4.465.
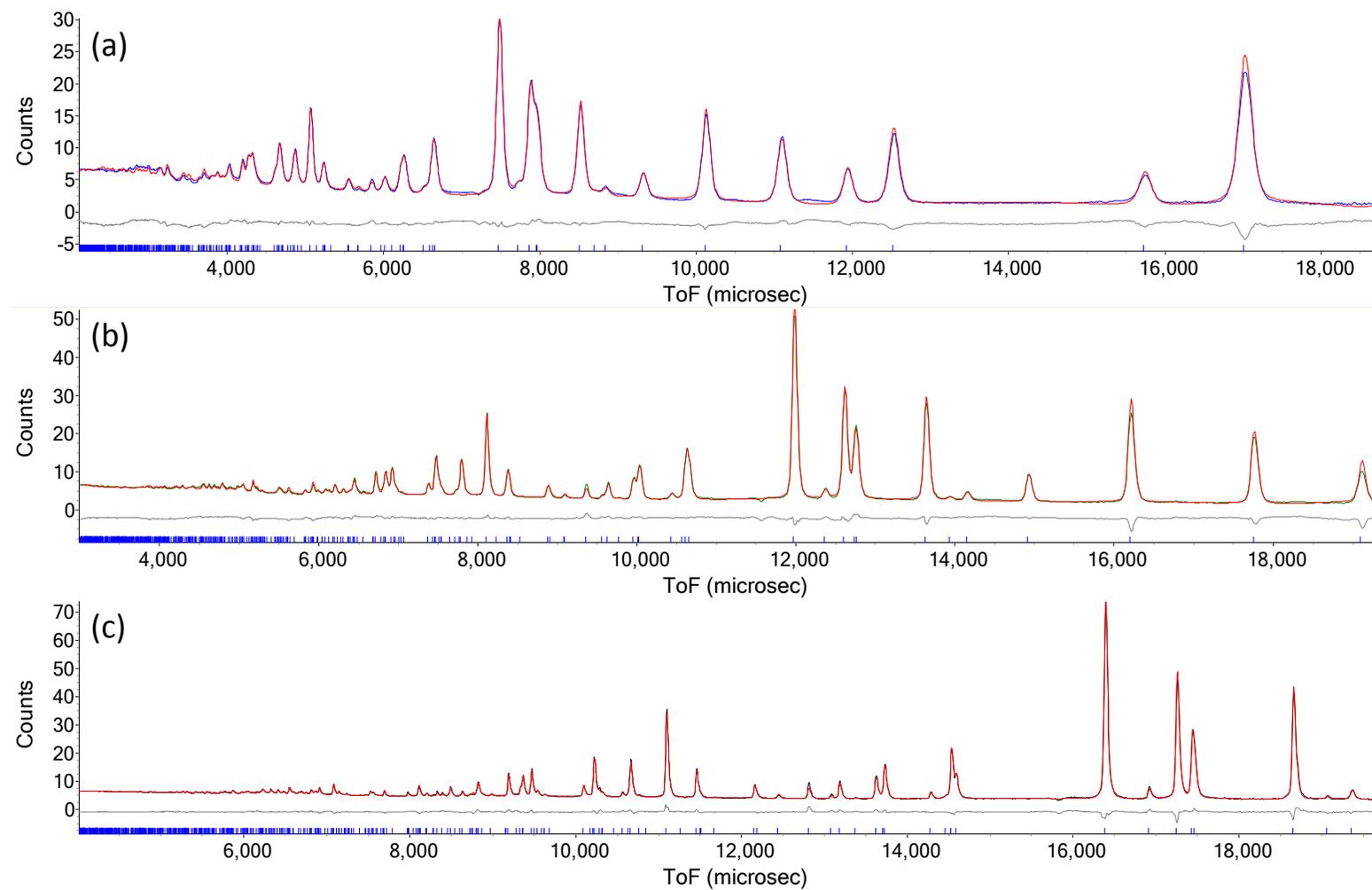
**Figure B.2 –** The Rietveld plots of Ba₃NbMoO₈.₅ at 600 °C from POLARIS (a) bank 3, $R_{wp}$ = 4.841%, $\chi^2$ = 9.247; (b) bank 4, $R_{wp}$ = 4.028%, $\chi^2$ = 11.123; (c) bank 5, $R_{wp}$ = 2.188%, $\chi^2$ = 3.711.
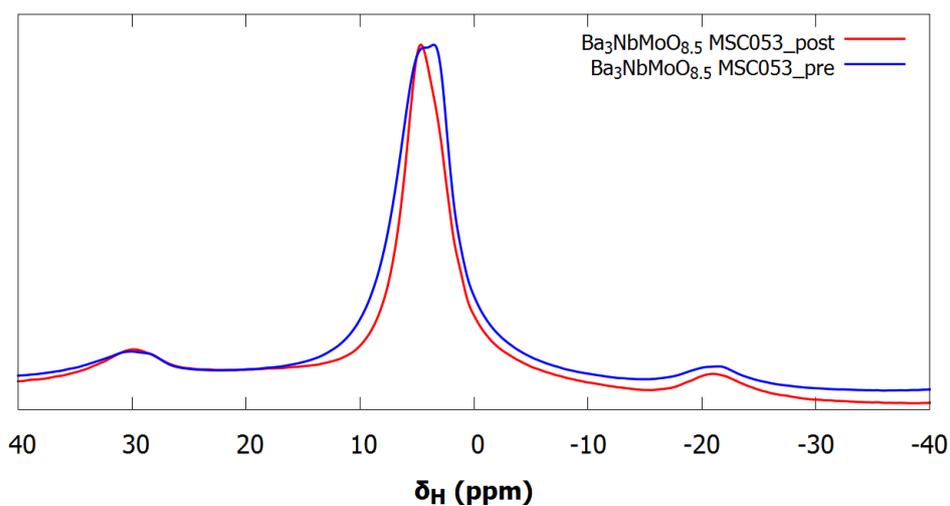
**Figure B.3 –** The $^1$H SSNMR spectra of Ba$_3$NbMoO$_{8.5}$ before being heated at 600 °C under vacuum (MSC053_pre) and after (MSC053_post).
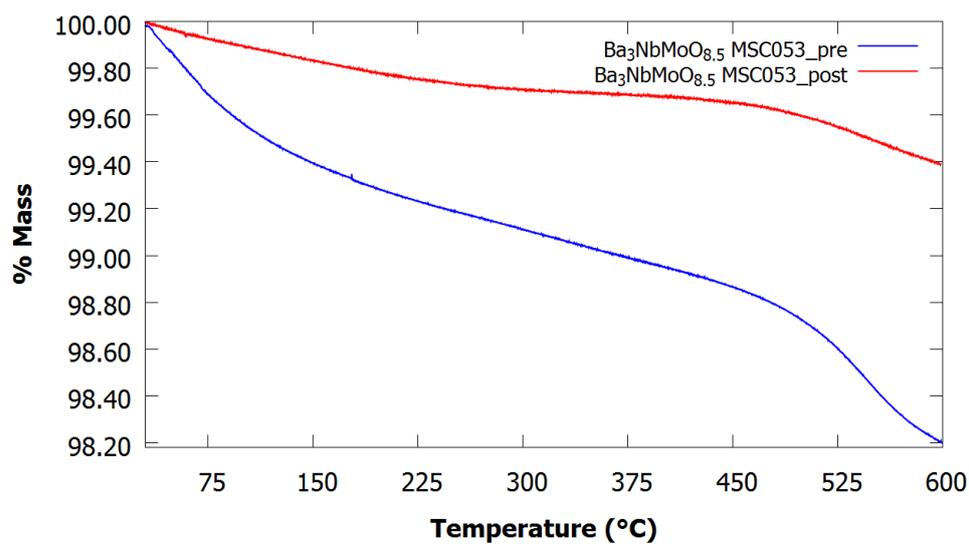


**Figure B.4 –** TGA under He atmosphere of Ba$_3$NbMoO$_{8.5}$ before being heated at 600 °C under vacuum (MSC053_pre) and after (MSC053_post).
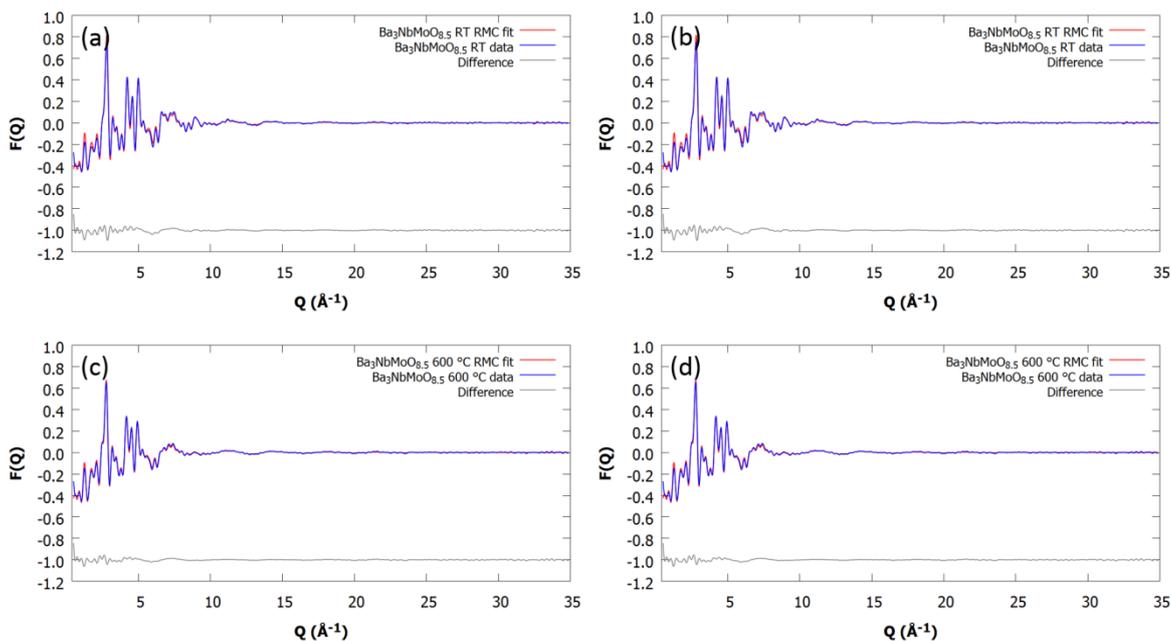
**Figure B.5** – Representative $F(Q)$ fits obtained from RMC analysis of $Ba_3NbMoO_{8.5}$ from the final configuration with the scale fitted: (a) room temperature **[SC1, P1]**, $\chi^2_{F(Q)}$ = 0.2241; (b) room temperature **[SC2, P1]**, $\chi^2_{F(Q)}$ = 0.2294; (c) 600 °C **[SC3, P1]**, $\chi^2_{F(Q)}$ = 0.1325; (d) 600 °C **[SC4, P1]**, $\chi^2_{F(Q)}$ = 0.1313.

## Appendix B.1 Python script details

The following python scripts were only used in the analysis of $Ba_3NbMoO_{8.5}$. Those that were also used for apatite analysis are included in Appendix A.

- *rmc_M_histogram.py* and *rmc_M_histogram_02.py*
    - Calculates the distance between Mo atoms and the ideal average crystallographic M1 and M2 sites (M2 on the 3*b* site) for atoms within a given radius ($r$ < 3.5 Å in this work) and appends these to separate histograms.
    - *rmc_M_histogram_02.py* does the same thing, but after Mo atoms have been labelled as 'Mo1' and 'Mo2'.
- *rmc_M1_M2_count.py*
    - Labels Mo atoms as 'Mo1' or 'Mo2', based on a given radius from first the M1 site ($r_1$ < 1.1 Å) and then, if still unlabelled, from the M2 site ($r_2$ < 1.2 Å) and counts how many atoms there are in each category. Also produces configurations with just the 'Mo1', 'Mo2' and unassigned 'Mo' atoms for further analysis.
- *rmc_M1_M2_local.py*
    - Uses the configurations with 'Mo1', 'Mo2' and the unassigned 'Mo' atoms in order to determine the arrangements of the Mo atoms as shown in Figure 6.14 in Chapter 6.
- *rmc_M_O_histogram_01.py*

- o Labels the Mo atoms as 'Mo1' and 'Mo2' using the same definition as *rmc_M1_M2_count.py*, then calculates the Mo1–O/'Te' (where 'Te' represent O2 and O3 atoms) and 'Mo2'–O/'Te' distances, appending them to two histograms.

- *rmc_M1_M2_angles.py*

  - o Labels Mo atoms as L as 'Mo1' and 'Mo2' using the same definition as *rmc_M1_M2_count.py*, then calculates the O/'Te'–'Mo1'–O/'Te' and O/'Te'–'Mo2'–O/'Te' bond angles in a given radius ($r < 3.05$ Å in this work) appends them to separate histograms.

  - o Additionally, appends the bond angles of Mo1 atoms with CN = 4, 5 and 6 into separate histograms.

  - o Calculates the $\tau$ values for the Mo1 with CN = 5 and appends the values to a histogram.

- *rmc2cgrds*

  - o Previously described in Appendix A. Modified the script for the O2 and O3 sublattice where atoms in the range of $0.55 < z < 0.75$ in the collapsed cell were all moved onto the $z = 0.667$ plane.